

Isomerisation Puzzles viewed with High Resolution Photoelectron Imaging

Benjamin Laws

July, 2018

A thesis submitted for the degree
of Doctor of Philosophy of
The Australian National University

Copyright by Benjamin Laws, 2018

Declaration

This thesis is an account of research undertaken between January 2015 and July 2018 at the Research School of Physics and Engineering, at the Australian National University, in Canberra, Australia.

This thesis contains no material that has been accepted for any other degree in any university. To the best of the author's knowledge and belief, it contains no material previously published or written by another person, except where due reference is made in the text.



Benjamin Laws
20 July 2018

Acknowledgements

I consider myself very lucky to have been given the opportunity to spend the last 4 years, working in such an incredible research environment. The decision to move across the ditch from New Zealand to Australia back in 2014, to pursue my post graduate study at the Australian National University, was initially made at short notice and with a fair amount of uncertainty. However this turned out to be one of the best decisions I've ever made, as I ended up working in an extremely interesting field, in an incredible research laboratory, and have managed to achieve some truly exciting results. Most importantly, I have been surrounded by amazing people, and have made friends for life.

The body of work presented in this thesis would not have been possible if it were not for the support and influence of others. None of the results presented here, would have been obtained if it were not for the help and advice of our excellent technical staff, Colin Dedman and Ross Tranter. Not only are they both great at solving the many electronic and mechanical problems that frequently occur in an experimental physics project like this, they are always happy to help discuss and implement new ideas, giving great advice on the best way to overcome a technical obstacle. There have been many times where I would have been totally lost without their support, and they have also taught me a lot!

There have been a lot of people who have been happy to give advice whenever it is needed, whether it is helping decode a surprise in a photoelectron spectrum, trying to understand a novel piece of molecular theory, or even finding the best way to phrase a sentence in a publication. I'd like to thank Brenton Lewis (ANU), for sharing his deep understanding of molecular spectroscopy, and his much appreciated advice. I also need to thank Bob Field (MIT) who has frequently given us advice on how to decode a spectrum, and understand some of the more nuanced aspects of molecular interactions, as well as Dan Neumark (Berkeley) and Hua Guo (New Mexico) who were instrumental in helping us achieve our vinylidene goal.

I also need to acknowledge the important role played by everyone in the Research School of Physics and Engineering, particular those in the Laser Physics Centre and the ex-AMPL crew. There are many people here who have contributed to making this an incredible place to come to work each day, with someone always available to bounce ideas off. It has also been a great opportunity to learn so much about everyone else's research, and the interesting science undertaken here. Thanks to funding from the Australian Research Council, I have also had the opportunity to visit the US three times to speak at the International Symposium on Molecular Spectroscopy, while visiting other leading laboratories in my field. This also allowed me to travel to Melbourne and Cairns, to speak at the Royal Australian Chemical Institute centenary congress, and at the International Conference on Photonic Electronic and Atomic Collisions.

I want to thank all the friends I've made here in Canberra over the last 4 years, who have helped make Australia feel like home. I also need to thank all my friends and family back home in New Zealand, including the University of Canterbury lecturers and Geraldine High teachers who had taught me so much, and particularly my parents who always encouraged me to work hard and aim high.

Finally, I need to give a massive thank you to my supervisor, Steve Gibson. Steve has been an incredible supervisor, and is the primary reason my time in Australia has been so successful. I have learnt so much off him, and he has allowed me to grow so much as a researcher. I have been very lucky to have a working relationship where we share an office space and work together everyday, which has meant he is always available to discuss new ideas or to help explain a difficult concept. He has always encouraged me to back myself, and given me the freedom to test any ideas I may have. I really could not have asked for a better supervisor, and owe Steve a lot for helping me get to where I am now.

This project was supported by funding from the Australian Research Council (Discovery Project Grant: DP160102585), while I was funded by an Australian Postgraduate Award and RSPE Supplementary Scholarship .

Abstract

Anion photoelectron spectroscopy has proven to be a versatile technique for studying transient neutral species, with very fast dynamics, as it obtains information from both the parent negative ion and the reactant neutral molecule. This technique is particularly useful for the study of chemical reactions where the transition state possess a stable anion. The development of velocity map imaging has greatly improved the spectral resolution and collector efficiency that may be achieved in charged particle detection, to allow for unprecedented detail in the recorded molecular spectra. In this work, a High Resolution Photoelectron Imaging (HR-PEI) spectrometer is used to investigate the nature of isomerisation.

A benchmark study of NO_2^- photodetachment reveals rotationally resolved structure, with a rapid change in the electron anisotropy behaviour near threshold used to decode the character of the highest occupied molecular orbital (HOMO). Measurements close to photodetachment threshold display additional high kinetic energy electron structure that cannot be associated with the ONO C_{2v} isomer. These additional fast electrons have the spectral signature of the C_s peroxy isomer NOO , with spectral analysis providing the first experimental evidence to confirm that the NOO isomer exists as a bound molecule. High resolution studies of similar atmospherically relevant molecules NO , O , and O_2 have been used for calibration, and determine new detail about these species.

A second section of this work tackles the long-standing problem of the vinylidene – acetylene isomerisation. The 1,2-hydrogen migration is a common mechanism in more complex organic reactions, making this an attractive area of research as a prototypical study. However, the dynamics of the vinylidene isomer are still poorly understood, in part due to conflicting experimental results. Photoelectron spectra of the vinylidene anion, presented in this work, reveal the presence of forbidden non-totally symmetric vibrational modes associated with a discrete jump in the anisotropy parameter. This is a consequence of Herzberg-Teller coupling between electronic states, and is essential for isomerisation to occur. Spectral signatures possessing an admixture of both vinylidene and highly excited acetylene local-bender character are discovered, providing a map of the doorway vibrational states through which the isomerization proceeds.

Similar molecules dicarbon and ethynyl are also studied, where the complex coupling mechanisms between the ground and first excited state of ethynyl provide more insight into the Herzberg-Teller interaction. The nature of dicarbon bonding is examined, with the anisotropy of C_2^- photodetachment determining the presence of a double bond, despite recent theoretical suggestions that a quadruple bond may be present.

Contents

Declaration	iii
Acknowledgments	v
Abstract	vii
I Introducing the isomerisation puzzles	3
1 Introduction	5
1.1 The missing isomer of nitrogen dioxide	5
1.2 The vinylidene-acetylene isomerisation problem	6
1.3 Isomerisation viewed with photoelectron imaging	7
2 Molecular Theory	11
2.1 The symmetry and structure of polyatomic molecules	11
2.1.1 Molecular term symbols	11
2.1.2 Character tables and irreducible representations	12
2.1.3 Electronic transitions	13
2.1.4 Vibrational transitions	15
2.1.5 Rotational transitions	18
2.2 Photodetachment mechanisms	20
2.2.1 Cross sections	21
2.2.2 Vibronic coupling mechanisms	24
3 The HR-PEI spectrometer	29
3.1 Spectrometer overview	29
3.2 Ion production	30
3.2.1 A single jet, 4-pin discharge source	31
3.2.2 Evolution of a dual jet source	33
3.3 Ion beam formation and mass separation	37
3.3.1 Simultaneous gating, bunching, and re-referencing	37
3.3.2 Time-of-flight mass spectroscopy	38
3.4 The Nd:YAG laser and optical parametric oscillator	39
3.4.1 Sunlite EX OPO	40
3.4.2 Direct YAG measurements	41
3.5 Imaging photoelectrons	42
3.5.1 Velocity map imaging and inverse Abel transforms	42
3.5.2 Detection and processing	46
3.5.3 Example O ⁻ measurement	48

II Nitrogen Dioxide - The discovery of a new isomer	53
4 Motivation	55
4.1 The history of NO ₂	55
4.1.1 Ions and photochemistry	55
4.2 Quantum structure of C_{2v} NO ₂	57
4.3 The peroxy isomer NOO	59
5 NO₂ and the Wigner filtering effect	61
5.1 Photoelectron spectroscopy of NO ₂ ⁻	61
5.2 Rotational Model of NO ₂ ⁻	65
5.2.1 Allowed and forbidden rotational levels	65
5.2.2 Selection rules and line intensities	66
5.2.3 NO ₂ rotational contour	68
5.3 Photoelectron angular distributions of NO ₂ ⁻ : The Wigner filtering effect	72
5.3.1 A general formula for molecular orbitals of any mixed character	72
5.3.2 Angular distributions of NO ₂ ⁻	73
5.3.3 A mixed <i>spd</i> anisotropy model of NO ₂ ⁻	76
5.3.4 Zero-core model and Dyson orbital approaches	77
6 Discovery of a new isomer	83
6.1 Fast electrons in the photoelectron spectrum of NO ₂ ⁻	83
6.1.1 Assigning the high eKE structure: O ⁻ and NO ⁻	85
6.1.2 Anomalous photofragment O ⁻	85
6.1.3 Absence of NO ⁻	86
6.2 Peroxy NOO	88
6.2.1 Assignment of NOO structure	88
6.2.2 Long photoelectron tails	90
6.2.3 Answer to the O ⁻ conundrum	91
6.2.4 Isomeric ratio	93
6.3 NOO ⁻ Photoelectron Angular Distribution	95
7 High resolution studies of calibration species	99
7.1 Benchmark measurements of NO ⁻	99
7.1.1 Spin orbit splitting in $X^2\Pi$ NO	100
7.1.2 A rotational band model of NO	101
7.1.3 NO ⁻ photoelectron angular distribution	105
7.2 A study of Oxygen	108
7.2.1 Photoelectron spectroscopy of O ⁻	109
7.2.2 Absolute cross-sections	112
7.2.3 Molecular oxygen	115
7.2.4 Hot band transitions	118
III Vinylidene - A mechanism for isomerisation	121

8 Motivation	123
8.1 The story of vinylidene	123
8.1.1 The lifetime conundrum	125
8.2 Introducing vinylidene	126
8.2.1 Vibrational levels	128
9 The other side of the barrier: Acetylene	131
9.1 An introduction to polyads	131
9.2 Local mode large amplitude motion	133
9.2.1 Transforming to local-mode coordinates	135
9.3 At the barrier to isomerisation	135
10 High resolution photoelectron imaging of vinylidene	139
10.1 Photoelectron spectra of vinylidene	139
10.1.1 Vinylidene photodetachment at 1064 nm	141
10.1.2 Rovibrational model of H ₂ CC	143
10.2 Anomalous anisotropy parameters	145
10.3 Excited states of vinylidene	148
10.3.1 Vinylidene photofragmentation	148
10.3.2 Excited state analysis	151
10.3.3 Temperature effects	153
11 Isomerisation at a barrier	157
11.1 Vibronic Coupling	157
11.1.1 The ¹ B ₂ state of vinylidene	159
11.1.2 Coupling strengths and transition moments	160
11.1.3 Forbidden mode transition intensities	163
11.2 Acetylene character inside vinylidene eigenstates	165
11.2.1 Searching for eigenstates with Cryo-SEVI	166
11.2.2 Full quantum dynamics and eigenstate decomposition	168
11.3 The unravelling of 1,2-hydrogen shifts	170
12 Puzzles of vinylidene relatives	173
12.1 Ethynyl and the coupling conundrum	173
12.1.1 Vibronic structure of the ethynyl radical	173
12.1.2 The photoelectron spectrum and coupling calculations	175
12.1.3 HR-PEI of C ₂ H ⁻ and C ₂ D ⁻	177
12.1.4 Questions from the anisotropy	182
12.2 Dicarbon and the bonding puzzle	184
12.2.1 Theoretical discrepancies	186
12.2.2 Problem solving with photoelectron spectroscopy	188
13 Concluding Remarks	197

Part I

Introducing the isomerisation puzzles

Introduction

In 1935 Eyring^[1], Evans and Polanyi^[2] simultaneously developed activated-complex theory to describe the dynamics of chemical reactions. This postulated that the rate of a reaction will be governed by the chemistry of transition state species. By definition, such species are short-lived in nature, and are unsuitable for detection in most standard spectroscopic experiments. However, anion photoelectron spectroscopy provides a versatile technique for the study of these transient states, as it obtains information from both the parent negative ion, and the neutral molecule in a photodetachment experiment^[3]. In fact, nearly any exotic or reactive neutral state may be studied if it supports a stable negative ion.

Here, we examine a specific class of chemical reactions involving isomerisation. In particular, the work of this thesis focuses on systems where one of the isomers is much less stable, a highly reactive radical for which the chemistry is virtually unknown. Anion photoelectron spectroscopy may be used to access these neutral transient states, providing evidence for the structure and dynamics of the highly reactive side of isomerisation barriers. Spectral signatures may also provide keys to understanding the mechanism of these isomerisation processes.

This work investigates long standing isomerisation problems, using high resolution photoelectron imaging (HR-PEI). Various other results are also discussed, including coupling in the ethynyl radical, and a solution to the dicarbon bonding puzzle.

1.1 The missing isomer of nitrogen dioxide

NO_2 , a brown toxic gas and key component of photochemical smog, has been the focus of numerous studies. However, the nitrite ion NO_2^- is less understood, with discussion based on only a handful of experimental results. In 1961 Clyne and Thrush^[4] first proposed the idea of a peroxy isomer of nitrogen dioxide, NOO , suggesting that this species may play an important role in the formation of NO in the atmosphere. In 1974, two NO_2^- photodetachment cross section experiments observed a long photoelectron tail^[5,6], that extended well below the accepted electron affinity of NO_2 ^[7]. The additional electrons were tentatively assigned to a possible isomer of nitrogen dioxide. This discovery initiated many future photodetachment studies, attempting to confirm the existence of NOO . However, none of them have found any further evidence to support the existence of a NOO isomer. *Ab-initio* calculations have been inconclusive, fuelling debate as to whether NOO represents a stable minimum on the NO_2 potential energy surface, or is merely a transient reaction intermediate. However, all the studies agree that if NOO exists, it will be a highly reactive, weakly bound radical.

The development of the velocity map imaging (VMI) technique has greatly improved the spectral resolution and collector efficiency that may be achieved in charged particle detection, to allow for unprecedented detail in the recorded molecular spectra. This allows the HR-PEI spectrometer at the Australian National University (ANU) to measure state of the art resolution, capable of resolving new spectral signatures in photoelectron exper-

iments. In this work, the rotational structure of C_{2v} NO₂ is revealed in the photoelectron spectrum, and for the first time, the missing peroxy NOO isomer of nitrogen dioxide is exposed, and spectroscopically characterised.

High resolution calibration studies

Like nitrogen dioxide, nitric oxide (NO) is also a prominent pollutant in the Earth's atmosphere. Consequently, many studies have focussed on the chemical and photophysical properties of this highly reactive radical. The negative ion, NO⁻ is a common prototype for the study of anion-cluster chemistry^[8], while the unusually small electron affinity of the neutral has received a lot of attention in photodetachment experiments^[9]. Photoelectron spectroscopy of NO⁻ provides a useful calibration species for the HR-PEI spectrometer, and is used in the search for NOO. The calibration measurements also reveal new spectral detail, redefining the electron affinity and providing additional information about this important radical.

Similarly, atomic and molecule oxygen provide useful calibration measurements, that also provide new spectroscopic information. As the electron affinity and fine-structure components of O⁻ are well defined from precise photoelectron microscopy experiments^[10], this species is used as a reference in HR-PEI experiments. For the atomic oxygen anion, short wavelength measurements access detachment to the excited O(¹D₂) state, helping to discern differences between experimental and theoretical predictions of the total photodetachment cross section of O⁻ at high energies.

1.2 The vinylidene-acetylene isomerisation problem

The isomerisation of vinylidene into linear acetylene is a long standing problem in the field of molecular spectroscopy. The 1,2-hydrogen shift is the simplest bond breaking isomerisation reaction in organic chemistry, and is a common mechanism in many complex reactions, making this an attractive area of research as a prototypical study. However, the dynamics of the vinylidene isomer are still poorly understood, in part due to conflicting experimental results. The story of vinylidene begins with the 1989 photoelectron experiment of the Lineberger group^[11], which observed multiple vibrational transitions of the neutral H₂CC isomer. However, the widths of these observed resonances have been commonly misinterpreted as the result of a sub-picosecond lifetime. This was followed by a Coulomb explosion imaging experiment at the Weizmann institute in 1998^[12], which recorded a 1:1 ratio of vinylidene:acetylene neutral isomers, 3.5 μ s after photodetachment, seriously contradicting the previous picosecond lifetime estimates.

Reconciling these two experimental results, while trying to understand the isomerisation reaction, has remained an unsolved problem. The reactivity and fast dynamics of the high energy vinylidene isomer preclude most experimental techniques, however on the negative ion potential energy surface it is the vinylidene geometry that is most stable, not the linear acetylene. Therefore, this problem is well suited to anion photoelectron spectroscopy. By studying H₂CC⁻ photodetachment using the HR-PEI spectrometer, new spectral signatures are found, that compliment other laboratory measurements and various theoretical calculations, to identify the vibrational doorway states through which the isomerisation proceeds.

Coupling in the ethynyl radical

The ethynyl radical C_2H is an attractive prototype for studying the effects of vibronic coupling in a molecule. A linear, triatomic radical, one may expect photodetachment of C_2H^- would produce a simple, well behaved spectrum. However various coupling mechanisms between the neutral ground $\tilde{X}^2\Sigma^+$ and low lying excited $\tilde{A}^2\Pi^+$ and $\tilde{A}^2\Pi^-$ electronic surfaces results in a complex manifold of vibrational levels around the $\tilde{\text{A}}$ origin.

As a small molecule, high level theoretical approaches may be applied to model these three interacting electronic states, to try and assign all of the structure present in the photoelectron spectrum of C_2H^- that has been measured by the Lineberger^[13] and Neumark^[14] groups. However discrepancies still exist between the assigned structure and observed spectral behaviour. By measuring the photodetachment of both C_2H^- and C_2D^- using HR-PEI, new information is obtained to help decode the complex coupling signatures.

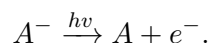
The dicarbon bonding puzzle

The dicarbon molecule appears to be a very simple homonuclear diatomic. However, the bonding structure of C_2 has long been a topic of debate, with various studies suggesting a C–C bond order of 2, 3, or 4. Standard qualitative theories also predict differing bond orders, with the Lewis structure predicting a quadruple bond, hybrid orbital theory predicting a triple bond, and molecular orbital theory predicting a double bond. Experimental bond lengths and dissociation energies measured in flame emission spectroscopy experiments^[15] suggest a bond order of 2 or 3. However, recent *ab-initio* calculations^[16] suggest a dicarbon bond order of 4.

Through measurements of the photoelectron angular distribution of the dicarbon anion at 355 nm, the molecular orbital structure is examined. The anisotropy measurements from this work determine the character of the orbitals involved in the detachment process, helping to define the C_2 bond order, solving this intriguing bonding puzzle.

1.3 Isomerisation viewed with photoelectron imaging

This work uses high resolution photoelectron imaging to search for spectroscopic signatures that may be related to the isomerisation problems. Experimentally, a mass isolated packet of ions is intersected by a laser beam. If the energy of the laser is higher than the binding energy of the target molecule, an electron will be detached,

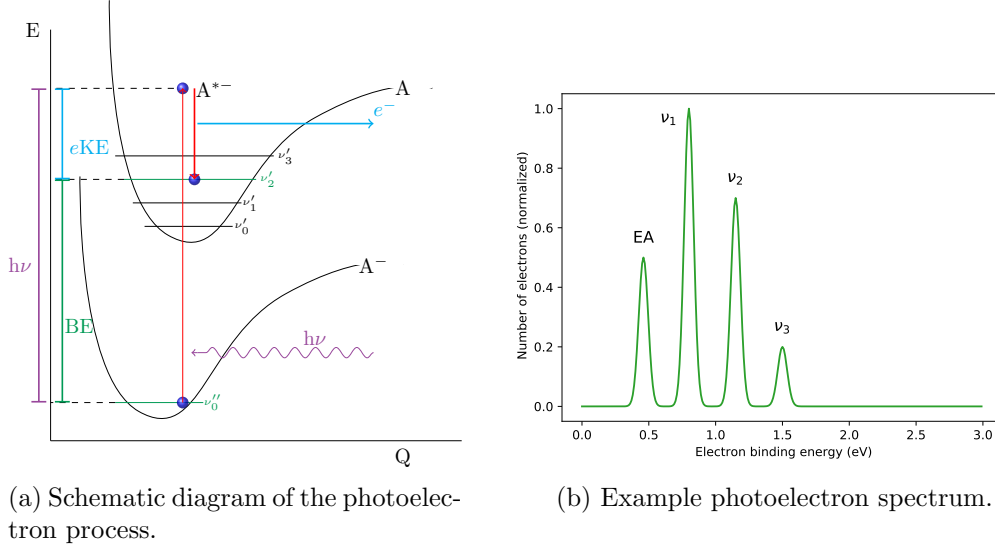


If the energy of the laser is known ($h\nu$), measuring the kinetic energy of the detached electron gives the binding energy,

$$\text{eBE} = h\nu - \text{eKE}.$$

Repeating this process for a large number of photons and ions will produce an electron energy distribution, with spectral resonances related to electronic and vibrational transitions in the neutral molecule, as depicted schematically in Fig. 1.1. This often yields the electron affinity, and relative energy structure of the neutral molecule. Hot band transitions, where the anion is not in the ground vibrational state, may also provide useful information

about the quantum structure of the negative ion. In very high resolution measurements it may be possible to resolve additional signatures, related to the rotational structure and spin-orbit coupling of the target molecule.



(a) Schematic diagram of the photoelectron process.

(b) Example photoelectron spectrum.

Figure 1.1: If a negative ion interacts with a photon (with $h\nu > eBE$), an electron will be emitted with kinetic energy $eKE = h\nu - eBE$. Measuring the electron kinetic energies from multiple detachment events gives an energy distribution similar to (b), where the resonances correspond to energy levels in the target neutral molecule.

Photoelectron angular distributions

While the photoelectron kinetic energy distribution reveals the electronic and vibrational structure of the neutral molecule, the angle at which an electron is ejected also holds valuable information. When an ion interacts with a photon, conservation of angular momentum governs that momentum of the outgoing electron must change by ± 1 . This creates two possible partial waves, $\ell + 1$ or $\ell - 1$.

Directly after detachment, the photoelectron and neutral molecule form a charge-induced dipole interaction that falls off rapidly at large r , and can be described by the form $V(r) \propto -1/r^4$. The outgoing photoelectron also experiences a centrifugal potential, related to the orbital angular momentum of the electron $V(r) \propto \ell(\ell+1)/r^2$. Unlike neutral photodetachment, where the strong Coulomb $-1/r$ interaction dominates the dynamics, in anion photodetachment this centrifugal term plays a significant role. This centrifugal barrier to detachment results in the Wigner threshold law,

$$\sigma \propto (eKE)^{\ell+\frac{1}{2}} \quad (1.1)$$

which describes how the photodetachment cross section varies with kinetic energy close to threshold, for a given ℓ .

This centrifugal barrier also affects the differential cross section. When photodetachment occurs with a linearly polarised light source, cylindrical symmetry is induced around the polarisation axis. The differential cross section for a solid angle $d\sigma/d\Omega$ is given by,

$$\frac{d\sigma}{d\Omega} = \frac{\sigma_{\text{total}}}{4\pi} [1 + \beta P_2(\cos \theta)], \quad (1.2)$$

where θ is the angle between the laser polarisation axis and the ejected photoelectron, P_2 is the second order Legendre polynomial, and β is the anisotropy parameter. The anisotropy parameter characterises the angular distribution of photoelectrons, with $\beta = +2$ corresponding to a distribution peaked parallel to the polarisation axis, $\beta = -1$ corresponding to a distribution peaked perpendicular to the polarisation, and $\beta = 0$ representing a perfectly isotropic distribution.

The photoelectron angular distribution relates to the interference of the $\ell + 1$ and $\ell - 1$ partial waves involved in the electron detachment, which hold information about the parent anion orbital. An example is given in Fig. 1.2, that shows photodetachment of NO^- at 1064 nm, with the laser polarisation aligned vertically. The photoelectrons are preferentially distributed around the horizontal of the image, indicative of a negative β parameter. Therefore, by measuring both the energetic and angular distribution of electrons in an anion photodetachment experiment, a more complete picture of the target molecule is constructed.

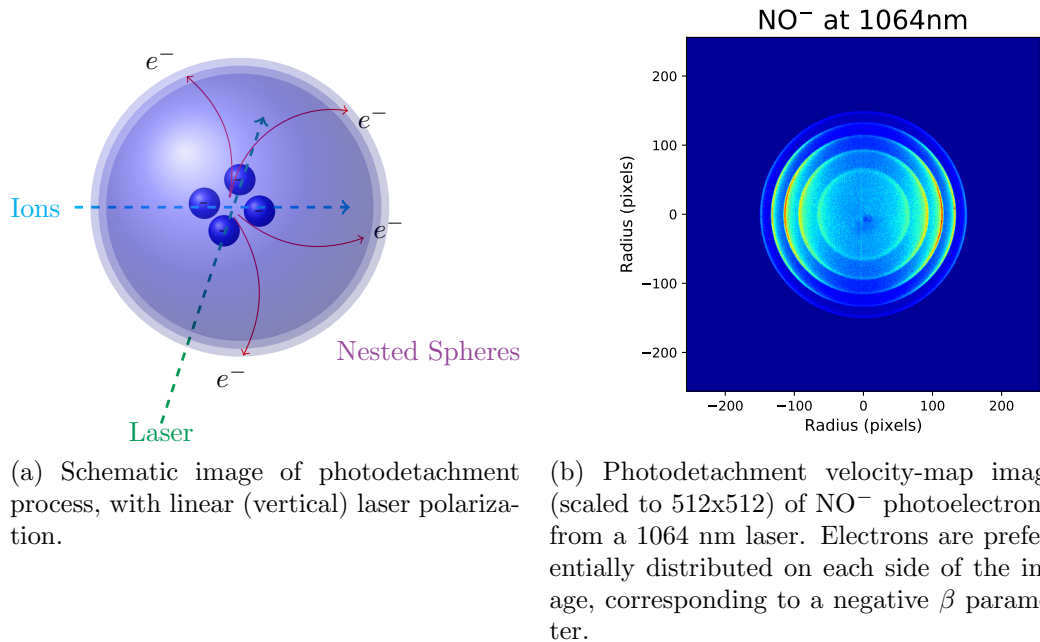


Figure 1.2: Photodetachment of an ion packet creates a series of nested 3D spheres, with electrons on the same sphere having identical kinetic energy. These nested spheres are then pancaked onto the detector by the VMI lens, as shown in (b). The angular distribution of these electrons is typically not isotropic, with the angular distribution characterised by the parameter β .

Electron detection using velocity map imaging

The first anion photoelectron spectroscopy (PES) experiment was reported in 1967 by Hall *et al.*^[17] where the electron affinity of Helium was investigated. Ions were produced in a hot-cathode source, and photodetached using a cw argon-ion laser. Electron kinetic energies were then measured using a hemispherical analyser. Continuous anion PES proved to be a versatile workhorse technique, and has since been used to study a large number of atomic and molecular species. This method was perfected by the Lineberger group, who recorded very high electron kinetic energy resolution using hemispherical analysers^[18]. In

1986 the first pulsed anion photoelectron experiment was reported by Posey *et al.*^[19], where spectra of O⁻, O₂⁻, and O₄⁻ were obtained using a pulsed Nd:YAG laser, with the electron energy distribution measured via time-of-flight of the detached electrons.

These experiments provided excellent electron kinetic energy resolution in the photoelectron energy distribution, with resolutions of $\sim 6 - 10$ meV typically reported for measurements from the Lineberger group^[20]. However, measuring angular distributions proved much more difficult, as this would require repeating measurements at different collection/polarisation angles, introducing problems related to interaction volumes and instrument drift. Consequently, while there is a rich catalogue of photoelectron spectra in the literature^[21], there are far fewer measurements of angular distributions.

The development of charged particle imaging provided good detection efficiency, while allowing for the angular distribution to be measured simultaneously with the kinetic energy distributions^[22]. However, early imaging techniques were impacted by distortion, which severely limited the energy resolution. It was not until the development of velocity map imaging by Eppink and Parker in 1997, that high resolution could be achieved in both the energetic and angular electron distributions^[23]. This made velocity map imaging an attractive method for photoelectron spectroscopy experiments, and has been particularly useful for the investigation of angular distributions. While early VMI instruments were still limited by the achievable energy resolution (with respect to traditional methods), more recent spectrometers (ANU^[24], Berkeley^[25]) now achieve μeV energy resolution, providing new opportunities in terms of the information that may be extracted from a photoelectron image. In particular, several traditional PES measurements hint at spectroscopic signatures for potential energy surface interactions, vibronic coupling, and angular distribution anomalies. Advanced VMI measurements may now investigate these observations, providing a better, more complete, window into these interactions. This work uses high resolution photoelectron imaging to examine transient species that exist near isomerisation barriers, where their dynamics are controlled by conical intersections. By building a more complete picture of the detachment process, new information may be obtained to help solve these isomerisation puzzles.

Molecular Theory

The research presented in this thesis employs a large amount of molecular and spectroscopic theory, with a concise description of concepts used throughout the work discussed here. More detailed theoretical concepts are introduced as required throughout the text.

2.1 The symmetry and structure of polyatomic molecules

While the concept of quantized energy levels was first introduced in Max Planck's quantum hypothesis in 1900, it was not until 1924 when Louis de Broglie introduced the concept of particle-wave duality, that a formal understanding of quantization occurred. In 1926 Erwin Schrödinger expanded on de Broglie's work, forming a general equation for any bound particle, now known as the Schrödinger wave equation. Schrödinger's equation,

$$i\hbar \frac{\partial}{\partial t} |\Psi(r,t)\rangle = \hat{H} |\Psi(r,t)\rangle \quad (2.1)$$

is the quantum mechanical analogue of Newton's laws in classical mechanics, able to describe the evolution of the quantum states of a physical system with time, where Ψ is the wavefunction of the quantum system and \hat{H} is the Hamiltonian operator. Stationary states, such as atomic and molecular orbitals, may be described by the time-independent form of the equation,

$$\hat{H} |\Psi\rangle = E |\Psi\rangle \quad (2.2)$$

where E is the corresponding energy of the stationary state Ψ . Famously, Schrödinger's equation for the single-electron hydrogen atom was solved by transforming the problem into polar coordinates, and separating the partial differential equation into three ordinary differential equations (ODE's), so that an exact solution was obtained. Boundary conditions required to solve the ODE's placed restrictions on the possible solution set, described by a set of quantum numbers n , ℓ , and m_ℓ . These quantum numbers could be related to the physical state of the electron, with n describing the energy of the electron, ℓ the magnitude of the angular momentum, and m_ℓ the direction of the momentum vector.

These quantum numbers, along with the spin of the electron S , uniquely define any electron in an atom, even though the Schrödinger equation may only be explicitly solved for the two body one-electron problem. A similar, larger set of quantum numbers are also able to describe the state of a molecular system, as will be described below.

2.1.1 Molecular term symbols

Atomic term symbols are used to define the quantum state of an atom, through a description of the angular momentum coupling. For light nuclei this is usually through an LS coupling scheme, where the total angular momentum $J = L + S$, while heavy nuclei exhibit jj coupling where $J = \sum_i j_i$. Similarly, molecular term symbols are often used to concisely describe the characteristics of a molecular state. For a linear molecule with cylindrical symmetry, the angular momentum vector of a single electron in the molecule

can be defined by the quantum number λ , where

$$\begin{aligned}\lambda = |m_\ell| &= 0 \quad 1 \quad 2 \quad 3 \dots \\ &= \sigma \quad \pi \quad \delta \quad \phi \dots\end{aligned}$$

Summing over every electron then gives the total projected orbital angular momentum of the molecule, defined by the quantum number Λ ,

$$\begin{aligned}\Lambda = \left| \sum_i m_{\ell_i} \right| &= 0 \quad 1 \quad 2 \quad 3 \dots \\ &= \Sigma \quad \pi \quad \Delta \quad \Phi \dots\end{aligned}$$

The total axial angular momentum of the molecule Ω is then given by the sum of the total orbital momentum Λ and the total spin momentum M_s ,

$$\Omega = \left| \Lambda + \sum_i m_{s_i} \right|$$

The characteristics of a molecular state may then be uniquely identified by it's orbital and spin angular momenta vectors using the molecular term symbol,

$$^{2S+1}\Lambda_\Omega$$

where S is the total spin of the molecule and $2S + 1$ is known as the multiplicity of the state. For homonuclear diatomics, additional labels are added to indicate if the state is symmetric (+) or anti-symmetric (-) with respect to reflection through a plane containing the internuclear axis, and whether the state has even (g) or odd (u) parity under inversion.

For less symmetric molecules were Λ is not well defined, the term symbol will often include the Mulliken symbol for the irreducible representation that represents the symmetry of the state. In spectroscopy, term symbols are often accompanied by an empirical labelling system, where the ground state is defined as X, with higher energy states with the same multiplicity consecutively labelled A, B, C, ... while states of a different multiplicity are labelled a, b, c, ... For a non-linear polyatomic molecule of C_{2v} symmetry one may see a state labelled,

$$\tilde{X} \ ^1A_1$$

representing a singlet ground state with A_1 symmetry.

2.1.2 Character tables and irreducible representations

Symmetry is a powerful tool for understanding the structure and dynamics of molecules, and so it is common practice to assign molecules into point groups, which describe the level of symmetry present. These classifications are based on 5 types of symmetry elements; rotation around axes (C_n), planes of symmetry (σ), inversion centres (i), rotation-reflection axes (s_n), and the identity operator (E).

Molecules may possess various combinations of these symmetry elements, with a larger number of symmetry elements corresponding to systems with higher overall symmetry. Possible combinations of elements form point groups, with any given molecule conforma-

tion able to be assigned to one of the point groups summarised in Table 2.1.

Table 2.1: Descriptions of the point group families, used to describe the symmetry elements of a molecule.

Group	Description
C_n	n -fold axis of symmetry, with no other symmetry element apart from the identity E . C_1 is a point group without any symmetry.
C_{nv}	n -fold axis of symmetry, and n planes of symmetry σ_v through the axis. C_{1v} only has a plane of symmetry, and is written as C_s .
	$C_{\infty v}$ has an ∞ -fold axis, corresponding to a non-symmetric linear molecule.
S_n	n -fold rotation-reflection axis, which implies other symmetry elements are present. S_2 implies an inversion centre and is written as C_i .
C_{nh}	n -fold axis of symmetry, perpendicular to a horizontal plane σ_h .
D_n	n -fold axis of symmetry, perpendicular to n two-fold axes.
D_{nh}	n -fold axis of symmetry, n vertical planes of symmetry σ_v , and a horizontal plane σ_h . $D_{\infty h}$ has an ∞ -fold axis, ie. a linear symmetric molecule.
T_d	Tetrahedral symmetry
O_h	Octahedral or cubic symmetry
I_h	Icosahedral or dodecahedral symmetry
K_h	Spherical, continuous rotation-inversion symmetry, ie. atoms

For each of the above point groups, a corresponding character table describes how each of the irreducible representations of the group behave under the relevant symmetry elements. As an example, the C_{2v} character table is shown below.

Table 2.2: Character table for the C_{2v} point group.

C_{2v}	E	$C_2(z)$	$\sigma_v(xz)$	$\sigma_v(yz)$	
A_1	1	1	1	1	z
A_2	1	1	-1	-1	R_z
B_1	1	-1	1	-1	x, R_y
B_2	1	-1	-1	1	y, R_x

From Table 2.2 we can see that the C_{2v} point group has 4 irreducible representations, two of which are symmetric (A_1, A_2) and two which are asymmetric (B_1, B_2). The table shows how each of these representations acts (symmetric/asymmetric) under the symmetry operators the identity (E), rotation of 180° about the z axis $C_2(z)$, and a reflection in the mirror planes $\sigma_v(xz)$ and $\sigma_v(yz)$. This information may be used to not only characterise the symmetry of a molecule's geometry, but also the symmetry of the electronic, vibrational, and rotational energy structure, as will be seen in later parts of this chapter.

2.1.3 Electronic transitions

The Born-Oppenheimer approximation proposes that in solving the Schrödinger equation (2.2), the motion of the atomic nuclei and electrons in a molecule may be treated as separable. This allows for the total wavefunction of the molecule Ψ to be decomposed into its electronic and nuclear (vibrational, rotational) components,

$$\Psi = \psi_{\text{electronic}} \times \psi_{\text{nuclei}}. \quad (2.3)$$

In molecular spectroscopy this approximation is often applied further, to also separate the vibrational and rotational components for independent treatment. For the single electron atom, a spherical Coulomb potential may be used to describe the electron motion,

$$\hat{H} = -\frac{\hbar^2}{2\mu} \nabla^2 - \frac{Ze^2}{4\pi\epsilon_0 r} \quad (2.4)$$

where \hbar is the reduced Planck constant, ∇ is the Laplacian operator, Ze is the charge of the nucleus, and ϵ_0 is the vacuum permittivity. Applying this Hamiltonian to the Schrödinger equation (2.2), and solving the radial part of the equation produces energy eigenvalues,

$$E_n = -\frac{1}{n^2} \frac{\mu c^2 Z^2 \alpha^2}{2} \quad (2.5)$$

where n is the principle quantum number and α is defined as the fine structure constant, with corresponding stationary states,

$$\psi_{nl}(r) = \sqrt{\left(\frac{2Z}{na_0^*}\right)^3 \frac{(n-\ell-1)!}{2n(n+\ell)!}} e^{-\rho/2} \rho^\ell P_{n-\ell-1}^{2\ell+1}(\rho) \quad (2.6)$$

where a_0^* is the reduced Bohr radius, $P(\rho)$ is the Laguerre polynomial, and ρ is defined as $\rho = 2Zr/na_0^*$. Each value of n defines a discrete energy level or electronic state of the atom.

For molecules, Eq. (2.2) becomes a vastly more complex multi-body problem, with electron-electron, electron-nuclei, and nuclei-nuclei interactions present. As such, exact solutions to the Schrödinger equation are unobtainable, with approximations required to model the electronic structure. These include a mean-field approximation, where each electron is treated one by one as moving in the mean electric field created by all the others. Corrections are then made to account for specific electron-electron correlation interactions.

Potential energy surfaces

Electronic states represent eigenvalues of the Schrödinger equation, and so for any fixed nuclei configuration, must have a constant energy (E_n). However, if the nuclei configuration changes, the energy of the electronic state will also change. Mapping out the energy variation of a state with respect to a nuclear coordinate produces a potential energy surface. While quantum numbers, the constants of the motion, and term symbols may be used to label an electronic state, the potential energy surface describes the nature of the state. Specifically, if a surface has no minimum the electronic state is unstable, whereas a surface with at least one minimum will be stable. However, occasionally a state may have a potential surface with multiple minima, with each well minima sometimes corresponding to a different isomer.

In general, different electronic states of a molecule will have distinct potential energy surfaces, with minima occurring at differing nuclear coordinates, which may change the symmetry and point group of the molecule. The steepness and depth of the surfaces may vary, with the slope of the well defining the vibrational frequency of the molecule,

$$\omega^2 = \frac{1}{\mu} \frac{\partial^2 V}{\partial Q^2} \quad (2.7)$$

where V is the potential energy and Q is the nuclear coordinate, while the depth of the well defines the dissociation energy D_e . A conical intersection is where two (or more) potential energy surfaces cross. At this point the potential energy surfaces are degenerate, and non-adiabatic coupling between the states becomes important. This leads to a breakdown in the Born-Oppenheimer approximation, as the coupling between the electronic and nuclear motion becomes non-negligible. If the overlapping states differ in multiplicity, an intersystem crossing may occur, which is a non-radiative process that reverses the spin of an electron.

Molecular fine structure

Fine structure refers to the observation of coupling between the spin of an electron and its orbital motion. As a rotating electric charge, electrons create a magnetic dipole moment given by $\mu_S = \gamma_s \mu_B \frac{S}{\hbar}$, where S is the spin angular momentum, μ_B is the Bohr magneton, and γ_s is the electron-spin g-factor. In cases with strong spin-orbit coupling, known as Hund's case (a), both L and S have well defined axial components Λ and Σ , with the total angular momentum given by $\Omega = \Lambda + \Sigma$. This creates sub levels within an electronic state with different total angular momenta Ω . The energy of these sub levels will also differ, as can be described by the Larmor and Thomas interactions. The Larmor interaction accounts for the energy associated with a magnetic moment being present in a magnetic field, while the Thomas interaction accounts for the curved trajectory of an electron, which finds that the energy shift between the levels is proportional to the dot product $\vec{L} \cdot \vec{S}$. Even in molecular species with strong spin-orbit coupling, the fine structure splitting is typically on the order of $\sim 1 - 100 \text{ cm}^{-1}$, much smaller than the average spacing of electronic states $\sim 10,000 - 100,000 \text{ cm}^{-1}$.

2.1.4 Vibrational transitions

Like electronic motion, the vibrational motion of a molecule is also quantised, and may be described using the harmonic oscillator approximation,

$$\hat{H} = \frac{\hat{p}^2}{2m} + \frac{1}{2}m\omega^2 \hat{x} \quad (2.8)$$

where \hat{p} and \hat{x} are the momentum and position operators, m is the molecule mass and ω is the vibrational frequency. Applying this Hamiltonian to the Schrödinger equation (2.2) produces energy eigenvalues,

$$E_v = \omega_e \left(v + \frac{1}{2} \right), \quad (2.9)$$

with corresponding stationary states,

$$\psi_v(x) = \frac{1}{\sqrt{2^v v!}} \left(\frac{m\omega_e}{\pi\hbar} \right)^{1/4} e^{-\frac{m\omega_e x^2}{2\hbar}} H_v \left(\sqrt{\frac{m\omega_e}{\hbar}} x \right), \quad (2.10)$$

where v is the vibrational quantum number, and $H_v(x)$ are the Hermite polynomials.

In general a molecule with N atoms will exhibit $3N-6$ different vibrational modes if it has a non-linear geometry, or $3N-5$ if it is linear. Linear molecules have an extra vibrational degree of freedom, to account for the axial symmetry which results in one less degree of rotational freedom. The shape of each of these vibrational modes is described by a set of normal mode vectors, which depict the forces that apply to each of the N

atoms at equilibrium during the oscillation. Vibrational motion may also be described by their internal coordinates, which describe the type of motion involved: stretching (symmetric/asymmetric), bending (scissoring), rocking, wagging, or twisting.

The symmetry of the vibrational modes of a molecule may be determined from the character tables introduced in section 2.1.2. An example of assigning vibrational modes for ethylene (C_2H_4) is given below.

Vibrational level symmetry

As a planar molecule with an inversion centre, C_2H_4 belongs to the point group D_{2h} . Therefore, the number of reducible representations may be determined by applying each of the symmetry operators in the first row of the D_{2h} character table (2.3) to C_2H_4 , while counting the number of atoms that remain stationary throughout the transformation. By multiplying this with the character contributions listed in Table 2.4 the reducible representations Γ_{red} may be calculated.

Table 2.3: Character table for the D_{2h} point group

D_{2h}	E	$C_2(z)$	$C_2(y)$	$C_2(x)$	i	$\sigma(xy)$	$\sigma(xz)$	$\sigma(yz)$	
A_g	1	1	1	1	1	1	1	1	$x^2y^2z^2$
B_{1g}	1	1	-1	-1	1	1	-1	-1	R_z xy
B_{2g}	1	-1	1	-1	1	-1	1	-1	R_y xz
B_{3g}	1	-1	-1	1	1	-1	-1	1	R_x yz
A_u	1	1	1	1	-1	-1	-1	-1	
B_{1u}	1	1	-1	-1	-1	-1	1	1	z
B_{2u}	1	-1	1	-1	-1	1	-1	1	y
B_{3u}	1	-1	-1	1	-1	1	1	-1	x

Table 2.4: Character contributions of common symmetry operators, for any point group

E	σ	C_2	i	C_3
3	1	-1	-3	0

Table 2.5: Counting the number of reducible representations for C_2H_4

C_2H_4	E	$C_2(z)$	$C_2(y)$	$C_2(x)$	i	$\sigma(xy)$	$\sigma(xz)$	$\sigma(yz)$
No. Stationary Atoms	6	0	0	2	0	6	2	0
Character Contribution	3	-1	-1	-1	-3	1	1	1
Γ_{red}	18	0	0	-2	0	6	2	0

The reducible representations Γ_{red} may be decomposed into a linear combination of irreducible representations, by taking the dot product of each Mulliken representation in the character table (ie A_g) with the reducible representations in Table 2.5. Dividing this by the total number of representations in the point group, in this case $h = 8$, and subtracting the translations and rotations given in the character table as x, y, z and R_x, R_y, R_z gives

the number of irreducible representations. The first four lines of working would read:

$$\begin{aligned} A_g &: (1 \times 18 + 1 \times -2 + 1 \times 6 + 1 \times 2)/8 - 0 = 3 \\ B_{1g} &: (1 \times 18 - 1 \times -2 + 1 \times 6 - 1 \times 2)/8 - 1 = 2 \\ B_{2g} &: (1 \times 18 - 1 \times -2 - 1 \times 6 + 1 \times 2)/8 - 1 = 1 \\ B_{3g} &: (1 \times 18 + 1 \times -2 - 1 \times 6 - 1 \times 2)/8 - 1 = 0 \end{aligned}$$

Completing this process for the rest of table gives the total number of Γ_{irrep} in C_2H_4 :

$$\Gamma_{\text{irrep}} = 3 \times A_g + 2 \times B_{1g} + B_{2g} + A_u + B_{1u} + 2 \times B_{2u} + 2 \times B_{3u}$$

This represents the number, and symmetry, of all allowed vibrational modes in C_2H_4 . As a non-linear molecule, the number of normal vibrational modes expected is $3 \times 6 - 6 = 12$ which is consistent with the number of Γ_{irreps} derived from the character table.

This is a powerful technique, as it allows for all of the vibrational modes of a molecule to be assigned to the correct symmetry simply from knowing the molecular geometry and the corresponding character table. This will prove a useful technique for the molecules studied in Parts II and III of this thesis.

Franck-Condon factors

In spectroscopy we are often interested in the energy and intensity of vibrational transitions - for photoelectron spectroscopy these are typically transitions from the vibrational ground state of the anion to vibrationally excited states of the neutral. While the position of a vibrational transition may be determined from equations similar to Eq. (2.9), the intensity of the transition is determined by selection rules, electric dipole transition moments (electronic), Franck-Condon factors (vibrational), and Hönl-London factors (rotational).

In the dipole moment approximation the intensity of a photodetachment transition from an initial state ψ_i'' to a final state ψ_f' is proportional to the electric dipole transition moment,

$$\langle \chi_f'(Q) \cdot \psi_f'(q, Q) | M(q, Q) | \psi_i'' \cdot \chi_i''(Q) \rangle \quad (2.11)$$

where ψ_i'' and ψ_f' are the electronic wavefunctions and χ_i'' and χ_f' are the vibrational wavefunctions for the anion and neutral target states respectively, while q and Q represent the electronic and nuclear coordinates. Assuming that the electric transition moment μ does not depend on the nuclear coordinates, the transition intensity will then be proportional to the square of the overlap integral of the initial and target vibrational wavefunctions,

$$|\langle \chi_f'(Q) | \chi_i''(Q) \rangle|^2 \quad (2.12)$$

which is known as the Franck-Condon factor.

For a polyatomic molecule with n vibrational normal mode coordinates (Q_n), the potential energy surface may be modelled by an n -dimensional harmonic oscillator well, with the vibrational wavefunction the product of $n \times$ one-dimensional harmonic oscillator wavefunctions. In the parallel approximation, the normal coordinates of the anion and neutral are assumed to be identical, allowing for the multidimensional Franck-Condon

factor to be written as a product of n one-dimensional wavefunction overlap integrals,

$$|\langle \chi'_f(Q) | \chi''_i(Q_1) \rangle|^2 = |\langle \chi'_1(Q_1) | \chi''_1(Q_1) \rangle \cdot \langle \chi'_2(Q_2) | \chi''_2(Q_2) \rangle \cdot \langle \chi'_3(Q_3) | \chi''_3(Q_3) \rangle \dots|^2 \quad (2.13)$$

where each overlap integral may be calculated analytically using the harmonic oscillator wavefunctions given in Eq. (2.10). When the normal mode coordinates of the initial and target state differ significantly, Duschinsky rotations may be used to account for the difference in coordinates.

2.1.5 Rotational transitions

The rotational energy and angular momentum of a molecule are also quantized, and may be described using the rigid rotor model,

$$\hat{H} = -\frac{\hbar^2}{2I} \nabla^2 \quad (2.14)$$

where I is the moment of inertia, given by $I = \sum_i m_i r_i^2$, \hbar is the reduced Planck constant, and ∇ is the Laplacian operator. As there is no resistance to rotation, the Hamiltonian only includes a kinetic energy term. Applying this to the Schrödinger equation (2.2) produces energy eigenvalues

$$E_J = BJ(J+1), \quad (2.15)$$

where J is the rotational quantum number and the rotational constant B is given by,

$$B = \frac{\hbar}{8\pi^2 c I}. \quad (2.16)$$

The corresponding stationary state eigenfunctions from Eq. (2.2) are the spherical harmonics $Y_J^m(\theta, \varphi)$ used in solving the one-electron hydrogen problem,

$$Y_J^m(\theta, \varphi) = \Theta(\theta)\Phi(\varphi) = \frac{1}{\sqrt{2\pi}} e^{im\varphi} \left[\frac{(2J+1)(J-|m|)!}{2(J+|m|)!} \right]^{1/2} P_J^{|m|}(\cos \theta), \quad (2.17)$$

where $P_J^{|m|}(\cos \theta)$ are the Legendre polynomials in $\cos \theta$.

For any molecule, three moments of inertia I_A , I_B , and I_C may be defined about three perpendicular axes through the centre of mass. The relative magnitude of these moments defines the symmetry of the rotation, and can be used to describe the allowed rotational transitions. The corresponding rotational constants (Eq. 2.16) are inversely proportional to these moments, and are typically defined with the primary rotational constant A as the largest constant (smallest moment) and C as the smallest constant (largest moment). There are four main distinctions used in describing the rotational properties of molecules, which are defined based on the relative rotational constants :

Linear molecule:	$A \approx \infty, B = C$
Spherical top:	$A = B = C$
Symmetric top:	Oblate top: $A = B < C$ Prolate top: $A < B = C$
Asymmetric top:	$C < B < A$

Each flavour of rigid rotor posses certain characteristics, with unique selection rules and line intensities which may be used to decode a rotational spectrum. Sometimes it may be

useful to treat molecules that are strictly an asymmetric top as an approximate symmetric top, when two of the unique moments are both much smaller or larger than the third. In this case, the amount of prolate (rugby ball shape) or oblate (disc shape) character can be determined by the parameter κ ,

$$\kappa = \frac{2[B - \frac{1}{2}(A + C)]}{A - C} \quad (2.18)$$

where a value of $\kappa = -1$ represents a pure prolate top, and $\kappa = 1$ a pure oblate top.

Hönl-London factors and line intensities

Similar to how Franck-Condon factors determine the intensity of a vibrational transition, Hönl-London factors calculate the line intensity of a rotational transition. In the dipole moment approximation, the intensity of a photodetachment transition from an initial rotational state ϕ_i'' to a final state ϕ_f' is given by,

$$I_{J,K} = C_v \cdot A(J,K) \cdot g(J,K) \cdot e^{\frac{-E(J,K)hc}{kT}} \quad (2.19)$$

where C_v is the vibrational Franck-Condon factor $|\langle \chi_i'' | \chi_f' \rangle|^2$, $A(J,K)$ is the square of the rotational line intensity (Hönl-London) factor, $g(JK)$ is the degeneracy of the rotational level, and $e^{\frac{-E(J,K)hc}{kT}}$ is the Boltzmann factor for the anion. In many cases the Hönl-London factor $A(J,K)$ may be calculated algebraically, and depends on the type of rotation (linear/spherical/symmetric/asymmetric) and the transition type (parallel or perpendicular). Expressions for these cases can be readily found in the literature^[26], with an example for a linear molecule and a symmetric top shown below,

Branch	Linear	Symmetric
R: $\Delta J = +1$	$\frac{(J+1+\Lambda)(J+1-\Lambda)}{J+1}$	$\frac{(J+1)^2 - K^2}{(J+1)(2J+1)}$
Q: $\Delta J = 0$	$\frac{(2J+1)\Lambda^2}{J(J+1)}$	$\frac{K^2}{J(J+1)}$
P: $\Delta J = -1$	$\frac{(J+\Lambda)(J-\Lambda)}{J}$	$\frac{J^2 - K^2}{J(2J+1)}$

Wigner 3-j symbols

Another method that may be used to determine the intensities of rotational transitions involves the use of Wigner 3-j symbols, which use symmetry considerations to aid in the addition of angular momenta. By approaching the problem from an angular momentum description, the rotational properties of a molecule may be examined.

First there are two important cases to consider: Hund's case (a) is where there is strong electrostatic coupling between the orbital angular momentum L and the \hat{z} axis, with the spin angular momentum S strongly coupled to L via spin-orbit interactions. The total angular momentum of the system is,

$$J = \Omega + R \quad (2.20)$$

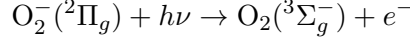
where Ω is the projection of the LS coupled angular momentum, and R is the rotational angular momentum of the nuclei. Whereas Hund's case (b) represents cases where there

is weak or no spin-orbit coupling, and the total angular momentum is represented by,

$$J = N + S \quad (2.21)$$

where N is the orbital and rotational angular momentum, and S is the spin.

The intensity of a rotational transition depends on whether the initial and final state are case (a) or case(b). Looking at the photodetachment of O_2^- as an example,



we see that $\text{O}_2^-(^2\Pi_g)$ is a Hund's case (a) molecule due to a large spin-orbit splitting, whereas $\text{O}_2(^3\Sigma_g^-)$ is Hund's case (b). Buckingham *et al.*^[27] showed that for a transition from case (a) to (b) the rotational Q factor, which contains the dependence of the total cross section on the rotational quantum numbers, took the general form,

$$Q(j_i, N'', \ell) = \sum_{\chi=j_i-1/2}^{j_i+1/2} (2\chi + 1) \begin{pmatrix} j_i & S'' & \chi \\ -\Delta\Lambda & \Sigma'' & \Lambda' - \Omega'' \end{pmatrix}^2 \begin{pmatrix} N' & \chi & J'' \\ -\Lambda' & \Lambda' - \Omega'' & \Omega'' \end{pmatrix}^2 \quad (2.22)$$

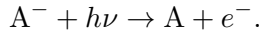
where j_i is the total angular momentum of the initial electron, and Λ and Σ are the axial components of the orbital and spin angular momentum respectively. The Q factor may then be evaluated by computing the 3-j symbols and summing χ from $j_i - 1/2$ to $j_i + 1/2$. For our oxygen example, $S'' = 1/2$, $\Lambda'' = 1$, $\Lambda' = 0$, so the Q factor becomes,

$$Q = \sum_{\chi=j_i-1/2}^{j_i+1/2} (2\chi + 1) \begin{pmatrix} j_i & 1/2 & \chi \\ 1 & \Omega'' - 1 & -\Omega'' \end{pmatrix}^2 \begin{pmatrix} N' & \chi & J'' \\ 0 & -\Omega'' & \Omega'' \end{pmatrix}^2 \quad (2.23)$$

Writing a rotational Q-factor in this form can prove very useful, as the 3-j symbols in Eq. (2.23) can be easily computed within a python language script, allowing for all of the rotational line intensities of a photodetachment transition to be evaluated. Substituting Eq. (2.23) into Eq. (2.19) and combining with the correct selection rules allows for the entire rotational spectrum of a molecule to be calculated, and has been used in this work to model the photoelectron spectrum of O_2^- , NO^- and C_2^- .

2.2 Photodetachment mechanisms

In the experiments presented in this work, photons from a pulsed laser source intersect a perpendicular beam of mass-isolated negative ions. If the photons are more energetic than the electron affinity (EA) of the target ion, photoelectrons will be emitted.



From the Beer-Lambert law, if an initial photon flux ϕ is incident on an ion packet with density ρ and cross section σ over a distance l , the outgoing photon flux will be given by,

$$\phi_{\text{out}} = \phi e^{-\rho\sigma l}. \quad (2.24)$$

For every photon that is absorbed by an ion, one photoelectron is emitted, therefore the current of photoelectrons produced is given by,

$$j_{\text{elec}} = \phi[1 - e^{-\rho\sigma l}]. \quad (2.25)$$

To maximise the number of photoelectrons recorded in a measurement, the ion beam is optimised to try and increase the ion density at the interaction region ρ , however the photodetachment cross section σ will also play an important role in determining the electron yield.

2.2.1 Cross sections

In the electric dipole approximation, the differential cross section for ejection of an electron from an ion using a linearly polarized light source is given by,

$$\frac{d\sigma}{d\Omega} = \frac{4\pi^2\alpha m k_f \nu}{\hbar} |\langle \Psi_f | \Sigma_n \hat{z}_n | \Psi_i \rangle|^2, \quad (2.26)$$

where Ψ_i and Ψ_f are the initial and final state wavefunctions, ν is the transition frequency, k_f is the wavenumber of the final state, α is the fine structure constant $\alpha = \frac{e^2}{4\pi\epsilon_0\hbar c}$, and the electric dipole moment is summed over all n electrons. The initial state wavefunction Ψ_i represents the anion, and can be described by a solution to the Schrödinger equation (2.2), while the final state wavefunction consists of the neutral molecule plus the ejected free electron.

After the photodetachment event, the effective potential describing the motion of the detached electron is of the form,

$$V_{\text{eff}}(r) = V(r) + \frac{l(l+1)\hbar^2}{2\mu r^2}. \quad (2.27)$$

Where $V(r)$ represents the interaction between the parent neutral molecule and the detached electron, and the second term represents the centrifugal barrier. In anion photoelectron spectroscopy, the neutral and outgoing electron form a charge-induced dipole interaction that falls off rapidly at large r , and can be described by the form $V(r) \propto -1/r^4$. Consequently, the free electron may be described by the equation,

$$|\phi_k\rangle = 4\pi \sum_{L=0}^{\infty} (-i)^L e^{ikL} \sum_{M=-L}^L Y_{LM}^*(\theta' \varphi'), \quad (2.28)$$

where k is the momentum of the electron and $Y_{LM}^*(\theta' \varphi')$ are the spherical harmonics. In the limit of large r , the equation for the free electron (2.28) is described by a plane wave plus a spherical wave. The initial and final state wavefunctions of Eq. (2.26) may then be written as,

$$\Psi_i = |\phi_i\rangle = \psi_{n\ell}(r) Y_{\ell m}(\theta, \varphi) \quad (2.29)$$

$$\Psi_f = |\phi_k; \phi_f\rangle = 4\pi \sum_{L=0}^{\infty} (-i)^L e^{ikL} \psi_{kL}(r) \sum_{M=-L}^L Y_{LM}(\theta, \varphi) Y_{LM}^*(\theta', \varphi'), \quad (2.30)$$

where n, ℓ, m and k, L, M are the quantum numbers of the anion and neutral respectively^[28]. In spherical polar coordinates, the electric dipole operator \hat{z} in Eq. (2.26) may

be written,

$$\hat{z} = r \cos \theta = \sqrt{\frac{4\pi}{3}} r Y_{10}(\theta, \varphi). \quad (2.31)$$

Therefore, substituting equations (2.30), and (2.31) into the dipole moment $\langle \Psi_f | \hat{z} | \Psi_i \rangle$ gives,

$$M_{fi} = \langle \Psi_f | \hat{z} | \Psi_i \rangle = 4\pi \sum_{L=0}^{\infty} (-i)^L e^{ikL} \langle \psi_{kL} | r | \psi_{n\ell} \rangle \sum_{M=-L}^L \sqrt{\frac{4\pi}{3}} Y_{LM}(\theta', \varphi') \langle Y_{LM} | Y_{10} | Y_{\ell m} \rangle. \quad (2.32)$$

However the expression above may be simplified by applying the dipole approximation. As angular momentum must be conserved, when a negative ion absorbs a photon, the outgoing electron must have momentum $L = \ell \pm 1$. This reduces the sum over L from $\sum_{L=0}^{\infty}$ to $\sum_{L=\ell-1}^{\ell+1}$. Furthermore, if linearly polarized light is used, $\Delta m = 0$, reducing the sum over M from $\sum_{M=-L}^L$ down to $M = m$. Orr *et al.*^[27] have shown that this allows for the integral over spherical harmonics in Eq. (2.32) to be evaluated,

$$\sqrt{\frac{4\pi}{3}} \langle Y_{Lm} | Y_{10} | Y_{\ell m} \rangle = (-1)^m \left[\frac{(2L+1)}{2\ell+1} \right]^{1/2} \langle L100 | \ell 0 \rangle \langle L1m0 | \ell m \rangle, \quad (2.33)$$

where $\langle L100 | \ell 0 \rangle \langle L1m0 | \ell m \rangle$ are the Clebsch Gordan coefficients. The differential cross section may then be written in terms of a sum over m ,

$$\frac{d\sigma}{d\Omega} = \frac{4\pi^2 \alpha k_f m \nu}{\hbar g_i} \sum_m |M_{fi}^{L=\ell-1} + M_{fi}^{L=\ell+1}|^2, \quad (2.34)$$

where M_{fi} are the transition dipole moments (Eq. 2.32) for the $L = \ell - 1$ and $L = \ell + 1$ partial waves of the ejected electron. Evaluating this expression, and simplifying using Clebsch Gordan formula and re-writing the expression in terms of Legendre polynomials gives,

$$\begin{aligned} \frac{d\sigma}{d\Omega} = & \frac{1}{4\pi} \frac{4\pi^2 \alpha k_f m \nu}{\hbar g_i} \left[\frac{\ell \chi_{\ell,\ell-1}^2 + (\ell+1) \chi_{\ell,\ell+1}^2}{3(2\ell+1)} \right] \\ & \left(1 + \frac{\ell(\ell-1)\chi_{\ell,\ell-1}^2 + (\ell+1)(\ell+2)\chi_{\ell,\ell+1}^2 - 6\ell(\ell+1)\chi_{\ell,\ell+1}\chi_{\ell,\ell-1} \cos \Delta_{\ell\pm 1}}{(2\ell+1)[\ell\chi_{\ell,\ell-1}^2 + (\ell+1)\chi_{\ell,\ell+1}^2]} P_2(\cos \theta) \right), \end{aligned} \quad (2.35)$$

where $\chi_{\ell,\ell\pm 1}$ denotes the radial integrals $\langle \psi_{k,\ell\pm 1} | r | \psi_{n,\ell} \rangle$, $\Delta_{\ell\pm 1}$ is the difference in the partial wave phase shifts ($\delta_{\ell+1} - \delta_{\ell-1}$), and $P_2(\cos \theta)$ is the second order Legendre polynomial. Importantly, the first part of this expression represents the total cross section of the detachment process,

$$\sigma_{\text{total}} = \frac{4\pi^2 \alpha k_f m \nu}{\hbar g_i} \left[\frac{\ell \chi_{\ell,\ell-1}^2 + (\ell+1) \chi_{\ell,\ell+1}^2}{3(2\ell+1)} \right], \quad (2.36)$$

while the second part includes what is known as the Cooper-Zare expression,

$$\beta_\ell = \frac{\ell(\ell-1)\chi_{\ell,\ell-1}^2 + (\ell+1)(\ell+2)\chi_{\ell,\ell+1}^2 - 6\ell(\ell+1)\chi_{\ell,\ell+1}\chi_{\ell,\ell-1} \cos \Delta_{\ell\pm 1}}{(2\ell+1)[\ell\chi_{\ell,\ell-1}^2 + (\ell+1)\chi_{\ell,\ell+1}^2]}, \quad (2.37)$$

which defines the anisotropy parameter β ^[29]. Therefore, the differential cross section for photodetachment from a linearly polarized light source can be written,

$$\frac{d\sigma}{d\Omega} = \frac{\sigma_{\text{total}}}{4\pi} (1 + \beta P_2(\cos \theta)). \quad (2.38)$$

Hanstorp coefficients

Equations (2.37) and (2.38) describe the angular distribution of photoelectrons from a photodetachment event in terms of the angular momentum of the anion orbital ℓ , the transition radial matrix elements $\chi_{\ell,\ell\pm 1}$ and a partial wave phase shift $\Delta_{\ell\pm 1} = (\delta_{\ell+1} - \delta_{\ell-1})$. These expressions are converted into a more usable form by introducing Hanstorp coefficients, which side steps the evaluation of the radial matrix elements $\chi_{\ell,\ell\pm 1}$. From the Wigner law, the photodetachment cross section close to threshold is given by,

$$\sigma \propto k^{2\ell+1}, \quad (2.39)$$

where k is the wavenumber of the ejected electron ($k = \sqrt{(2m\epsilon)}$, where m is the mass and ϵ the kinetic energy of the electron) and ℓ is the angular momentum quantum number^[30]. Therefore, the photodetachment cross section depends on the electron kinetic energy. Taking the ratio of the cross sections for the $\ell + 1$ and $\ell - 1$ partial waves gives,

$$\frac{\sigma_{\ell+1}}{\sigma_{\ell-1}} \propto \frac{\epsilon^{\ell+3/2}}{\epsilon^{\ell-1/2}} = \epsilon^2. \quad (2.40)$$

As the cross section $\sigma_{\ell\pm 1}$ is proportional to the square of the corresponding radial transition element $\chi_{\ell,\ell\pm 1}$ Hanstorp^[31] showed that the ratio of transition moments could be approximated as,

$$\frac{\chi_{\ell,\ell+1}^2}{\chi_{\ell,\ell-1}^2} = A_\ell^2 \epsilon^2, \quad (2.41)$$

where A_ℓ^2 is the proportionality constant known as the Hanstorp coefficient. The application of Wigner's threshold law in determining the energy dependence of these terms, and applying it over large energy ranges (spanning several electron volts), has been questioned in the past, as it is strictly only valid at very small kinetic energies^[32–34]. However, many successful and diverse applications of Hanstorp's approach suggest that while the Wigner predicted cross sections of partial waves are not valid above threshold, the laws prediction of cross-section ratios is much more robust^[24,31,35–37]. This suggests that while Hanstorp coefficients are derived from the Wigner threshold law, as they only apply to ratios of cross sections the approach is still valid at kinetic energies well above threshold^[34].

This allows for the energy dependence of an angular distribution to be examined explicitly, with the behaviour described using Hanstorp coefficients and phase shifts $\Delta_{\ell\pm 1}$. For example, detachment from a p anion orbital is described by substituting $\ell = 1$ into the Cooper-Zare expression (2.37) which gives,

$$\beta_p = \frac{2A_1^2 \epsilon^2 - 4A_1 \epsilon \cos \Delta_{\ell\pm 1}}{1 + 2A_1^2 \epsilon^2}, \quad (2.42)$$

where $A_1^2 = \frac{1}{\epsilon^2} \frac{\chi_{1,2}^2}{\chi_{1,0}^2}$. If experimental anisotropy measurements are recorded at various detachment energies, the data may be fitted to Eq. (2.42) to determine the fitting constants

A_1 and $\cos \Delta_{\ell \pm 1}$.

2.2.2 Vibronic coupling mechanisms

The term vibronic coupling is used to describe the interaction between the nuclear and electronic motion of a molecule, and usually involves a breakdown in the Born-Oppenheimer approximation, with the total wavefunction of the molecule no longer separable into its electronic and nuclear components (Eq. 2.3). These interactions are often identified by abnormalities in a molecular spectrum, and may proceed through a variety of different coupling mechanisms. A description of the coupling mechanisms that play an important role in the work of this thesis are given below.

Herzberg-Teller coupling

Herzberg-Teller coupling involves an interaction between potential energy surfaces, that is mediated through vibrational transitions. This often allows for formally forbidden electronic transitions to occur, due to mixing between different electronic states through a vibrational promoter.

For typical cases, where there is no strong coupling between the electronic and nuclear motion of a molecule, the Born-Oppenheimer approximation may be invoked,

$$\Psi_{jt}^{\text{CA}}(r, Q) = \psi_j^0(r, Q_0)\chi_{jt}^{\text{CA}}(Q), \quad (2.43)$$

where ψ_j^0 is the electronic wavefunction of the j^{th} electronic state at a specified set of fixed nuclear coordinates Q_0 , and $\chi_{jt}(Q)$ is the vibration-rotation wavefunction of the nuclear motion. This is often called the crude adiabatic (CA)^[38,39] or static wavefunction^[40]. However for cases where the coupling between the nuclear and electronic motion is not negligible, perturbation theory may be applied to include the nuclear-electronic interactions in the wavefunction description,

$$\Psi_{jt}(r, Q) = \Psi_{jt}^{\text{CA}}(r, Q) + \sum_{kr \neq jt} \frac{\langle \psi_{jt}^{\text{CA}} | \Delta U | \psi_{kr}^{\text{CA}} \rangle}{E_{jt}^{\text{CA}} - E_{kr}^{\text{CA}}} \psi_{kr}^{\text{CA}}(r, Q), \quad (2.44)$$

where $\Psi_{jt}^{\text{CA}}(r, Q)$ is the crude adiabatic wavefunction (Eq. 2.43), and ΔU represents the change in the potential when moving from the fixed nuclear coordinate Q_0 to the displaced coordinate Q .

This may be rewritten in terms of the Herzberg-Teller expansion (more detail will be given in chapter 11),

$$\Psi_{jt}(r, Q) = \psi_j^0(r, Q_0)\chi_{jt}^{\text{CA}}(Q) + \sum_{k \neq j} \sum_r \sum_n \gamma_{kr,jt}^n \psi_k^0(r, Q_0)\chi_{kr}^{\text{CA}}(Q). \quad (2.45)$$

In Eq. (2.45) the first term $\psi_j^0(r, Q_0)\chi_{jt}^{\text{CA}}(Q)$ represents the typical allowed transitions of the j^{th} electronic state, while the second term $\gamma_{kr,jt}^n \psi_k^0(r, Q_0)\chi_{kr}^{\text{CA}}(Q)$ represents the vibronic coupling between electronic states ψ_j and ψ_k acting through the vibrational promoter mode χ_{kr} . The term $\gamma_{kr,jt}^n$ is known as the mixing coefficient. Each summation in the expansion may be linked to a corresponding energy state, with $\sum_{k \neq j}$ summing over the electronic states, \sum_r summing over vibrational states, and \sum_n summing over the promoter modes.

From symmetry considerations it can be shown that vibronic Herzberg-Teller coupling will only occur when,

$$\Gamma_{kr} \otimes \Gamma_{jt} \not\subseteq \Gamma_{\text{totally symmetric}} \quad (\text{and } Q_n \text{ is not totally symmetric}).$$

The wavefunction of a molecule may then be written in short hand as the sum of the formally allowed transitions and the forbidden vibronic transitions,

$$|\Psi_{jt}\rangle = |\psi_j \chi_{jt}\rangle + \gamma_{kr,jt} Q_n |\psi_k \chi_{kr}\rangle, \quad (2.46)$$

which highlights how the vibronically coupled transitions are linked to the k^{th} electronic state, not the original j^{th} state.

Anharmonic coupling

Anharmonic coupling involves the interaction between different vibrational modes within an electronic state, and has been shown to play an important role in the distribution of vibrational energy, with anharmonically coupled vibrations often the preferential pathway for relaxation. The simplest example of anharmonic coupling may be found in combination bands, where two or more vibrational modes are excited simultaneously.

In the dipole and harmonic oscillator approximations, the transition moment for a fundamental vibrational transition from $v_1 = 0$ to $v_1 = 1$ is given by,

$$\langle \Psi_f | \vec{\mu} | \Psi_i \rangle = \langle 1 | Q_1 | 0 \rangle = \frac{1}{\sqrt{2}} \left(\frac{\partial \mu}{\partial Q_1} \right)_0 \quad (2.47)$$

where $Q_1 = q_1(m\omega_1/\hbar)^{1/2}$ with q_1 the normal mode coordinate and ω_1 the vibrational mode frequency. However for the $v_1 + v_2$ combination band transition $|0, 0\rangle$ to $|1, 1\rangle$ the transition moment becomes,

$$\begin{aligned} \langle 1, 1 | \vec{\mu} | 0, 0 \rangle &= \left(\frac{\partial \mu}{\partial Q_1} \right)_0 \langle 1, 1 | Q_1 | 0, 0 \rangle + \left(\frac{\partial \mu}{\partial Q_2} \right)_0 \langle 1, 1 | Q_2 | 0, 0 \rangle + \left(\frac{\partial^2 \mu}{\partial Q_1 \partial Q_2} \right)_0 \langle 1, 1 | Q_1 Q_2 | 0, 0 \rangle \\ &= \mu_{v_1}^{\text{MA}} + \mu_{v_2}^{\text{MA}} + \mu^{\text{EA}}. \end{aligned} \quad (2.48)$$

Hence the total transition moment of a combination band has three components, a mechanical anharmonicity (MA) term for each vibrational mode and an electrical anharmonicity term. Under the harmonic oscillator approximation the MA terms both vanish, and a non-zero value can only be obtained if the potential function V is anharmonic and includes cubic and higher order terms. If the higher order terms are neglected, the MA terms may be written as,

$$\mu_{v_1}^{\text{MA}} = \frac{1}{4\hbar\omega_1} \left(\frac{\partial \mu}{\partial Q_1} \right)_0 \left(\frac{\partial^3 V}{\partial^2 Q_1 \partial Q_2} \right)_0 \quad (2.49)$$

$$\mu_{v_2}^{\text{MA}} = \frac{1}{4\hbar\omega_2} \left(\frac{\partial \mu}{\partial Q_2} \right)_0 \left(\frac{\partial^3 V}{\partial^2 Q_2 \partial Q_1} \right)_0. \quad (2.50)$$

$$(2.51)$$

For the third term, Nishida *et al.*^[41] have shown that perturbation theory may be used to

write the electronic anharmonicity as,

$$\mu^E = \frac{1}{2} \left(\frac{\partial^2 \mu}{\partial Q_1 \partial Q_2} \right)_0. \quad (2.52)$$

From these expressions we can see that anharmonic coupling is likely to be strongest between vibrational modes with large anharmonicity in their potential wells.

Renner-Teller coupling

Renner-Teller coupling is an interaction that involves rovibronic coupling in linear molecules with degenerate electronic states. In degenerate vibrational modes, a new quantum number ℓ_i may be introduced representing the angular momentum corresponding to the bending vibration. This takes a magnitude of $\hbar\ell_i$ where $\ell_i = v_i, v_i - 2, v_i - 4, \dots, 1$ or 0. The total vibrational angular momentum is then given by,

$$\ell = \hbar \left| \sum_i (\pm \ell_i) \right|, \quad (2.53)$$

where the \pm accounts for the orientation with respect to the symmetry axis. In the Born-Oppenheimer approximation, the different vibronic energy levels ℓ_i are degenerate, however in systems where significant coupling between the electronic and nuclear motion lead to a break down in this approximation, the degeneracy in ℓ_i is lost.

This can be described by picturing the potential energy surface during a vibration. When a linear molecule is bent during vibrational motion, the surface of the degenerate electronic state (V) splits into two (V^+ and V^-). However the effect of the potential splitting on the resultant vibrational levels can be complex to understand, as the two potentials V^+ and V^- are in contact and so vibrational levels may be able to jump between the potentials. In fact, it has been shown that only Σ vibronic levels may be rigorously assigned to either potential, with Π and Δ levels belonging to both^[26].

Jahn-Teller theorem

The Jahn-Teller theorem states that stability and degeneracy are not possible simultaneously unless the molecule is linear^[42]. This has been observed in many cases, where geometric distortions occur to non-linear molecules to remove a degeneracy in an electronic state. This distortion can also lead to a splitting in the potential energy surface, similar to the Renner-Teller effect mentioned above.

This can be extended to cases where degeneracy-symmetry breaking occurs in a non-degenerate state due to the influence of a low lying excited state, known as the pseudo Jahn-Teller effect. Coupling between the nondegenerate ground state and degenerate low lying excited state can contribute significantly to instability in both states^[43].

Interplay of coupling processes

In some cases, decoding a molecules spectrum may be further complicated by the interplay of multiple coupling mechanisms. One example of this is seen in vinylidene in chapter 11, where the forbidden vibrational mode 5^1 interacts through anharmonic coupling with the Herzberg-Teller transition 1^16^1 . Another example is investigated in chapter 12 where

the ethylene radical (C_2H) exhibits a combination of Herzberg-Teller, Renner-Teller, and pseudo Jahn-Teller couplings.

In C_2H , Herzberg-Teller coupling is observed between the ground $\tilde{X}^2\Sigma^+(1A')$ and first excited degenerate $\tilde{A}^2\Pi(2A', 1A'')$ electronic states, which is manifested in forbidden transitions involving odd quanta of the non-symmetric bending mode v_2 . However Renner-Teller coupling results in the normally degenerate $\tilde{A}^2\Pi$ state splitting into two distinct potential energy surfaces $\Pi^+(2A')$ and $\Pi^-(1A'')$. Furthermore, due to the small energy spacing between the \tilde{X} and \tilde{A} states, a pseudo Jahn-Teller interaction also couples the $\Sigma^+(1A')$ and $\Pi^+(2A')$ surfaces.

To calculate the effect of these coupling processes, non-adiabatic coupling corrections may be applied, as shown by Carter *et al.*^[44,45] For the case of C_2H , 3 electronic states need to be included, the degenerate $\tilde{A}^2\Pi$ Renner-Teller pair, and the nearby $\tilde{X}^2\Sigma^+$. The rovibronic wavefunction representing the neutral molecule Ψ_f may be written as an expansion over the three contributing states,

$$\Psi_f = \sum_{\xi} \psi_e^{\xi} \sum_k C_{fk}^{\xi} \phi_{fkm}^{\xi}, \quad (2.54)$$

where ψ_e^{ξ} is the diabatic electronic wavefunction, ϕ_{fkm}^{ξ} is the spin-rovibrational wavefunction. ξ represents the electronic states used in the expansion, in this case $\xi = \Sigma^+(1A'), \Pi^+(2A'), \Pi^-(1A'')$. The transition dipole moment $\langle \Psi_i | \mu | \Psi_f \rangle$ may then be calculated, by expanding the dipole operator μ and spin-rovibrational functions ϕ_{ikm}^{ξ} in terms of Wigner rotation matrices using Euler angles.

This demonstrates how the electronic-nuclear interactions of a molecule, which are normally neglected under the Born-Oppenheimer approximation, can sometimes have a large effect on the energetic structure of a molecule. The above mechanisms will prove vital in understanding some of the anomalies observed in the spectroscopic results of this work.

The HR-PEI spectrometer

The experimental results presented in this body of work were obtained using the ANU's state of the art, high resolution photoelectron imaging (HR-PEI) spectrometer. An overview of the spectrometer is given here, along with descriptions of the key aspects of the spectrometer apparatus, and any modifications that have been made throughout this work. A more detailed description of the design and technical specifications of the apparatus is given by Roberts^[46].

3.1 Spectrometer overview

Conceptually, a successful photodetachment experiment requires four basic components:

- (i) An ion source, to produce the ion of interest
- (ii) Mass separation, to isolate the target ion
- (iii) A photon source, to detach electrons
- (iv) A detection scheme, to measure the photoelectrons

The first step may be achieved by injecting a mixture of precursor gasses into a vacuum chamber, through a pulsed-jet discharge/ioniser. When the discharge strikes, a soup of different ions and molecules are formed, which are then drawn through a skimmer via electrostatic lenses into the next section of the spectrometer. A mass spectrometer (quadrupole or time-of-flight) is then used to isolate the target ion, where a laser (with a suitable wavelength) is used to detach an electron. Finally, an electron kinetic energy analyser, such as time-of-flight, hemispherical, or velocity map imaging detector may be used to measure the detached electrons, so that a photoelectron spectrum (and possibly an angular distribution) may be constructed.

A key feature of the ANU's spectrometer is that the entire beamline is in-line, as opposed to the right-angle spectrometers common in the literature^[23]. Introducing a right angle causes the characteristics of the ion beam kinetic energy distribution to be mapped onto the detector, resulting in a loss of resolution. By keeping the entire spectrometer in-line, the energy distribution of the ion packet is perpendicular to the imaging plane and does not get mapped onto the detector.

An image of the spectrometer is displayed in Fig. 3.1, alongside a schematic diagram identifying the key components. The entire 7m long beamline is kept under vacuum via 3 turbo pumps, a diffusion pump, and 4 backing rotary pumps. Ion production starts at the left side of the image, with ions accelerated towards the right side, where electrons are detached using a Continuum Powerlite 9010 Nd:YAG pumped OPO/OPA laser, before being mapped to a detector with a VMI lens. The electrons are detected using a pair of 75mm microchannel plates (MCP) and a phosphor screen, with the fluorescence events imaged by a 2048×2048 pixel monochrome CCD camera (PCO 2000). Each camera frame is transferred to a computer for real time processing, centroiding electron positions with sub-pixel accuracy.

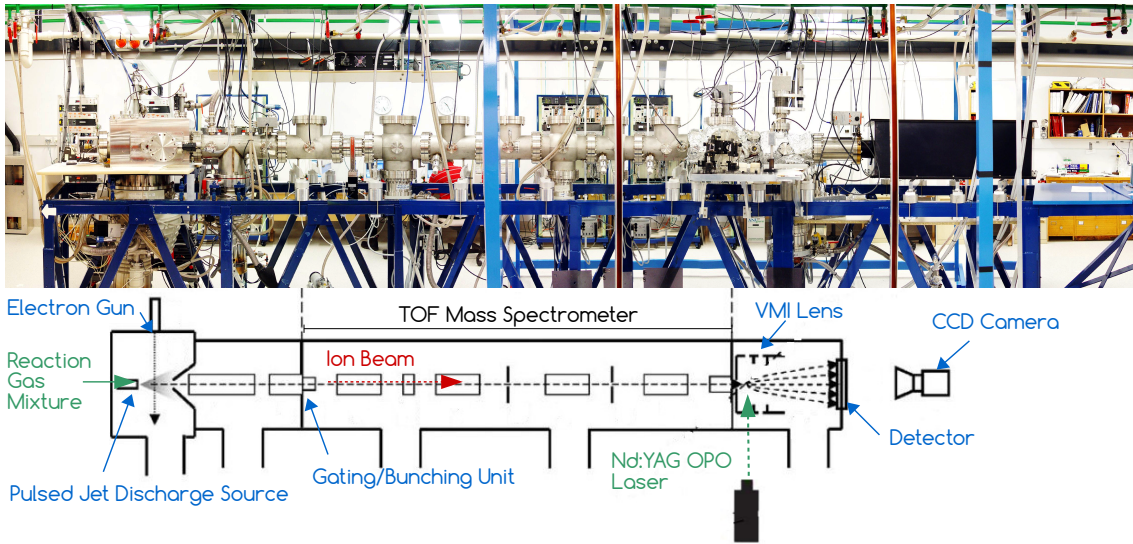


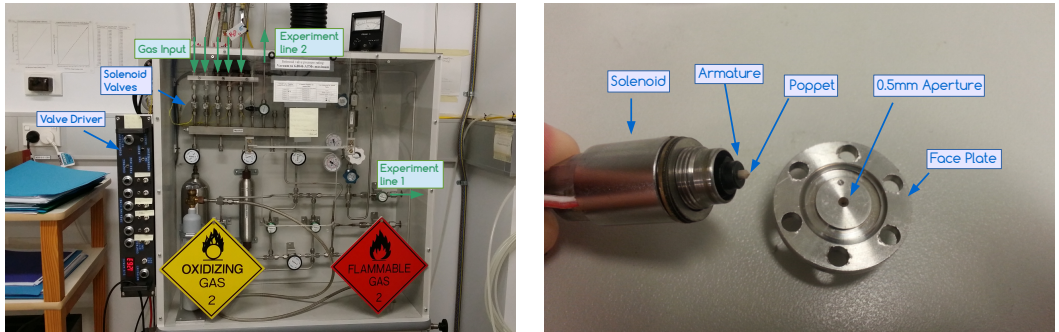
Figure 3.1: Photograph of the 7m long HR-PEI spectrometer at the ANU, with a schematic diagram shown alongside. Ions are produced in the source chamber (left hand side) and then separated along the time of flight mass spectrometer. Electrons are photodetached from the target ion using a Nd:YAG OPO/OPA laser, with electrons mapped onto a detector (right hand side) using velocity map imaging.

3.2 Ion production

The production of an intense, stable, yield of the desired target species is often the hardest step of the experiment, and a limiting factor on the spectral quality. While some species, such as O^- , are readily produced in a single gas discharge, other more exotic species require careful tweaking of the source gas mixture, discharge voltage/pulse-width, and various timing parameters. For some experiments, the physical discharge source has also been modified.

Depending on the target molecule, precursor gases are mixed in the gas manifold shown in Fig. 3.2a. Throughout this work, the gases O_2 , N_2O , H_2 , C_2H_4 , CH_4 , C_2D_4 , and Ar , have all been used. When developing an ion production recipe, the choice of gas is not the only important factor, with the mixing ratio, the backing pressure in the manifold, and the pressure inside the vacuum chamber, all vital to producing a usable ion source. The gas mixture is transported to the beamline, and injected into the source vacuum chamber through a Parker series 9 pulsed solenoid valve, where a controlled burst of gas enters the source chamber through a small 0.5 mm aperture. Typical operating conditions use a gas backing pressure of ~ 2 atmospheres, which is injected into the source chamber at 30 Hz through a pulsed jet with an opening time of $\sim 150 \mu s$. When the high pressure gas in the manifold pipeline is introduced into the vacuum through this small aperture, the gas adiabatically expands^[47]. For an adiabatic process no heat is exchanged with the surrounds ($dQ = 0$), so the work done by the gas during the expansion must come from a loss of internal energy of the molecules ($dU = -dW$), cooling the gas. Furthermore, if the aperture is larger than the mean free path of the gas, significant vibrational and rotational cooling can be achieved through inelastic collisions of the molecules, as was first demonstrated by Osborn *et al.*^[48] for the production of internally cold $N_2O_2^-$ ions.

To reduce pumping requirements, Smalley *et al.*^[49] showed that for a high pressure expanding jet, an expansion region bounded by the barrel shock and Mach disk (known as



(a) Gas manifold used for mixing the precursor gas mixtures. Gases enter the manifold from the top through solenoid controlled valves, to ensure the gases are mixed at the correct ratio and pressures. The mixture then exits at the right, and is piped to the inlet valve of the beamline.

(b) Pulsed valve used to introduce gas mixture into the vacuum chamber. The poppet is seated in the spring loaded armature, and seals against the 0.5mm aperture in the face plate. When the solenoid fires the armature is pulled back, releasing a burst of gas into the chamber.

Figure 3.2: Precursor gasses are mixed with various pressures and ratios in order to maximise production of the ion of interest. The gas mixture enters the beamline through a Parker valve at 30 Hz, where the gas molecules supersonically expand through a 0.5 mm aperture into the vacuum chamber.

the cone of silence) acts as if it is expanding into a vacuum, regardless of the background pressure. Thereby, a skimmer sampling from inside this region will produce a high density, very cold, directional beam of ions^[50,51]. To make sure the skimmer samples from the correct part of the flow it must be placed between the jet face and the shock front, a distance given by,

$$\ell = 0.67d \left(\frac{P_0}{P_B} \right)^{\frac{1}{2}}, \quad (3.1)$$

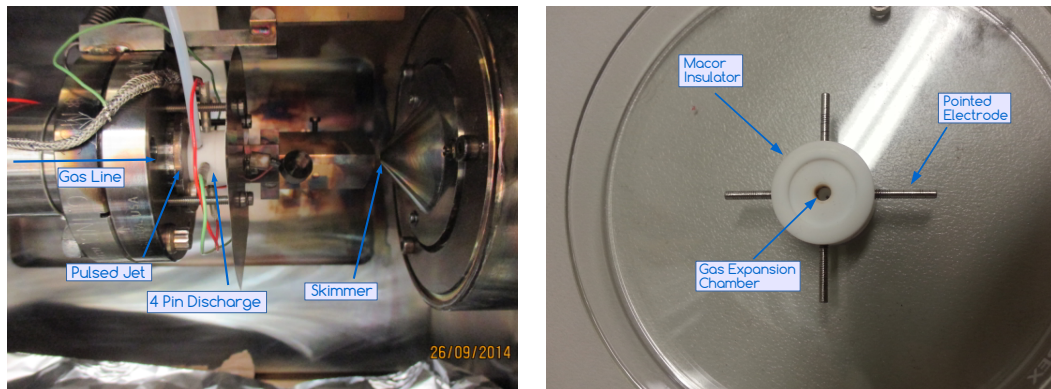
where P_0 and P_B are the source gas and chamber pressures respectively, and d is the diameter of the aperture^[49].

3.2.1 A single jet, 4-pin discharge source

Gas expansion occurs inside a cylindrical macor discharge chamber which is attached to the pulsed-valve front face. Four equally spaced pointed electrodes protrude into the cylindrical chamber, as shown in Fig. 3.3. During the gas-expansion an adjustable high-voltage discharge is applied across two opposing pin electrodes, while the other two electrodes are held at ground. This ionises the gas molecules inside the mica chamber. By varying the discharge voltage (0-3000 V), pulse-length (10-100μs), timing delay, and pulse-shape, the conditions inside the source can be manipulated to preferentially produce certain ions. The discharge is also seeded by an electron gun, to help improve stability of the source^[46]. The result is a large, rotationally and vibrationally cooled, soup of various ions and molecules. Ions from the coldest part of the expansion are then drawn into the next stage of the spectrometer through a skimmer, via electrostatic lenses in the secondary chamber, where they are accelerated to 500 eV before entering a bunching/re-referencing unit.

This method of ion production has been successfully used within the ANU spectrometer for many years, and has proven to be especially well suited to producing high yield stable sources of ions such as O^- , O_2^- , NO^- , OH^- , and NO_2^- , and was employed in this work

for the majority of results presented in chapters 4-7.



(a) Photo of single jet 4 pin discharge, inside the source chamber of the spectrometer. Gas from the manifold flows from the left, and is injected via the pulsed-valve into a discharge chamber, which generates a soup of cold ions and molecules. The skimmer on the right hand side extracts ions from the coldest section of the expansion into the second chamber of the spectrometer.

(b) The discharge chamber, made of a macor insulating material, with 4 pointed electrodes protruding into the hollow centre.

Figure 3.3: Pulsed-valve high-voltage discharge source located within the anion source chamber (a), with details of the discharge chamber shown in (b).

Searching for vinylidene

The vinylidene anion, studied in chapters 8-11 of this thesis, is difficult to produce with the standard single jet discharge normally employed in the ANU spectrometer. As such, various ion sources were developed throughout this work, in an attempt to optimise H_2CC^- production.

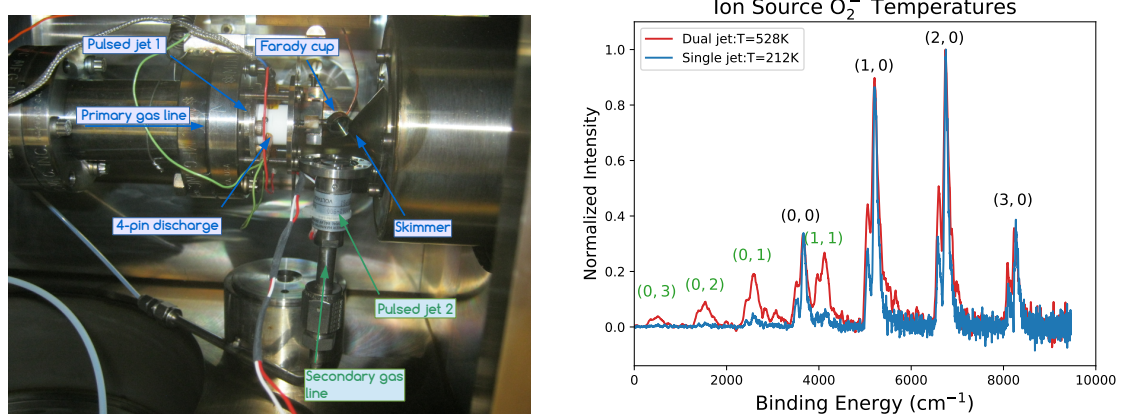
There have been previous attempts to study the vinylidene molecule via photolysis of vinyl cyanide (CH_2CHCN), however only limited success had been achieved through this method^[52,53]. While a Time-Resolved Fourier Transform Infra Red (TR-FTIR) spectroscopy study of the photolysis products of CH_2CHCN at 193 nm was able to confirm the dominant presence of H_2CC , the experimental constraints coupled with the highly excited state of the vinylidene molecules thwarted attempts to analyse the data^[52]. A later high resolution Chirped-Pulsed millimetre-Wave (CPmmW) spectroscopy study attempted to resolve the issues in the TR-FTIR study, but were unable to record any measurement of the vinylidene molecule^[53]. One possible explanation for this is that photolysis generates molecules in a rotationally hot state. Therefore photodetachment of a cold vinylidene anion appears to be the best chance to obtain a high resolution vinylidene measurement.

Previous success has been reported, using the reaction of O^- ions with ethylene gas (C_2H_4). A 1975 flow-drift tube experiment by Linedinger *et al.*^[54] found vinylidene production to be the dominant channel of this reaction, however a repeat of this experiment in 1990 by Grabowski *et al.*^[55] found $\text{C}_2\text{H}_4\text{O}$ to be the dominant product, with only 29% of the reaction proceeding through the H_2CC^- channel. The lesson here, being that small variations in the source conditions can have a large impact on the vinylidene yield produced.

3.2.2 Evolution of a dual jet source

To try and replicate the $O^- + C_2H_4 \rightarrow H_2CC^- + H_2O$ pathway which has provided successful vinylidene production in past studies, a dual jet source was developed and trailed in this work, based on the design of Lineberger^[56]. However as highlighted above, the fragility of H_2CC^- production ensures that developing an optimised source is no easy task.

Initially, a second Parker pulsed jet valve was installed in the source chamber, perpendicular to the primary jet, as shown in Fig. 3.4. This new jet was connected to a secondary gas line, allowing for different gas mixtures and pressures to be used in each gas line, to try and produce different ions in cross beam expansion. However, despite extensive testing with various gas and experimental parameters, this simple dual source design was not able to improve on the single jet performance. In fact, it was found that adding the secondary jet dramatically increased the ion source temperature, decreasing the ion yield, limiting the spectral quality. This is likely due to collision effects between the perpendicular expansions. In usual operation, the skimmer is positioned inside the cone of silence of the gas expansion so as to only sample from the cold, directional part of the flow. However, when two expansions intersect, this changes the shape of the flow and collapses the cone of silence. Consequently, the skimmer samples hotter, less directional ions with non-zero perpendicular velocities. The result of this can be seen in Fig. 3.4 where O_2^- photoelectron spectra at 1064 nm, measured using a single jet and a dual jet source, are shown for comparison. The dual jet source produced hotter ions ($T=528K$ cf. $212K$), demonstrated by the presence of hot bands, and the differing ratio of the fine structure components in the dual jet spectrum.



(a) First iteration of a dual jet source. The primary gas line enters the chamber from the left, and the gas expands through a 4 pin discharge. The primary expansion can be crossed by a secondary expansion using a second jet, perpendicular to the first. Different gases may be used in each gas line in an attempt to produce the desired target ion.

(b) Photoelectron spectrum of O_2^- at 1064 nm measured using a single jet source (—) and a dual jet source (—). The dual jet source has a much higher temperature, resulting in more intense hot bands.

Figure 3.4: Design and performance of the initial dual jet source. The cross beam expansion introduces turbulence to the flow, destroying the cone of silence and resulting in a hotter source temperature.

To overcome these issues, the Lineberger^[56] source design configuration was implemented, as shown in Fig. 3.5. One of the major limitations in the first source iteration was the lack of x,y,z adjustment for the secondary pulse-valve jet. By mounting the second valve directly to the first valve, correct transverse (x) alignment could be assured, while sliding poles created mobility in the vertical (y) and longitudinal (z) directions. The size of the pulse-valve front flange was also reduced, so that the primary pulse-valve could be moved closer to the skimmer. Furthermore, the specifications for the discharge and pulse-valve jet faces were matched to the values of Lineberger's design, in order to recreate the results from their lab. This involved moving from a 4-pin discharge on the primary (horizontal) jet to a two plate discharge on the secondary (vertical), where a thin Teflon insulator separates 2 stainless steel disks with a small hole (for the gas expansion) in the centre. A small 1mm aperture is machined into the jet/discharge interface in order to improve the adiabatic cooling, including a 40° conical nozzle to improve the directionality of the expansion. The pulse-valve front flange on the primary valve is also modified to include a 40° conical nozzle and an even smaller 0.5mm aperture.

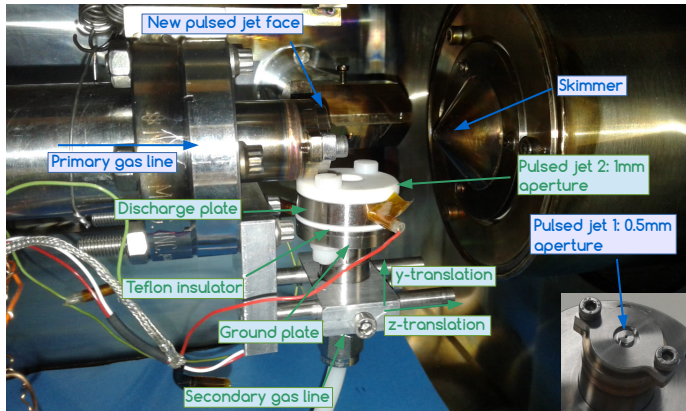


Figure 3.5: Modified dual jet source, involving a two-plate discharge based on the Lineberger^[56] design. Custom jet faces were machined, with 1mm/0.5mm apertures and a 40° conical nozzle, to improve the adiabatic cooling of the gas during the expansion.

With this arrangement, the source conditions of Linberger's laboratory in Colorado should be able to be replicated exactly within the ANU spectrometer. However this still failed to produce a stable vinylidene anion yield. As such, various other gas combinations were tried, with the resulting mass spectra shown in Fig. 3.5. The best results were achieved with a mixture of ethylene, oxygen, and argon in the discharge line, where the argon is used as a buffer gas to assist with cooling. Yet, the vinylidene ion signal produced was still insufficient for a photoelectron signal to be measured with a low signal to noise ratio, while the ions that were produced were still hotter than ions produced in a single jet source. Surprisingly, a large fluoride ion signal was also present in the mass spectra in Fig. 3.6. This was traced to the Teflon insulator, which was replaced with a Macor disc to remove the F⁻ signal.

Modification of the source continued, with some of the designs shown in Fig. 3.7. First, the original 4-pin discharge was temporarily mounted to the secondary (vertical) pulsed jet, so that its performance could be tested against the 2-plate design from Fig. 3.5. The 4-pin discharge was found to produce higher ion counts, however issues arose with gas leaking between the jet and discharge chamber, while a large fluoride signal dominated the mass spectrum due to the Teflon faceplate, used for mounting. Therefore, a new

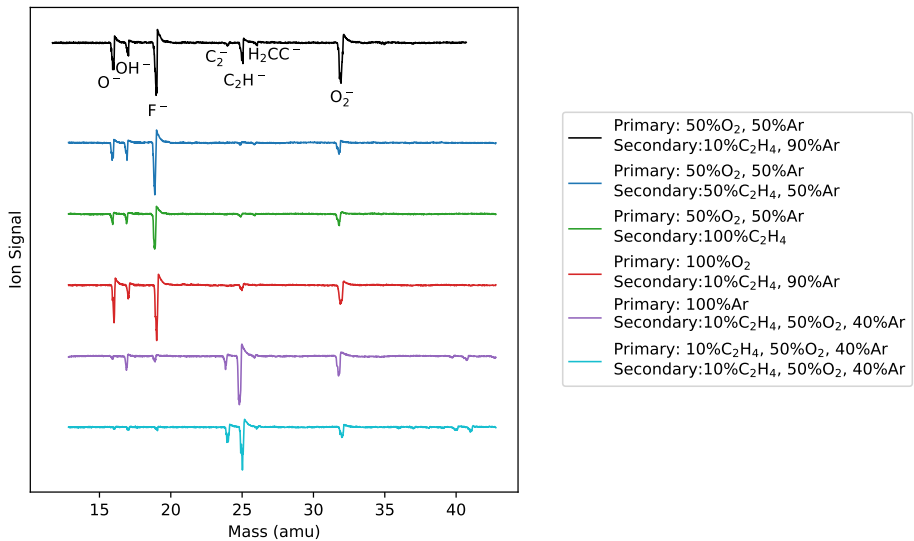
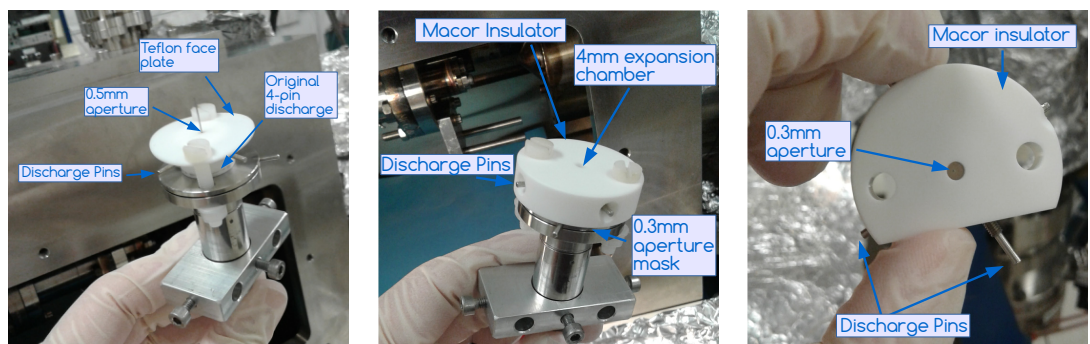


Figure 3.6: Mass spectra from different gas mixtures using a dual valve source. An ethylene/oxygen mixture in the discharge line proved most successful at producing vinylidene, but still could not achieve high ion yields.

purpose-designed 4-pin chamber was machined out of Macor for a sealed fit to the gas jet. Next, 0.3mm and 0.5mm aperture masks were introduced between then discharge and jet to investigate the effect this may have on the adiabatic cooling. O₂⁻ spectra measured with the mask in (0.3mm/0.5mm) vs mask out (1mm) confirmed that a smaller aperture did lead to a significant increase in the gas cooling. Finally, a new 4-pin discharge chamber was also produced to mount on the primary (horizontal) jet valve. This chamber featured a 0.3mm aperture and 4mm expansion chamber for efficient cooling, within a hemispherical disc shape, with the bottom cutaway in order to allow the two pulsed jets to be placed close together to achieve optimal expansion overlap. By having discharges on both the primary and secondary jets, the effect of having a vertical vs horizontal discharge could also be examined.



(a) The original 4-pin discharge source was temporarily mounted to the secondary pulsed jet, in order to test the performance of a 4-pin vs 2-plate discharge.

(b) A new 4-pin discharge designed for the secondary jet was machined using Macor. A 0.3mm aperture mask sits between the jet/Macor faces to help improve adiabatic cooling.

(c) A new 4 pin discharge was also machined for the primary jet, with a 0.3mm aperture and 4mm expansion chamber to help improve the adiabatic cooling.

Figure 3.7: Evolution of the discharge source.

Optimal conditions were found with the 4-pin discharge on the primary (horizontal) pulsed-valve jet firing, with a buffer gas expansion out of the secondary jet to help with ion cooling. The jet-to-jet and jet-to-skimmer proximities also proved important, with best results obtained when the skimmer is aligned with the expansion beam cross over point, as shown in Fig. 3.8. It is this configuration that lead to the vinylidene results that are presented in chapters 8-11.

From this study, a few key requirements for a optimum ion source can be defined,

- The 4-pin discharge out performs a 2-plate design.
- Having the main discharge in-line with the beam (horizontal jet) ensures the coldest ions are selected by the skimmer and reduces the transverse velocity, which is important for high resolution VMI.
- With a cross beam expansion, it is important for the skimmer to be close to both jet openings to ensure it samples from the coldest part of the beam.
- Teflon is not a good choice of insulating material, as it may result in a large fluoride ion signal.

The discharge is controlled by a pair of home-built power supplies, one of which is held at constant voltage, while the second adds an additional high voltage pulse which is responsible for ionisation. Under typical operating conditions, the constant voltage is held at 800-1200V (depending on the target ion) with an additional pulse voltage of up to 1600V. The width of the discharge can also be varied, from $\sim 10 - 100\mu\text{s}$, while the shape of the discharge can be modified using an inbuilt variable resistor. The discharge and pulsed jets operate at 30Hz, with the jet pulse and discharge fire times controlled by a BNC digital delay generator (DDG). The jet opening lengths are varied using a Parker valve driver, which can also add a delay between the primary and secondary jet times.

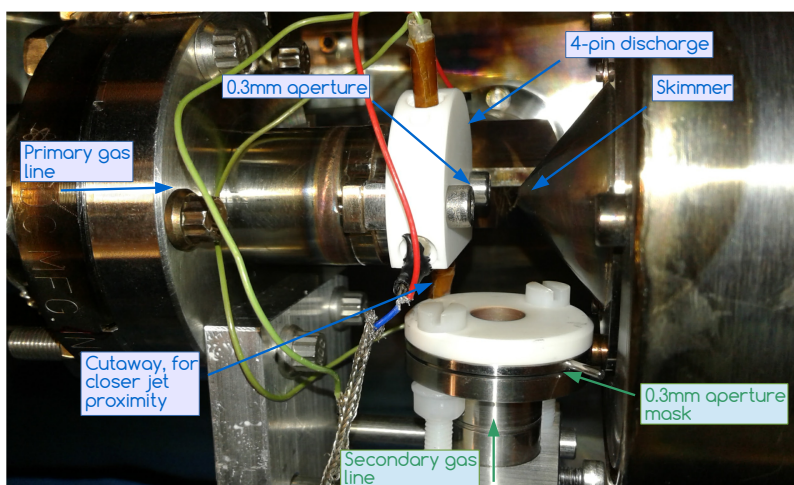


Figure 3.8: Final dual-jet source design. A 4 pin discharge, with an 0.3mm aperture, is mounted to the primary (horizontal) jet. The main expansion is crossed by a buffer/reactive gas expansion from the secondary (vertical) jet. The proximity of the jets to each other and to the skimmer is important in ensuring a cold, directional, ion beam is obtained.

3.3 Ion beam formation and mass separation

Once the ions have been created in the discharge, the resulting soup of ions needs to be transformed into a stable pulsed beam, so that the ion of interest may be mass isolated for photodetachment. First, the ions are drawn through the skimmer, which separates the source chamber from the other vacuum chambers. The skimmer has a flat conical shape with a 2mm aperture diameter, and directs the ions from the coldest part of the gas expansion into a well defined beam, with low divergence. It also allows differential pumping between the two chambers. Behind the skimmer are a series of 3-element electrostatic lenses, which focus the ion beam, while accelerating it to a beam energy of 500 eV. This provides a collimated, constant energy beam, which may be used for mass separation.

3.3.1 Simultaneous gating, bunching, and re-referencing

To prepare the above ion beam for mass separation, three transformations need to be applied. First, the beam must be gated to from discrete ion packets before it can enter a mass spectrometer^[57]. Even though the ANU employs a pulsed source, the duration of the pulse is longer than the desired ion packet duration, so a method to extract only a short packet of ions from the longer pulse is required. Secondly, it is desirable to re-reference the ion beam to ground, in order to simplify the transport optics along the remainder of the beamline, as otherwise successively higher lens voltages will be required. This is easily achieved by using a potential switch, whereby a cylinder along the path is rapidly changed from 500V to 0V so that the ions inside the cylinder during the switch will exit at ground potential, but with unchanged kinetic energy^[19].

The third requirement arises from the low photodetachment count rates that have proved problematic in previous spectrometers. Maximising the photoelectron count rate is especially important for difficult to measure species, such as vinylidene, where the total ion count rate from the source is relatively low or unstable. One way to address this is to introduce axial bunching, where a long gated ion packet (80mm) may be bunched to match the dimensions of the laser beam (2mm), resulting in an increase in the ion density at the interaction region by a factor of 40. This is achieved by applying a variable voltage across the ion packet, essentially providing a kick voltage to the ions at the end of the packet, so that they catch up to the front of the ion packet by the time they reach the interaction region. Because the ANU spectrometer is in-line, introducing an axial velocity spread will not effect the VMI resolution, as only off-axial components are mapped into the image.

Previous spectrometers have used three separate electrostatic devices to achieve each of these beam transformations, however the HR-PEI spectrometer at the ANU employs one single device to simultaneously accomplish each of these tasks. A schematic diagram of the novel gating/bunching/re-referencing unit employed in the ANU spectrometer, is shown in Fig. 3.9. Ions from the foreoptics enter the unit from the left at +500V, where a fast MOSFET (metal-oxide-semi-conductor field-effect transistor) switch switches the cylinder potential (at 30 Hz) from +500 V to +0 V, re-referencing the ions inside the cylinder to ground^[58]. This simultaneously gates the ions into a discrete 80 mm long packet, with ions outside of the cylinder deflected. Instead of using a continuous cylinder, a series of closely spaced aluminium rings are used, intersected with insulating macor spacers. These rings are biased through a resistor chain, producing a uniform axial electric field. In order to bunch the ion packet, when the front of the cylinder (A) is switched to ground, the

back of the cylinder (B) is switched to a variable kick voltage $-V_{\text{bunch}}$. This produces an additional voltage gradient, accelerating the ions at the back of the packet so that by the time they reach the interaction region, they have caught up to the ions at the front. This bunches the 80 mm packet to 2 mm, increasing the ion density by a factor of 40. The kick voltage required to bunch an ion packet of length ℓ over a drift length L is given by,

$$\Delta E = \frac{2E\ell}{L}, \quad (3.2)$$

where E is the energy of the beam, and ΔE is the kick energy. Therefore, bunching an 80 mm packet at 500 eV over a ~ 2 m flight tube requires a kick voltage of ~ 40 V.

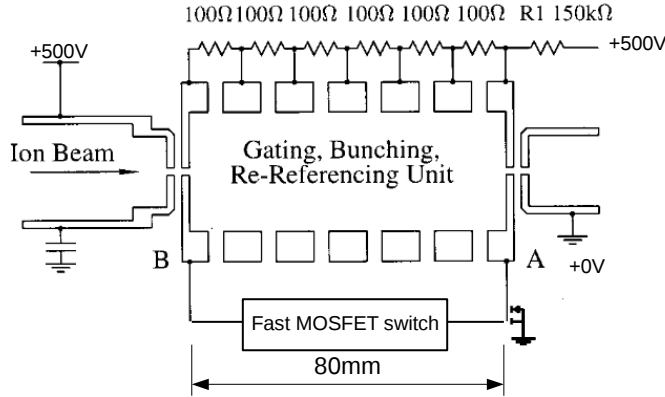


Figure 3.9: Gating/bunching/re-referencing unit employed in the ANU spectrometer. Ions from the foreoptics enter the unit from the left at +500V, where a fast MOSFET switch switches the unit potential from +500V to +0V, re-referencing the ions inside the cylinder to ground. A series of closely spaced aluminium rings, intersected with insulating macor spacers, are biased through a resistor chain, producing a uniform axial electric field. When the front ring is switched to ground, the back of the cylinder switches to a kick voltage $-V_{\text{bunch}}$ introducing a voltage gradient to bunch the ion packet^[58,59].

3.3.2 Time-of-flight mass spectroscopy

A time-of-flight (TOF) mass spectrometer may be easily implemented into the HR-PEI spectrometer due to the pulsed, in-line nature of the apparatus. Mass separation enables the target ion of interest to be selected from the packet of ions, resulting in a pure, one-species measurement at the interaction region. After the gating/bunching/re-referencing unit the ions, with a kinetic energy of 500 eV and 0 V potential, enter a 2 m long high vacuum drift tube. Two Heddle pairs of Einzel lenses transport the ions down the flight tube, with the first pair of Einzel lenses focusing the ion packet through an aperture which defines the packet size at the interaction region, while the second pair of Einzel lenses focuses the ion packet through a second aperture to define the beam divergence^[60]. As the ions all have the same kinetic energy, heavier ions will have a longer flight time, as given by

$$t = \frac{L\sqrt{m}}{\sqrt{2E}}, \quad (3.3)$$

where m is the mass of the ion, E the beam energy (500 eV), and L the flight distance (2 m). A retractable 18 mm diameter micro channel plate (MCP) can be lowered into the

beam path to measure the arrival times of ions, which is then converted to ion mass via Eq. (3.3), along with their relative intensities. Numerous experimental parameters may then be varied to find the optimal conditions for maximising the anion signal corresponding to the species of interest.

3.4 The Nd:YAG laser and optical parametric oscillator

Velocity-mapped photodetachment experiments require a linearly polarised, high flux, narrow bandwidth, photon source. Linear polarisation, orthogonal to ion beam and parallel with the detector, induces cylindrical symmetry on the velocity-mapped image, which is an essential requirement of the inverse-Abel transformation employed in the analysis. Meanwhile, the ion packet that reaches the interaction region (approximately cylindrical with a 2mm length and 2mm diameter), often has a low ion density - therefore a high photon flux is required to ensure sufficient photodetachment events occur in order to obtain adequate statistics, to reveal all of the target structure. Finally, as the experiment measures electron kinetic energies, which can be related to the energy levels in the molecule via $eBE = h\nu - eKE$, a narrow laser bandwidth is important as any spread in the laser energy $h\nu$ is mapped directly into the image.

To satisfy all of the above conditions, a Continuum Powerlite Precision II 9010 Nd:YAG pulsed laser is employed. This laser operates at 10Hz, producing 5ns pulses with energies up to 2000 mJ at 1064 nm^[61]. While the source side of the lab operates at 30 Hz, the imaging side (Laser/VMI/Camera) operates at 10 Hz. The source side is operated at the higher frequency, with only every third packet involved in photodetachment, as this has proven to help improve the stability of the ion source^[46]. The Nd:YAG laser is seeded by a NP Photonics fibre laser to improve the stability of the pulses, with the YAG pulse shape monitored by a photodiode during operation, to ensure a good quality pump beam for the Continuum Sunlite EX OPO.

A diagram of the Nd:YAG laser used in this work is given in Fig. 3.10. Flash lamps, powered by a large capacitor bank within the laser power supply, charge the oscillator rod which lases at 1064 nm when the Q-switch is fired. The laser beam then passes through two amplifying rods to reach a pulse energy of up to \sim 2000 mJ. To allow for various detachment wavelength options, the beam passes through two nonlinear KDP crystals for generation of the second (532 nm), third (355 nm), and fourth (266 nm) harmonics from the YAG fundamental (1064 nm). Dichroic mirrors are then used to clean the beam to ensure only a single wavelength is transported to the experiment.

An important feature of the Precision II 9010 laser system is the ability to externally trigger the Q-switch and flash lamp discharge times, enabling the laser system to be synchronised to the ion beam. Temporally intersecting a 5ns laser pulse with the pulsed ion packet from the beamline requires high precision in the Q-switch timing. In order to optimise the temporal overlap of the ion packet and laser pulse a Q-scan is performed, where the Q-switch is varied in regular increments while the number of photoelectron counts per shot is measured. This ensures that the laser will be fired at the correct time, to optimally intersect the ion packet from the beamline and maximise the number of events recorded.

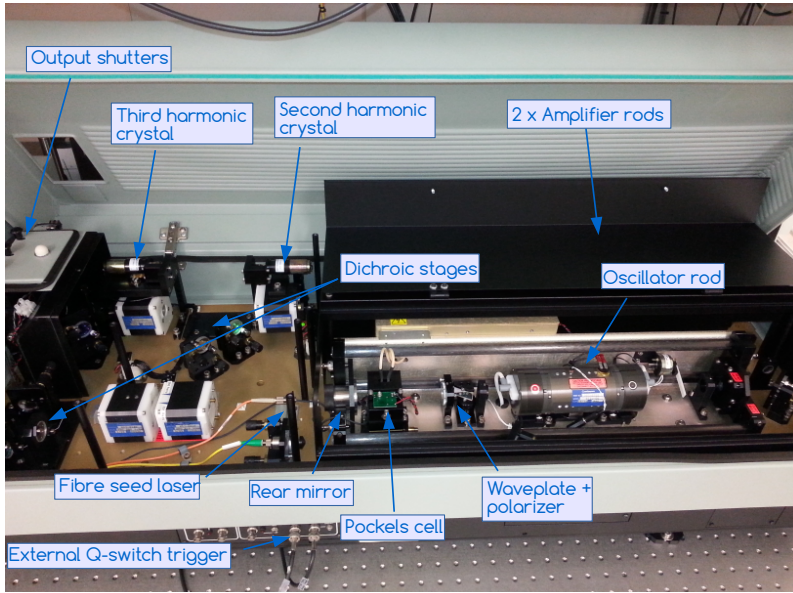


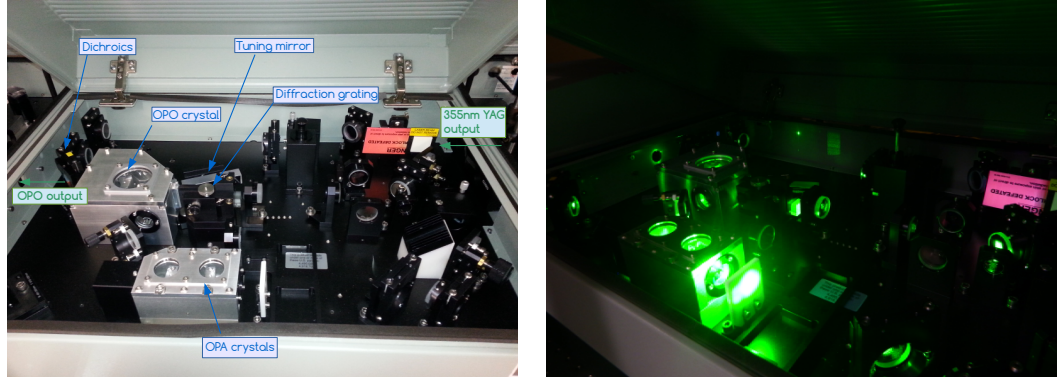
Figure 3.10: Nd:YAG Powerlite Precision II 9010 laser, used in this work. The oscillator rod is charged via flash lamps powered by a large capacitor bank within the laser power supply. When the Q-switch fires lasing at 1064 nm occurs, seeded by the NP photonics fibre laser. The photons are transported to two amplifying rods, producing 5ns pulses with energies up to 2000 mJ. Nonlinear KDP harmonic crystals may then be used to convert the 1064 nm photons to the second (532 nm), third (355 nm), or fourth (266 nm) harmonic.

3.4.1 Sunlite EX OPO

For cases where flexibility in the detachment wavelength is required, the third harmonic of the Nd:YAG (355 nm) is used to pump a Sunlite EX optical parametric oscillator (OPO). The OPO system is a tunable high efficiency source, capable of generating narrowband radiation in the visible and near infra-red spectral region between 445 – 1750 nm. Optical parametric processes involve three photon interactions, where one pump photon splits into a pair of less energetic ones. The two photons produced typically do not have the same energy, with the high energy photon referred to as the signal and the low energy photon the idler. This is achieved in the Sunlite EX OPO by employing a nonlinear beta-barium borate (BBO) crystal with a birefringence axis. For a given angle between the crystal axis and pump beam, only one pair of signal/idler frequencies will conserve angular momentum. The signal/idler frequencies for a given phase matching angle is given in Fig. 3.12. By tuning the birefringent axis based on this calibration curve, the output photon source may be tuned to any desired frequency between 445 and 1750 nm. A narrow bandwidth (of less than 0.1 cm^{-1}) is achieved by operating in the ExtRA ordinary plane of the crystal, as opposed to the ordinary plane, as the narrow crystal acceptance angle of the ExtRA ordinary plane restricts the bandwidth of the oscillating radiation. An image of the OPO is presented in Fig. 3.11.

The system is controlled via computer software, scanning to any desired wavelength by angular tuning the relevant crystals based on calibration tables. The exact wavelength is measured using a High Finesse WS⁷ Super Precision wavemeter. The laser output from the EX OPO is then transported to the interaction region, using a series of optics, including Glan-Laser polarisers to ensure vertical polarisation of the laser. An additional Sunlite FX-1 UV doubling crystal may be used to produce wavelengths less than 455 nm, however

this further reduces the pulse energy (1-2 mJ, cf. 5-50 mJ) which has proved problematic.



(a) Sunlite EX OPO used in this work. The 355 nm output of the Nd:YAG is tuned to the desired frequency via a parametric 3-photon process using nonlinear BBO crystals. The input beam is split by a beam splitter, with one arm going through the oscillator crystal, tuning mirror, and diffraction grating, which then seeds the other arm of the beam as they pass together through the amplifier crystals.

(b) Photo of the OPO in operation at 550 nm. This is achieved by setting a phase matching angle of $\sim 32^\circ$ between the crystal axis and pump beam, so that, by conservation of momentum, the 355 nm photons split into a 550 nm signal beam and a 999 nm idler beam.

Figure 3.11: The Sunlite EX OPO laser used in this work, which acts as a coherent tuneable photon source with narrow bandwidth.

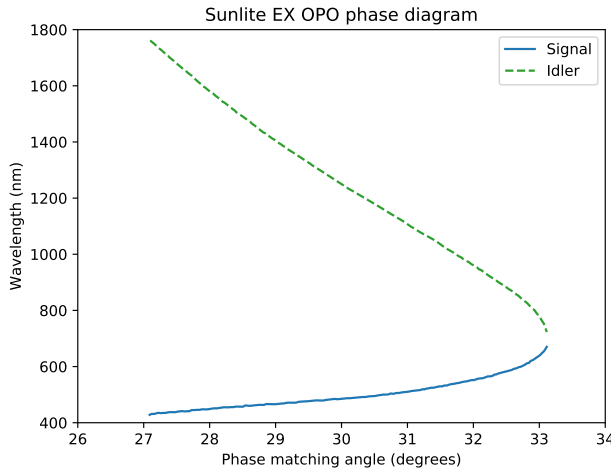


Figure 3.12: OPO phase matching diagram, showing the signal and idler frequencies which correspond to a particular angle between the crystal axis and laser pump beam. This allows for the laser frequency to be tuned to anywhere within the range 445-1750 nm.

3.4.2 Direct YAG measurements

While the YAG laser was originally installed to operate as a pump laser for an OPO, modifications were made to the laser connecting chamber to allow for the direct YAG

output to be used in the experiment. This mode of operation has limited wavelength flexibility (1064, 532, 355, and 266 nm) but provides much higher pulse energies ($\sim 300 - 2000$ mJ) than what can be achieved with the OPO ($\sim 5 - 50$ mJ). From the Beer-Lambert law, the number of photoelectron emitted in a pulse is given by,

$$j_{\text{elec}} \phi [1 - e^{-\rho\sigma\ell}], \quad (3.4)$$

where j_{elec} is the current of photoelectrons, ϕ is the photon flux, ρ is the density of ions, σ the photodetachment cross section, and ℓ the interaction path length. Therefore the number of photodetachment events to occur is directly proportional to the number of incident photons. This makes direct Nd:YAG measurements a very useful mode of operation for target species with low ion counts. It can also be useful for primary measurements of a new target molecule, where a high count rate can quickly reveal the important aspects of the target molecule.

The laser exits the Nd:YAG, where a dichroic mirror deflects the beam through an exit port installed in the chamber connecting the YAG and OPO lasers. A series of prisms then transport the beam from the optics table over towards the ion beam, passing through a $\lambda/2$ waveplate and BBO polariser to ensure high purity vertical laser polarisation is achieved at the experiment. The laser beam is then telescoped down to a 2mm spot size before entering the ion beam interaction region through an entry window. A picture of the interaction region is given in Fig. 3.13.

Spatial overlap of the 2mm ion packet and 2mm laser pulse can also prove difficult. Right angle prisms are used to steer the laser beam through the interaction region, while electrostatic x,y,z deflectors on the second potential switch can be used to steer the ion beam. The centre of the interaction region is marked as a line on the optical bench, providing a reference point to aid with the alignment, with vertical alignment achieved using marked rulers.

3.5 Imaging photoelectrons

Arguably the most important step of this experiment is the collection and measurement of the ejected photoelectrons, as this process can have a large impact on the final quality and resolution of the spectroscopic data obtained. A picture of the interaction region of the spectrometer is presented in Fig. 3.13, with annotation identifying the processes involved in the detection scheme. Ions are transported to the interaction region via the time-of-flight optics, which delivers a bunched 2mm packet of the target ion. The Q-switch of the laser is then fired, with the laser pulse entering the interaction region through a UV fused silica vacuum port window, perpendicular to the ion beam trajectory. The spectrometer uses a velocity-map imaging lens to map the detached electrons onto a 75 mm MCP detector, preserving the energetic and angular electron information.

3.5.1 Velocity map imaging and inverse Abel transforms

Using velocity map imaging, photoelectrons are mapped onto the detector such that the radial position on the screen only depends on their electron velocity, independent of anion source position in the VMI lens. This resolves the non-point source blurring and trajectory deflection problems that limited the achievable resolution in traditional grid-electrode imaging methods, allowing for high precision, detailed images^[62]. Meanwhile, the imaging

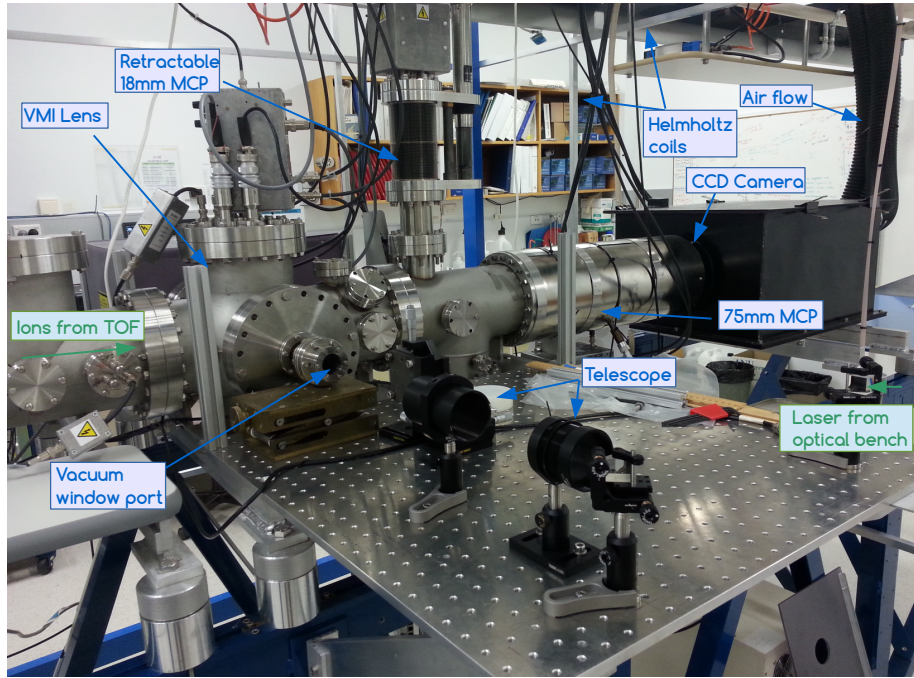


Figure 3.13: Interaction/imaging section of the spectrometer. The laser beam from the Nd:YAG OPO/OPA is steered through the vacuum window port into the interaction region. Photoelectrons are then mapped onto the 75 mm MCP detector using velocity map imaging.

lens also conserves the angular properties of the dejected electrons, while boasting a full 4π steradian collection angle with 100% collector efficiency. The result, is that the 3D sphere of events created in the detachment process gets pancaked into a 2D projection on the detector. By exploiting the cylindrical symmetry induced by the vertical laser polarisation, an inverse Abel transformation may be applied to the 2D projection to recreate the information in the 3D electron sphere.

A schematic diagram of the imaging apparatus is shown in Fig. 3.14. Ions from the time-of-flight chamber enter through a second potential switch, which isolates the target ion packet from the rest of the beam, while simultaneously re-referencing the packet to the repeller lens voltage. Detachment then occurs between the repeller and extractor lenses. The ratio of voltages of the three element lens are set so that the detached electrons are focused onto the detector such that their radial position on the screen only depends on their speed, even when electrons are detached from different spatial positions inside the interaction region, with fast electrons imaged to the detector edge and slower electrons imaged to the centre.

The ratio between the repeller and extractor lens voltages depends on the desired focal length, or distance from the lens to the detector (800mm). However, the ratio may be further refined using measurements of O^- at a fixed wavelength, while fine adjustments to the lens ratio are made. A plot of a transition full-width-at-half-maximum (FWHM) as a function of E_v/R_v has a parabolic shape with a minimum at $E_v/R_v = 0.7535$, corresponding to the best focus of the VMI lens. To ensure this ratio is always maintained, the lenses are controlled by a pair of finely-adjustable high-voltage power supplies, with the true voltages continuously measured using high precision multimeters. While the ratio of the lens voltage must remain constant, the magnitude may be varied depending on the kinetic

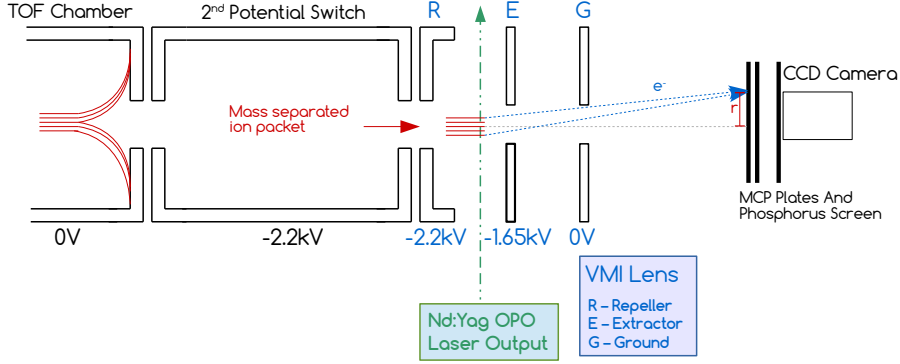


Figure 3.14: A schematic diagram of the imaging region of the spectrometer. A second potential switch isolates the target ion mass packet from the ion beam, while simultaneously re-referencing the ions to the repeller lens voltage. Detachment occurs between the repeller and extractor lenses, with the resulting electrons focused onto the detector such that their radial position only depends on the radial speed of the electron, with fast electrons imaged to the detector edge and slower electrons at the detector centre.

energy of the detached electrons. Results presented in this work have used a variety of VMI lens repeller voltages, from -150 V to -2900 V.

Photoelectrons produce a series of nested spheres, where electrons on the same sphere must have the same speed (and thus kinetic energy). The VMI lens pancakes the 3D nested spheres into a 2D projection on the detector, as shown in Fig. 3.15. The 2D projection $P(x, y)$ of a 3D object $I(x, y, z)$ is described mathematically by,

$$P(x, y) = \int_{-\infty}^{\infty} I(x, y, z) dz. \quad (3.5)$$

In the special case where the object $I(x, y, z)$ posses cylindrical symmetry, this expression may be described algebraically.

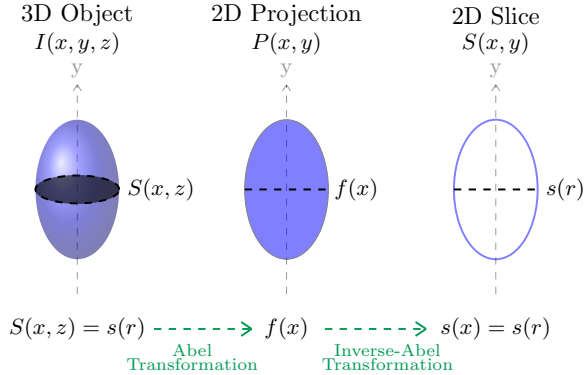


Figure 3.15: Diagram of the projection and reconstruction process involved in velocity-mapped image analysis. The 3D sphere of electrons is pancaked onto the detector via the VMI lens. A 2D slice, in the plane parallel to the detector, can then be reconstructed using an inverse Abel transformation.

By exploiting the cylindrical symmetry of the problem, induced by the linear laser polarisation, a 2D slice of the sphere (parallel to the imaging plane) may be recreated

using an Inverse Abel transformation. Consider an infinitesimal horizontal slice $S(x, z)$ through our 3D object $I(x, y, z)$, as depicted in Fig. 3.15. We may describe the projection of the cross-sectional slice $S(x, z)$ onto the line $f(x)$ with the following equation,

$$f(x) = P(x, y_0) = \int_{-\infty}^{\infty} S(x, z) dz = 2 \int_0^{\infty} S(x, z) dz. \quad (3.6)$$

The cylindrical symmetry in $I(x, y, z)$ infers that $S(x, z)$ will be circularly symmetric, and may be expressed in polar coordinates as $S(x, z) = s(r)$ where $r^2 = x^2 + z^2$ and $dz = \frac{r}{\sqrt{r^2 - x^2}} dr$. Applying a change of variables from z to r in Eq. (3.6) then gives,

$$f(x) = 2 \int_x^{\infty} \frac{s(r)r}{\sqrt{x^2 - r^2}} dr, \quad (3.7)$$

which is known as the Abel transformation, and describes the 2D projection of a cylindrically symmetric 3D object. From Fourier transform convolution theory the inverse transformation is then defined as

$$s(r) = \frac{1}{\pi} \int_r^{\infty} \frac{df/dx}{\sqrt{x^2 - r^2}} dx. \quad (3.8)$$

This is known as an inverse Abel transformation. By evaluating this formula at each vertical point along the axis of cylindrical symmetry (y), the measured 2D projected image is transformed into a 2D slice image. This removes the background from all of the photoelectrons not emitted in the plane of the detector, to reproduce a slice through the original 3D electron distribution. From this, all of the spectroscopic information from the photodetachment event is able to be extracted, including the electron kinetic energy and angular distributions. An example of the VMI detection and image reconstruction process is shown for O_2^- in Fig. 3.16.

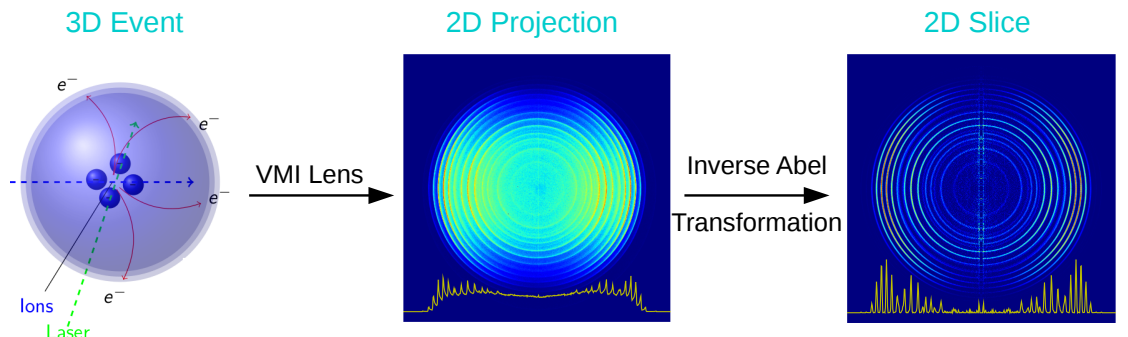


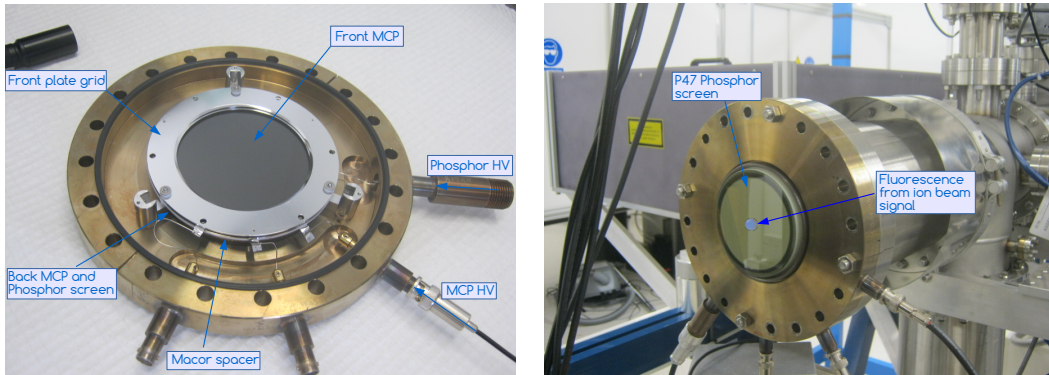
Figure 3.16: Example of the VMI analysis process, including a measured, and inverse Abel transformed, velocity-mapped image of O_2^- photodetachment at 455 nm. The yellow line shows the intensity profile across the image centre.

There are multiple methods available for iterating Eq. (3.8) while dealing with the singularity at $z = 0$. The results in this work are analysed using a python script written by Stephen Gibson (ANU), to implement the inverse Abel transformation based on the approach of Hansen and Law^[63,64]. This approach employs a Kalman filter (least-squares estimation) in the recursive process to handle noise in the measured data set. Importantly, it allows for images of arbitrary size to be processed, with larger image sizes providing more

detail at the expense of greater statistical uncertainty in the individual pixel positions. The example of a raw and inverted velocity-mapped image of O_2^- at 455 nm, given in Fig. 3.16, highlight how the removal of the projection background reveals clear quantized energy levels of the target molecule.

3.5.2 Detection and processing

The ANU spectrometer employs two detectors, a retractable 18mm diameter microchannel plate (MCP) that is used for ion beam optimisation, and a 75mm diameter imaging MCP detector used to record the velocity-mapped photoelectron events. The main 75mm detector, shown in Fig. 3.17, consists of two matched 75mm Burle microchannel plates and a P47 phosphor screen. When a photoelectron strikes the first MCP this initiates a cascade of electrons which propagates through the plate. These electrons then strike the second MCP, which further amplifies the signal. However, as the signal propagates through the plate it will become slightly displaced, so to account for this the second MCP is anti-aligned to the first to ensure that the final signal exiting the second MCP will be at the original location. The amplified electron signal then strikes the P47 phosphor screen, causing the phosphor to fluoresce which is recorded by a CCD PCO 2000 2048×2048 pixel monochrome camera. Each camera frame is transferred to a computer at a 10 Hz repetition rate and is processed in real time to identify electron events, centroiding position to a sub-pixel accuracy, to eliminate camera image noise from the accumulated velocity-map image.



(a) Main imaging detector assembly. Two MCP's are stacked between Macor spacers on top of a phosphor screen.

(b) Back side of the imaging detector stack, showing the phosphor screen. The blue fluorescence visible is due to an ion beam signal striking the MCP stack, causing a cascade of electrons to hit the phosphor screen. Individual fluorescent spots represent a single ion event on the detector.

Figure 3.17: Components of the detection scheme used in the spectrometer. Electrons are velocity-mapped to the MCP stack, causing a cascade of electrons to strike a phosphor screen. The resulting fluorescence is recorded using a CCD camera, with electron positions centroided and sent to the control computer for analysis.

An image of the velocity-mapped photodetached electrons at the detector is then obtained through binning the centroided electron-event positions into a rectangular pixel-grid image, which may be of arbitrary pixel number. A large image pixel count provides more detail at the expense of greater statistical uncertainty in individual pixel intensities. The

velocity-map image is centred and then circularised by an angular dependent radial scaling determined by comparing adjacent radial slice intensity profiles. This correction is applied to the raw (x, y)-centroid coordinates before forming the velocity-map image, to eliminate any requirement for image pixel intensity interpolation. The inverse Abel transformation described above (Eq. 3.8) is then applied to return a slice image of the 3D photoelectron distribution for analysis.

Absolute energy calibration of photoelectron spectra may then be verified using measurements of published species, typically including O^- ^[24] and O_2^- ^[65], that cover a similar radial area of the detector. The radial position of an electron on the detector is given by

$$r = \sqrt{eKE} \times \sqrt{\frac{1000}{|V_r|} \frac{100}{R2E}}, \quad (3.9)$$

where r is the radial position on the detector, eKE is the kinetic energy of the electron, V_r is the VMI repeller voltage, and $R2E$ is a calibration factor (scaled by 100) dependent on the spectrometer and operating conditions, with values typically between $\sim 1.15 - 1.25$ depending on how the image is circularised. By comparing circularised photoelectron spectra against known spectroscopic species, the correct $R2E$ calibration factor may be applied. Known second order effects of the velocity map imaging lens, cause a small deviation in the relationship between detector radial position and electron kinetic energy. This effect has been characterised, using calibration measurements of O_2^- as shown in Fig. 3.18. In most experiments this is a negligible effect, however for high precision spectra, a radial dependent $R2E$ factor may be used.

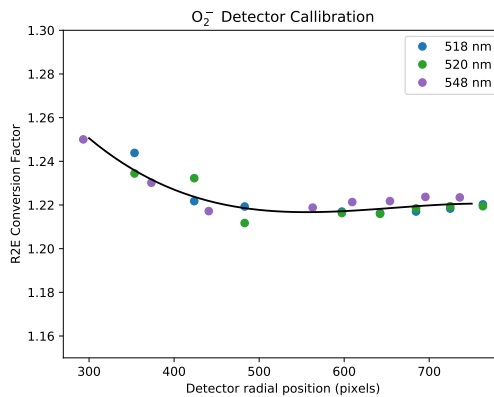


Figure 3.18: Demonstration of the small variations that occur to the $R2E$ factor at different regions of the detector.

During a measurement, we wish to only measure the detached electrons, and not the ionic or neutral molecules that are also present. This is achieved by switching the detector on and off, as the photoelectrons will reach the detector before the ions and other fragments. However MCP's have an inherently high capacitance due to their structure, which makes rapidly switching from high to low voltages difficult, especially as the switching requirement of the experiment require a very short on time of $\sim 15\ \mu s$, to be continuously switching at 10 Hz. This problem is overcome by applying a base and a boost voltage to the plates. A base voltage of 1350 V, just below the minimum voltage required to achieve gain, is continuously supplied to the plates. When a trigger is received from the experiment control a fast Behlke switch quickly boosts the voltage up to 2000 V, essentially

switching the gain of the plates on so that incident electrons will be detected. After a $15\ \mu\text{s}$ window the plates switch back down to 1350 V, effectively turning the gain off. This reduces the voltage swing required from 2000 V to the much more achievable 650 V, while still ensuring that only the photoelectrons are detected.

Every aspect of the experimental set-up has been carefully designed to obtain the highest possible precision in the final image, which means even very small electric/magnetic fields can have a relatively large effect on the final resolution. To account for this, three orthogonal $2.4 \times 2.4 \times 2.4$ m pairs of Helmholtz coils surround the imaging section of the spectrometer, with the currents carefully selected so as to cancel out static magnetic fields present in the laboratory. The entire imaging section is also enclosed in a shell of Mu-metal to shield from any DC magnetic fields that may arise.

3.5.3 Example O⁻ measurement

An example of the image processing method, used in constructing a photoelectron spectrum, is shown here for a 355 nm photodetachment measurement of O⁻. The raw velocity map image is presented in Fig. 3.19, consisting of 6,924,704 electrons from 50,000 laser shots. Two electronic transitions are observed, O(³P_{2,1,0}) \leftarrow O⁻(²P_{3/2,1/2}) (outer ring) and O(¹D₂) \leftarrow O⁻(²P_{3/2,1/2}) (inner ring).

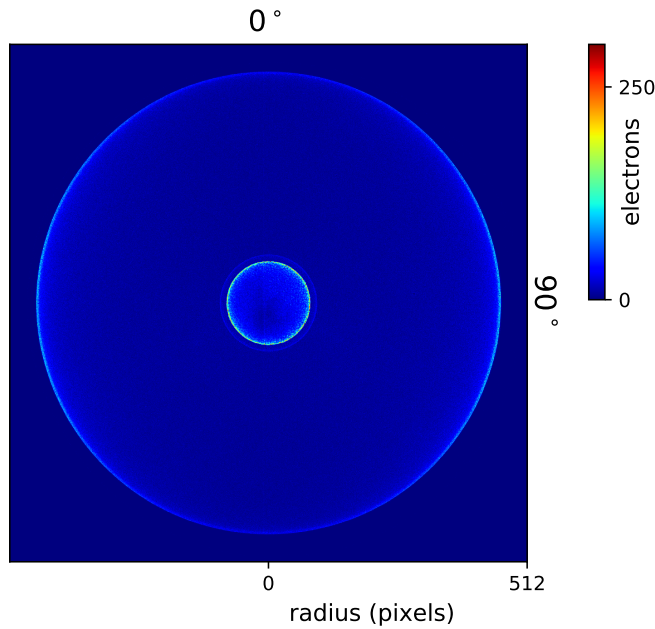
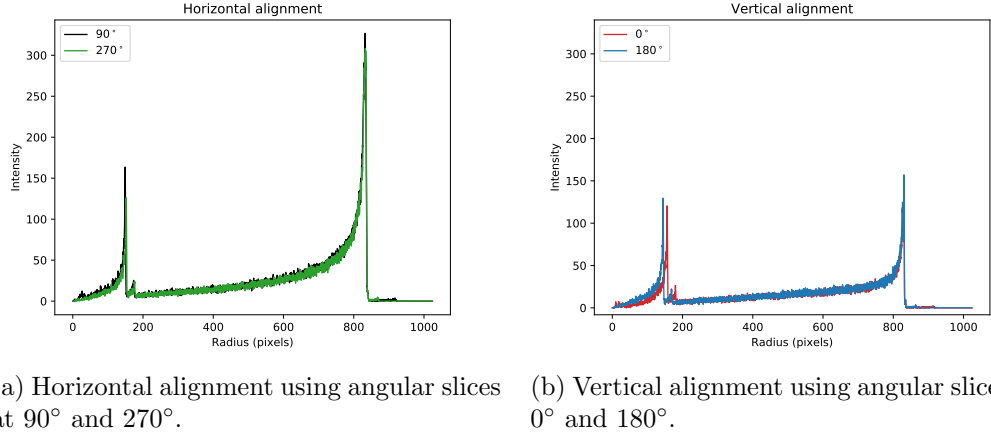


Figure 3.19: Velocity map image of O⁻ photodetachment at 355 nm, consisting of 6,924,704 electrons from 50,000 laser shots. Laser polarisation is aligned vertically, with 0° defined at the top of the image.

First, the geometric centre of the image is defined by taking angular slices (10°) of the image at 0° , 90° , 180° , and 270° , as shown in Fig. 3.20. The centre x coordinate is found by calculating the shift required to match the radial intensities of the 90° and 270° slice profiles. Likewise, the y coordinate is determined from vertical alignment of the 0° and 180° slices. This shift is then applied to the binned image file, so that the image will be centred in the square pixel grid. Once centred, the image may be corrected for small radial distortions that occur due to aberrations from the optical camera and electrostatic VMI



(a) Horizontal alignment using angular slices at 90° and 270° . (b) Vertical alignment using angular slices at 0° and 180° .

Figure 3.20: Defining the image geometric centre by comparing angular slice profiles.

lenses. A trace peak program, developed by Gascooke^[66,67] and implemented by Gibson, follows the position of the main spectral features as a function of image angle. This allows for deviations from a circular image to be identified. Fig. 3.21 demonstrates how the position of the peaks corresponding to transitions $O(^3P_2) \leftarrow O^-(^2P_{3/2})$, $O(^1D_2) \leftarrow O^-(^2P_{3/2})$, and $O(^1D_2) \leftarrow O^-(^2P_{1/2})$, vary around the image. Morphing the image by this small correction factor produces a centred, circularised image that may then be used to construct a photoelectron spectrum. The required corrections are typically very small (less than ~ 10 pixels), but are important for the image angular integration (section 3.5.1). Image processing is carried out using python language programs written by Gibson at the ANU, with some of the code now available online^[64,67].

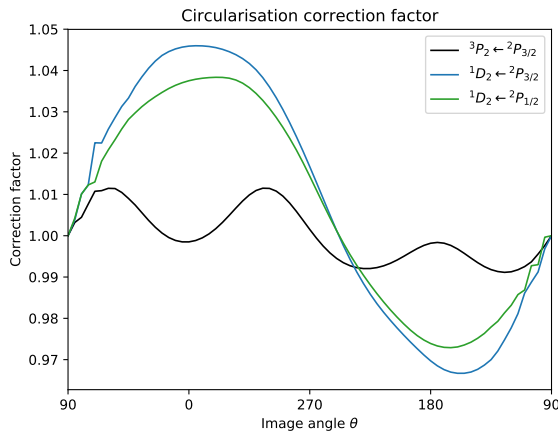


Figure 3.21: Radial correction factor as a function of angle.

Once inverted, angular integration produces a radial electron distribution as a function of the detector radius. This is then placed on an electron kinetic energy scale, using Eq. 3.9, to construct a photoelectron spectrum, as shown in Fig. 3.22. At $\sim 11,800\text{ cm}^{-1}$ 3 peaks are observed, corresponding to the fine-structure transitions $O(^3P_{2,1,0}) \leftarrow O^-(^2P_{3/2,1/2})$, while 2 peaks at $\sim 27,600\text{ cm}^{-1}$ correspond to the excited state $O(^1D_1) \leftarrow O^-(^2P_{3/2,1/2})$ transitions. By fitting Gaussian functions to each fine structure transition, using the known geometric constants from the calculations of Scharf and Godefroid^[68], the anion source

temperature and spectral resolution may be determined. The ground state $^3P_2 \leftarrow ^2P_{3/2}$ transition has a full-width-half-maximum (FWHM) of $75.7(6)$ cm $^{-1}$ (93 μ eV), while the excited state $^1D_2 \leftarrow ^3P_{3/2}$ transition has a FWHM of only $13.5(2)$ cm $^{-1}$ (16.7 μ eV), demonstrating the excellent resolution of the HR-PEI spectrometer over a wide range of electron kinetic energies.

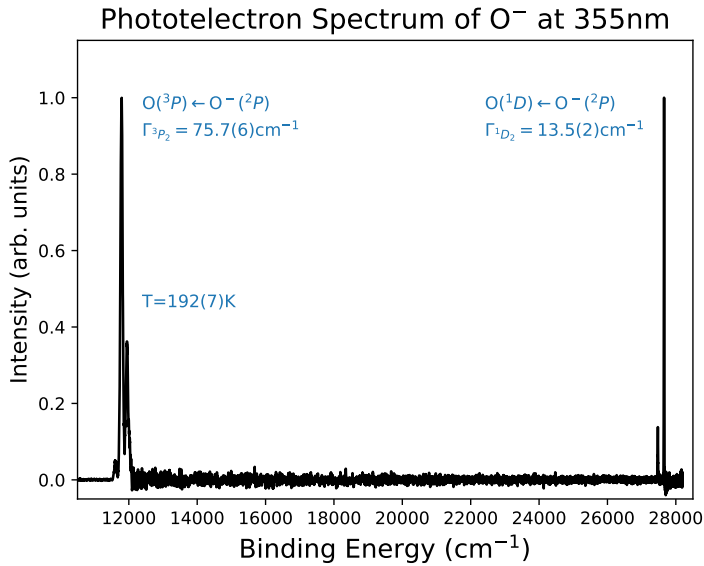


Figure 3.22: Photoelectron spectrum of O $^-$ at 355 nm, highlighting the HR-PEI spectrometers μ eV resolution.

The angular anisotropy parameter, defined in Eq. 2.38, may be determined by taking angular slices (10°) of the inverted velocity map image. Plotting the integrated intensity of each slice against $P_2(\cos \theta)$, where P_2 is the second order Legendre polynomial, produces a linear relationship with slope equal to β , as shown in Fig. 3.23. At the top of the image, $P_2(\cos 0^\circ) = 0.5(3 \times 1^2 - 1) = +1$ and the intensity is at a minimum, whereas at the horizontal, $P_2(\cos 90^\circ) = 0.5(3 \times 0^2 - 1) = -0.5$ and the intensity is at a maximum, corresponding to a negative anisotropy parameter.

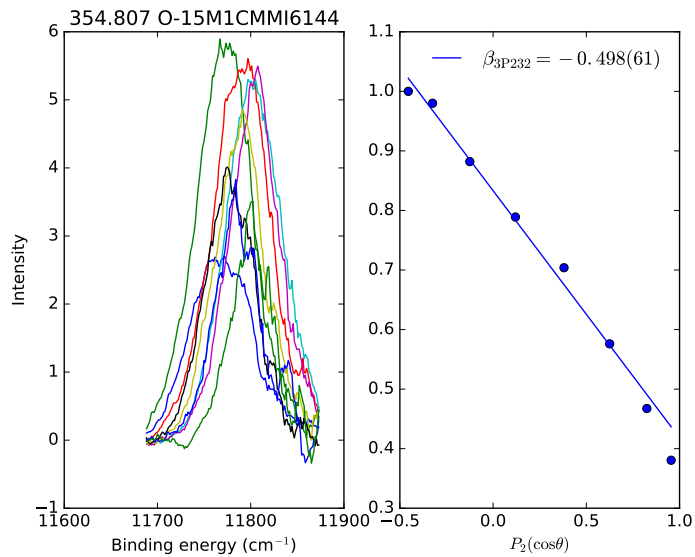


Figure 3.23: Determination of the $\text{O}(^3P_2) \leftarrow \text{O}^-(^2P_{3/2})$ anisotropy parameter. The intensity is most intense at the horizontal ($P_2(\cos\theta) = -0.5$), and least intense at the top of the image ($P_2(\cos\theta) = +1$), indicative of a negative β parameter.

Part II

Nitrogen Dioxide - The discovery of a new isomer

Motivation

Part II of this thesis focuses on the triatomic molecule Nitrogen dioxide (NO_2), a common atmospheric pollutant. Particular attention is paid to the possibility of different isomers, and the role this may play on the dynamics of the molecule - a common theme throughout this body of work. This study reveals the first observation of a new peroxy NOO isomer, on the way to providing an in-depth investigation into the photochemical properties of the parent ONO molecule. High resolution studies of similar atmospherically relevant species NO^- , O_2^- , and O^- are recorded for calibration, with new detail determined.

4.1 The history of NO_2

Nitrogen dioxide, a brown toxic gas formed in most combustion processes, is an abundant atmospheric pollutant and a key component of photochemical smog^[69]. High concentrations of NO_2 in the atmosphere may lead to various health risks in humans, including higher risks of lung cancer and heart failure^[70]. Consequently, there are many regulations in place, particularly in areas of high traffic density, in an attempt to limit the levels of NO_2 in the atmosphere^[71].

Nitrogen dioxide, along with nitric oxide (NO), also play a vital role in determining the distribution of ozone in the Earth's atmosphere^[72]. These compounds may be found naturally in the stratosphere, and help cycle ozone to molecular oxygen^[73]. However due primarily to emissions from diesel motor engines and thermal power plants, nitric oxides (NO_x) are also present in the troposphere, where they act as very efficient green house gases^[74,75]. As a result, trying to understand the photochemical and reactive properties of the neutral NO_2 molecule has been the focus of many previous studies^[76-83].

4.1.1 Ions and photochemistry

The literature on the NO_2^- negative ion is much less complete, with most of the scientific discussion based on only a handful of experimental results. The nitrite anion (NO_2^-) is a very desirable focus for spectroscopy studies, due to the significant role it plays in the Earth's atmosphere. Most reactions in the lower atmosphere occur with neutral start and end states, but often pass through ionic intermediates, making the study of these transient species vital in order to fully understand the processes occurring^[46]. However, it is in the upper atmosphere, where photoionisation and photofragment processes become important drivers of the chemistry, that the importance of the NO_2^- ion becomes more prevalent^[73,82]. In this region, the high density of UV photons available to partake in photochemistry translates into a larger density of ions and radicals. Valuable information may be obtained from total photodetachment cross section experiments of the NO_2^- ion, which has led multiple studies to try and measure the cross section behaviour as accurately as possible.

The first photodetachment measurement of NO_2^- was reported in 1969 by Peter Warneck^[84], where nitrogen dioxide ions were produced in a gas discharge, and subsequently photodetached using a mercury-xenon light source. The total number of photoelectrons

emitted was measured as a function of the photon energy, allowing for the cross section, and electron affinity of the ion (3.1(5) eV), to be determined.

In 1974 the Brauman^[6] and Lineberger^[5] groups both measured the total photodetachment cross section of NO_2^- , using a Hg-Xe arc and dye laser light source respectively. Improved experimental set-ups allowed for a more accurate determination of the total cross section, with a smaller NO_2 electron affinity of 2.36(1) eV defined, cf. 3.1(5) eV in the earlier study. In both the Brauman and Lineberger measurements, a long photoelectron tail was observed well beyond the electron affinity threshold, with both papers showing photodetachment at energies as low as 1.8 eV. These additional electrons were attributed to a possible peroxy isomer of NO_2 , NOO , a radical that was first postulated to exist by Clyne and Thrush in 1961^[4]. The observation of long photoelectron tails provided the first experimental evidence that may support this suggestion. However, as the experiments only measured the total photoelectron yield, providing limited spectral information, they were unable to confirm this hypothesis. The possibility of a new isomer prompted further investigation, with Huber *et al.*^[85] reporting on excited NO_2^- photodetachment, followed by a wide-range cross section experiment by Woo *et al.*^[86]. But neither of these studies found any evidence of a NOO isomer.

Using their zero-core-contribution model, Clodius *et al.*^[87] modelled the photodetachment cross section from a purely theoretical approach. This model was extended to predict differential cross sections and electron distribution anisotropies. It was suggested that the differing behaviour of s partial waves near threshold may produce an interesting result in the anisotropy curve, where the angular distribution would rapidly become isotropic at very low kinetic energies. However no experimental NO_2^- anisotropy information was available to test this prediction.

In 1988 the Lineberger group^[88] measured the first photoelectron spectrum of NO_2^- , using an argon ion laser and a hemispherical analyser to record the energy of the detached electrons. This resolved multiple vibrational transitions, corresponding to the electronic ground state transition $\text{NO}_2 \tilde{X}^2 A_1 \leftarrow \text{NO}_2^- \tilde{X}^1 A_1$, and redefined the electron affinity at 2.273(5) eV. Despite the large number of transitions observed, all of the spectral structure may be completely described by simple overtone and combination progressions in two totally symmetric vibrational modes of the ground state. One year later, the Neumark group^[89] measured the NO_2^- photoelectron spectrum using the third, fourth, and fifth harmonics (355, 266, and 213 nm) of a Nd:YAG laser. The additional photon energy allowed for transitions to the excited states $\tilde{A}^2 B_2$ and $\tilde{C}^2 A_2$ to be measured, providing the first direct observation of the dark $\tilde{C}^2 A_2$ electronic state, which is dipole forbidden in standard one-photon optical experiments. None of the above photoelectron experiments found any evidence of a peroxy NO_2 isomer, which started to create doubt about its existence. Multiple theoretical studies attempted to solve this dilemma, with *ab-initio* calculations of Meredith *et al.*^[90] providing estimates for the vibrational and electronic energy structure of possible peroxy and cyclic isomers. By calculating potential energy surfaces along the $\text{N} + \text{O}_2$ reaction coordinate, Walch^[91] predicted that NOO should form a very shallow minimum, with a small barrier of ~ 0.3 kcal/mol to dissociation. No further experimental studies have been able to find any evidence of the NOO isomer.

More recent *ab-initio* studies have been reported, including an investigation into the geometry of the NO_2^- anion^[92] and the conical intersection between the neutral $\tilde{X}^2 A_1$ and $\tilde{A}^2 B_2$ potential energy surfaces^[93]. Both of these studies use the experimental results of Lineberger and Neumark for comparison to their models, despite the experimental measurements occurring ~ 30 years ago. This highlights both the quality of the original

experiments, but also the need for new higher resolution spectra that can provide more spectral detail.

As such, the photoelectron spectrum of NO₂⁻ is reinvestigated using the HR-PEI spectrometer. The use of velocity map imaging allows for both the energetic and angular information to be obtained over a large energy range with high resolution. This helps resolve new spectral detail, and exposes spectroscopic signatures of the elusive NOO peroxy isomer.

4.2 Quantum structure of C_{2v} NO₂

Before discussing the results of this study it is useful to first examine the underlying structure of the target species, as this will be essential for the analysis of any spectra obtained. Symmetry plays an important role in understanding both the physical and energetic structure of molecules, and may be used to anticipate the expected spectral behaviour. From a simple valence shell electron pair repulsion (VSEPR) description, both neutral and ionic NO₂ will be angular in geometry. As planar molecules with a 2-fold symmetry line through the central N atom, Table 2.1 confirms that both NO₂ and NO₂⁻ belong to the C_{2v} point group.

Equilibrium geometries of the ground state of NO₂ may be determined using high level *ab-initio* code, with calculations reported in this work carried out using NWChem^[94] and Q-Chem^[95] software packages. Unless stated otherwise, calculations presented in this work are generally computed at the CCSD(T) level of theory with a cc-pVTZ basis - often considered the gold standard of *ab-initio* methods^[96,97]. Experimental values for the bond lengths and angles may also be obtained, through high resolution microwave spectroscopy of the neutral^[79] and photoelectron spectroscopy measurements of the anion^[88]. A list of theoretical and experimental geometric values, obtained from both this work and past studies, is presented in Table 5.3 at the end of chapter 5.

Vibrational levels

As a non-linear triatomic molecule, the vector motion of NO₂ vibrations will be constrained to one of three (3N – 6) normal modes. The symmetry (and subsequent participation in a photoelectron spectrum) of each vibrational mode may be determined from the C_{2v} character, given in Table 4.1.

Table 4.1: Character table of the C_{2v} point group. Γ_{red} for each symmetry element as applied to NO₂ is also included.

C_{2v}	E	$C_2(z)$	$\sigma(xz)$	$\sigma(yz)$	
A_1	1	1	1	1	z
A_2	1	1	-1	-1	R_z
B_1	1	-1	1	-1	x, R_y
B_2	1	-1	-1	1	y, R_x
No. Stationary Atoms	3	1	1	3	
Character Contribution	3	-1	1	1	
Γ_{red}	9	-1	1	3	

Applying the method from section 2.1.4 to Table 4.1 shows that the total number of

irreducible representations is,

$$\Gamma_{\text{irrep}} = 2A_1 + B_2.$$

Only the 2 totally symmetric A_1 vibrational modes will be active in a photoelectron spectroscopy experiment, with the antisymmetric B_2 mode forbidden. The vectors depicting these normal modes, along with their vibrational frequency, may be computed through *ab-initio* methods using quantum chemistry code. Coupled cluster CCSD(T) geometry optimisation and harmonic frequency calculations were computed with a cc-pVTZ basis using NWChem^[94] software, with the resulting vectors shown in Fig. 4.1. The calculated normal mode frequencies are listed in Table 5.3 at the end of chapter 5, for comparison to experimental and other theoretical values.

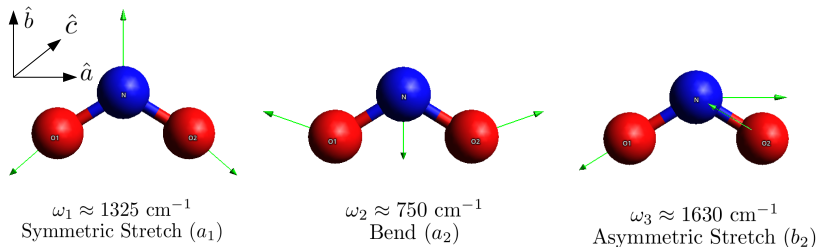


Figure 4.1: Normal mode vectors of the vibrational modes of \tilde{X}^2A_1 NO_2 , calculated at the CCSD(T) cc-pVTZ level.

Rotational levels

From the equilibrium geometries listed in Table 5.3, the moment of inertia ($I = \sum_i m_i r_i^2$) around each of the three symmetry axes, depicted as \hat{a} , \hat{b} , \hat{c} in Fig. 4.1, may be calculated. The corresponding rotational constants are defined by Eq. (4.1),

$$A = \frac{\hbar}{8\pi^2 c I}. \quad (4.1)$$

where I is the moment of inertia around axis \hat{a} , c is the speed of light, and \hbar is Planck's constant. Like vibrational frequencies, rotational constants are usually quoted in units of wavenumbers (cm^{-1}).

The rotational constants for NO_2 and NO_2^- are listed in Table 5.3. A small moment of inertia around an axis results in less resistance to rotation in that direction, equating to a larger rotational constant (Eq. 4.1), and therefore a larger energy spacing between adjacent levels. For nitrogen dioxide, $A > B \approx C$, so most of the rotational energy will be distributed around the principal \hat{a} axis. Strictly speaking, as all three constants are unique NO_2 is an asymmetric top, however as $B \approx C$ it may be treated in the limit of a prolate symmetric top. The amount of prolate character can be quantified by the parameter κ , defined as

$$\kappa = \frac{2[B - \frac{1}{2}(A + C)]}{A - C}. \quad (4.2)$$

A value of $\kappa = -1$ describes a perfect prolate top ($A > B = C$), while $\kappa = 1$ corresponds to a pure oblate symmetric top ($A = B > C$). Asymmetric tops with three unique constants

will lie somewhere between these two limits.

Substituting the constants of NO_2 from Table 5.3 into Eq. (4.2) gives $\kappa_{\text{NO}_2} = -0.99$, and $\kappa_{\text{NO}_2^-} = -0.97$. As both these values are close to the prolate limit ($\kappa = -1$) it is valid to treat both states of nitrogen dioxide as prolate tops.

4.3 The peroxy isomer NOO

The possibility of a NOO peroxy isomer was first discussed by Clyne and Thrush^[4], who postulated that NOO could play an important intermediate role in the formation of NO in the atmosphere through the reaction



Such a pathway for forming NO may have a large effect on nitric oxide cooling in the D-region of the ionosphere^[98,99]. Various experimental and theoretical studies have attempted to confirm the existence of NOO, however currently there is still debate about whether NOO represents a stable minimum on the NO_2 potential energy surface or is merely a transient reaction intermediate^[90,91,100]. While early experimental studies suggested evidence supporting an NOO isomer^[5,6], more recent studies have failed to find any sign of its existence.

Unlike the C_{2v} ONO isomer, calculations suggest that NOO will be a planar molecule with no other lines of symmetry, making it a member of the C_s point group. The equilibrium geometry of the ground states of both NOO and NOO^- are determined using CCSD(T) *ab-initio* geometry optimisation calculations, with the resulting geometric constants presented at the end of chapter 6 in Table 6.1. As NOO has not been directly observed, there are no previous experimental values available for comparison to these calculations.

Vibrational levels

As a non-linear triatomic molecule, the vibrational motion of peroxy NOO will also be constrained to three ($3N - 6$) normal mode vectors. The symmetry of each vibrational mode may be assigned by looking at the character table for the correct point group. The C_s character table, including the number of reducible representation for each symmetry element as applied to NOO is presented in Table 4.2.

Table 4.2: Character table of the C_s point group. Γ_{red} for each symmetry element applied to NOO is also included.

C_s	E	σ_h	
A'	1	1	x, y, R_z
A''	1	-1	z, R_x, R_y
No. Stationary Atoms	3	0	
Character Contribution	3	1	
Γ_{red}	9	3	

Calculating the number of irreducible representations from Table 4.2 gives,

$$\Gamma_{\text{irrep}} = 3A'.$$

Therefore peroxy NOO has three totally symmetric vibrational modes, all of which may be present in a photoelectron spectroscopy experiment. The vectors depicting these normal modes, along with their vibrational frequency, are computed through *ab-initio* coupled cluster CCSD(T) calculations, with a cc-pVTZ basis using NWChem^[94] software. The resulting vectors are shown in Fig. 4.2, with the normal mode frequencies listed in Table 6.1 at the end of chapter 6.

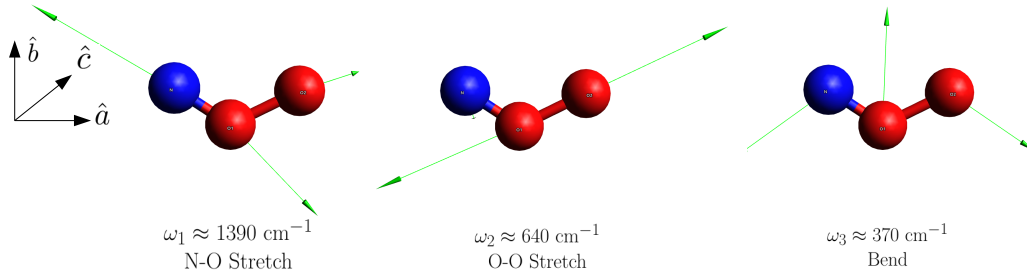


Figure 4.2: Normal mode vectors of the vibrational modes of \tilde{X}^2A' peroxy NOO, calculated at the CCSD(T) cc-pVTZ level.

Rotational levels

By evaluating the moment of inertia $I = \sum_i m_i r_i^2$ around each axis from the geometric constants in Table 6.1, the rotational constants of NOO and NOO^- may be calculated. The NOO rotational constants (Table 6.1), show that $A > B \approx C$, similar to the C_{2v} ONO isomer. Using Eq. (4.2) to quantify the level of prolate character gives values of $\kappa_{\text{NOO}^-} = \kappa_{\text{NOO}} = -0.97$, confirming that NOO may also be validly treated as a prolate symmetric top. This suggests that both isomers will possess similar rotational structure. However due to the higher symmetry present in ONO, the selection rules will differ.

Often the $J'_0 \leftarrow J''_0$ origin of a rotational band does not occur at the maximum peak intensity of the unresolved Gaussian vibrational transition. Therefore, measuring the transition energy by simply taking the maximum peak position may introduce an inaccuracy to the result. To account for this, Engelking^[101] developed a symmetric top approximation to predict the shift in the rotational band head based on the relative size of the rotational constants. For a prolate symmetric top the approximate band shift is given by,

$$E' - E'' \approx k_b T \left[B'/B'' + A'/2A'' - \frac{3}{2} \right] + (B'' - B')/3, \quad (4.4)$$

where k_b is the Boltzmann constant (in $\text{cm}^{-1}\text{K}^{-1}$) and T is the rotational temperature (in K). For a rotational temperature of ~ 200 K this predicts a NOO band shift of $E' - E'' \approx 25 \text{ cm}^{-1}$.

NO₂ and the Wigner filtering effect

To investigate the energetic and photophysical properties of the nitrogen dioxide anion, $e^- + \text{NO}_2(\tilde{X}^2\text{A}_1) \leftarrow \text{NO}_2^-(\tilde{X}^1\text{A}_1) + h\nu$ photodetachment was studied using the ANU's HR-PEI spectrometer. The 1988 and 1989 NO₂⁻ photoelectron measurements of Lineberger^[88] and Neumark^[89] are still considered state of the art, despite being ~ 30 years old, and before the development of velocity map imaging. Therefore, reinvestigating this problem with the HR-PEI spectrometer should reveal new spectroscopic detail, and allow for both the energetic and angular information from this detachment process to be examined. In particular, it is hoped that careful analysis of these spectra may help in obtaining accurate values for spectroscopic constants including the electron affinity (EA) and vibrational frequencies (ω_e) of the anion. Investigation of angular distribution energy dependence may also reveal useful information about the anion orbital structure.

5.1 Photoelectron spectroscopy of NO₂⁻

Nitrite anions (NO₂⁻) are produced by passing pure nitrous oxide (N₂O) gas through a pulsed nozzle, at a stagnation pressure of 2 atmospheres. The gas molecules then supersonically expand into the source vacuum chamber, while passing through a pulsed high voltage discharge, as described in section 3.2. The gas rapidly cools during the adiabatic expansion, resulting in a large soup of cold molecules and ions. This adiabatic cooling typically results in a post-discharge ion temperature of ~ 200 K, ensuring that the majority of ions measured will be in the ground vibrational state, with only 1 or 2 hot bands usually present. The ions are then mass isolated by time of flight, and photodetached using either a Sunlite OPO or Nd:YAG laser.

A velocity-map image of the photoelectrons collected from 355 nm photodetachment of mass isolated NO₂⁻, using the third harmonic of a Nd:YAG laser, is presented in Fig. 5.1. The raw image (left) shows a 2D projection of the 3D photodetachment event, while the inverted image (right) represents a 2D slice. The image consists of 15,233,347 electrons, from 175,000 laser shots at a repeller voltage of -2200 V. Each of the rings observed in Fig. 5.1 may be assigned to a different $e^- + \text{NO}_2(\tilde{X}^2\text{A}_1) \leftarrow \text{NO}_2^-(\tilde{X}^1\text{A}_1) + h\nu$ vibrational electron detachment transition, with the fastest electrons at the outer edge and slowest near the detector centre. The electron angular distribution is clearly centred around the poles of the image, signalling a large positive anisotropy. The corresponding photoelectron spectrum is shown in Fig. 5.2.

The origin peak $1_0^0 2_0^0$ is readily identifiable in Fig. 5.2, near the electron affinity of 2.273 eV as measured in Lineberger's work^[88], while the remaining transitions in the spectrum may be understood by examining patterns. Three distinct vibrational progressions are observed in the spectrum, all with a vibrational spacing of 750 cm⁻¹, suggesting a $\sim 2_0^n$ structure. Furthermore, as the starting point of each progression differs by 1325 cm⁻¹, the three vibrational patterns may be assigned to the transitions $1_0^0 2_0^n$, $1_0^1 2_0^n$, and $1_0^2 2_0^n$.

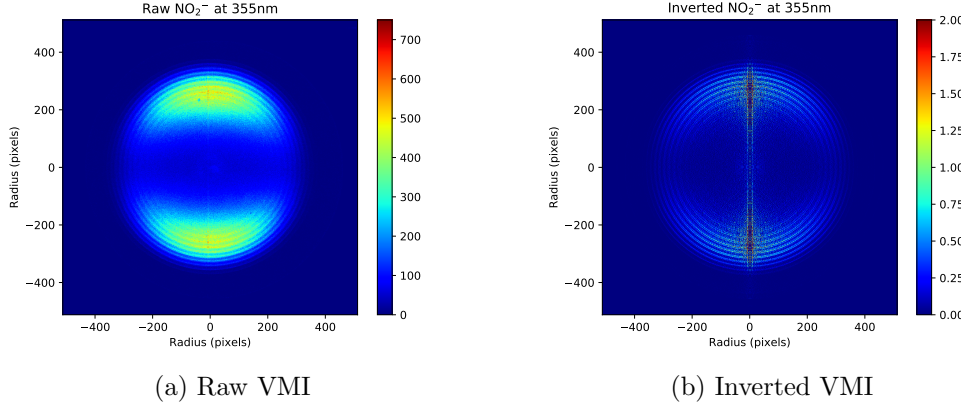


Figure 5.1: Raw (left) and inverted (right) velocity-map images of 355 nm photodetachment from NO_2^- .

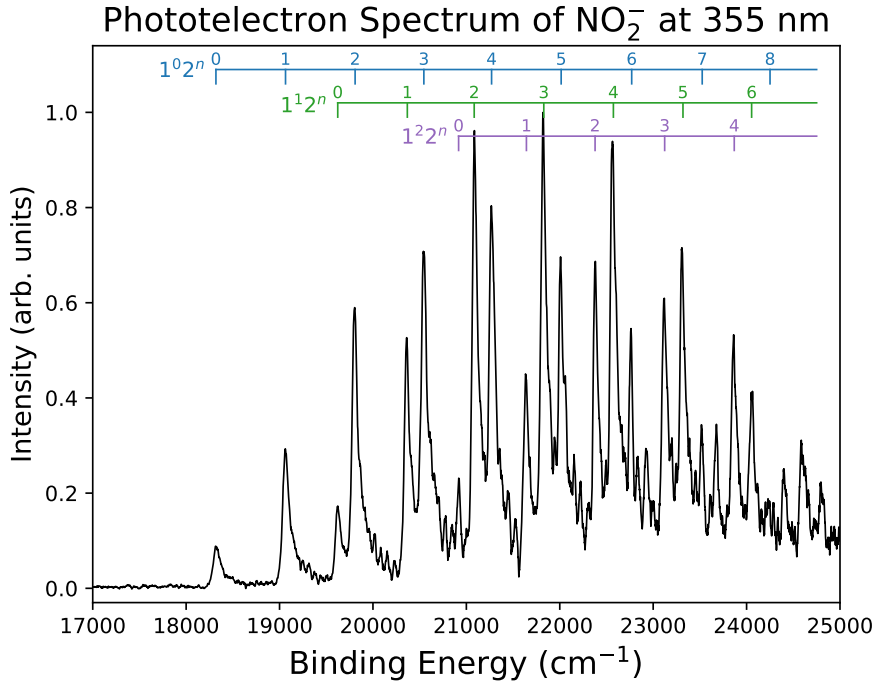


Figure 5.2: Photoelectron spectrum of $\text{NO}_2(\tilde{X}^2\text{A}_1) \leftarrow \text{NO}_2^-(\tilde{X}^1\text{A}_1) + h\nu$ photodetachment at 355 nm.

Under the harmonic oscillator approximation, the position of each vibrational transition may be given by,

$$G(\nu_1, \nu_2) = \text{EA} + \omega_1(\nu_1 + \frac{1}{2}) + \omega_2(\nu_2 + \frac{1}{2}) + \chi_{11}(\nu_1 + \frac{1}{2})^2 + \chi_{22}(\nu_2 + \frac{1}{2})^2 + \chi_{12}(\nu_1 + \frac{1}{2})(\nu_2 + \frac{1}{2}) - \text{ZPE}, \quad (5.1)$$

where EA is the electron affinity and ZPE is the zero point energy. Hence, fitting the measured peak positions in Fig. 5.2 to Eq. (5.1) will allow the harmonic constants ω_1 , ω_2 , and the anharmonic constants χ_{11} , χ_{22} , χ_{12} , of the two active vibrational modes to be determined. These values are presented at the end of this chapter in Table 5.3,

for comparison to computational and previous experimental measurements. This confirms that the vibrational constants of the neutral determined in this work are in good agreement with the high resolution microwave spectroscopy measurements of Lovas *et al.*^[79].

Photoelectron spectra were measured at a range of photodetachment wavelengths, using the Sunlite OPO, with the spectra presented together in Fig. 5.3. This allows for anisotropy parameters to be measured at a range of electron kinetic energies, while helping to find optimal experimental operating conditions. Close to threshold higher resolution is achieved, however less vibrational transitions are observed. This result also reveals the presence of additional electron structure at $\sim 11,000 \text{ cm}^{-1}$, well below the EA of NO_2 .

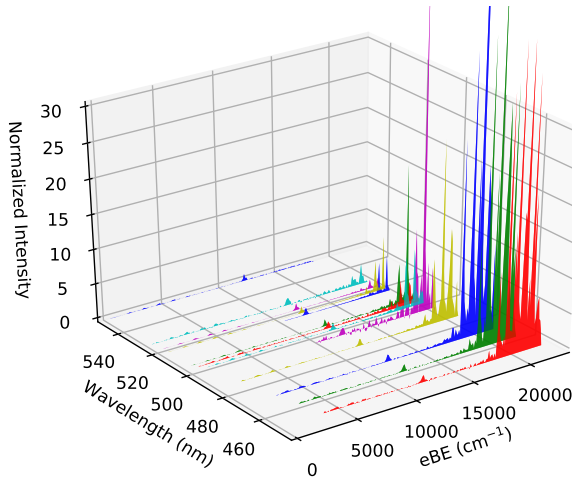


Figure 5.3: Photoelectron spectra of NO_2^- taken at a range of detachment wavelengths from 450 nm to 550 nm using the Sunlite Ex OPO. Close to threshold higher resolution is achieved, however less vibrational transitions are observed.

An optimum resolution measurement was recorded at 469 nm, where the slower electrons allowed for a lower repeller voltage (500 V cf 2200 V for the 355 nm measurement) while still accessing enough vibrational transitions (7) to contain useful information about the target vibrational structure. Velocity-map images (raw and inverted) of the 7,027,295 photoelectrons collected from 469 nm photodetachment of mass isolated NO_2^- are presented in Fig. 5.4. Each ring observed in the velocity-mapped image may be assigned to a $e^- + \text{NO}_2(\tilde{X}^2\text{A}_1) \leftarrow \text{NO}_2(\tilde{X}^1\text{A}_1) + h\nu$ vibrational electron detachment transition, with the $1_0^0 2_0^0$ origin transition at the outer edge of the detector. Comparison to the 355 nm velocity map image in Fig. 5.1, shows that moving to a longer wavelength with a lower repeller voltage significantly improves the spatial resolution, allowing for extra detail to be observed. The cost of this is the reduction in the number of total rings (vibrational transitions) observed. The 469 nm velocity map image also shows a positive anisotropy, with the electron angular distribution centred around the poles.

The corresponding photoelectron spectrum is presented in Fig. 5.5, with the observed peaks assigned to vibrational transitions based on the 355 nm spectrum in Fig. 5.2. At 469 nm 7 vibrational transitions are observed (cf. 21 transitions at 355 nm) which are assigned to the progressions $1_0^0 2_0^n$ and $1_0^1 2_0^n$. Two additional peaks are observed that are not present in the 355 nm spectrum, with one of the peaks occurring at a lower binding

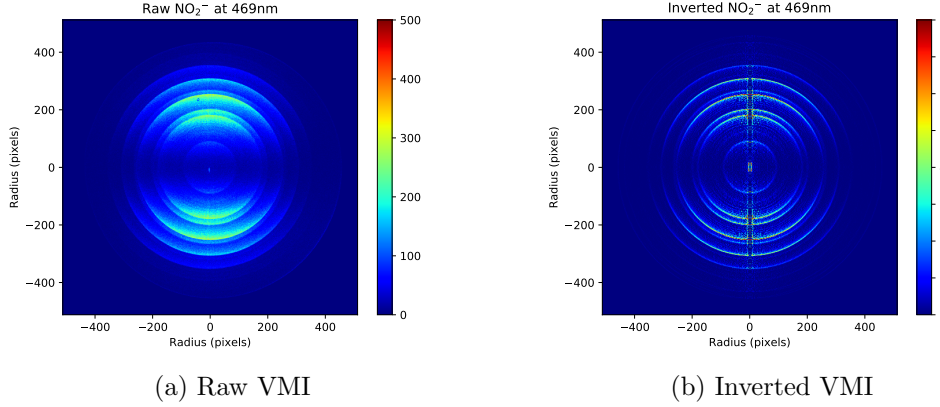


Figure 5.4: Raw (left) and inverted (right) velocity-map images of 469 nm photodetachment from NO_2^- .

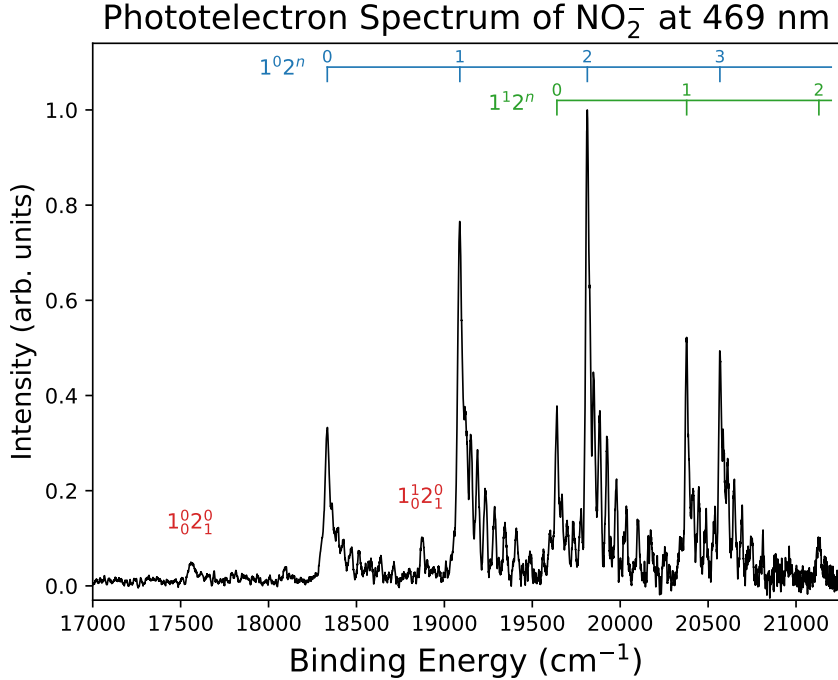


Figure 5.5: Photoelectron spectrum of $\text{NO}_2(\tilde{X}^2\text{A}_1) \leftarrow \text{NO}_2^-(\tilde{X}^1\text{A}_1) + h\nu$ photodetachment at 469 nm. Two hot bands 1_0^{020} and 1_0^{120} are evident, and rotational structure is resolved.

energy than the origin. The presence of these transitions is explained by vibrational hot bands, due to NO_2^- anions that are not in the ground vibrational state. Depending on the source operating conditions, the HR-PEI spectrometer at the ANU will often observe a small number of ions produced in the first or second vibrational level, with hot transitions readily identified by their sensitivity to source temperature. While hot ion temperatures are typically avoided as this often results in a more polluted spectrum, in small quantities the appearance of hot bands may provide valuable information on the vibrational structure of the target negative ion.

The hot bands in Fig. 5.5 are assigned to the vibrational transitions 1_0^{020} and 1_0^{120} . This allows for the vibrational frequency of the ω_2 bending mode of the anion to be determined,

with a frequency of $\omega_2 = 780(20) \text{ cm}^{-1}$ extracted from the spectrum. This is in excellent agreement with the previous measurement of Lineberger *et al.*^[88] of $\omega_2 = 776(30) \text{ cm}^{-1}$.

The improved resolution in the 469 nm photoelectron spectrum reveals rotational structure that was not present in any of the previous measurements. This may allow for new spectroscopic information to be examined, including the rotational constants of both the neutral and ionic species, and will provide a better estimation of the anion source temperature. However first, a full rotational model will need to be constructed.

5.2 Rotational Model of NO_2^-

In order to decode the new rotational structure resolved in Fig. 5.5, the transition selection rules and line intensities need to be examined. By employing symmetry considerations and molecular theory, this structure may be modelled and understood, as is discussed below.

5.2.1 Allowed and forbidden rotational levels

With three distinct rotational constants (see Table 5.3) NO_2 is strictly an asymmetric top, however as $A > B \approx C$ it may be treated in the prolate top limit. To understand how this molecule may behave, we can consider the quantisation of its angular momentum.

For any molecule, the total angular momentum J is quantised, while for symmetric tops the projection of this angular momentum onto the principle (\hat{a}) axis K is also quantised. It follows that $|K| \leq |J|$. Furthermore, as K may be aligned in either the positive or negative \hat{a} direction, $\forall |K| > 0$ there are 2 degenerate energy levels. For an asymmetric top this degeneracy is lost, and we replace the quantum number K with K_a and K_c , representing the projection of the total angular momentum onto the major (\hat{a}) and minor (\hat{c}) axes respectively. Another common representation for the rotational energy levels in an asymmetric top is to introduce the parameter $\tau = -J, -J+1, \dots, J-1, J$, with energy levels labelled in order of increasing energy.

If we let ψ_r be the rotational eigenfunction of the system, then $|\psi_r|^2$ gives the probability of finding the various orientations of the molecule with respect to the axis $\hat{a}, \hat{b}, \hat{c}$. Operators C_2^a , C_2^b , and C_2^c describe a 180° rotation around these axes, and may be used to describe the nature of a rotational level. Symmetry considerations enforce that any rotation of 180° about one of these axes must give the same probability, hence the magnitude of $|\psi_r|$ must remain unchanged under these operations, however the sign $+/-$ may vary. The rotational levels may be distinguished by their behaviour (+ or -) under these operations, giving rise to 4 possible symmetries as shown in Table 5.1. Note that $C_2^b = C_2^a \times C_2^c$, so only two of these operators are needed to uniquely define the symmetry of a level.

Table 5.1: Classification of rotational levels of an asymmetric top^[102].

Dennison	Mulliken	C_2^c	C_2^b	C_2^a
++	A	+	+	+
+-	B_c	+	-	-
-+	B_b	-	-	+
--	B_a	-	+	-

Due to the high symmetry present in NO_2 , simple geometric arguments may be made to determine which rotational levels are allowed to be occupied. NO_2 has a line of symmetry along the \hat{b} axis, which means that the overall symmetry of the rotational level is defined

by the behaviour under C_2^b . Furthermore, Dennison^[103] has shown that for planar C_{2v} molecules (such as NO_2) the symmetry of consecutive rotational levels follows a distinct pattern,

- C_2^a : Lowest energy level (τ_{-J}) = +,
then consecutive levels up are $-,-,+,-,-,\dots$
- C_2^c : Highest energy level (τ_{+J}) = +,
then consecutive levels down are $-,-,+,-,-,\dots$

Consequently, for the special case where the line of symmetry is along the \hat{b} axis, the overall symmetry of the rotational energy levels alternates between symmetric and antisymmetric, with τ_{-J}/τ_{+J} antisymmetric for odd J and symmetric for even J, as shown in Fig. 5.6.

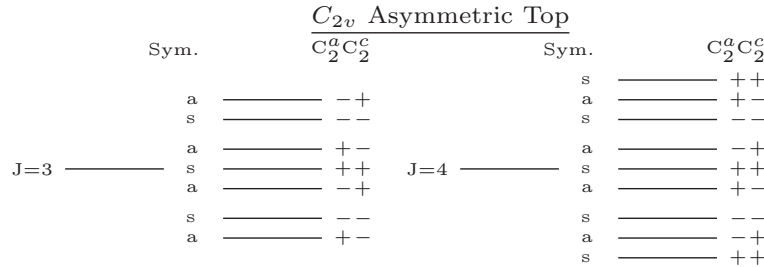


Figure 5.6: Symmetry of rotational levels of a C_{2v} asymmetric top for odd and even J, with levels labelled s for symmetric and a for antisymmetric.

When a symmetric molecule has two identical nuclei, the statistical weightings of symmetric : antisymmetric levels is determined by their corresponding nuclear spin. In the case where the nuclear spin is zero (as in oxygen in NO_2), symmetry considerations show that only rotational levels where the total eigenfunction is symmetric under exchange of the two nuclei can be occupied, thus making all antisymmetric levels forbidden. Combining this result with Fig. 5.6 reveals that the allowed rotational levels in NO_2 are:

$$\begin{aligned} \text{For } J \text{ even: } \tau &= -J, -J+2, \dots, J-2, J \\ \text{For } J \text{ odd: } \tau &= -J+1, -J+3, \dots, J-3, J-1 \end{aligned}$$

This effectively reduces the number of rotational levels from $2J+1$ down to J and $J+1$ for odd and even J respectively, reducing the total number of rotational levels that need to be considered in a photoelectron experiment, in both the neutral and the anion, by a factor of 2.

5.2.2 Selection rules and line intensities

Next, the correct selection rules need to be identified in order to determine which transitions are allowed to occur. As both NO_2 and NO_2^- have a permanent dipole moment, $\Delta J = 0, \pm 1$. However as the dipole is aligned along the \hat{b} axis, signalling a perpendicular transition, transitions with $\Delta J = 0$ will be strongest^[39]. Furthermore, only transitions which satisfy the following symmetry rules are allowed^[102,104]

$$++ \leftrightarrow -- \quad \text{and} \quad +- \leftrightarrow -+ .$$

However, we already know that only totally symmetric levels ($++$ or $--$) are allowed to be occupied in NO_2 . Therefore, the only transitions that will be observed in the photoelectron spectrum are

$$++ \leftrightarrow --.$$

While the rotational and vibrational energies of a molecule may largely be treated separately, we do need to include vibronic effects due to coupling between these two motions. For this, we can introduce the vibrational angular momentum quantum number ℓ , to quantify the projection of the vibrational angular momentum along the symmetry axis of the vibrational mode,

$$\ell_i = v_i, v_i - 2, v_i - 4, \dots, 0 \text{ or } 1 \quad \text{and } \forall \ell_i > 0, g_i = 2$$

$$\ell = |\Sigma_i \pm \ell_i|$$

where the degeneracy $g_i = 2$ for $\ell_i > 0$ arises from the angular momentum aligning along the axis in either the positive or negative direction. Furthermore, an even vibrational level will have even ℓ_i , while for an odd vibrational level ℓ_i will be odd (see section 2.2.2 for more detail). For a C_{2v} molecule such as NO_2 , symmetry considerations enforce that

$$\begin{aligned} \Gamma_{rve}(\text{ion}) \otimes \Gamma_{rve}(\text{neutral}) &\subset \Gamma^* && \text{for } \ell \text{ even} \\ \Gamma_{rve}(\text{ion}) \otimes \Gamma_{rve}(\text{neutral}) &\subset \Gamma^{(s)} && \text{for } \ell \text{ odd} \end{aligned}$$

where Γ_{rve} is the rotational/vibrational/electronic wavefunction, Γ^* is the antisymmetric set and $\Gamma^{(s)}$ is the symmetric set. No change in rotational symmetry is associated with a transition where $\Delta K_a = 0$ so this represents a symmetric transition, whereas $\Delta K_a = \pm 1$ transitions are antisymmetric^[105]. When combined with the rules for the vibronic quantum number ℓ_i , we can see that the ΔK_a selection rules for NO_2 transitions are

$$\begin{aligned} \Delta K_a = 0 && \text{for } v_i \text{ odd} \\ \Delta K_a = \pm 1 && \text{for } v_i \text{ even.} \end{aligned}$$

The prolate symmetric top approximation may then be applied to determine the positions of each allowed rotational level. Moving from an asymmetric top towards a symmetric top (via the parameter κ) the energy separation between levels K_a and K_c approaches zero, recreating the $g_i = 2$ degeneracy of the symmetric top limit. Therefore, assuming the $K_a \approx K_c = K$ (as $\kappa \approx -1$) just two quantum numbers are needed to define the energy position of each level,

$$E(J, K)_{A,B} = BJ(J+1) + (A-B)K^2. \quad (5.2)$$

The values obtained using this prolate symmetric top approximation for NO_2 are in excellent agreement with the exact $\epsilon_{J,\tau}$ values calculated explicitly by King for asymmetric molecules with $\kappa \neq -1$ ^[106].

The above discussion defines the allowed $e^- + \text{NO}_2(\tilde{X}^2A_1) \leftarrow \text{NO}_2^-(\tilde{X}^1A_1) + h\nu$

rotational transitions, while Eq. (5.2) calculates the corresponding transition energies. All that remains is calculation of the relative transition intensities. The intensity of a line will depend on five variables:

- (i) the population density of the initial anion rotation level, as determined by the Boltzmann factor $e^{\frac{-E(J,K)hc}{kT}}$
- (ii) the statistical weight of the levels, $g(J,K) = J$ or $(J+1)$ for J odd or even
- (iii) the Franck-Condon overlap of the vibrational wavefunctions, $C = |\langle \chi_i | \chi_f \rangle|^2$
- (iv) the Hönl London factor $A(J,K)$, which is proportional to the square of the rotational transition moment summed over all orientations of J
- (v) the electronic transition dipole moment, $|\langle \psi_i | \vec{\mu} | \psi_f \rangle|^2$

The transition intensity is then given by,

$$I \propto |\langle \psi_i | \vec{\mu} | \psi_f \rangle|^2 \times C \times A(J,K) \times g(J,K) \times e^{\frac{-E(J,K)hc}{kT}}. \quad (5.3)$$

By employing the symmetric top approximation the transition moment terms $A(J,K)$ may be calculated algebraically. For a perpendicular transition of a prolate symmetric top the Hönl London factors are given by,

$$\text{for } \Delta J = +1 : \quad A_{J,K\pm 1} = \frac{(J+2 \pm K)(J+1 \pm K)}{(J+1)(2J+1)} \quad (5.4)$$

$$\text{for } \Delta J = 0 : \quad A_{J,K\pm 1} = \frac{(J+1 \pm K)(J \mp K)}{J(J+1)} \quad (5.5)$$

$$\text{for } \Delta J = -1 : \quad A_{J,K\pm 1} = \frac{(J-1 \mp K)(J \mp K)}{J(2J+1)}, \quad (5.6)$$

where the \pm refers to $\Delta K \pm 1$ ^[103].

5.2.3 NO₂ rotational contour

A python program was written to implement this model with spectroscopic parameters adjusted to fit the experimental photoelectron spectra measured in this work. A rotational band contour is constructed using the selection rules and line intensities outlined above, for a set of initial guess parameters including ω_e , $\omega_e \chi_e$, A , B , and C , (for both NO₂ and NO₂⁻), as well as experimental parameters such as the anion temperature and spectrometer resolution. Each parameter is then adjusted using a least-squares algorithm to achieve the best fit between the model and experimental spectra. Initially, in order to test the selection rules, the model is fitted over one vibrational band at a time, as shown in Fig. 5.7, for the origin peak $1_0^0 2_0^0$, the first peaks of each progression $1_0^0 2_0^1$, $1_0^1 2_0^0$, and the hot band transition $1_0^0 2_1^0$. This also provides better initial guesses for the various fitting parameters, to help the model home in on the correct values when fitted to the entire spectrum.

The rotational fits presented in Fig. 5.7 generally show good alignment with the structure positions along the energy axis, with the slight exception of peak $1_0^0 2_0^1$ (top right corner). This is possibly due to a known second order effect of the velocity map image lens, which causes small deviations in the relationship between detector radial position and electron kinetic energy (see section 3.5.2). In most experiments this is a negligible effect,

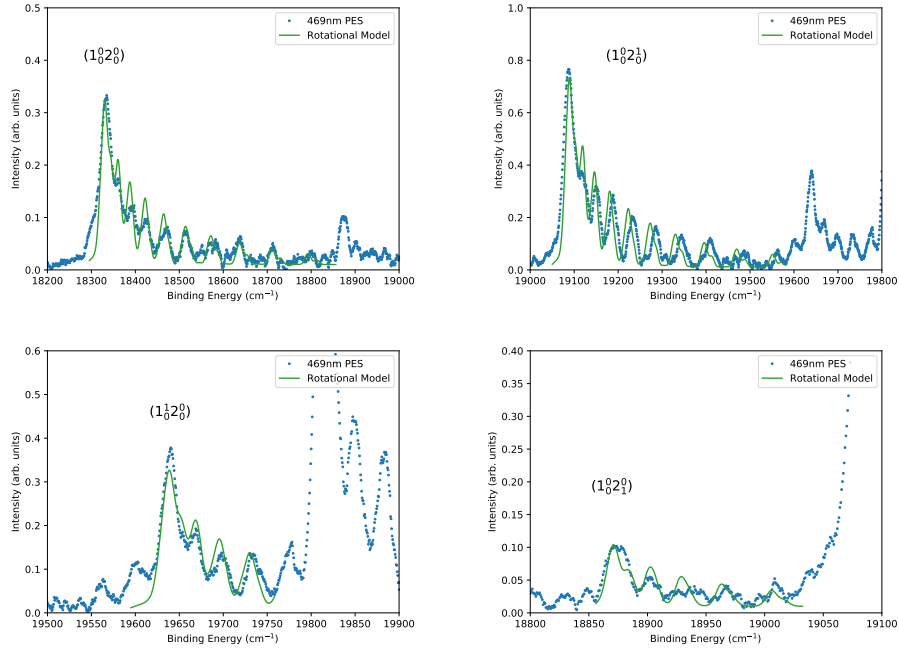


Figure 5.7: Rotational model fitted to individual vibrational bands in the 469 nm photodetachment spectra of NO_2^- .

and can be corrected for using a radial-dependent R2E conversion factor from calibration O_2^- measurements. However it may be responsible for the slight distortion in the $1^0_0 2^1_0$ spectrum, causing the rotational structure to be slightly misaligned with the model.

By analysing these individual bands, the effect of varying the rotational constants and anion source temperature may be examined. Importantly this allows for different relative strengths of the P, Q, R branches ($\Delta J = -1, 0, +1$) to be tested. As $\text{NO}_2(\tilde{X}^2\text{A}_1) \leftarrow \text{NO}_2^-(\tilde{X}^1\text{A}_1)$ is a perpendicular transition, the Q branch ($\Delta J = 0$) is expected to be strongest, but comparisons to the experimental data allow for the dominance of this band to be quantified. Best fits were achieved when the Q branch was enhanced by a factor of 5 relative to the P and R branches.

The rotational model fitted to the entire spectrum is shown in Fig. 5.8. From the shape of the rotational tails on peaks $1^0_0 2^n_0$ and $1^1_0 2^n_0$ a rotational source temperature of $T = 198(7)$ K is extracted, which is a typical value for the HR-PEI spectrometer. Importantly, when this temperature is used to determine the relative intensities of the hot bands in Fig. 5.9 there appears to be good agreement between the experiment and the model, indicating similar temperatures for the rotational and vibrational distributions. Furthermore, the Gaussian functions fitted to each rotational line vary from a FWHM of 15 cm^{-1} near the detector centre to 20 cm^{-1} at the detector edge, demonstrating the $\Delta E \propto E$ characteristic of the VMI lens. It is the high spectral resolution of this work that allows for the usually hidden rotational structure to be observed.

Importantly, this model is able to extract a value for the rotational constants of both the neutral and anion from the experimental photoelectron spectrum. While the rotational constants of the neutral are well defined from high resolution microwave spectroscopy experiments^[79], the corresponding constants for the anion geometry are less well known. As a prolate symmetric top model was used, only two rotational constants are given, despite NO_2 possessing 3 distinct constants. However as $B \approx C$ the model value B may be

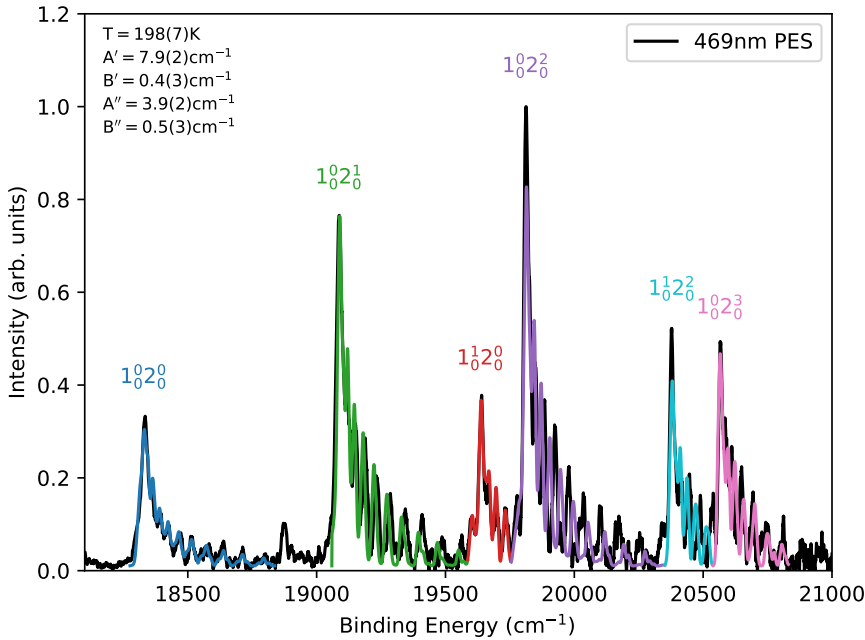


Figure 5.8: Rotational fit over the entire 469 nm photoelectron spectra of NO_2^- . From this, a source temperature of $T = 197(8)$ K was determined, with a FWHM ranging from $\Gamma_{0,0} = 20 \text{ cm}^{-1}$ to $\Gamma_{0,3} = 15 \text{ cm}^{-1}$.

considered an average of these two smaller constants. The HR-PEI rotational constants are listed in Table 5.3 alongside previous experimental and theoretical estimates, with the neutral constants determined from this work shown to be in excellent agreement with the previous microwave measurements of Lovas *et al.*^[79]. Good agreement is also achieved between the CCSD(T) calculations and the experimental anion rotational constants .

From the rotational model fit in Fig. 5.8, the position of the $(v'_0, J'_0, K'_0) \leftarrow (v''_0, J''_0, K''_0)$ origin transition is measured at $18333(7) \text{ cm}^{-1}$, defining a value for the EA of NO_2 . This is in excellent agreement with the previous value measured by Lineberger *et al.* of $18330(40) \text{ cm}^{-1}$ ^[88], however greater precision is achieved in this work due to the resolution of rotational structure, which helps define the true band origin.

To better illustrate the detail of the rotational structure, the model calculation is displaced from the experimental spectrum in Fig. 5.9. As can be seen, the rotational model successfully recreates all of the structure resolved in the photoelectron spectrum. This study reveals rotationally resolved structure in the photoelectron spectrum of NO_2^- for the first time. The spectrum provides for fitting a structurally detailed rovibrational model that faithfully reproduces the spectrum, providing accurate spectroscopic constants for the neutral and lesser studied anion species.

Study of the rotational structure of NO_2 is a beautiful example of how a solid understanding of symmetry principles may aid in decoding molecular spectra. Comparisons to experimental measurements have validated the theoretical model developed here, helping to provide a better understanding of the geometric and energetic structure of this vastly important atmospheric molecule.

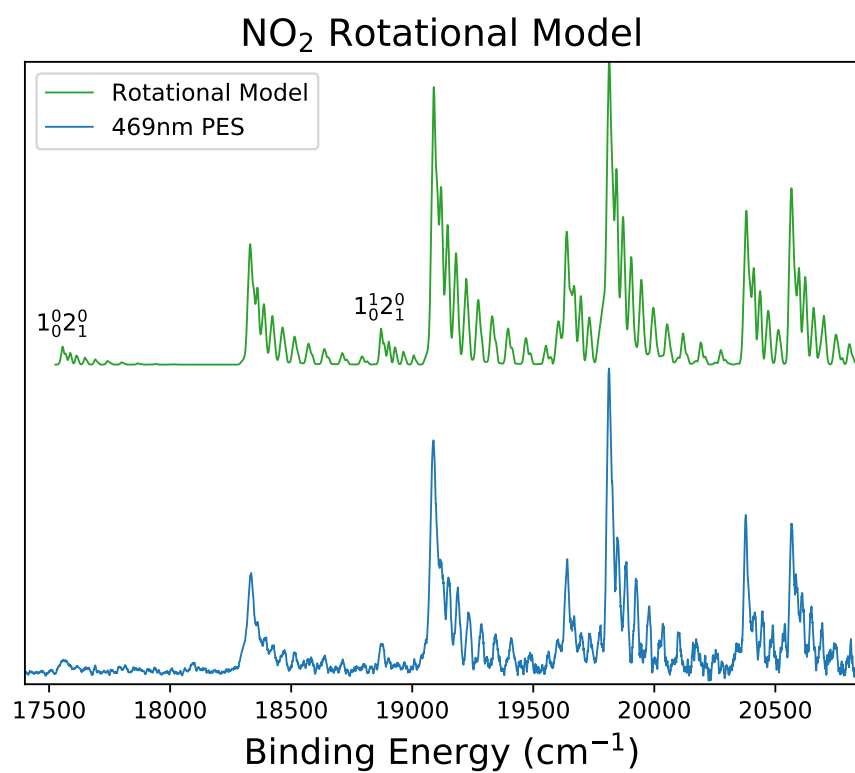


Figure 5.9: Comparison between the NO_2 rotational model (top) and the experimental 469 nm photoelectron spectrum (bottom). As can be seen the model recreates the structure present in the spectrum, including the weak hot bands 1_{02}^0 and 1_{02}^1 .

5.3 Photoelectron angular distributions of NO₂⁻: The Wigner filtering effect

While studying the radial distribution of photoelectrons reveals useful information about the energy structure of a molecule, this section now focuses on the angular distribution of the photoelectrons. In the experimental velocity-mapped images of NO₂⁻ in Fig. 5.1 and Fig. 5.4, it was noted that the angular intensity is not isotropic, with a higher electron density observed at the poles of the image, and a lower electron density at the hemisphere. The anisotropy of a distribution is a specific characteristic of the target molecule being studied, and the photoelectron kinetic energy, and allows for the angular information to be decoded, uncovering the nature of the parent anion molecular orbital. The photoelectron angular distributions of NO₂⁻ photodetachment at various wavelengths (355 nm to 550 nm) are examined here, to characterise the nitrite anion photodetachment orbital.

5.3.1 A general formula for molecular orbitals of any mixed character

In the velocity map images presented in this thesis (Figs. 5.1 and 5.4) the polarisation axis is vertical with respect to the image, defining the axis of cylindrical symmetry. The differential cross section in this case is well known, and is given by,

$$\frac{d\sigma}{d\Omega} = \frac{\sigma_{\text{total}}}{4\pi} [1 + \beta P_2(\cos\theta)], \quad (5.7)$$

where β is the anisotropy parameter and θ is the detachment angle. For atomic (ℓ) photodetachment, the outgoing electron may be represented by the superposition of $\ell \pm 1$ partial waves, as described by the well known Cooper-Zare formula^[29],

$$\beta_\ell = \frac{\ell(\ell-1)\chi_{\ell,\ell-1}^2 + (\ell+1)(\ell+2)\chi_{\ell,\ell+1}^2 - 6\ell(\ell+1)\chi_{\ell,\ell+1}\chi_{\ell,\ell-1}\cos\Delta_{\ell\pm 1}}{(2\ell+1)[\ell\chi_{\ell,\ell-1}^2 + (\ell+1)\chi_{\ell,\ell+1}^2]}, \quad (5.8)$$

where $\chi_{\ell,\ell\pm 1}$ is the radial transition dipole matrix element for the $\ell \pm 1$ partial wave emitted from the initial atomic orbital ℓ , and $\Delta_{\ell\pm 1}$ is the difference in the corresponding phase shifts ($\delta_{\ell+1} - \delta_{\ell-1}$).

The anisotropy of a photoelectron distribution varies with electron kinetic energy. Close to threshold, the $\ell - 1$ partial wave dominates the detachment process, with the $\ell + 1$ wave becoming more prominent at higher energies. This energy dependence may be linked to the behaviour of the radial transition matrix elements in Eq. (5.8), as characterised by the Wigner threshold law^[31]. The relationship between β and $e(\text{KE})$ (and the interference between the $\ell \pm 1$ partial waves) is an important relationship to study, as it may provide additional information about the anion detachment orbital.

The picture becomes more complex for molecules, where more than two partial waves may be involved in the detachment process. Some anionic molecules, such as O₂⁻^[65], NO⁻^[107], and C₂H₂⁻^[11], possess a highest occupied molecular orbital (HOMO) with dominant singular character and behave similarly to atomic anions, however most molecular orbitals exhibit a mixed characteristic with no definite singular value for ℓ ^[34,108]. This may be thought of as a relaxation of the ℓ selection rule, due to a loss in spherical symmetry, resulting in the participation of more than two partial waves. Interestingly, accounting for the contribution of multiple partial waves is not as complex as it may at first seem. The work of Sichel^[109] and Orr^[27] show that the denominator from Eq. (5.8) is related to

these partial cross section,

$$\sigma_\ell \propto \frac{\ell\chi_{\ell,\ell-1}^2 + (\ell+1)\chi_{\ell,\ell+1}^2}{2\ell+1}, \quad (5.9)$$

where σ_ℓ represents the overall cross section of the two interfering $\ell+1$ and $\ell-1$ photodetachment channels. For molecules, the total cross section may then be found by summing over contributing σ_ℓ , $\sigma_{\text{total}} = \sum_\ell \sigma_\ell$ ^[108]. Comparison of the rotationally averaged photoelectron angular distribution model for diatomics of Orr^[27] with the Cooper-Zare expansion of Khuseynov^[108], show that in a general form, the total anisotropy parameter β may be described as a weighted average of these composite $\ell+1/\ell-1$ interference parameters^[108]

$$\beta = \frac{\sum_\ell \beta_\ell \sigma_\ell}{\sigma_{\text{total}}}, \quad (5.10)$$

where from Eq. (5.8) and Eq. (5.9) it is seen that,

$$\beta_\ell \sigma_\ell = \frac{\ell(\ell-1)\chi_{\ell,\ell-1}^2 + (\ell+1)(\ell+2)\chi_{\ell,\ell+1}^2 - 6\ell(\ell+1)\chi_{\ell,\ell+1}\chi_{\ell,\ell-1} \cos(\Delta_{\ell\pm 1})}{(2\ell+1)^2}. \quad (5.11)$$

Substituting Eq. (5.9) and Eq. (5.11) into Eq. (5.10) gives,

$$\beta = \frac{\sum_\ell \gamma_\ell \left[\ell(\ell-1)\chi_{\ell,\ell-1}^2 + (\ell+1)(\ell+2)\chi_{\ell,\ell+1}^2 - 6\ell(\ell+1)\chi_{\ell,\ell+1}\chi_{\ell,\ell-1} \cos(\Delta_{\ell\pm 1}) \right] / (2\ell+1)}{\sum_\ell \gamma_\ell \left[\ell\chi_{\ell,\ell-1}^2 + (\ell+1)\chi_{\ell,\ell+1}^2 \right]}, \quad (5.12)$$

where γ_ℓ is the fractional contribution of the $\ell \pm 1$ partial waves. Comparison between Eq. (5.12) and Eq. (5.8) show that the additional character is accounted for by summing the atomic-case Cooper-Zare numerator and denominator individually over each fractional contribution of angular momentum ℓ . This method now provides a general formula, which may be used to model the anisotropy parameter β for detachment from any mixed character molecular orbital.

5.3.2 Angular distributions of NO_2^-

NO_2^- photoelectron angular distributions were examined for a variety (355 nm to 550 nm) of detachment wavelengths, with the measured anisotropy parameters for $\text{NO}_2(\tilde{X}^2A_1) \leftarrow \text{NO}_2^-(\tilde{X}^1A_1)$ photodetachment plotted as a function of electron kinetic energy in Fig. 5.10. The experimental β parameters show an anomalous jump in anisotropy near threshold, jumping from $\beta \sim 0$ to $\beta \sim +1.7$. This behaviour is unusual for molecular photodetachment, but has been predicted for NO_2^- in previous zero-core-contribution calculations^[86,87]. Despite this prediction occurring in 1983, Fig. 5.10 provides the first experimental evidence of this near-threshold behaviour in NO_2^- . To understand what causes the phenomenon, the molecular orbital structure of NO_2^- must be examined.

Molecular orbitals may be constructed from a linear combination of atomic orbitals possessing the correct symmetry. NO_2^- has 12 contributing atomic orbitals ($2s$, $2p_x$, $2p_y$, $2p_z$ on N, O_a, and O_b) that will combine to form 12 molecular orbitals. 5 will have A₁ symmetry, $4 \times B_2$, $2 \times B_1$, and $1 \times A_2$. Ordering the orbitals in terms of energy and applying the aufbau principle gives a σ non-bonding HOMO of A₁ symmetry. This orbital is formed from a combination of the $2p_y$ and $2p_z$ orbitals of the oxygen's adding out of phase with the $2p_z$ orbital of the nitrogen, resulting in a mixed sd molecular orbital with very

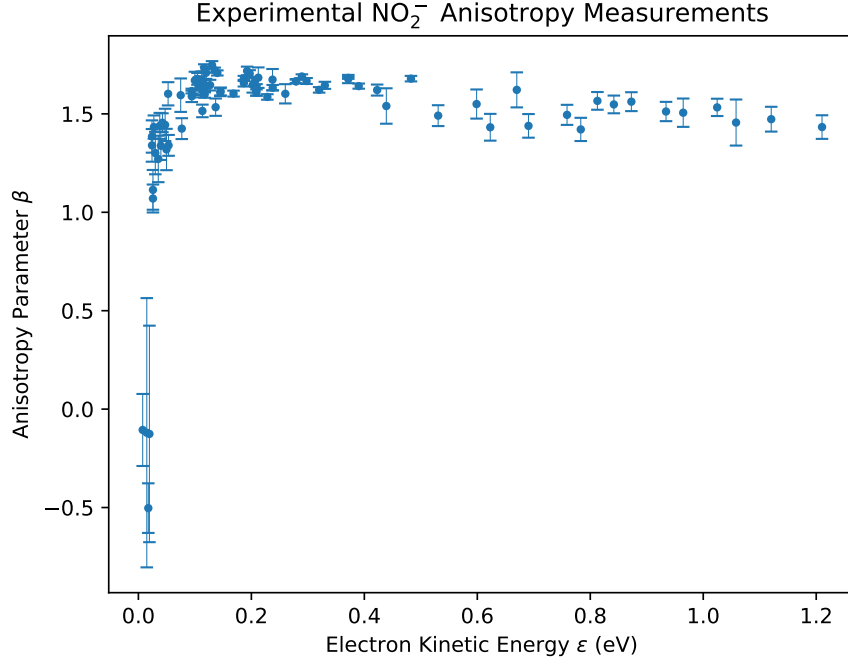


Figure 5.10: Anisotropy parameters for $\text{NO}_2(\tilde{X}^2A_1) \leftarrow \text{NO}_2^-(\tilde{X}^1A_1)$ photodetachment measured at a range of wavelengths from 355 nm to 550 nm and a number of strong vibrational transitions. The data shows a sudden drop in the anisotropy parameter close to threshold.

little net p character. From this, the partial waves involved in the detachment process may be identified. For detachment from an orbital with s , p , and d character, the contributing partial waves are listed in Table 5.2, along with the corresponding cross section behaviour near threshold.

Table 5.2: Partial waves involved in photodetachment from a s, p, d orbital

Orbital Character	Partial Wave Character	σ_{thresh}	$\frac{d\sigma}{d\epsilon}_{\text{thresh}}$
s	p	$\sigma(\epsilon) \propto \epsilon^{3/2}$	$\frac{d\sigma}{d\epsilon}_{\epsilon=0} \rightarrow 0$
p	s	$\sigma(\epsilon) \propto \epsilon^{1/2}$	$\frac{d\sigma}{d\epsilon}_{\epsilon=0} \rightarrow \infty$
	d	$\sigma(\epsilon) \propto \epsilon^{5/2}$	$\frac{d\sigma}{d\epsilon}_{\epsilon=0} \rightarrow 0$
d	p	$\sigma(\epsilon) \propto \epsilon^{3/2}$	$\frac{d\sigma}{d\epsilon}_{\epsilon=0} \rightarrow 0$
	f	$\sigma(\epsilon) \propto \epsilon^{7/2}$	$\frac{d\sigma}{d\epsilon}_{\epsilon=0} \rightarrow 0$

The partial wave behaviour near threshold may be examined, to try explain the sudden drop in the anisotropy in Fig. 5.10. From the Wigner threshold law, the cross section of a wave close to threshold follows $\sigma(\epsilon) \propto k^{2\ell+1}$, where $k = (2m\epsilon)^{1/2}$ [30]. Therefore, the energy dependence of the cross section will follow $\sigma(\epsilon) \propto \epsilon^{(2\ell+1)/2}$ [31]. This behaviour is plotted for all of the partial waves from Table 5.2 in Fig. 5.11. From this plot, it is clear that the near threshold behaviour of the s partial wave differs dramatically from the behaviour of the other partial waves. Furthermore, at very low kinetic energies any s partial wave that is present will dominate the overall behaviour. From Table 5.2 we can

see that an s partial wave will originate if there is any p character in the anion molecular orbital.

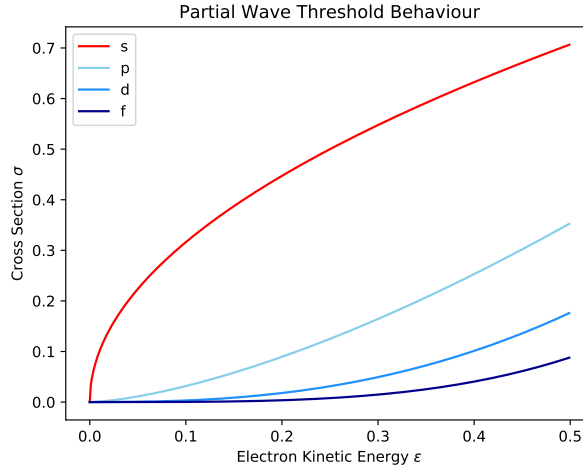


Figure 5.11: Illustration of the Wigner filtering effect, showing the different behaviour of partial waves close to threshold. The s -waves will dominate the detachment process at very low kinetic energies, regardless of the fractional contribution.

As discussed above, the HOMO of NO_2^- only has a small amount of p orbital character, due to the $2p$ orbitals of the oxygen's adding out of phase with the $2p_z$ orbitals on the nitrogen. However, close to threshold this small amount of character is amplified by the Wigner filtering effect (illustrated in Fig. 5.11), which selects out the s partial wave due to its differing behaviour close to threshold. This leads to the surprising result, whereby close to threshold the small amount of p orbital character present dominates the entire photoelectron angular distribution. As the kinetic energy moves above threshold this effect rapidly diminishes, as the other partial waves start to contribute and the mixed sd orbital character then begins to dominate.

At threshold p character is expected to dominate, so substituting $\ell = 1$ into the Cooper-Zare equation (5.8) gives,

$$\beta_p = \frac{6\chi_{1,2}^2 - 12\chi_{1,2}\chi_{1,0}\cos\Delta_{\ell\pm 1}}{3[\chi_{1,0}^2 + 2\chi_{1,2}^2]}. \quad (5.13)$$

The Wigner threshold law may be used to determine how the ratio of matrix elements $\chi_{\ell,\ell\pm 1}$ scale with kinetic energy (see section 2.2.1). Eq. (5.13) may then be rewritten in terms of Hanstorp coefficients^[31],

$$\beta_p = \frac{2A^2\epsilon^2 - 4A\epsilon\cos\Delta_{\ell\pm 1}}{1 + 2A^2\epsilon^2}, \quad \text{where } \frac{\chi_{1,2}^2}{\chi_{1,0}^2} = A\epsilon. \quad (5.14)$$

Eq. (5.14) illustrates explicitly how β scales with electron kinetic energy. Close to threshold, we see that as $\epsilon \rightarrow 0$, $\beta \rightarrow 0$. This is consistent with the data in Fig. 5.10 where at $\epsilon \sim 0$, $\beta \sim 0$, confirming that NO_2^- behaves like a p orbital at threshold. Conversely, the s orbital behaviour, which is predicted to dominate above threshold, may be examined by

substituting $\ell = 0$ into Eq. (5.8),

$$\beta_s = \frac{2\chi_{0,1}^2}{\chi_{1,0}^2} = 2. \quad (5.15)$$

Again this behaviour is reflected in Fig. 5.10. As detachment moves above threshold, an anomalous jump in β is observed from $\beta \sim 0$ to $\beta \sim 1.67$. This represents moving out of the Wigner filtering region, to where the s orbital character starts to dominate. The increase in β is less than +2 due to mixing with the d orbital character also present. As ϵ increases further, β slowly decreases as the higher angular momenta waves start to contribute more to the detachment process.

5.3.3 A mixed *spd* anisotropy model of NO₂⁻

With the structure of the NO₂⁻ HOMO and behaviour of the contributing partial waves determined, a mixed *spd* equation may be constructed to model the anisotropy of NO₂⁻ detachment both at and above threshold. Substituting $\ell = 0, 1, 2$ into our mixed character adaptation of the Cooper-Zare formula, Eq. (5.12), gives

$$\beta_{s,p,d} = \frac{\gamma_s[2\chi_{0,1}^2] + \frac{1}{3}\gamma_p[6\chi_{1,2}^2 - 12\chi_{1,2}\chi_{1,0}\cos\Delta_{2,0}] + \frac{1}{5}\gamma_d[2\chi_{2,1}^2 + 12\chi_{2,3}^2 - 36\chi_{2,1}\chi_{2,3}\cos\Delta_{3,1}]}{\gamma_s[\chi_{0,1}^2] + \gamma_p(\epsilon)[\chi_{1,0}^2 + 2\chi_{1,2}^2] + \gamma_d[2\chi_{2,1}^2 + 3\chi_{2,3}^2]}, \quad (5.16)$$

where γ_s , γ_p , γ_d are the fractional percentage of s , p , d character of the orbital. From the above discussion γ_p will likely be small, dominating the photodetachment dynamics at threshold, before quickly diminishing in importance at higher energies.

To convert Eq. (5.16) into a more usable form, Hanstorp coefficients may be introduced to explicitly describe how β will vary with kinetic energy ϵ . From the Wigner threshold law, $\sigma_\ell \propto \epsilon^{\ell+1/2}$ ^[30], so taking the ratio of $\ell \pm 1$ waves gives,

$$\frac{\sigma_{\ell+1}}{\sigma_{\ell-1}} \propto \frac{\epsilon^{\ell+3/2}}{\epsilon^{\ell-1/2}} = \epsilon^2. \quad (5.17)$$

The cross section $\sigma_{\ell\pm 1}$ is proportional to the square of the relevant radial matrix element $\chi_{\ell,\ell\pm 1}^2$, so following on from Eq. (5.17),

$$\frac{\chi_{\ell,\ell+1}^2}{\chi_{\ell,\ell-1}^2} = A_\ell^2 \epsilon^2, \quad (5.18)$$

where A_ℓ is a proportionality coefficient, commonly known as a Hanstorp coefficient^[31]. The use of Wigner's threshold law to determine the energy dependence of these terms, applying it over large energy ranges (spanning several electron volts), is commonly criticised as, being a threshold law, it is strictly only valid at very small kinetic energies^[32–34]. However, a large magnitude of successful and diverse applications of Hanstorp's approach suggest that while the Wigner predicted cross sections of partial waves are not valid above threshold, the laws prediction of cross-section ratios is much more robust^[24,31,35–37]. This suggests that even though Hanstorp coefficients are derived from the Wigner threshold law, as they apply to ratios of cross sections, the approach is still valid at kinetic energies well above threshold^[34].

In order to apply this approach to Eq. (5.16), we may factor $\chi_{1,0}^2$ out of the γ_s terms,

factor $\chi_{2,1}^2$ from the γ_p terms, and divide the numerator and denominator by $\chi_{1,0}^2$. Letting the expected small phase shifts $\cos \Delta_{2,0} = \cos \Delta_{3,1} = 1$ leads to,

$$\beta_{s,p,d} = \frac{2\gamma_s \frac{\chi_{0,1}^2}{\chi_{1,0}^2} + \frac{1}{3}\gamma_p \left(6\frac{\chi_{1,2}^2}{\chi_{1,0}^2} - 12\frac{\chi_{1,2}}{\chi_{1,0}} \right) + \frac{1}{5}\gamma_d \frac{\chi_{2,1}^2}{\chi_{1,0}^2} \left(2 + 12\frac{\chi_{2,3}^2}{\chi_{2,1}^2} - 36\frac{\chi_{2,3}}{\chi_{2,1}} \right)}{\gamma_s \frac{\chi_{0,1}^2}{\chi_{1,0}^2} + \gamma_p \left(1 + 2\frac{\chi_{1,2}^2}{\chi_{1,0}^2} \right) + \gamma_d \frac{\chi_{2,1}^2}{\chi_{1,0}^2} \left(2 + 3\frac{\chi_{2,3}^2}{\chi_{2,1}^2} \right)}. \quad (5.19)$$

With the equation rewritten in terms of ratio's of matrix elements, Eq. (5.18) can be applied to Eq. (5.19), giving

$$\beta_{s,p,d} = \frac{2\gamma_s B_1 \epsilon + \frac{1}{3}\gamma_p (6A_1^2 \epsilon^2 - 12A_1 \epsilon) + \frac{1}{5}\gamma_d B_2 \epsilon (2 + 12A_2^2 \epsilon^2 - 36A_2 \epsilon)}{\gamma_s B_1 \epsilon + \gamma_p (1 + 2A_1^2 \epsilon^2) + \gamma_d B_2 \epsilon (2 + 3A_2^2 \epsilon^2)}, \quad (5.20)$$

where,

$$A_1^2 = \frac{1}{\epsilon^2} \frac{\chi_{1,2}^2}{\chi_{1,0}^2} \quad A_2^2 = \frac{1}{\epsilon^2} \frac{\chi_{2,3}^2}{\chi_{2,1}^2} \quad B_1 = \frac{1}{\epsilon} \frac{\chi_{0,1}^2}{\chi_{1,0}^2} \quad B_2 = \frac{1}{\epsilon} \frac{\chi_{2,1}^2}{\chi_{1,0}^2}.$$

Eq. (5.20) is a full variable mixed *spd* character model for the angular distribution of detached electrons from NO_2^- . A constraint may be added to the fractional contribution γ parameters, with $\gamma_s + \gamma_p + \gamma_d = 1$. This allows for the model to be applied over the full range of detachment energies, including both the near threshold and high kinetic energy regions.

The *spd* model fitted to the experimental NO_2^- anisotropy parameters measured in Fig. 5.10 is presented in Fig. 5.12. By first fitting only to the above-threshold region, the relevant s/d Hanstorp coefficients of $A_2 = 0.51(6) \text{ eV}^{-1}$ and $B_2 = 0.07(3) \text{ eV}^{-1}$, along with an approximate orbital character composition of 45% *s* to 55% *d* was determined. The remaining parameters were then evaluated by fitting the mixed *spd* model over the entire energy range. This extracted values for the remaining Hanstorp coefficients of $A_1 = 4.4(8) \text{ eV}^{-1}$ and $B_1 = 19(6) \text{ eV}^{-1}$. These values relate to the ratio of radial matrix elements and depend on the characteristics of the parent anion orbital. Khuseynov *et al.*^[108] have shown how Hanstorp coefficients may be explicitly linked to the radial and effective charge parameters of the relevant orbital, however more work is needed before these values may be derived in a pure *ab-initio* fashion. The model also determines the character of the NO_2^- orbital, which is found to possess 2% *p*, 44% *s*, and 54% *d* character. From Fig. 5.12 it can be seen that the mixed *spd* model Eq. (5.20) developed above, recreates the experimental anisotropy data over the entire energy range. The sudden anomalous jump in β close to threshold is attributed to the Wigner filtering effect, which amplifies the small amount (2%) of *p* orbital character due to the differing near-threshold behaviour of the *s* partial wave. As this effect rapidly diminishes above threshold, the relative *p* character contribution decreases, resulting in a jump in β from ~ 0 to ~ 1.67 . This phenomenon is clearly captured by the variable *spd* model.

5.3.4 Zero-core model and Dyson orbital approaches

With a full partial wave description of the angular distribution of electrons from NO_2^- now developed, comparisons may be made with *ab-initio* based approaches. One such approach is the zero-core-contribution model developed by Woo *et al.*^[87], which was first used to predict the anisotropy parameter of NO_2^- photodetachment in 1983. Due to the complexity of

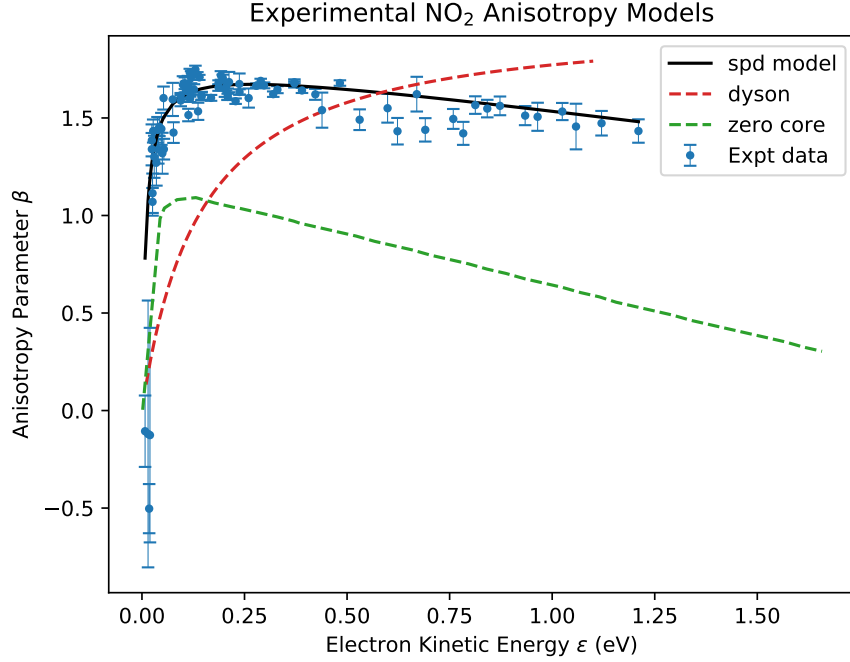


Figure 5.12: Anisotropy parameters from NO_2^- photodetachment over a range of wavelengths from 355–550 nm. The large jump in the anisotropy parameter at threshold from $\beta \sim 0$ up to $\beta \sim 1.67$ is a direct observation of the Wigner filtering effect on the partial waves. The mixed *spd* model Eq. (5.20), developed in the text, is shown in black, and clearly reproduces the experimental data over the entire energy range. Zero-core (— · —)^[87], and Dyson orbital (— · —)^[110] models (discussed in the text) are also shown.

the problem, several robust approximations may be employed. The Born-Oppenheimer approximation proposes that the nuclear and electronic wavefunctions may be treated as separable due to the differing time-scales of their motion, $\Psi(n, e) = \psi_{\text{nuclear}}(n) \times \psi_{\text{electronic}}(e)$. Furthermore, rotational transitions and some electron correlations are also neglected, reducing the multi-electron problem to a one-electron problem.

In the dipole approximation, the differential cross section for photodetachment from a molecule with C_{2v} symmetry is given by^[111],

$$\frac{d\sigma}{d\Omega} = F(v'', v') 2\pi \frac{e^2}{\hbar c} \frac{m_e k \omega}{\hbar} \times |\langle c^n(A)cB \rangle|^2 \times \int |\langle \phi_f | \hat{e} \cdot \vec{r} | \phi_i \rangle|^2 d\tau / 8\pi^2. \quad (5.21)$$

$F(v'', v')$, the Franck-Condon factor, represents the overlap of the initial state (anion) and final state (neutral) vibrational wavefunctions. These may be calculated using *ab-initio* software by determining the normal mode vectors (such as in Fig. 4.1) from a harmonic frequency calculation. Programs such as ezSpectrum may then be used to project the corresponding vibrational wavefunction from the normal mode vectors, in order to evaluate overlap integrals. Franck-Condon factors can also be determined experimentally from photoelectron spectra (such as Fig. 5.1) from the relative peak heights of the vibrational transitions.

The term $|\langle c^n(A)cB \rangle|^2$ is known as the fractional parentage coefficient, where the highest occupied molecular orbital of the anion has $(n + 1)$ electrons and symmetry c ,

while A is the symmetry of the neutral electronic state and B is the symmetry of the anion state^[87]. For detachment from NO_2^- both electronic states have A_1 symmetry, while as discussed earlier, the HOMO has A_1 symmetry with $n = 1$. Therefore, $|\langle c^n(A)cB \rangle|^2 = 1$. $d\tau$ represents an integration over the three Euler angles of the molecule, with the $\frac{1}{8\pi^2}$ term in Eq. (5.21) to account for this averaging of the cross section over all orientations.

This leaves the transition dipole moment $|\langle \phi_f | \hat{e} \cdot \vec{r} | \phi_i \rangle|^2$ as the only term remaining to evaluate, in order to calculate the differential cross section. The zero-core-contribution approximation is used to describe the initial state ϕ_i and final state ϕ_f wavefunctions, by setting a core region of the bound molecular orbital, ϕ_i , inside which the wavefunction is assumed to be zero. The outside of this core region may then be constructed from the linear combination of atomic orbitals. As discussed in section 5.3.2, the HOMO of NO_2^- is of A_1 symmetry, with contributions from the 2_{p_y} and 2_{p_z} orbitals of the oxygen's adding out of phase with the 2_{p_z} orbital of the nitrogen. Mathematically, this may be described as the combination of the three orbitals,

$$\begin{aligned}\phi_{N_z}(r) \\ \phi_{O_z}(r) &= \phi_{p_z}(r_2) + \phi_{p_z}(r_3) \\ \phi_{O_y}(r) &= \phi_{p_y}(r_2) - \phi_{p_y}(r_3),\end{aligned}$$

where ϕ_x are the relevant zero-core wavefunctions^[111], to form the bound molecular orbital,

$$\phi_i = N [c_n \phi_N + c_o (\phi_{O_z} \cos \delta + \phi_{O_y} \sin \delta)]. \quad (5.22)$$

The bound molecular orbital of Eq. (5.22) depends on mixing coefficients c_n , and c_o , the normalization constant N , and the angle δ between the symmetry axis of the combined oxygen orbitals with respect to the molecular symmetry. The ratio of mixing coefficients may be determined by solving the electronic secular equation, using the electron affinities of NO_2 , O, and N to get a mixing ratio of $c_o/c_n = -1.183$ ^[87]. The negative sign confirms the out of phase addition of the N and O orbitals, responsible for the small quantity of net p orbital character. Orbital analysis by Gimarc *et al.* suggests the oxygen orbital align along the N–O bond, giving an angle of $\delta \sim 60^\circ$ ^[112].

For the final state, the neutral atom plus detached electron can be described by a plane wave representation of the detached photoelectron, interacting with the same bound molecular orbital of Eq. (5.22),

$$\phi_f = \phi_k - \langle \phi_k | \phi_i \rangle \phi_i, \quad (5.23)$$

where the electron plane wave $\phi_k = (2\pi)^{-3/2} e^{i\vec{k} \cdot \vec{r}}$. Using these descriptions for the initial and final state wavefunctions, the transition dipole moment from Eq. 5.21 may be calculated. This was done by Woo *et al.*^[87] with their resulting model prediction for the anisotropy parameter β shown in Fig. 5.12 (—). It is clear from the figure that this zero-core-contribution model accurately predicts the shape of the anisotropy curve, correctly predicting the anomalous jump in β close to threshold due to the amplification of the small amount of p orbital character at low energies. This is particularly impressive given there has previously been no experimental NO_2^- photoelectron angular distribution data for comparison. The zero-core model however does underestimate the magnitude of β above threshold, predicting $\beta_{\max} \sim 1.1$ cf. $\beta_{\max} \sim 1.67$, which is possibly due to the choice of parameters c_n , c_o , and δ . The choice of parameter δ in particular has been

shown to impact the magnitude of β ^[87], suggesting that a variation of these parameters may lead to a better fit to the experimental data.

Another theoretical approach that may be used to describe angular distributions involves the construction of Dyson orbitals. Unlike the zero-core model where two (identical) bound molecular orbitals are used to describe both the initial and final states of the molecule individually, Dyson orbitals may be constructed to represent the overlap between the $\phi^{(n)}$ and $\phi^{(n-1)}$ states, where^[113]

$$\phi_{if}^d = \sqrt{N} \int \phi_i^{(n)}(1, \dots, n) \phi_f^{(n-1)}(2, \dots, n) dn. \quad (5.24)$$

These orbital overlaps may be calculated using quantum chemistry software packages, such as Q-Chem^[95,114]. Again the weak field limit and dipole approximations may be applied to determine that the differential cross section will depend on the transition dipole moment, as shown in Eq. (5.21). However by introducing Dyson orbitals (Eq. 5.24) and by assuming strong orthogonality between ϕ_{if}^d , ϕ_k , and $\phi_f^{(n-1)}$, the transition dipole moment may be rewritten as^[115]

$$\left| \langle \phi_f | \hat{e} \cdot \vec{r} | \phi_i \rangle \right|^2 = \left| \langle \phi_{if}^d | \hat{e} \cdot \vec{r} | \phi_k \rangle \right|^2, \quad (5.25)$$

where the detached electron is again represented by a plane wave, $\phi_k = (2\pi)^{-3/2} e^{i\vec{k}\cdot\vec{r}}$. Dyson orbitals were constructed for photodetachment from NO_2^- , with the resulting anisotropy curve shown in Fig. 5.12 (— — —). It can be seen in the figure that the Dyson orbital approach recreates the general shape of the anisotropy curve, but underestimates the rapid jump in β at threshold. This behaviour of Dyson orbitals has been observed in previous studies, due to the sensitivity of the anisotropy parameter β on the asymptotic behaviour of the orbitals^[110]. The essential quantity that determines β in the calculation is the ratio of partial cross sections $\sigma_{\ell+1}/\sigma_{\ell-1}$, making the anisotropy curve very sensitive to errors in $\sigma_{\ell+1}$ and $\sigma_{\ell-1}$. By artificially varying the ratio $\sigma_{\ell+1}^2/\sigma_{\ell-1}^2$ by a constant factor, better agreement with experimental results may sometimes be obtained^[110].

From this study, an anomalous jump in the anisotropy parameter β from NO_2^- photodetachment is observed, which is attributed to a Wigner filtering effect on the *s* partial wave, amplifying the small level (2%) of net *p* orbital character close to threshold. Furthermore, applying a general formula to the detachment process results in a mixed *spd* model that is able to recreate the experimental anisotropy data. From careful analysis of the relevant orbital, *ab-initio* based methods also recreate this effect, however with both a zero-core model and a Dyson orbital approach model parameters still need to be fitted to experimental data in order to fully recreate the results. The experimental data presented here allows for these models to be tested and improved, while providing the first experimental evidence of the anomalous jump in β which was predicted for NO_2^- .

Table 5.3: Comparison between calculated and experimental values for the geometric and vibrational properties of $\text{NO}_2 \tilde{X}^2\text{A}_1$ and $\text{NO}_2^- \tilde{X}^1\text{A}_1$. Bond lengths are listed in Å, and rotational constants are in cm^{-1} .

	Molecular Geometry					
	r	θ (degrees)	A	B	C	κ
<u>$\text{NO}_2 \tilde{X}^2\text{A}_1$</u>						
CCSD(T) cc-pVTZ ^a	1.196	134.8	8.18	0.43	0.41	-0.99
QCISD(T) ^b	1.2064	133.9				
HR-PEI ^c			7.9(2)	0.4(3)	0.4(3)	
PES ^d	1.194	133.9				
Microwave ^e	1.19389	133.857	8.001(4)	0.434(2)	0.410(2)	-0.99
<u>$\text{NO}_2^- \tilde{X}^1\text{A}_1$</u>						
CCSD(T) cc-pVTZ ^a	1.261	116.6	3.94	0.46	0.41	-0.97
QCISD(T) ^b	1.2743	115.793				
HR-PEI ^c			3.9(2)	0.5(3)	0.5(3)	
PES ^d	1.25(2)	118(2)				
Vibrational Frequencies (cm^{-1})						
	$\omega_1(a_1)$	$\omega_2(a_1)$	$\omega_3(b_2)$	χ_{11}	χ_{22}	χ_{12}
<u>$\text{NO}_2 \tilde{X}^2\text{A}_1$</u>						
CCSD(T) cc-pVTZ ^a	1325	750	1630			
QCISD(T) ^b	1314	747	1602			
HR-PEI ^c	1323(8)	753(3)		-5.4(2)	-0.48(7)	-6.5(4)
PES ^d	1316(9)	748(4)		-3(3)	-0.6(4)	-2(1)
Microwave ^e	125.3(1)	750.1(2)	1633.8(1)	-5.47(3)	-0.47(2)	-6.43(2)
<u>$\text{NO}_2^- \tilde{X}^2\text{A}_1$</u>						
CCSD(T) cc-pVTZ ^a	1350	795	1320			
QCISD(T) ^b	1303	775	1256			
HR-PEI ^c		780(20)				
PES ^d	1284(30)	776(30)				

^a calculations of this work, computed with NWChem software.

^b calculations of Liang *et al.*^[92] using a quadratic configuration interaction method.

^c values from photoelectron spectra taken in this work, Fig. 5.2 and Fig. 5.9.

^d values from photoelectron spectra of Lineberger *et al.*^[88]

^e values from microwave spectroscopy study of the neutral by Lovas *et al.*^[79]



Discovery of a new isomer

The work in the previous chapter defined an electron affinity for NO_2 of $18333(7) \text{ cm}^{-1}$, representing the minimum amount of energy required to detach an electron from ground state NO_2^- anions. This sets a cut-off wavelength of $\sim 545 \text{ nm}$, below which photodetachment will not occur. Similarly, measurements just above this threshold should only produce very slow electrons

However a series of HR-PEI NO_2^- photodetachment measurements near threshold observed additional high kinetic energy electron structure, that cannot arise from the C_{2v} ONO isomer. Furthermore, these additional fast electrons continue to be observed at long wavelengths, well below the threshold of 545 nm . These unexpected fast electrons lead to the discovery, validation, and characterisation of a new C_s NOO peroxy isomer of NO_2 , as will be discussed in this chapter.

6.1 Fast electrons in the photoelectron spectrum of NO_2^-

The last chapter focused on high resolution photoelectron spectra of NO_2^- measured at wavelengths below 500 nm , where the rotational structure and angular distribution could be investigated in detail. However, as the detachment laser is scanned to longer wavelengths ($> 500 \text{ nm}$) a surprising phenomenon was observed, where photoelectrons with very high kinetic energies were detected, even close to photodetachment threshold. This effect is visible in the velocity-mapped image of NO_2^- photodetachment, measured at 519 nm , in Fig. 6.1. As described in section 3.5, the radial position of a detached electron in a velocity-map image only depends on the kinetic energy, with slow electrons at the image centre and fast electrons at the detector edge. From the electron affinity of the target molecule, and the detachment laser wavelength, the maximum kinetic energy of the detached photoelectrons is given by

$$\begin{aligned} h\nu - \text{EA}(\text{NO}_2) &= \text{eKE}_{\max} \\ 2.389 - 2.273 &= 0.116 \text{ eV}. \end{aligned}$$

As $\text{eKE} \propto r$, this maximum kinetic energy may be converted to a radial limit on the velocity-map image, which is shown in red on the axes of Fig. 6.1. Any electron which is photodetached from NO_2^- (with an EA of $18333(7) \text{ cm}^{-1}$) must be contained inside this red radial limit of the VMI. In the velocity map image in Fig. 6.1, there are a couple of clear rings inside this region, which may be assigned to $\text{NO}_2(\tilde{X}^2A_1) \leftarrow \text{NO}_2^-(\tilde{X}^1A_1) + h\nu$ vibrational electron detachment transitions, as we saw for $< 500 \text{ nm}$ detachment in Chapter 5. However, surprisingly there is also clear structure outside of this radial limit, including a single ring mid-radial on the detector, and a set of small ripples right on the detector edge. This structure represents fast electrons with high kinetic energies, which can not originate from $\tilde{X}^1A_1\text{NO}_2^-$. The velocity-map image was inverted and analysed to construct the photoelectron spectrum, as presented in Fig. 6.2.

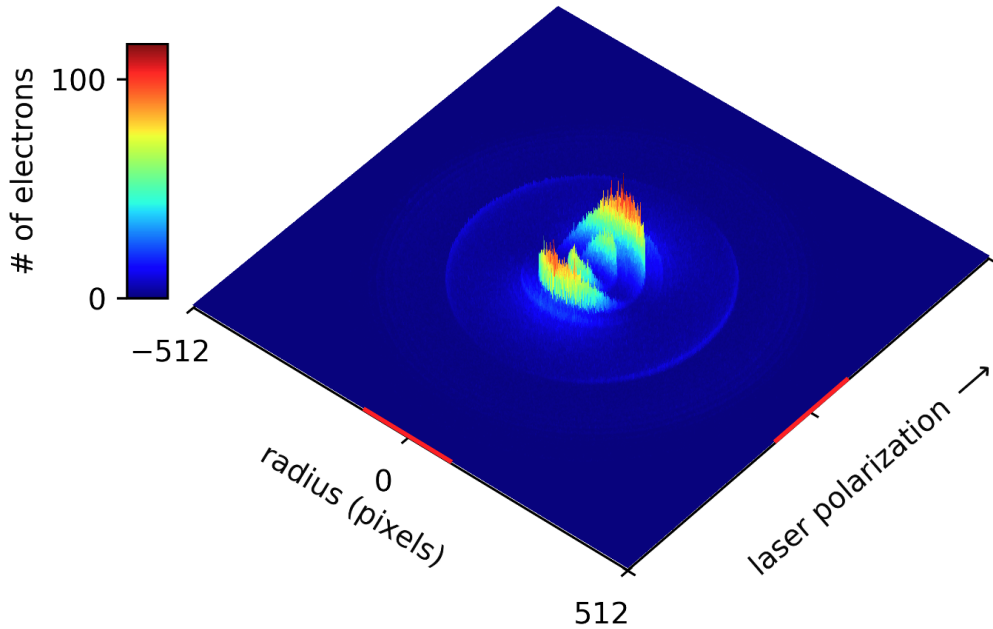


Figure 6.1: Velocity-map image of 519 nm photodetachment of NO_2^- . Photoelectrons detached from NO_2^- must be contained to the detector centre (shown in red), with fast electrons outside this region evidence of a new NNO isomer. The mid-radial ring represents O^- detachment with the outer ripples NOO^- , as discussed in the text.

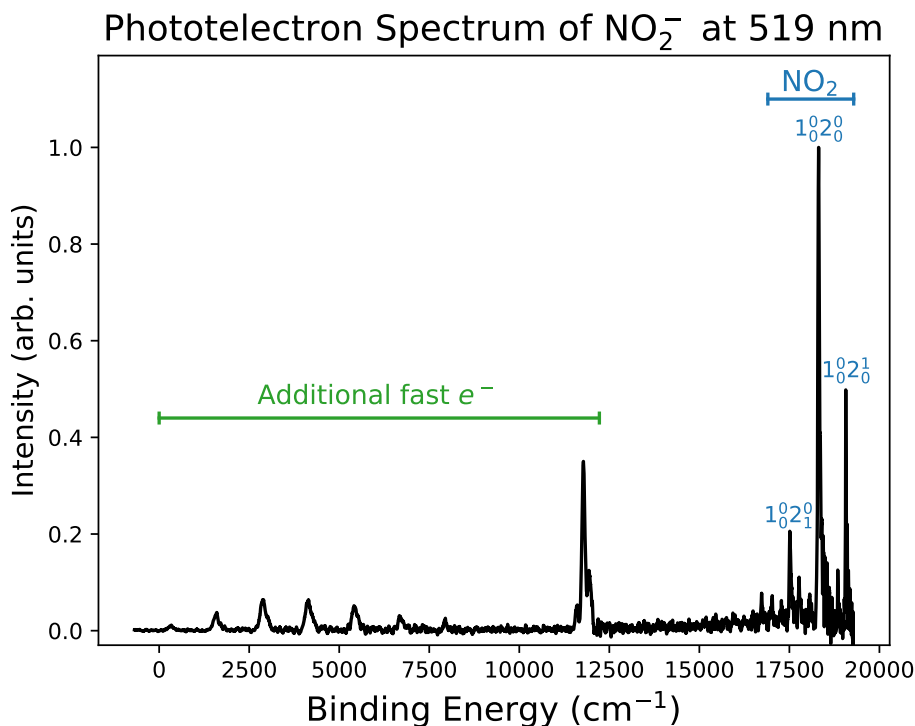


Figure 6.2: Photoelectron spectrum of NO_2^- at 519 nm. The high binding energy peaks are assigned to $\text{ONO}(\tilde{X}^2\text{A}_1) \leftarrow \text{ONO}^-(\tilde{X}^1\text{A}_1) + h\nu$ vibrational electron detachment transitions (shown in blue). At lower binding energies, additional high eKE structure (shown in green) is observed, which cannot be assigned to C_{2v} NO_2^- .

6.1.1 Assigning the high eKE structure: O^- and NO^-

The photoelectron spectrum confirms the presence of structure with high eKE. Furthermore, the observed peak at $\sim 11,000 \text{ cm}^{-1}$ is characteristic of O^- photodetachment, while the fast electron ripples at the detector edge appear similar to what might occur from NO^- photodetachment. With NO_2^- as our target, the presence of these photofragments may not seem surprising. However bond dissociation energies may be calculated using thermodynamic cycles, $\Delta H_f(\text{A}^-) = \Delta H_f(\text{A}) - \text{EA}(\text{A})$, with known thermochemical information of the neutral^[116] and electron affinities from the literature^[21]. The energy required to produce O^- photofragments is given by,

$$\begin{aligned} D_0(\text{NO} \cdots \text{O}^-) &= \Delta H_f(\text{NO}) + \Delta H_f(\text{O}^-) - \Delta H_f(\text{NO}_2^-) \\ &= \Delta H_f(\text{NO}) + \Delta H_f(\text{O}) - \text{EA}(\text{O}) - \Delta H_f(\text{NO}_2) + \text{EA}(\text{NO}_2) \\ &= D_0(\text{NO} \cdots \text{O}) + \text{EA}(\text{NO}_2) - \text{EA}(\text{O}) \\ &= 3.120 + 2.273 - 1.461 = 3.932 \text{ eV}. \end{aligned} \quad (6.1)$$

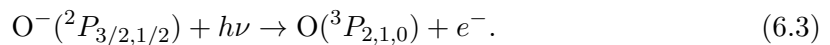
Whereas the energy required to produce NO^- photofragments is,

$$\begin{aligned} D_0(\text{O} \cdots \text{NO}^-) &= \Delta H_f(\text{O}) + \Delta H_f(\text{NO}^-) - \Delta H_f(\text{NO}_2^-) \\ &= \Delta H_f(\text{O}) + \Delta H_f(\text{NO}) - \text{EA}(\text{NO}) - \Delta H_f(\text{NO}_2) + \text{EA}(\text{NO}_2) \\ &= D_0(\text{O} \cdots \text{NO}) + \text{EA}(\text{NO}_2) - \text{EA}(\text{NO}) \\ &= 3.120 + 2.273 - 0.026 = 5.367 \text{ eV}. \end{aligned} \quad (6.2)$$

Both of these dissociation energies are much larger than the photon energy at 519 nm (2.389 eV), so at this detachment wavelength, both of these photofragment channels are energetically closed. This would appear to rule out the possible presence of O^- and NO^- . However to check this hypothesis, photoelectron measurements of mass isolated O^- and NO^- were carried out under identical conditions to the NO_2^- spectrum for comparison to the spectral elements in Fig. 6.2.

6.1.2 Anomalous photofragment O^-

The photoelectron spectrum of O^- is well known^[24,117], as will be discussed in section 7.2, with photodetachment to ground-state $\text{O} \ ^3P_2$ involving 6 fine-structure transitions,



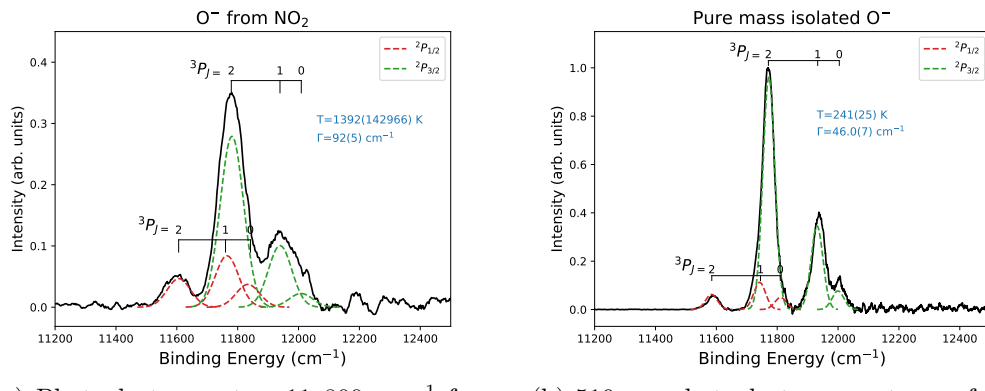
The relative intensity of each spin-orbit transition in the photoelectron spectrum depends on the degeneracy of the level, given by $g_i = (2J + 1)$, and the population of the anion level as determined by the Boltzmann factor,

$$I \propto g_i e^{-\frac{E}{k_b T}}, \quad (6.4)$$

where E is the relative energy of the anion fine-structure level, T is the temperature of the anion, and k_b is the Boltzmann constant. Gaussian functions may be fitted to the spectra to represent the 6 transitions. The ratio of intensities (area) of $^3P_2 \leftarrow ^2P_{3/2} : ^3P_2 \leftarrow ^2P_{1/2}$, taking into account the geometric fine-structure intensity ratios^[118], may then be used to determine the anion source temperature, while the FWHM of the Gaussian fit defines the spectral resolution. The ability to accurately and easily determine the source temperature

and spectrometer resolution make O^- a very useful target for spectrometer diagnostics. Consequently, oxygen is often measured alongside more complex species to quickly check the calibration, temperature, and resolution of the spectrometer operating conditions.

A photoelectron spectrum of O^- was measured under identical conditions, and at the same detachment wavelength, as the NO_2^- spectrum, with the result shown in Fig. 6.3. In both spectra the same triplet structure is observed, centred around $11,800 \text{ cm}^{-1}$. This confirms the presence of O^- in the NO_2^- spectrum (Fig. 6.2), despite Eq. (6.1) stating that the photofragmentation channel should be closed at 519 nm. For the mass isolated O^- measurement a source temperature of $T = 241(25) \text{ K}$ and resolution of $\Gamma_{2P_{3/2}} = 46.0(7) \text{ cm}^{-1}$ were established, typical of the apparatus at this wavelength^[24]. However fitting the fine-structure transitions to the photofragment O^- from Fig. 6.2 gives a FWHM of $\Gamma_{2P_{3/2}} = 91.0(5) \text{ cm}^{-1}$, twice as wide as regular O^- , and a temperature of $T = 1392(142966) \text{ K}$, which clearly represents a failing in the fitting program. Closer inspection finds that the ratio of intensities $^3P_2 \leftarrow ^2P_{3/2} : ^3P_2 \leftarrow ^2P_{1/2}$ in the oxygen spectrum are purely statistical, based solely on the degeneracy of the levels. This represents equally populated anion fine-structure levels, causing the failure in the temperature modelling. This is an unusual phenomenon, which has not been observed in this lab before, suggesting that the photofragment O^- is produced in a thermally excited state.



(a) Photoelectrons at $\sim 11,800 \text{ cm}^{-1}$ from the 519 nm NO_2^- photoelectron spectrum or Fig. 6.2

(b) 519 nm photoelectron spectrum of mass isolated O^- , recorded under identical experimental conditions.

Figure 6.3: Comparison between the photofragment O^- observed in the NO_2^- photoelectron spectrum (left) and a mass isolated O^- measurement recorded under the same experimental conditions (right). Gaussian functions are fitted to the fine-structure transitions to determine the anion source temperature and FWHM (see text).

6.1.3 Absence of NO^-

To identify the fast electron ripples observed at the detector edge in the 519 nm spectrum of NO_2^- , a photoelectron measurement of NO^- was recorded at the same wavelength, under identical operating conditions. The NO^- spectrum is presented alongside the fast electrons from NO_2 in Fig. 6.4 for comparison, to test the hypothesis that photofragment NO may be present, despite the high dissociation energy calculated in Eq. (6.2).

At first glance it appears NO may be present, as both spectra posses a similar diatomic-like vibrational progression with a very small electron affinity. However at closer inspection some important discrepancies between the two measurements may be noted. Most notable

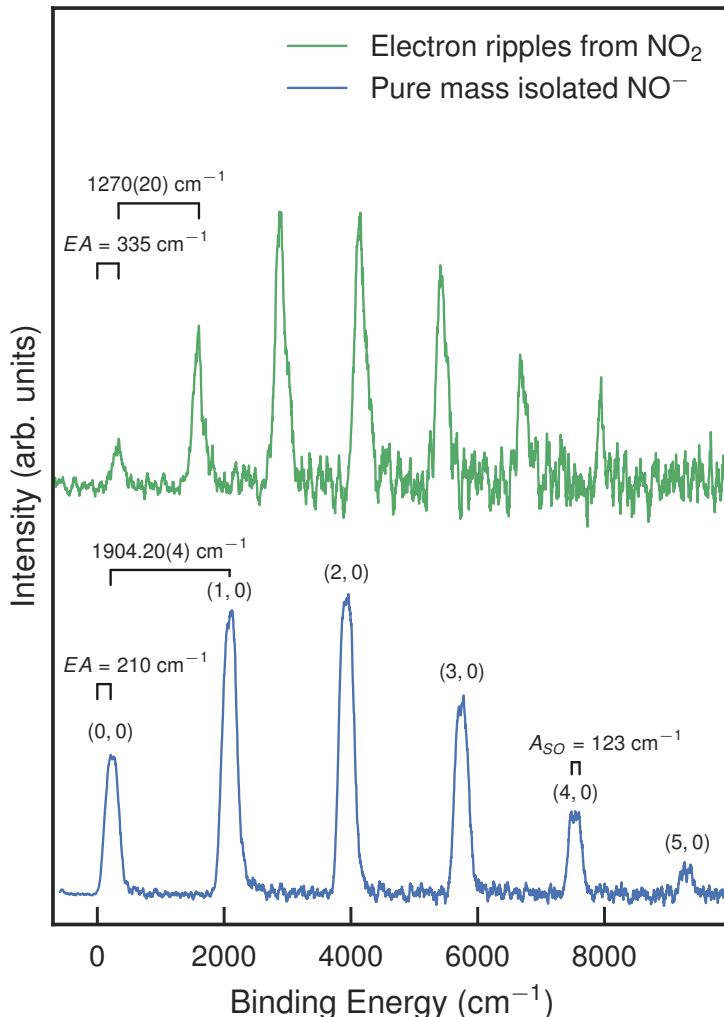


Figure 6.4: Comparison between the fast photoelectrons observed on the detector edge in the NO_2^- photoelectron spectrum (top), and a mass isolated NO^- 519 nm measurement recorded under the same experimental conditions (bottom). A 630 cm^{-1} difference in vibrational spacings and a 125 cm^{-1} shift in the electron affinity rules out the possibility of photofragment NO^- in Fig. 6.2.

is the difference in the vibrational spacing of the two spectra of $\sim 630 \text{ cm}^{-1}$. A shift in vibrational frequency of this magnitude is too large to simply arise from an external field or vibrational stark effect, suggesting that there must be a structural difference between the two molecules measured^[119]. Furthermore, while both species exhibit unusually small electron affinities, a discrepancy of $\sim 125 \text{ cm}^{-1}$ still exists between the two measurements, which is too large a shift to be caused by a calibration error. Both spectra also display different peak shapes, with the flat-topped NO vibrational features a consequence of the $\sim 123 \text{ cm}^{-1}$ ^[120] spin-orbit splitting of the doublet $\tilde{X}^2\Pi$ NO ground state, while the electron ripples from NO_2^- form much sharper singlet-like transitions.

From the above spectral analysis, it is clear that the fast electron ripples measured on the detector edge are not a signature of NO^- . However, the question of where these fast electrons are coming from remains. The time-of-flight mass spectrometer ensures that any ion in the interaction region when the laser fires must have a mass of 46 atomic mass

units, while the NO_2^- in the experiment is produced in an adiabatic expansion of pure nitrous oxide (N_2O) gas through a pulsed jet discharge. Therefore, it would seem that these electron ripples must be a signature of another isomer of NO_2 .

6.2 Peroxy NOO

Despite being first proposed in 1961 by Clyne and Thrush^[4], there is still debate over the existence of NOO as a bound isomer^[90,91,100]. The only experimental evidence for the existence of NOO comes from two NO_2^- photoelectron cross section studies published in 1974, where an observed long photoelectron tail is attributed to the presence of a peroxy isomer^[5,6]. However, experimental limitations in the apparatus did not allow for confirmation or characterisation of this assignment, as will be discussed in more detail in section 6.2.2. Furthermore, the presence of the tail is sensitive to anion production methods, with multiple future measurements all unable to observe any spectral signatures of NOO ^[85,86,88,89,121]. However, the observation of high kinetic energy electron structure in the velocity map image in Fig. 6.1 may be able to finally confirm the existence of NOO .

6.2.1 Assignment of NOO structure

To confirm the presence of peroxy NOO in the spectrum in Fig. 6.2, *ab-initio* structure and frequency calculations were run using NWChem software^[94] at the CCSD(T) level of theory with a cc-pVTZ basis set. The detailed results from these calculations are presented in section 4.3, with geometric, rotational, and vibrational constants listed at the end of this chapter in Table 6.1.

A key result to come from this *ab-initio* study is the prediction of values for the normal mode frequencies, specifically the N–O stretch $\omega_1 \sim 1390 \text{ cm}^{-1}$ and the O–O stretch mode $\omega_2 \sim 640 \text{ cm}^{-1}$, which happen to be in agreement with the observed structure from the NO_2 electron ripples. This gives further evidence that these electrons are a signature from a new NOO peroxy isomer, with the vibrational spacing of the main progression in the NOO spectrum, shown in Fig. 6.4, of $\omega_1 = 1270(20) \text{ cm}^{-1}$ able to be readily assigned to the N–O stretch mode from the *ab-initio* calculations.

The diatomic-like spectrum of Fig. 6.4, with one clearly dominant vibrational progression, is unusual for polyatomics. However it has been shown that this is a typical characterisation for polyatomic molecules containing a weak central bond, with a similar phenomenon observed in a recent microwave spectroscopy measurement of HOON^[122]. This suggests that it is the long O–O bond in peroxy NOO that is responsible for the suppression of modes ω_2 and ω_3 . Close inspection of the peroxy spectrum (see Fig. 6.5) does reveal some evidence of these other modes, with the asymmetric peak shape revealing additional structure at the high binding energy side of each main peak. This may be assigned to the $1_0^n 2_0^2$ combination band, with an O–O stretch frequency of $\omega_2 = 720(10) \text{ cm}^{-1}$, which is also in agreement with the calculated value. The $1_0^n 2_0^1$ progression, appearing between the dominant peaks, is more suppressed. Another possible reason for this is the presence of the $\text{NOO} \rightarrow \text{NO} + \text{O}$ dissociation pathway, which lies along the ω_2 O–O stretching coordinate. Importantly, all of the spectral structure in the peroxy spectrum may be assigned to the calculated vibrational modes, as shown in Fig. 6.5, with agreement between the measured and calculated vibrational frequencies, confirming the presence of the NOO isomer in the original velocity-map image, Fig. 6.1.

The electron affinity of NOO is established from Fig. 6.5, in relation to the NO species.

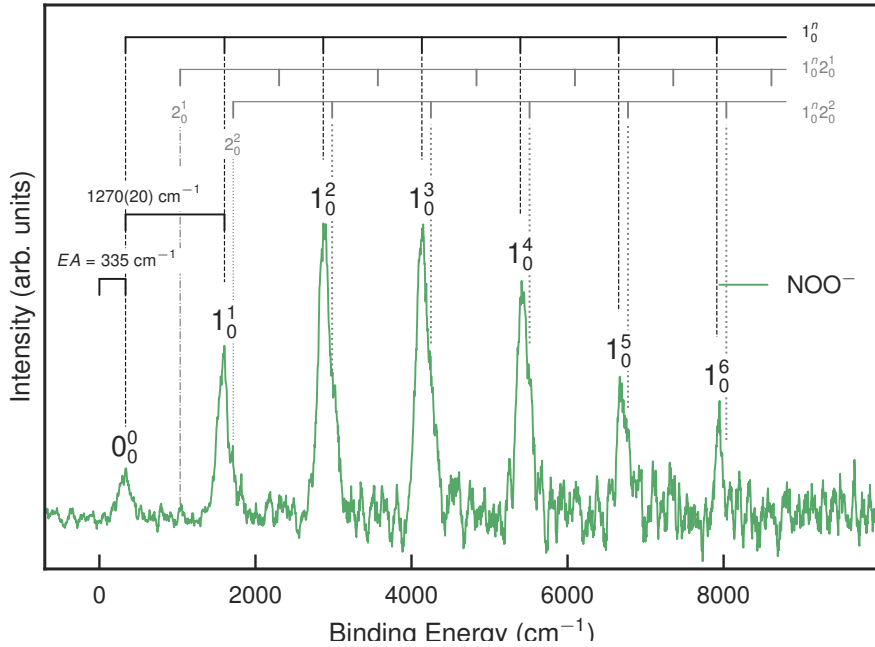


Figure 6.5: NOO peroxy photoelectron spectrum at 519 nm. All of the spectral structure may be assigned to vibrational progressions $1_0^n 2_0^0$, $1_0^n 2_0^1$, and $1_0^n 2_0^2$, with vibrational frequencies in agreement with values in table 6.1.

Comparison to NO is required to account for the rotational band head shift - the effect where the origin of the rotational band, required for an accurate determination of the electron affinity, typically does not occur at the maximum intensity of the vibrational peak. One way to approximate the rotational band head shift is to apply Engelking's approximation^[101], which predicts the shift based on the rotational symmetry of the target molecules. For a prolate symmetric top, such as NOO, the band shift is calculated by Eq. (6.5) and for a linear molecule, such as NO, the band shift is calculated by Eq. (6.6),

$$\langle E' - E'' \rangle \approx k_b T \left[B'/B'' + A'/2A'' - \frac{3}{2} \right] + (B'' - B')/3, \quad (6.5)$$

$$\langle E' - E'' \rangle \approx k_b T [B'/B'' - 1] + (B'' - B')/3, \quad (6.6)$$

where k_b is the Boltzmann constant (in $\text{cm}^{-1}\text{K}^{-1}$), and A and B are the rotational constants of the target molecule. Using the rotational constants for NOO in Table 6.1 and for NO from section 7.1 gives a similar band shift for both species of $\langle E' - E'' \rangle \approx 25 \text{ cm}^{-1}$. However comparison between Engelking's approximation on systems where the exact rotational band shift is known, such as in O_2 , reveals that it may overestimate the magnitude of the shift. In order to extract a more accurate value for the band shift, and corresponding electron affinity, a full rotational model of NO was constructed to determine the exact band shift in NO^- photodetachment. This model and corresponding results are examined in detail in section 7.1. Importantly for the work here, the rotational model found an exact band shift of only 11 cm^{-1} for NO. As Engelking's approximation suggests a similar band shift for both NO and NOO that same 11 cm^{-1} shift was applied to Fig. 6.5. This gave a peroxy electron affinity of $\text{EA}(\text{NOO}) = 335(30) \text{ cm}^{-1}$ [$0.042(4)\text{eV}$].

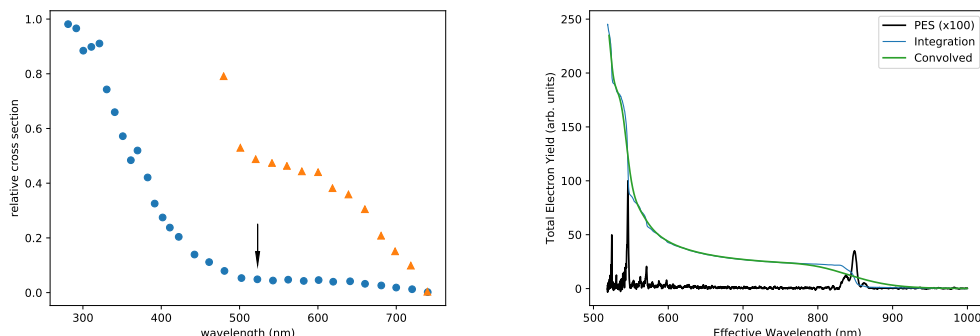
This value is substantially smaller than previous *ab-initio* estimates for the EA, which ranged between $1.8\text{--}2.2 \text{ eV}$ ^[90]. However, as was noted in that study, accurate electronic

affinity calculations are notoriously difficult, with uncertainties arising due to the importance of electron correlation. Various calculations were run in this work using NWChem^[94] and Q-Chem^[114] software packages, with the results suggesting an EA < 0.5 eV, however the calculations did not converge to a consistent value. Previous experimental estimates for the electron affinity were also overestimated, suggesting an EA \sim 1.6 – 1.8 eV^[5,6], however this discrepancy will be explained below.

6.2.2 Long photoelectron tails

The first experimental evidence for a possible peroxy NOO isomer came from two photoelectron cross section experiments published in 1974 by the Brauman and Lineberger groups^[5,6]. In these experiments the total photoelectron yield was measured using a hemispherical analyser, as a function of NO_2^- detachment wavelength, to measure the energy dependent total cross section. At this point in time, the electron affinity of NO_2^- was defined as 2.36(1) eV, corresponding to a threshold wavelength of $\lambda \sim 525$ nm, below which photodetachment is closed.

The experimental data in both of these studies observed a long wavelength photoelectron tail (see Fig. 6.6), persisting at wavelengths substantially longer than 525 nm, with the electron signal finally stopping at ~ 750 nm. As the electrons in the long-tail could not arise from the standard C_{2v} isomer of NO_2^- , they were attributed to the possible existence of a peroxy isomer, which was assigned an electron affinity of 1.6–1.8 eV based on the length of the photoelectron tail^[6]. This value has been used as reference point for the following theoretical studies of Meredith^[90] and Walch^[91].



(a) Photoelectron yield measurement of NO_2^- by the Brauman group, reproduced from Ref^[6]. Experiment shows a long photoelectron tail that persists below the EA of NO_2^- . A similar curve was also measured by the Lineberger group^[5].

(b) Integrated NO_2^- photoelectron spectrum (Fig. 6.2) for comparison with the electron yield experiment (a). The PES is shown in black, with the integrated curve in blue, and the convoluted curve shown in green.

Figure 6.6: Integration of the photoelectron spectrum of Fig. 6.2 demonstrates that the long photoelectron tail measured by the Brauman^[6] and Lineberger^[5] groups was in fact a signature of O^- , not the peroxy NOO^- isomer.

These values seem to contradict the value measured in this work, however this may be explained by examining the difference in the experimental apparatus, notably the different detection systems. Hemispherical analysers have a small entry angle and count the number of electrons at a given pass energy. By scanning the analyser voltage, the number of

electrons may be counted at a variety of pass energies. This differs substantially to velocity-map imaging where along with a full 4π steradians collection angle, a wide range of energies are measured at the same time. It is this feature which provided 3 distinct energy regimes of electron signals (ONO^- , O^- , NOO^-), which were indistinguishable in the original studies. From Fig. 6.2 we know that photofragment O^- , an ion which has an electron affinity of 1.4611 eV^[123], is present in the photoelectron spectrum of NO_2^- . The EA of O^- is very similar to where the observed photoelectron tail in Fig. 6.6 ends, suggesting that the electrons measured in these previous studies (and assigned to the peroxy isomer) were actually a measurement of the photofragment O^- . The substantial (> 2 eV) difference in kinetic energy of electrons detached from ONO^- and NOO^- , as well as the relatively small intensity of the NOO^- signal, would explain why these fastest electrons were not detected in the original studies.

Integration of the HR-PEI photoelectron spectrum, convoluted to simulate the lower resolution of the total yield measurements as shown in Fig. 6.6, has a very similar shape to the total electron yield results. This is not an exact simulation of the original experiments, as the electrons were measured at a single wavelength, neglecting the wavelength dependence of the cross section. However this should be a secondary effect as long as the fixed wavelength measurement is away from threshold, with the curve expected to be slowly varying.

From Fig. 6.6 it is clear that the integrated photoelectron spectrum of this work does match the shape of the cross section experiments published in 1974. Importantly, from both graphs a drop in the photoelectron tail at 700–800 nm is observed, however we can now see that this occurs as the laser passes below the EA of the O^- photofragment. This explains the apparent discrepancies in the estimated electron affinity, with the previous estimates unaware of the presence of O^- in the detachment spectrum.

6.2.3 Answer to the O^- conundrum

It is unsurprising that photofragment O^- may have been mistaken for NOO^- , given that Eq. (6.1) demonstrates that NO_2^- fragmentation should not occur at wavelengths longer than ~ 315 nm. Yet, Fig. 6.2 clearly shows that O^- is present in the photoelectron spectrum of NO_2^- at 519 nm. However, now that the presence of a peroxy NOO isomer has been established, this may also help explain the surprising presence of O^- in Fig. 6.2. Calculating the dissociation energy for the NOO^- isomer using NWChem software^[94] at the CCSD(T) level gives a value of $D_0(\text{NO}\cdots\text{O}^-)\sim 0.13$ eV, much smaller than the corresponding value for the C_{2v} isomer of $D_0(\text{ON}\cdots\text{O}^-)=3.932$ eV. Importantly, at a detachment wavelength of 519 nm (2.39 eV), the photofragment channel of NOO^- will be open. Hence, the presence of O^- in the photoelectron spectrum of Fig. 6.2 provides further evidence for the existence and successful detection of this new peroxy NOO isomer.

The source of photofragment O^- also helps explain the anomalous distribution of the anion fine structure levels measured in Fig. 6.3. Unlike standard O^- photodetachment, where the anion temperature may be extracted from the Boltzmann factor for the relative intensities of the $^3P_2 \leftarrow ^2P_{3/2} : ^3P_2 \leftarrow ^2P_{1/2}$ transitions, the photofragment O^- was found to have a purely statistical distribution of the anion levels, non-thermal in nature.

This anomalous behaviour may now be explained using a simple energy balance,

$$\begin{aligned} E_{\text{excess}} &= h\nu - D_0(\text{NO}\cdots\text{O}^-) \\ &= 2.39 - 0.13 \\ &= 2.26 \text{ eV}. \end{aligned}$$

Due to the weak peroxy $\text{NO}\cdots\text{O}^-$ bond, ~ 2.26 eV of excess energy is available from the photofragment process which may be distributed into the internal and translational motion of the fragments, accounting for the non-thermal distribution of the anion fine structure levels. This also explains the anomalous broadening observed in Fig. 6.3 ($\Gamma = 91 \text{ cm}^{-1}$, cf. $\Gamma = 46 \text{ cm}^{-1}$), which may be attributed to the additional translation energy of the fragment. A similar effect has been observed by Han and Johnson^[124], where photodissociation of O_2^- anion clusters resulted in highly vibrationally excited O_2^- ions.

To confirm that all of the measured photoelectrons in Fig. 6.1 have been correctly assigned, with no other photodestruction channels open, the spectrometer may be run in a ‘time-of-flight detection mode’, rather than the standard VMI mode. Photodetachment of mass isolated NO_2^- occurs as before, however instead of fast-switching the MCP’s to only detect the photoelectron signal, they are set at a constant voltage to detect all of the photoproducts from the experiment. Rather than measuring the energetics of electrons with the VMI lens, the temporal signal of the products are measured using a fast oscilloscope. This converts the imaging section of the spectrometer into a second time-of-flight stage, where all of the photodestruction products are separable by mass and charge, as shown in Fig. 6.7.

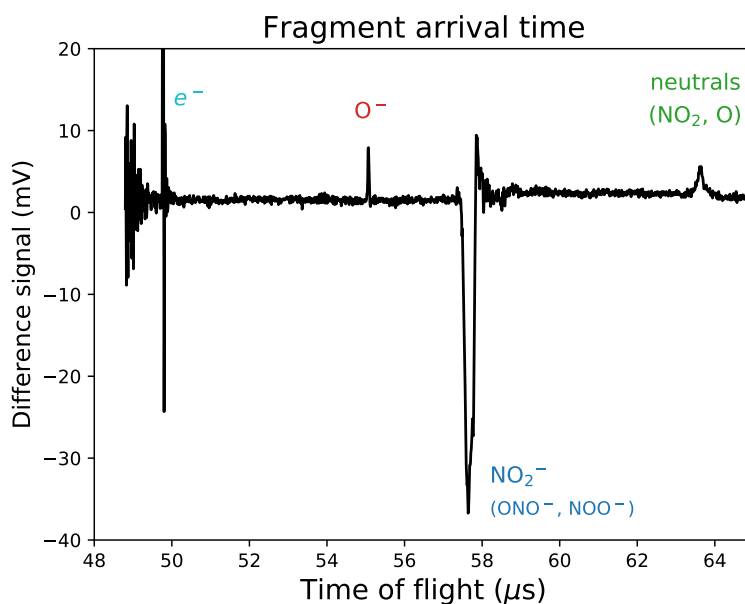


Figure 6.7: Second time-of-flight MCP voltage signal for 519 nm NO_2^- photodetachment, minus the baseline signal with the laser turned off. Four temporal signals are observed, the photoelectron signal, O^- ions, NO_2^- ions, and the corresponding neutral molecules.

To assign the observed temporal signals, a timing program was written in python to calculate the expected time-of-flight for fragments based on their mass and charge, accounting for the dimensions of the spectrometer, and the voltages of the lenses. From

this, 4 temporal signals were detected and assigned:

- (i) photoelectrons, from ONO^- , NOO^- , and O^-
- (ii) a residual O^- ion signal
- (iii) a residual NO_2^- ion signal
- (iv) the corresponding neutrals (NO_2, O)

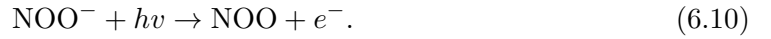
This measurement provides a couple of key results. First, the residual O^- ion signal is present only when the laser is turned on, confirming that NOO^- is in fact a bound species, with two photons required to form the mid-radial O^- ring in Fig. 6.1



Second, there are no additional un-assigned signals present, confirming there are no other photofragment/photochemical channels open that have not been accounted for,



Therefore, we can confidently say that the fast electron ripples observed on the detector edge must be a direct measurement of the peroxy NOO isomer itself,



6.2.4 Isomeric ratio

Given the potential atmospheric implications of this new isomer, estimating it's abundance will be important. The ratio of NOO^- : ONO^- produced in the experiment may be estimated using the Beer-Lambert law for absorption, while assuming that the total cross section of peroxy NOO (fragmentation plus detachment) is a similar order of magnitude to C_{2v} NO_2^- photodetachment above threshold.

During the experiment, 20 mJ laser pulses photodetached an average of 10 electrons per laser shot, with 12.5% from NOO^- , 25% from O^- , and 62.5% from ONO^- . This corresponds to $1.25 \times \text{NOO}(e^-) + 2.5 \times \text{O}(e^-) + 6.25 \times \text{ONO}(e^-)$ for every $\sim 5.2 \times 10^{16}$ photons. The Beer-Lambert law states the absorption of photons will depend on the number density of the ion and the cross section, as given by Eq. (6.11)

$$\ln \left(\frac{I_{\text{out}}}{I_{\text{in}}} \right) = -n\sigma, \quad (6.11)$$

where $I_{\text{out/in}}$ is the intensity of photons out/in to the interaction region, n is the ion number density, and σ is the total photodetachment cross section. First we will look at the dominant ONO^- electron signal, where using the known cross section for NO_2^- at 519 nm of $\sigma_{\text{ONO}} = 1 \times 10^{-19} \text{ cm}^2$ ^[5,88], and the values from above noting that $I_{\text{out}} = I_{\text{in}} - e^-$, gives a number density of

$$n_{\text{ONO}} = 1202 \text{ cm}^{-2}.$$

Next we may do a similar calculation to determine the number of O^- photofragments produced. Using the known cross section at $\lambda = 519 \text{ nm}$ of $\sigma_{\text{O}} = 6.5 \times 10^{-18} \text{ cm}^2$ ^[125], gives a number density of

$$n_{\text{O}} = 7.4 \text{ cm}^{-2}.$$

Finally we may look at the NOO signal, however here we need to account for two channels: fragmentation + detachment. In this case, $I_{\text{out}} = I_{\text{in}} - n_{\text{O}} - e^-$, and $\sigma_T = \sigma_p + \sigma_f$. If we assume that the total cross section of NOO is similar to other molecules above threshold, $\sigma_T \sim 7 \times 10^{-18} \text{ cm}^2$ ^[5,125] we can estimate a number density for the peroxy isomer of,

$$n_{\text{NOO}} \sim 23.8 \text{ cm}^{-2}.$$

Taking the ratio of number densities for the two NO_2 isomers then gives,

$$\frac{n_{\text{NOO}}}{n_{\text{ONO}}} \approx 2\%. \quad (6.12)$$

This confirms that the majority of ions produced in the gas discharge are the standard C_{2v} isomer, however a non-negligible number of the C_s peroxy isomer are also produced. A large calculated barrier to isomerization ($\sim 1.3 \text{ ev}$ ^[110]) makes interconversion unlikely.

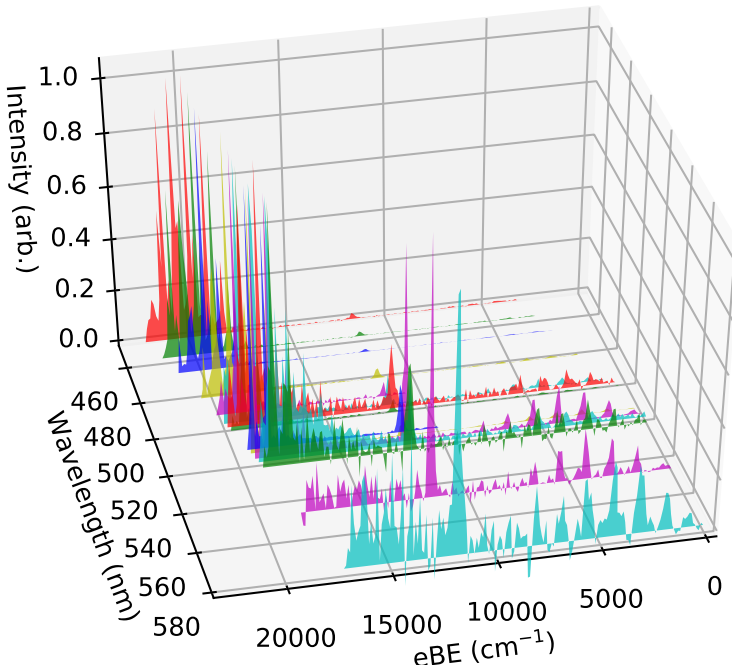


Figure 6.8: Photoelectron spectra of NO_2^- taken at a range (450–580 nm) of detachment wavelengths, normalised to the NO_2^- structure. Peroxy NOO structure is evident, but only significant in measurements above $\sim 500 \text{ nm}$.

Figure 6.8 shows a series of NO_2^- PES measurements at a range (450 – 580 nm) of detachment wavelengths, revealing the peroxy structure. At shorter wavelengths the C_{2v} isomer dominates the spectrum, making NOO hard to distinguish. Conversely, at wavelengths above the EA of C_{2v} ONO, good ion beam alignment becomes difficult to achieve due to the significantly lower total photoelectron count. At 519 nm the observed electron signal from C_{2v} ONO^- is suppressed by the Wigner threshold law, enhancing the

apparent signal from NOO⁻, yet still strong enough to help achieve good beam overlap, resulting in a high electron count and clean spectrum. This is why Fig. 6.1 has been the focus of the peroxy analysis.

A few longer wavelength measurements were also made to test whether NOO⁻ could still be measured well above the EA of ONO, providing further evidence for this new isomer. The velocity map images in Fig. 6.9 show that an electron signal could still be detected up to a wavelength of 650 nm, however at this stage signal to noise issues meant that while the velocity-mapped image still showed the presence of photofragment O⁻, the signal was too low to extract a useful photoelectron signal.

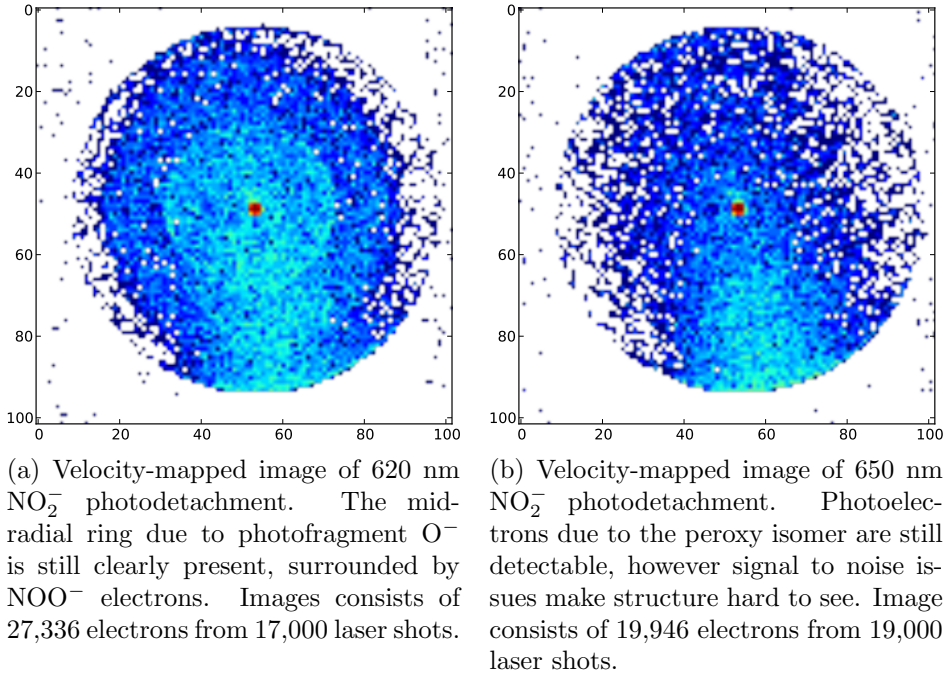


Figure 6.9: Long wavelength velocity-map images of NO₂⁻ photodetachment. Presence of the peroxy isomer means electrons are still detected a long way below the EA of C_{2v} ONO.

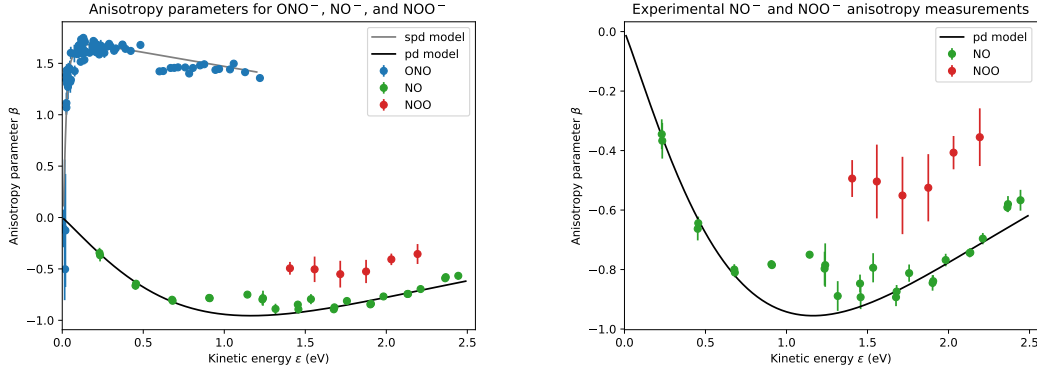
6.3 NOO⁻ Photoelectron Angular Distribution

At first glance, the velocity-map image Fig. 6.1 shows an angular distribution for the (NOO⁻) electrons on the detector edge that looks fairly isotropic, while the mid-radial (O⁻) electrons have a clear negative anisotropy parameter, opposite in sign to the central (ONO⁻) electrons.

In section 6.1 we saw that the photoelectron spectrum of NOO⁻ was very similar to that of NO⁻, suggesting that NOO⁻ may be more similar to NO⁻ than it is to its isomer ONO⁻. Therefore, comparing the photoelectron angular distributions (PADs) of these three species may provide a useful insight into the behaviour of this new peroxy isomer. The PAD of ONO⁻ was discussed in detail in section 5.3, while the PAD of NO⁻ will be discussed in section 7.1, with their resulting anisotropy curves plotted in Fig. 6.10.

Experimental anisotropy parameters for NOO⁻ were also obtained, by fitting Eq. (5.7) to radially integrated transition intensities from Fig. 6.1. For a single image quadrant, the intensity variation is linear in $P_2 \cos \theta$, with slope equal to $\beta \times$ intercept. The resulting

anisotropy parameters are plotted in Fig. 6.10 alongside β parameters from ONO^- and NO^- .



(a) Anisotropy parameters for ONO^- (blue), NO^- (green), and NOO^- (red) photodetachment. The ONO^- data may be represented by a *spd* model, while NO^- is modelled by a pure *d* curve.

(b) Comparison of NO^- (green) and NOO^- (red) anisotropy parameters. Both species have a negative β , however NOO^- is notably more isotropic than NO^- .

Figure 6.10: Experimental anisotropy parameters measured for ONO^- , NO^- , and NOO^- . ONO^- has a positive β , opposite in sign to the other two species. While NOO^- appears to be similar to NO^- , it is significantly more isotropic.

From Fig. 6.10 it can be seen that the NOO^- anisotropy is similar to NO^- , both negative, opposite in sign to that for ONO^- . This result is not entirely surprising, given the similarities in the PES and EA of NOO^- and NO^- (see Fig. 6.4). It is important to note however there are still differences between the anisotropy parameter curves of NOO^- and NO^- , with the peroxy curve notably more isotropic.

This observation becomes significant when compared to recent work of the Sanov group^[8,37,126], where solvated molecules were studied to probe the effect of solvation on photoelectron angular distributions. Interestingly, it was found that photodetachment from solvated NO^- molecules typically resulted in more isotropic distributions^[8], similar to what is seen between NOO and NO in Fig. 6.10. While it was shown that the strength of this effect was dependent on the nature of the solvent molecule, and the corresponding anionic resonances, even for solvents where no resonances were present (H_2O) a loss in anisotropy was still observed. This observation, combined with the weak O–O peroxy bond, suggests that the NOO isomer may behave similar to a solvated nitrous oxide molecule.

Ab-initio Hartree-Fock calculations were computed using NWChem software^[94] to predict the shape of the peroxy NOO^- HOMO, with the result shown in Fig. 6.11, alongside orbital calculations for the HOMO of ONO^- . The stark difference in the orbital structure of the two isomers helps to explain the opposite sign in the anisotropy of their distributions. Dividing the HOMO of C_s peroxy NOO into two parts, it may be noted that the orbital structure around the NO moiety appears similar to the standard diatomic π^* antibonding orbital of NO^- that would be expected if the terminal O were not present. Likewise, the orbital section around the terminal oxygen appears similar to a standard *p* orbital. This is consistent with the picture of NOO behaving similarly to a NO molecule solvated with an oxygen atom, explaining the positive shift in β relative to NO^- . This minor character mixing also explains why the peroxy normal vibrational modes ω_1 (N–O

stretch) and ω_2 (O – O stretch) remain largely uncoupled, with the dominant N – O mode similar to a damped version of the bond vibration in nitrous oxide.

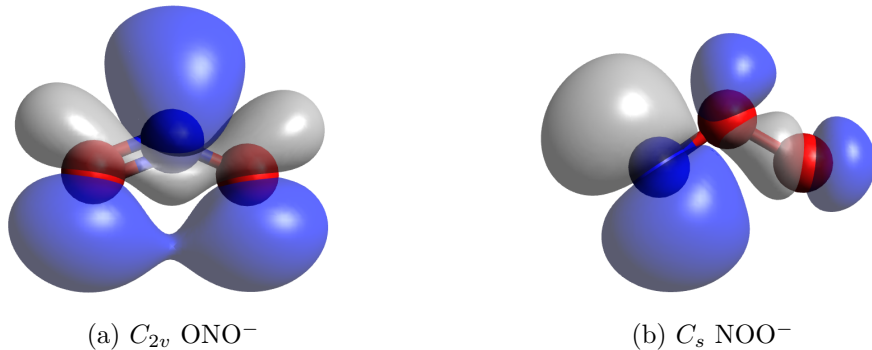


Figure 6.11: Orbital diagrams of the highest occupied molecular orbital in C_{2v} ONO⁻ and C_s NOO⁻, calculated using NWChem software. The ONO⁻ orbital has a symmetry plane through the center of the N atom, whereas the NOO⁻ orbital appears similar to a combination of a π^* antibonding NO and an atomic p orbital.

The work in this chapter highlights how unexpected outcomes may sometimes provide the most exciting results. By carefully analysing all of the possible sources of the additional electrons in the photoelectron spectrum of NO₂⁻, the existence of a new peroxy NOO isomer has been confirmed. From this study, spectral characteristics of this isomer have also been investigated to determine an electron affinity of 335(30) cm⁻¹, much lower than the previous theoretical and experimental estimates, due to the presence of photofragment O⁻. The similarities between NO and NOO have also been examined through both the energetic and angular distribution of photoelectrons, showing that structurally NOO behaves more like NO than it does ONO. With the existence of this isomer now confirmed, future work will be able to investigate the abundance of this molecule in nature, along with any possible atmospheric/photochemical consequences this may have.

Table 6.1: Calculated and experimental values for the geometric and vibrational properties of $\text{NOO}(\tilde{X}^2\text{A}')$ and $\text{NOO}^-(\tilde{X}^1\text{A}')$. Bond lengths are listed in Å, and rotational constants are in cm^{-1} .

	Molecular Geometry					
	$r_{\text{N}-\text{O}}$	$r_{\text{O}-\text{O}}$	θ (degrees)	A	B	C
<u>$\text{NOO} \tilde{X}^2\text{A}'$</u>						
CCSD(T) cc-pVTZ ^a	1.198	1.376	120.8	4.08	0.45	0.40
CASSCF ^b	1.255	1.365	118.6			
<u>$\text{NOO}^- \tilde{X}^1\text{A}'$</u>						
CCSD(T) cc-pVTZ ^a	1.201	1.520	119.6	3.64	0.40	0.36
CCSD ^c	1.217	1.503	119.9			
Vibrational Frequencies (cm^{-1})						
	$\omega_1(a')$	$\omega_2(a')$	$\omega_3(a')$	χ_{11}	χ_{22}	χ_{12}
<u>$\text{NOO} \tilde{X}^2\text{A}'$</u>						
CCSD(T) cc-pVTZ ^a	1390	640	370			
CASSCF ^b	1116	761	356			
HR-PEI ^d	1270(20)	720(10)				
<u>$\text{NOO}^- \tilde{X}^2\text{A}'$</u>						
CCSD(T) aug-cc-pVTZ	1543	696	464			
CCSD ^c	1605	765	640			
HR-PEI ^d						

^a calculations of this work, computed with NWChem software.

^b MC-SCF calculations of Meredith *et al.*^[90].

^c CCSD calculations of Meredith *et al.*^[90] (CASSCF method diverged for NOO^-).

^d values from NOO photoelectron spectrum taken in this work, Fig. 6.5.

High resolution studies of calibration species

While part II of this thesis so far has focussed on nitrogen dioxide, other similar molecules are also investigated for calibration purposes, and as high resolution studies. This section focuses on NO^- , O^- , and O_2^- , all of which are important elements in the Earth's atmosphere. They provide useful calibration of the spectrometer, and are often measured in parallel with the larger molecule experiments. The high resolution of the HR-PEI spectrometer resolves new detail, particularly in relation to negative ions that are not as well studied in the literature, providing more information about the structure and photophysical properties of these important species.

7.1 Benchmark measurements of NO^-

Nitric oxide (NO) is a highly reactive free radical, and the smallest of the nitrogen oxides (NO_x) family. Like other nitrogen oxides (such as NO_2), nitric oxide is a prominent air pollutant, produced primarily from internal combustion engine emissions and thermal power stations, and contributes to the formation of smog, acid rain, and tropospheric ozone^[73]. NO readily reacts with molecular oxygen to form the brown toxic gas NO_2 ,



a damaging pollutant, that has been discussed in chapters 5 and 6. A similar reaction also occurs with ozone in the stratosphere,



that may play a role in depletion of the ozone layer. NO will also react with any volatile organic compounds to form photochemical smog. As such, the role of neutral NO in the atmosphere has been the centre of numerous studies^[100,127–133]. In the upper atmosphere where a lot of these processes takes place, the role of negative ions becomes important due to the availability of UV photons to partake in photoionisation and photofragmentation reactions. However despite this, the literature on the NO^- anion spectroscopy is still much less complete.

The first photoelectron spectroscopy study of the NO^- ion was reported in 1972 by Siegel *et al.*^[134], with ions produced using a glowing discharge source of N_2O , and subsequently photodetached with an argon ion laser. A hemispherical analyser recorded the electron kinetic energies, to construct the photoelectron spectrum. From the position of the origin transition, accounting for rotational and spin-orbit effects, the small electron affinity for NO of $0.024^{+0.01}_{-0.005}$ eV was established.

In gaseous media, it is often energetically preferable for negative ions to form clusters, surrounded by a solvent neutral molecule. These cluster ions are known to be important to

the photochemistry of the upper atmosphere. Clustering of ions is also observed in solution, with ion-induced nucleation involved in various biological processes^[135]. As a result, the study of cluster anions has received considerable attention from many research groups^[126]. These studies also provide a molecular level view of the anion-cluster interactions, while examining the effect of solvation on the energy structure of the charged solute. Due to its importance in atmospheric and biological systems as an ionic cluster, $\text{NO}^-(\text{Y})_n$ (where Y is the nature of the neutral solvent and n represents the size of the cluster), has been the focus of many studies in the literature. In 1987 Coe *et al.*^[135] reported on photoelectron spectra of $\text{NO}^-(\text{N}_2\text{O})_{n=1,2}$, which found that the cluster spectra strongly resembled that of free NO^- , except shifted slightly to higher binding energies. The electron affinity of the cluster was also found to increase with cluster size. In 1988, resonance stabilised $\text{NO}^-\cdot\text{NO}$ clusters were observed in the photoelectron spectroscopy study of N_2O_2^- of Posey and Johnson^[136]. This dimer likely represents a second minimum of the potential surface along the $\text{O}^- + \text{N}_2\text{O} \rightarrow \text{NO}^- + \text{NO}$ reaction coordinate. In order to examine the effect the choice of solvent has on the ion-cluster interactions, a 2002 study by Hendricks *et al.*^[137] investigated $\text{NO}^-(\text{Y})_n$ clusters of Y = Ar, XE, N₂O, H₂S, NH₃, H₂O, and C₂H₄(OH)₂. This confirmed that the nature of the solvent can strongly influence the solvation interactions of the ion cluster, with examination of the solvation stabilisation energy as a function of n able to predict the geometry of the cluster.

In 2007 Velarde *et al.*^[37] reinvestigated detachment of $\text{NO}^-(\text{N}_2\text{O})_n$ clusters using photoelectron imaging, allowing for the effect of solvation on the angular anisotropy to be examined. This study found that the presence of N₂O solvent molecules drastically reduced the anisotropy of the ion-cluster photoelectron distribution. However, in similar experiments for $\text{NO}^-(\text{H}_2\text{O})_n$ the effect of solvation on the anisotropy was significantly lower. This suggested that the reduction in anisotropy of $\text{NO}^-(\text{N}_2\text{O})_n$ photodetachment was caused by electron scattering by the solvent from anionic resonances. A following study by Grumblung *et al.*^[8] confirmed that the loss of anisotropy in $\text{NO}^-(\text{N}_2\text{O})_n$ clusters is primarily due to resonant interactions with the N₂O solvent, as opposed to solvent-induced perturbations. The nature of the neutral solvent has also been shown to influence the dissociation dynamics of $\text{NO}^-(\text{Y})_n$ ion clusters in photofragmentation coincidence experiments^[138].

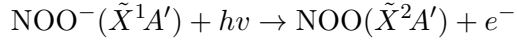
For the effect of solvation to be accurately investigated, the photoelectron spectrum of free NO^- ions needs to be well understood. In 1989 Travers *et al.*^[9] measured the photoelectron spectrum of NO^- to obtain a more accurate determination of the electron affinity. This confirmed that the NO^- anion is only stable with respect to auto-detachment in its ground vibrational level, with a very small electron affinity of 0.0026(5) eV. Subsequent *ab-initio* calculations^[139] and electron scattering experiments^[140,141] support this small value for the EA.

The photoelectron spectrum of NO^- is reinvestigated here, using the HR-PEI spectrometer. High resolution measurements provide new spectral detail, allowing for better comparison to the solvation studies, while defining precise spectroscopic constants useful in atmospheric modelling.

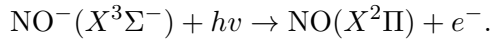
7.1.1 Spin orbit splitting in $X^2\Pi$ NO

In chapter 6 a photoelectron spectrum of NO^- was measured at 519 nm, to compare with the high kinetic energy electron structure observed in the spectrum of NO_2^- . This measurement (Fig. 6.4) was able to rule out the possibility of NO^- fragmentation, which

was a key step in verifying the discovery of the peroxy NOO isomer. While the peroxy NOO and NO spectra share many similarities, one of the key differences is the shape of the transition peak, with sharp pointed peaks observed for NOO as opposed to a flat top seen in NO. The difference in the peak shape is attributed to different fine-structure between the molecules. Peroxy NOO detachment measures the electronic transition,



whereas NO detachment measures the transition,



The peroxy transition goes from a ${}^1A'$ state to a ${}^2A'$ state, but appears as a singlet–singlet transition in the measured spectrum. This is because the spin orbit splitting of the ${}^2A'$ state is much smaller than the resolution of the spectrometer. However, the situation is different for the NO transition. While the ${}^3\Sigma^-$ has little spin-orbit splitting, the neutral ${}^2\Pi$ state has a splitting of $\sim 123 \text{ cm}^{-1}$, which should be large enough to resolve using the HR-PEI spectrometer for slow electron velocities.

In the 519 nm photoelectron spectrum (Fig. 6.4) signs of the doublet NO splitting begin to be observed in the (3,0) and (4,0) vibrational transitions, however the resolution is insufficient to fully resolve the fine-structure transitions. One reason for this lies with the abnormally small electron affinity of NO^- of 0.026(5) eV, which means at a detachment wavelength of 519 nm the photoelectrons have kinetic energies of $\sim 2.4 \text{ eV}$. As one of the characteristics of the velocity-map imaging lens used in this experiment is a linear relationship between the energy resolution and the kinetic energy of the images particle, the high energies involved quickly become a limiting factor. To overcome this, the laser system was modified with a new optical path built from the laser to the beamline, so that the direct 1064 nm output of the Nd:YAG could be used. This halves the kinetic energy of the photoelectrons, from 2.4 to $\sim 1.2 \text{ eV}$, and increases the photon intensity, from pulse energies of $\sim 40 \text{ mJ}$ to $> 100 \text{ mJ}$.

NO^- ions were produced in a pulsed discharge of N_2O gas, and detached with 100 mJ 1064 nm laser pulses. The resulting photoelectron spectrum, containing 16,076,061 electrons is presented in Fig. 7.1. The raw velocity-mapped image is shown as an inset. The first 5 vibrational transitions of the neutral ground state are observed, each clearly showing the doublet fine-structure components. In order to extract precise spectroscopic constants, a rotational band model is constructed to determine where the true origin of each transition lies.

7.1.2 A rotational band model of NO

A rotational band model for the $\text{NO}(X^2\Pi) \leftarrow \text{NO}^-(X^3\Sigma^-)$ transition is constructed using similar methods to those used in sections 2.1.5 and 5.2. The Rydberg-Klein-Rees (RKR) inversion method^[142] was used to calculate the $\text{NO}^-(X^3\Sigma^-)$ and $\text{NO}(X^2\Pi)$ potential energy curves (Fig. 7.2), from which vibrational wavefunctions χ may be calculated to give the overlap Franck-Condon factors $|\langle \chi_f | \chi_i \rangle|^2$.

For the rotational structure, the angular momentum coupling scheme for both the neutral and ionic species needs to be determined. The anion ${}^3\Sigma^-$ state belongs to Hunds case (b), where there is small/no spin orbit coupling, however the neutral ${}^2\Pi$ state belongs to Hunds case (a) as it experiences strong spin orbit (LS) coupling. The positions of the

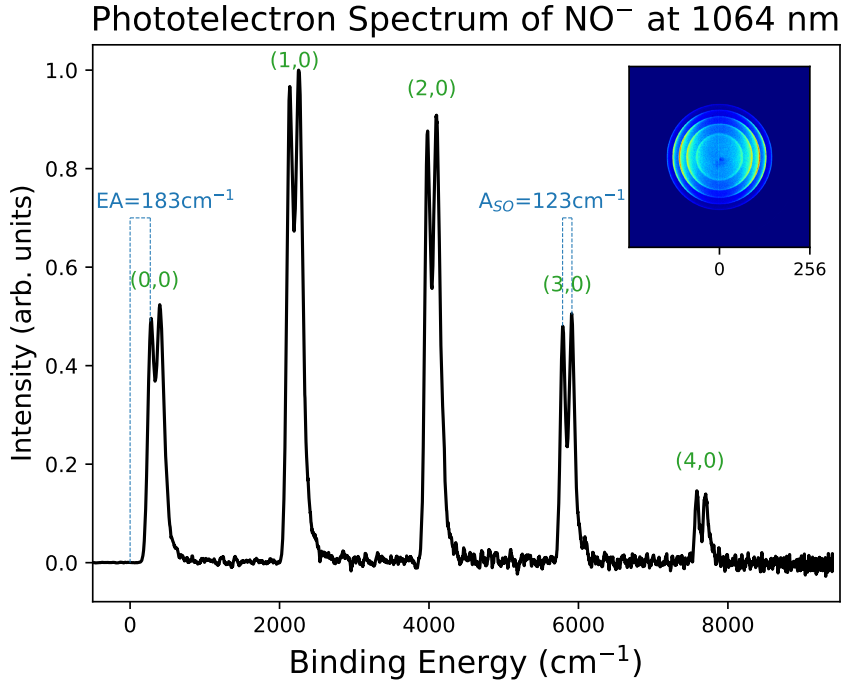


Figure 7.1: Photoelectron spectrum of NO^- measured at 1064 nm, illustrating vibrational transitions of the $\text{NO}^-(X^3\Sigma^-) \rightarrow \text{NO}(X^2\Pi)$ detachment. Raw velocity-mapped image is shown in the inset. The ${}^2\Pi$ doublet fine-structure is clearly resolved, with a measured spin-orbit splitting of $A_{SO} = 123(2) \text{ cm}^{-1}$.

rotational lines may then be determined using the formula of Kramers^[143,144]. For the initial anion ${}^3\Sigma^-$ state, the fine structure of each rotational level is given by,

$$F_1 = BN(N+1) - \frac{2\lambda(N+1)}{2N+3} + \gamma(N+1) \quad (7.3)$$

$$F_2 = BN(N+1) \quad (7.4)$$

$$F_3 = BN(N+1) - \frac{2\lambda N}{2N-1} - \gamma N \quad (7.5)$$

where F_1 , F_2 , and F_3 are the triplet fine structure components, N is the total nuclear (rotational+orbital) angular momentum quantum number, B is the rotational constant, and constants λ and γ can be obtained from the literature^[144]. Plotting the fine structure levels as a function of N shows that for $N \leq 10$: $F_3 < F_1$, whereas for $N > 10$: $F_3 > F_1$. Furthermore, a pattern in the rotational levels may be observed, with the total angular momentum J able to be given by $J = N - F + 2$.

Similarly we can work out the position of the rotational levels in the neutral ${}^2\Pi$ state using the formula for Hunds case (a),

$$F_\Omega = B \left((J + 1/2)^2 - \Lambda^2 + (1 - \Omega) [(2J + 1)^2 + Y(Y - 4)\Lambda^2]^{1/2} \right) \quad (7.6)$$

where Ω is the axial projection of the total angular momentum, taking values of $1/2$ and $3/2$ for ${}^2\Pi$, J is the total angular momentum quantum number, Λ is the orbital angular momentum (for NO $\Lambda = 1$), and Y is the ratio of the fine structure and rotational

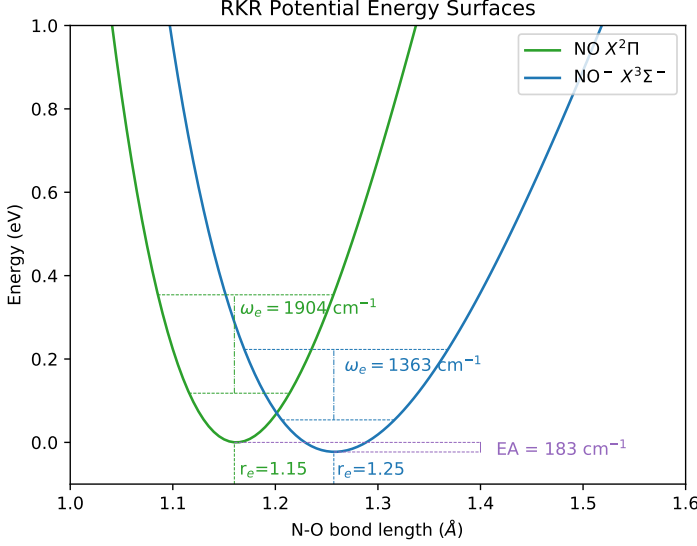


Figure 7.2: Potential energy curves for NO($^2\Pi$) and NO⁻($^3\Sigma^-$) ground electronic states constructed using the RKR inversion method, using spectroscopic constants from CCSD(T) calculations.

constants $Y = A_{so}/B$. In this case, the total angular momentum J is able to be given by $J = N + \Omega - 1$. Note that for a Π state there is no $N=0$ level. The effective spacing between the $F_{3/2}$ and $F_{1/2}$ fine structure levels is then given by,

$$F_{3/2} - F_{1/2} = -B [(2J + 1)^2 + Y(Y - 4)]^{1/2}. \quad (7.7)$$

For Hunds case (a), the spin orbit coupling constant A_{SO} is much larger than the rotational constant B . Therefore $y - 4 \approx Y$, while $-B\sqrt{(J + \frac{1}{2})^2 - 1} \approx -BJ$ ^[145]. The effective fine structure spacing then becomes,

$$A_{\text{effec}} = F_{3/2} - F_{1/2} = A_{SO} - 2B. \quad (7.8)$$

From these equations the rotational energy level structure of NO⁻ $X^3\Sigma^-$ and NO $X^2\Pi$ may be established. However, for a full rotational band model the transition intensities will also need to be determined. As NO is a diatomic molecule, the method of Buckingham *et al.*^[27] may be used, which employs Wigner 3-j symbols to calculate the angular momentum couplings involved in the transitions. For the case of NO⁻($X^3\Sigma^-$) + $h\nu \rightarrow$ NO($X^2\Pi$) + e⁻ photodetachment, the Q-factor for a case (b) to case (a) transition is,

$$Q = \sum_{\chi=j_t-1/2}^{j_t+1/2} (2\chi + 1) \begin{pmatrix} j_t & S' & \chi \\ 1 & \Omega' - 1 & -\Omega' \end{pmatrix}^2 \begin{pmatrix} J' & \chi & N'' \\ -\Omega' & \Omega' - \Lambda'' & \Lambda'' \end{pmatrix}^2, \quad (7.9)$$

where j_t is the total angular momentum of the initial electron, and Λ is the axial component of the orbital angular momentum. The Q factor may then be computed by computing the 3-j symbols and summing χ from $j_t - 1/2$ to $j_t + 1/2$. For the case of NO, $S' = 1/2$, $\Lambda' =$

$1, \Lambda'' = 0, \Delta\Lambda = 1, \Omega = \Lambda + \Sigma$, so the Q-factor becomes,

$$Q = \sum_{\chi=j_t-1/2}^{j_t+1/2} (2\chi + 1) \begin{pmatrix} j_t & 1/2 & \chi \\ 1 & \Omega' - 1 & -\Omega' \end{pmatrix}^2 \begin{pmatrix} J' & \chi & N'' \\ -\Omega' & \Omega' & 0 \end{pmatrix}^2, \quad (7.10)$$

which can be computed for every transition from level N'' in the anion to J', Ω' in the neutral.

From this, a rotational band model is written using python, with the model fitted to the experimental photoelectron spectrum from Fig. 7.1. This is shown for the first 4 vibrational transitions in Fig. 7.3. As can be seen, the rotational model is able to recreate the rotational band shape of the experimental data, including the spin orbit fine structure. An anion source temperature of $T = 191(8)$ K is extracted, which is typical for the spectrometer, while the energy resolution ranges from $\Gamma_{(3,0)} = 24(1)$ cm $^{-1}$ at the detector centre to $\Gamma_{(0,0)} = 65(1)$ cm $^{-1}$ at the detector edge, consistent with the $\Delta E \propto E$ characteristic of the VMI lens.

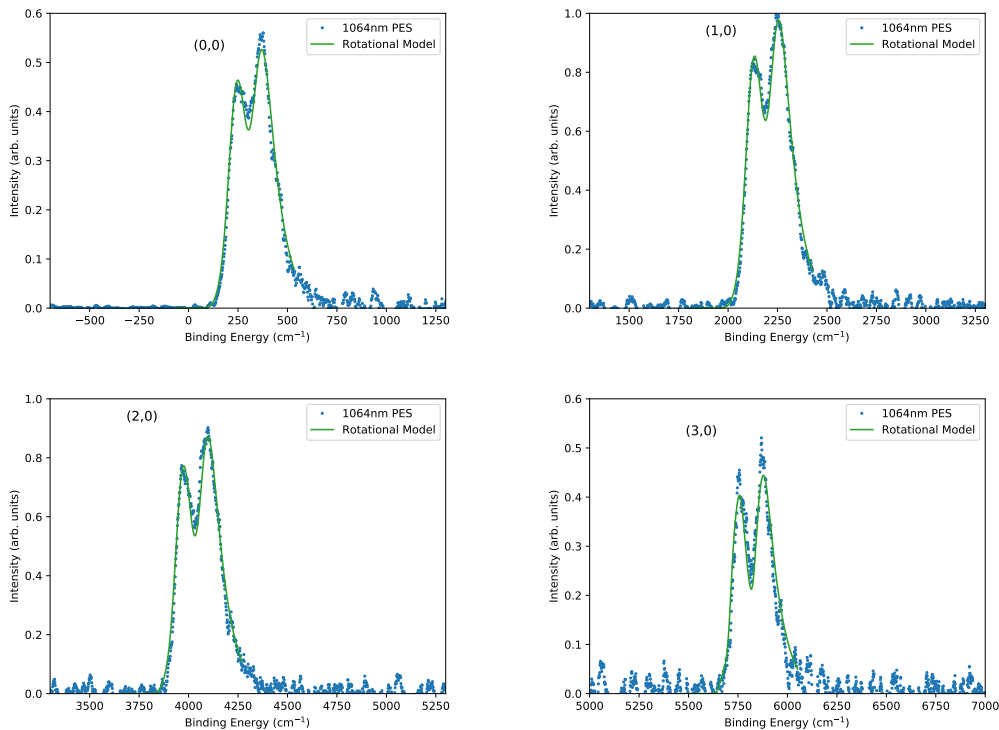


Figure 7.3: Rotational model of the 1064 nm NO photoelectron spectrum in Fig. 7.1, for vibrational transitions (0,0), (1,0), (2,0), and (3,0).

One useful piece of information that may be gained from this model is the calculation of the rotational band head shift. In the photoelectron spectrum in Fig. 7.1 the maximum of the peak intensity does not necessarily align with the origin of the rotational band. Calculating the true band origin positions for the $\Omega' = 1/2$ and $\Omega' = 3/2$ transitions for the $v' = 1$ peak,

$$\Delta N = 0, \quad N'' = N' = 1, \quad \Omega' = 1/2, \quad F'' = 3 : \quad Q13(1) = 2058.6 \text{ cm}^{-1}$$

$$\Delta N = 0, \quad N'' = N' = 1, \quad \Omega' = 3/2, \quad F'' = 3 : \quad Q33(1) = 2180.7 \text{ cm}^{-1}.$$

Compared to the experimental peak maximums of $\Omega'_{1/2}$: 2068.7 cm⁻¹ and $\Omega'_{3/2}$: 2192.9 cm⁻¹ this gives band shifts of $\Omega_{1/2} = 10.1$ cm⁻¹ and $\Omega_{3/2} = 12.1$ cm⁻¹. By applying these corrections to the measured peak positions in the photoelectron spectrum, a more accurate value for the true transition energies may be obtained. Applying this band origin shift allows for precise determination of spectroscopic constants, which are presented in Table 7.1. By calibrating the spectrum to the vibrational frequency ω_e of the NO $X^2\Pi$ state, well defined from neutral microwave spectroscopy studies^[146,147], an accurate value for the electron affinity may be determined. From the high resolution spectra presented here, a value of EA = 183(3) cm⁻¹ is determined, 27 cm⁻¹ smaller than, but within the experimental error of, the previously accepted value from the measurements of Travers *et al.*^[9] of EA = 210(40) cm⁻¹. An effective splitting of the $\Omega = 3/2$ and $\Omega = 1/2$ fine structure levels of $A_{\text{effec}} = 120(2)$ cm⁻¹ is determined, giving a spin orbit coupling constant of $A_{SO} = 123(2)$ cm⁻¹. A precise value for the anion rotational constant of $B = 1.454(2)$ cm⁻¹ is also extracted, similar to the previously measured value of $B = 1.42(7)$ cm⁻¹^[134].

Table 7.1: Spectroscopic constants (cm⁻¹) of NO $X^2\Pi$ and NO⁻ $X^3\Sigma^-$, extracted from the HR-PEI photoelectron spectrum of this work (Fig. 7.1), compared to previous measurements.

	HR-PEI	Previous Work	<i>ab-initio</i> ^a
<u>NO $X^2\Pi$</u>			
A_{SO}	123(2)	123.1(3) ^b	
ω_e	1904(2)	1904.20(4) ^c	1956
$\omega_e x_e$	11.8(6)	14.07(5) ^c	
B	1.684(3)	1.6961(1) ^b	1.683
<u>NO⁻ $X^3\Sigma^-$</u>			
EA	183(3)	210(40) ^d	
B	1.454(2)	1.42(7) ^e	1.50

^a CCSD(T) calculations with cc-pVTZ basis using NWChem software^[94]

^b from vibration-rotation spectroscopy of Johns *et al.*^[146]

^c from flash-photolysis spectroscopy of Engleman and Rouse^[147]

^d from photoelectron spectroscopy of Travers *et al.*^[9]

^e from photoelectron spectroscopy of Siegel *et al.*^[134]

7.1.3 NO⁻ photoelectron angular distribution

The use of velocity mapped imaging allows for precise anisotropy measurements of NO⁻ detachment to be obtained. As we have seen in other cases in this thesis, anisotropy parameters can provide a useful insight into the character of the detachment orbital. The $2\pi^*$ orbital of NO⁻ $X^3\Sigma^-$, involved in the photodetachment, was computed using NWChem software^[94] and is shown in Fig. 7.4. As can be seen, this orbital looks a lot like a standard atomic d orbital, with a small amount of asymmetry between the N and O sides. Employing the Cooper-Zare equation (Eq. 2.37) for detachment from a d orbital suggests that the anisotropy of NO⁻ photodetachment will follow,

$$\beta_d = \frac{2 + 12A_2^2\epsilon^2 - 36A_2\epsilon \cos(\Delta_{\ell\pm 1})}{5[2 + 3A_2^2\epsilon^2]}, \quad (7.11)$$

where A_2 is the Hanstorp coefficient $A_2 = \frac{1}{\epsilon^2} \frac{\chi_{2,3}^2}{\chi_{2,1}^2}$, and $\Delta_{\ell\pm 1}$ is the difference in the partial wave phase shifts.

However Khuseynov *et al.*^[108] have suggested a more accurate representation of the $2\pi^*$ orbital may be obtained by employing a mixed pd model. They found that the asymmetry in the NO^- orbital could be recreated using the function $|\psi\rangle = (1 - \gamma_d)|p\rangle + \gamma_d|d\rangle$ where $\gamma_d = 0.985$. As we saw in chapter 5, detachment from an orbital of mixed character can be modelled by summing over all the contributing partial waves. For a mixed pd model, the anisotropy curve becomes,

$$\beta_{pd} = \frac{2\gamma_p[\chi_{1,2}^2 - 2\chi_{1,2}\chi_{1,0}\cos\Delta_{2,0}] + \frac{2}{5}\gamma_d[\chi_{2,1}^2 + 6\chi_{2,3}^2 - 18\chi_{2,1}\chi_{2,3}\cos\Delta_{3,1}]}{\gamma_p[\chi_{1,0^2} + 2\chi_{1,2}^2] + \gamma_d[2\chi_{2,1}^2 + 3\chi_{2,3}^2]}, \quad (7.12)$$

where $\chi_{\ell,\ell\pm 1}$ are the radial matrix elements for the $\ell \pm 1$ partial wave, and $\Delta_{\ell\pm 1}$ are the corresponding phase shift differences. Simplifying this expression by noting that $\gamma_p = 1 - \gamma_d$, letting $\cos\Delta = 1$ to account for the expected small phase shifts, and multiplying the numerator and denominator by $\frac{\chi_{1,2}^2}{\chi_{1,0^2}\chi_{2,1}^2}$ gives,

$$\beta_{pd} = \frac{2(1 - \gamma_d)B_2\epsilon[A_1^2\epsilon^2 - 2A_1\epsilon] + \frac{2}{5}\gamma_dA_1^2\epsilon^2[1 + 6A_2^2\epsilon^2 - 18A_2\epsilon]}{(1 - \gamma_d)B_2\epsilon[1 + 2A_1^2\epsilon^2] + \gamma_dA_1^2\epsilon^2[2 + 3A_2^2\epsilon^2]} \quad (7.13)$$

where the Hanstorp coefficients are defined as,

$$A_1 = \frac{1}{\epsilon} \frac{\chi_{1,2}}{\chi_{1,0}} \quad A_2 = \frac{1}{\epsilon} \frac{\chi_{2,3}}{\chi_{2,1}} \quad B_2 = \frac{1}{\epsilon} \frac{\chi_{1,2}^2}{\chi_{2,1}^2}.$$

By measuring the anisotropy parameter for NO^- photodetachment at various energies, fitting to Eq. (7.13) allows for the Hanstorp coefficients to be determined.

From the high resolution NO^- photoelectron spectra measured at 1064nm (Fig. 7.1) and 519nm (Fig. 6.4) anisotropy parameters β were obtained by fitting the angular intensity distribution to Eq. 2.38, with the results presented in Fig. 7.4. Both the pure d (Eq. 7.11) and mixed pd (Eq. 7.13) models were used to describe the results. From the pure d model, a Hanstorp coefficient of $A_2 = 0.58(2)$ eV⁻¹ was obtained along with a phase shift of $\cos\Delta = 0.99(2)$. This justifies setting the phase shifts to zero in the derivation of the pd model. Using the mixed pd model, Hanstorp coefficients of $A_1 = 0.8(1)$ eV⁻¹, $A_2 = 0.53(5)$ eV⁻¹, and $B_2 = 9(2)$ eV⁻¹ are obtained.

From the graph it can be seen that both curves have a similar shape, and pass through most of the data points, as is reflected in both models providing a similar value for the coefficient A_2 . However, the main difference in the curves occurs near threshold. By definition, as the kinetic energy ϵ approaches threshold, a d detachment curve will intersect $\beta = 0.2$. However as the pd curve tends towards $\epsilon \rightarrow 0$, the anisotropy curve intersects $\beta = 0$. This occurs as even though the p character only accounts for $\sim 1.5\%$ of the $2\pi^*$ orbital, at low kinetic energies the low angular momentum wave (s) dominates the overall behaviour (a similar effect was observed in the spd mixed orbital of NO_2^- in chapter 5). Consequently, for most kinetic energies the small p character may be neglected and a pure d approximation is able to describe the detachment process. However, close to threshold this approximation breaks down, and including the small amount of p orbital character into the model becomes important.

An interesting observation in Fig. 7.4 occurs at energies at about 1.2 eV, where 3 of

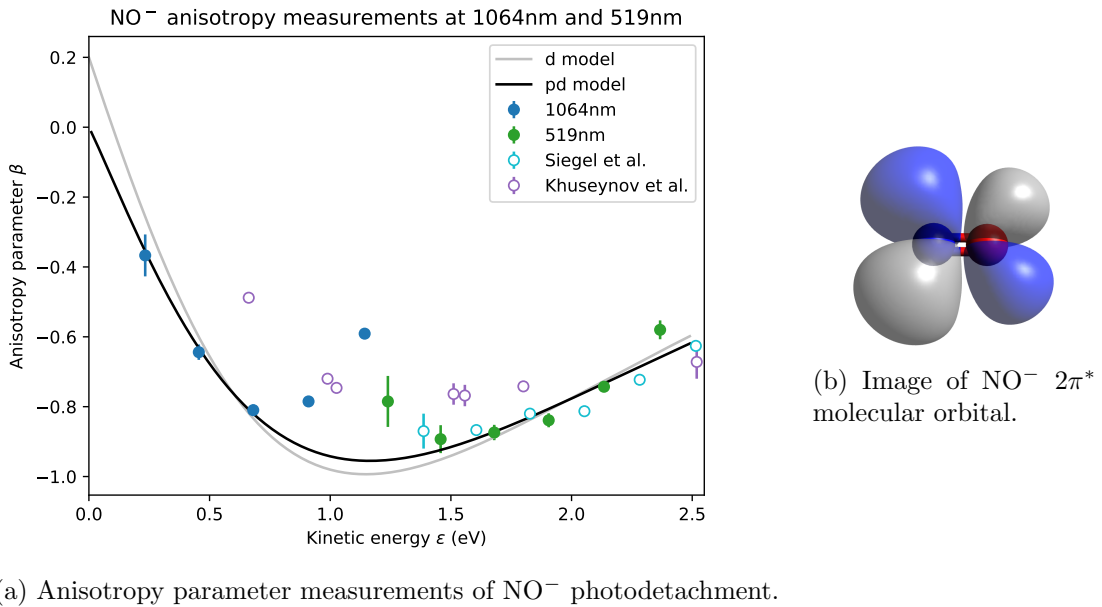
(a) Anisotropy parameter measurements of NO^- photodetachment.

Figure 7.4: Anisotropy parameters β were measured for NO^- photodetachment at 1064nm (●) and 519nm (●). The experimental data was fitted to a pure d and a mixed pd anisotropy curve. Previous measurements of Siegel *et al.*^[134] and Khuseynov *et al.*^[108] are also included.

the data points appear to deviate from the expected behaviour. To try and uncover the reason behind this, repeated measurements were taken at various wavelengths, however they produced the same result, with a β parameter for the (0,0) origin transition at 1064nm of ~ -0.6 , more positive than the expected ~ -0.9 . To further investigate this in the future, measurements at different wavelengths may be able to help. Particularly useful will be wavelengths where a different vibrational transition will produce an electron with kinetic energy ~ 1.2 eV. Specifically, this will occur at $\lambda \sim 830, 735, 650$ or 580 nm.

The anisotropy measurements of this work are in good agreement with the results of Siegel *et al.*^[134] at high kinetic energies. However, the results of Khuseynov *et al.*^[108] appear slightly more isotropic at low kinetic energies. One possibility for this is that the current work includes measurements from all 5 vibrational transitions, whereas the anisotropy parameters of Khuseynov all correspond to the same vibrational transition $\text{NO}(X^2\Pi, v' = 2) \leftarrow \text{NO}^-(X^3\Sigma^-, v'' = 0)$. This potential vibrational effect may also contribute to the anomalous β behaviour around $eKE \sim 1.2$ eV.

This benchmark study of $\text{NO}(X^2\Pi) \leftarrow \text{NO}^-(X^3\Sigma^-)$ photodetachment illustrates the ability of the HR-PEI spectrometer to determine spectroscopic constants with state of the art precision. From the rotational modelling, accurate values for the electron affinity, spin-orbit splitting, and rotational constants of nitrous oxide were obtained, which may help provide better molecular input for future atmospheric modelling. By studying the angular distribution of photoelectrons the performance of a pure d versus a mixed pd model could be tested, while the interesting phenomenon observed at detachment energies around $eKE \sim 1.2$ eV may need to be further investigated in future studies.

7.2 A study of Oxygen

Measurements of atomic and molecular oxygen are useful for calibration of the HR-PEI spectrometer, and are often measured in parallel with other molecule experiments. Atomic oxygen is useful, as the absence of vibrational and rotational structure allows for the transition origin, energy resolution, and source temperature, all to be determined precisely, from the relative intensities of the $^3P_2 \leftarrow ^2P_{3/2}$ and $^3P_2 \leftarrow ^2P_{1/2}$ fine structure transitions. As the geometric ratio of the fine-structure intensities are well known from the 3-j symbol calculations of Scharf and Godefroid^[68], the relative intensities observed in a photoelectron spectrum will be determined by the Boltzmann factor for the anion. However, characterisation of the spectrometer has found that due to second-order imaging effects, the radius to kinetic energy conversion factor, from detector radial position to electron kinetic energy, may vary slightly across the detector radius (as shown in Fig. 3.18). Therefore, higher accuracy in the reported transition energies may be obtained using a molecular oxygen measurement, as this exhibits vibrational transitions across a large energy range. As the vibrational energy structure of neutral O₂ is well defined, an O₂ PES may be used to check the calibration of the spectrometer as a function of the detector radius. O₂ is especially useful for calibration at long wavelength, below the EA of O⁻.

Atomic and molecular oxygen are vital species in the Earth's atmosphere, with their reactive and photophysical properties of great interest to atmospheric and biological chemists. In the upper atmosphere, the role of negative ions becomes prevalent, due to the photoionisation and photofragmentation processes that are key drivers of the photochemistry in the stratosphere. This results in a magnitude of different ions and radicals being found in much higher densities than what is found in the lower atmosphere^[82,90]. These ions are also common in solution, usually in the form of anionic clusters, where they partake in a variety of biological and charge transfer processes.

Consequently, the O⁻ anion has been the centre of numerous theoretical and experimental studies. The spectroscopic study of O⁻ has been ongoing since the 1940's, where Vier *et al.*^[148] determined an electron affinity of 3.0(1) eV. However, it was not until 1985 that a precise value for the electron affinity was determined, with a tuneable-laser photodetachment threshold experiment of Neumark *et al.*^[149] defining an EA of 11,784.645(6) cm⁻¹. This work also measured a spin-orbit splitting between the anion $^2P_{3/2}$ and $^2P_{1/2}$ levels of 117.13(5) cm⁻¹. Novel photoelectron microscopy studies of Blondel *et al.*^[10,150] later definitively defined the electron affinity at 11,784.676(7) cm⁻¹, with a spin orbit splitting of 117.084(14) cm⁻¹.

The angular distribution of O⁻ photoelectrons has also received considerable attention, with early photoelectron spectroscopy measurements of Siegel *et al.*^[151] and Hanstorp^[31] determining an average anisotropy parameter across the 6 fine-structure transitions. Later high resolution photoelectron spectroscopy measurements of Breyer *et al.*^[152] reported anisotropy parameters for 3 of the fine-structure transitions, however it was not until 2007 that Cavanagh *et al.*^[24] resolved β parameters for 5 fine-structure transitions, using the HR-PEI spectrometer of this work. More recent studies have investigated photodetachment transitions to the O(¹D) excited state, including a 266 nm reflectron experiment of Domesle *et al.*^[153], as well as photodetachment threshold spectroscopy of O(³P)^[117,154].

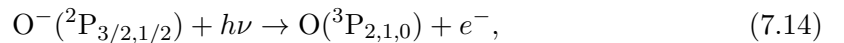
Photodetachment cross sections for O⁻ have also been studied, with the first measurement in 1965 by Branscomb *et al.*^[155], to both the ground O(³P) and excited O(¹D) electronic states of the neutral atom. These original measurements still provide a challenge for theoretical interpretation, as atomic oxygen is an open-shell system where both corre-

lation and polarisation effects are likely to play an important role^[156]. Photodetachment cross sections to the ground state of O(³P) were measured again by Lee *et al.*^[157] and more recently in 2016 by Genevriez *et al.*^[158], however less data is available for photodetachment to the excited O(¹D) state. Various theoretical studies have attempted to model the photodetachment cross sections, predominantly using R-matrix^[159] approaches, however discrepancies arise between the predicted behaviours^[156,158,160]. This is partly due to differences in the experimental data. While the previous measurements all agree near the O(³P) threshold, the more recent values of Genevriez are noticeably higher than the original measurements of Branscomb above threshold.

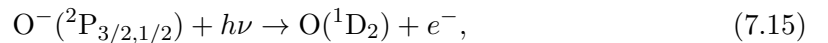
Photoelectron spectra of O⁻ are investigated here, using the HR-PEI spectrometer. New short wavelength measurements help to characterise the electron anisotropy parameter at high kinetic energies, while the relative intensities of the O(³P)↔O⁻(²P) and O(¹D)↔O⁻(²P) transitions provides new information about the photodetachment cross section of the O(¹D) state.

7.2.1 Photoelectron spectroscopy of O⁻

Many O⁻ photoelectron spectra have been measured during the course of this work, spanning a large range of detachment wavelengths and experimental parameters. The electron affinity of oxygen is well defined, with a definitive value of EA=1.4611135(12) eV determined from photodetachment microscopy studies^[10]. Wavelengths shorter than 850 nm will photodetach O⁻(²P) to the neutral ground state O(³P),



giving 6 fine-structure transitions. The excited ¹D₂ state of neutral oxygen lies 1.969 eV above the ³P₂ state, with wavelengths shorter than 361.6 nm required for detachment to occur.



For atomic species, the energy of a fine-structure level is given by,

$$E_J = \frac{A_{SO}}{2} [J(J+1) - L(L+1) - S(S+1)]. \quad (7.16)$$

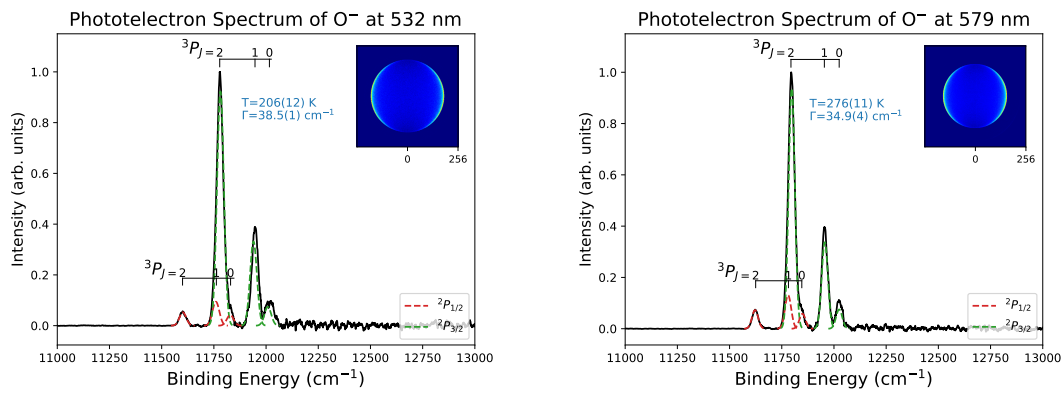
Therefore, the effective splitting of two levels J' and J'' is given by,

$$A_{\text{effec}} = E_{J'} - E_{J''} = \frac{A_{SO}}{2} [J'(J'+1) - J''(J''+1)]. \quad (7.17)$$

To obtain a high resolution spectrum of O(³P)↔O⁻(²P) detachment, O⁻ ions were produced in a pulsed discharge of pure O₂ gas. The ions were then accelerated, mass separated, and photodetached using both the Sunlite OPO system and direct Nd:YAG output. While the energy resolution of velocity mapped-imaging is proportional to the kinetic energy of the mapped particle - with the highest resolution achieved close to threshold - a degeneracy between the idler and signal beams of the OPO near 750 nm (see Fig. 3.12) limits the power achievable near this wavelength. Consequently, the best O⁻ measurements of this work were taken at 579 nm with the OPO, and 532 nm with the second harmonic of the Nd:YAG. These photoelectron spectra are presented in Fig. 7.5, along with Gaussian fits of the fine-structure transitions.

Both measurements were recorded with a VMI repeller voltage of -1100V, expanding

the image so it would occupy the entire detector. The 579 nm spectrum contains 6,837,244 electrons, more than the 2,779,172 electrons in the 532 nm image. The first measurement has a colder fitted source temperature of $T=206(12)$ K cf. $T=276(11)$ K, with both spectra recording similar energy resolutions of $\Gamma = 34.9 - 38.5 \text{ cm}^{-1}$. As a function of kinetic energy this correlates to a spectrometer resolution of $\Delta E/E \sim 0.6\%$ and $\sim 0.5\%$ respectively, close to the benchmark resolution of 0.4% previously set by the ANU HR-PEI spectrometer^[24]. By calibrating the spectrum to the well defined O⁻ electron affinity, the spin-orbit splitting of the $^2P_{3/2,1/2}$ anion is determined to be $A_{\text{effec}} = 181(7) \text{ cm}^{-1}$, which is in agreement with the accepted value in the literature of $177.084(14) \text{ cm}^{-1}$ ^[10]. This corresponds to an anion spin-orbit coupling of $A_{SO} = -121(5) \text{ cm}^{-1}$. The fine structure of the $^3P_{2,1,0}$ neutral is set to the known splittings of $A_{2 \leftarrow 1} = 158.265 \text{ cm}^{-1}$ and $A_{2 \leftarrow 0} = 226.977 \text{ cm}^{-1}$.

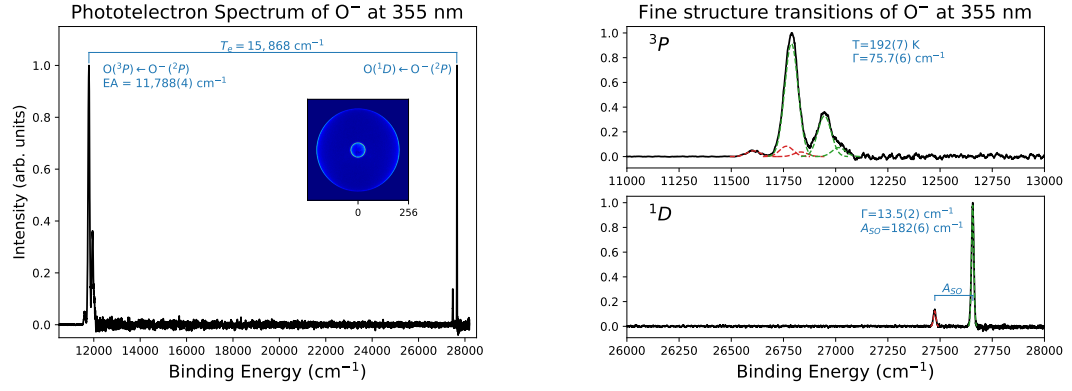


(a) O⁻ spectrum, measured at 532 nm with the direct Nd:YAG output. (b) O⁻ spectrum, measured at 579 nm with the OPO.

Figure 7.5: Photoelectron spectra of O⁻, showing the O($^3P_{2,1,0}$) \leftarrow O⁻($^2P_{1/2,3/2}$) fine structure transitions. Raw velocity-mapped images are inserted in the top right corner. An anion fine structure splitting of $A_{\text{effec}} = 181(7) \text{ cm}^{-1}$ is determined.

Detachment yielding the O(1D) excited state may also be investigated by shifting to shorter wavelengths. O(1D_2) \leftarrow O⁻($^2P_{3/2,1/2}$) photodetachment was measured using the 3rd (355 nm) and 4th (266 nm) harmonics of the Nd:YAG laser, with the photoelectron spectrum at 355 nm presented in Fig. 7.6. As detachment to the singlet D state is close to threshold, a high resolution of $\Gamma_{1D} = 13.5(2) \text{ cm}^{-1}$ is achieved. But even though the O(3P) transition produces electrons with kinetic energy over 2 eV a respectable resolution of $\Gamma_{3P} = 75.7(6) \text{ cm}^{-1}$ is achieved, with fine structure transitions still resolved. This illustrates one of the key advantages of the HR-PEI spectrometer, with high resolution measurements still achievable for high electron energies.

From the calibrated photoelectron spectrum in Fig. 7.6, an experimental value for the electron affinity of EA = 11,788(4) cm^{-1} is obtained, which is in agreement with the precise value determined by photoelectron microscopy^[10]. From the O(1D_2) \leftarrow O⁻($^2P_{1/2}$) and O(1D_2) \leftarrow O⁻($^2P_{3/2}$) transitions of the upper state, an anion spin orbit splitting of $A_{\text{effec}} = 182(6) \text{ cm}^{-1}$ is determined. This value agrees with both the anion splitting measured in the ground O(3P) state, and the literature microscopy value, which confirms an accurate energy calibration may be achieved over the entire range of the detector.



(a) O⁻ spectrum at 355 nm, showing detachment to both the ³P and ¹D neutral states. (b) Fine structure transitions from O⁻(²P_{1/2,3/2}) to the ³P and ¹D neutral states.

Figure 7.6: Photoelectron spectrum of O⁻ at 355 nm showing detachment to both the ³P and ¹D neutral states. From the ratio of the ²P_{1/2} to ²P_{3/2} fine structure transition intensities, a source temperature of T=192(7) K is determined, along with an anion spin orbit splitting of A_{effec} = 182(6) cm⁻¹.

Angular distributions

From the inset of the raw velocity-mapped image of O⁻ photodetachment in Fig. 7.6, it is clear that at 355 nm O(³P_{2,1,0})←O⁻(²P_{1/2,3/2}) photodetachment displays a strong negative anisotropy parameter, whereas O(¹D₂)←O⁻(²P_{1/2}) detachment appears more isotropic. This is not unexpected, given the ¹D transition is close to threshold and detachment is from a *p* orbital. However by measuring both detachment channels at different wavelengths, the energy dependence of their anisotropy parameters may be investigated, providing determination of the Hanstorp coefficients and partial wave phase shifts.

The anisotropy parameter for a *p*-detachment orbital electron follows the Cooper-Zare expression with $\ell = 1$,

$$\beta_p = \frac{2A_1^2\epsilon^2 - 4A_1\epsilon \cos \Delta_{\ell\pm 1}}{1 + 2A_1^2\epsilon^2}, \quad (7.18)$$

where the Hanstorp coefficient A₁ is defined as the ratio of radial matrix elements $A_1^2\epsilon^2 \sim \frac{\chi_{1,2}^2}{\chi_{1,0}^2}$. Eq. (7.18) is a result of the electric-dipole selection rule $\ell' = \ell \pm 1$, describing the interference between the *s* and *d* detachment partial waves. At low kinetic energies the lower angular momentum *s* wave will dominate the process, resulting in a more isotropic distribution close to threshold, as is observed for detachment yielding ¹D₂ in Fig. 7.6.

O⁻ anisotropy parameters were measured at a variety of detachment wavelengths, from 266 nm up to 800 nm. These experimental data points were fitted to the Cooper-Zare equation for *p*-orbital detachment (Eq. 7.18), as shown in Fig. 7.7. Detachment to the ground state, O(³P₂)←O⁻(²P_{3/2}), is shown in blue, while detachment to the excited state O(¹D₂)←O⁻(²P_{3/2}) is shown in green. It can be seen that photodetachment to both states follow a similar shaped anisotropy curve, however detachment to the ¹D₂ state follows a gentler slope, with the minimum in the anisotropy occurring at a larger kinetic energy. This is reflected in the value for the Hanstorp coefficients extracted from the fits. For ³P₂, A₁ = 0.49(4) eV⁻¹ with $\cos \Delta_{\ell\pm 1} = 0.92(1)$ while for ¹D₂, A₁ = 0.31(8) eV⁻¹ with $\cos \Delta_{\ell\pm 1} = 0.95(3)$. Qualitatively, this infers that the *d* partial wave contributes more at

low energies for $^3\text{P}_2$ detachment as opposed to $^1\text{D}_2$ detachment. While the anisotropy of $\text{O}(^3\text{P}_{2,1,0}) \leftarrow \text{O}^-(^2\text{P}_{1/2,3/2})$ photodetachment has been well studied by Cavanagh *et al.*^[24], the new 266 nm measurement of this work provides useful insight into the behaviour of $\text{O}(^1\text{D}_2) \leftarrow \text{O}^-(^2\text{P}_{3/2})$ detachment away from threshold.

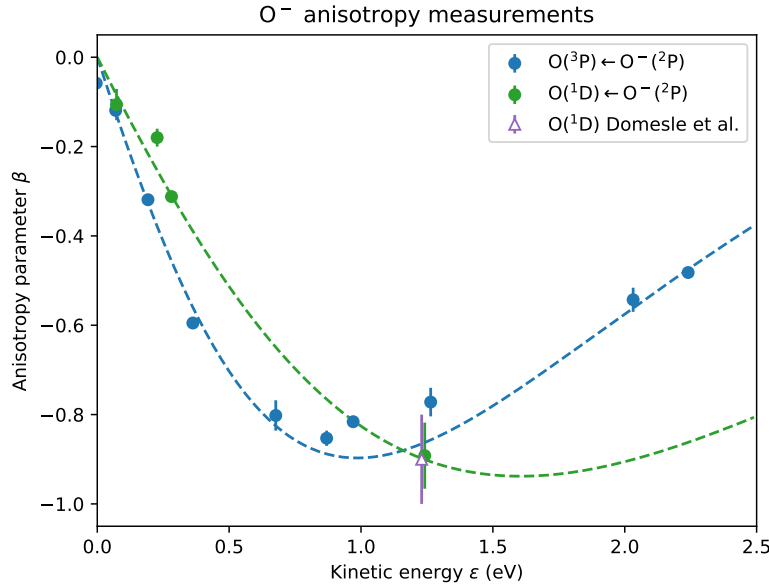


Figure 7.7: Anisotropy parameters for $\text{O}(^3\text{P}_2) \leftarrow \text{O}^-(^2\text{P}_{3/2})$ and $\text{O}(^1\text{D}_2) \leftarrow \text{O}^-(^2\text{P}_{3/2})$ photodetachment at various wavelengths. The experimental data points are fitted to the Cooper-Zare equation for p -orbital detachment (Eq. 7.18). The 266 nm measurement of Domesle *et al.*^[153] is also included (\triangle).

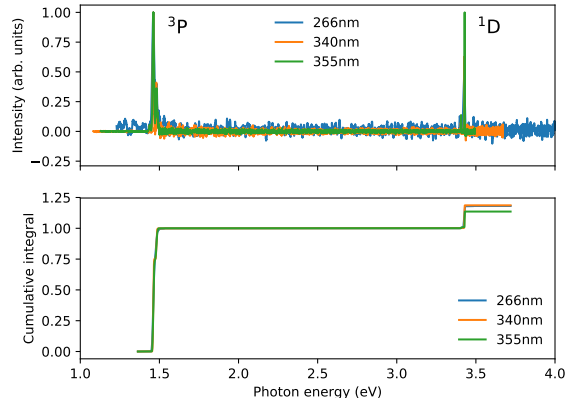
7.2.2 Absolute cross-sections

Absolute photodetachment cross sections are important for atmospheric modelling calculations and, near transition thresholds, contain information about the internal energy structure of the target species. They also provide a good test for theoretical computation scattering codes such as the widely used R-matrix program^[159]. Oxygen anion photodetachment producing ground state $\text{O}(^3\text{P})$ atoms has been well studied, however discrepancies between results still exist. This is highlighted by a recent measurement of $\text{O}(^3\text{P}) \leftarrow \text{O}^-(^2\text{P})$ detachment by Genevriez *et al.*^[158] which reports total cross sections that are 20% larger than all previous experimental values. These values are claimed to be the result of an improved experimental technique, and are consistent with independent R-matrix calculations also suggesting a cross section 20% to 35% above previous results^[156,158]. Conversely, much less is known about detachment to produce excited state $\text{O}(^1\text{D})$ atoms. In 1965 Branscombe *et al.*^[155] measured O^- photodetachment cross sections, over photon energies up to 4 eV, which included near threshold measurements of $\text{O}(^1\text{D}) \leftarrow \text{O}^-(^2\text{P})$. However there have been no reports of experimental $\text{O}(^1\text{D})$ absolute cross-sections since.

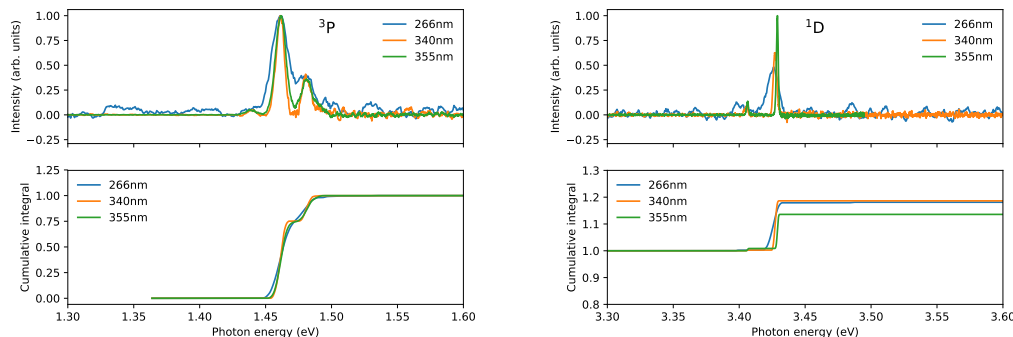
Typically velocity-map imaging photoelectron spectroscopy is better suited to measuring differential cross-sections and anisotropy parameters, as opposed to absolute cross-sections. This is because the experiment ion and photon densities are not precisely known,

and may fluctuate significantly throughout a measurement. However, in the case of short wavelength detachment of O^- , total $O(^1D)$ relative cross sections may be calculated by comparing the ratio of integrated intensities of $O(^3P) : O(^1D)$ from measured photoelectron spectra, with the known total cross section of $O(^3P)$.

Photoelectron spectra from O^- detachment were measured at 355 nm, 340 nm, and 266 nm, with the cumulative integral of each spectrum plotted as shown in Fig. 7.8. At each transition ($^3P, ^1D$) threshold, a step in the cumulative graph is observed, describing the shape of the photodetachment total cross section. Levels may also be observed inside each large step, representing the onset of the different fine-structure components. However, as mentioned above, the cumulative graph alone can not be converted to an absolute cross section as other key experimental parameters are unknown. The ratio between the step size at the onset of the 3P and 1D transitions on the other hand, may be used to determine the cross section of one state, if the other state is known. The calculated ratios for each wavelength are given in Table 7.2.



(a) Photoelectron spectra of O^- at 355 nm, 340 nm, and 266 nm, shown along with the cumulative integral of each spectra.



(b) Cumulative integral over the $O(^3P) \leftarrow O^-(^2P)$ transition. Steps in the cumulative spectra represent the onset of each fine structure transition.

(c) Cumulative integral over the $O(^1D) \leftarrow O^-(^2P)$ transition. The relative $^3P_2 : ^1D_2$ step height may be used to calculate the total cross section.

Figure 7.8: Cumulative integrals of O^- photoelectron spectra at 355 nm, 340 nm, and 266 nm. By comparing the relative height of the 3P and 1D onset steps, the absolute cross section for the latter may be calculated from the known 3P photodetachment cross section.

Table 7.2: Ratio of O(¹D) and O(³P) onset step sizes at various detachment wavelengths, used to calculate total cross sections.

	266 nm	340 nm	355 nm
$\frac{I(^1D)}{I(^3P)}$:	0.232	0.244	0.171
$\sigma (10^{-18} \text{cm}^2)$:	7.52	7.60	7.15

As expected, the ratio at 355 nm is notably lower than the other two measurements as a result of the Wigner threshold law. By multiplying these step ratios with the absolute cross section of O(³P) \leftarrow O([−](²P)) as measured by Branscombe *et al.*^[155], absolute cross section measurements of O(¹D) \leftarrow O([−](²P)) were calculated and plotted in Fig. 7.9, alongside previous measurements and theoretical calculations. It is seen that the absolute magnitude of the various R-matrix calculations vary by as much as 20%, making interpretation of the results unclear. The 2003 R-matrix calculation of Wu *et al.*^[160] (---) follow the original O(³P) measurements of Branscomb^[155] (●) and Lee^[157] (†) after scaling by $\times 0.7$, to correct a publication scale factor error. However, the R-matrix calculations of Bartschat^[156] (—) and Genevriez^[158] (—) suggest a much larger value for the oxygen cross section, a proposition supported by the recent experimental measurements of Genevriez *et al.*^[158] (◇).

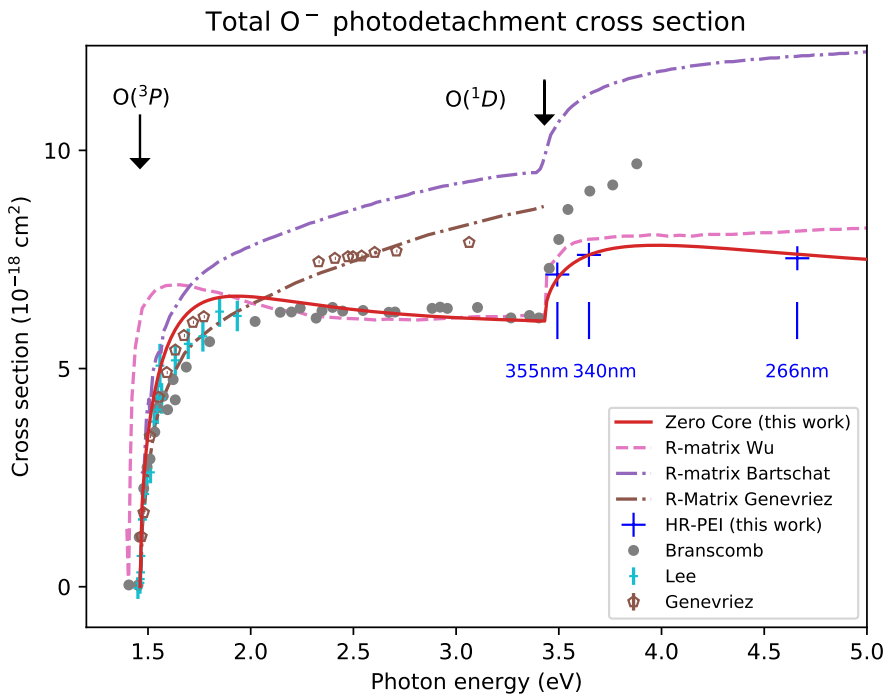


Figure 7.9: Total cross section measurements of O[−] photodetachment to both O(³P) and O(¹D) states. Cross section measurements for the ¹D state are calculated from the spectra presented in this work (+) in relation to the ³P measurements of Branscomb *et al.*^[155] (●). Experimental measurements by Lee^[157] (†) and Genevriez^[158] (◇) are also included, along with theoretical R-matrix calculations by Wu^[160] (---), Bartschat^[156] (—) and Genevriez^[158] (—). A zero-core-contribution model based on the work of Stehman and Woo^[161,162] is fitted to the experimental data points (—).

From the ratios in Table 7.2 and the above threshold measurements of Branscomb^[155], absolute cross sections for O⁻ photodetachment above the ¹D threshold were calculated (+). These measurements provide the first indication of the O⁻ photodetachment cross section above the excited state threshold. From this work, it appears the total cross section decreases slightly at high photon energies - a trend also observed above the ³P threshold - opposite to the gradual increase predicted by the R-matrix calculations. The zero-core-contribution (ZCC) model of Stehman and Woo^[161,162] may also be used to describe the variation in the cross section detachment, fitting two parameters, the ZCC radius (r_0) and the detachment partial wave phase shift (Δ). By fitting the ZCC model to the ³P data of Branscomb and ¹D data of this work, values of $r_0 = 1.4 \text{ \AA}$, $\cos \Delta = -0.925$ and $r_0 = 1.8 \text{ \AA}$, $\cos \Delta = -0.95$ was obtained for detachment to ³P and ¹D respectively. Note that these are the same phase shift values that were obtained from studying the differential cross section (via β) in Fig. 7.7.

While the HR-PEI spectrometer is not normally used for measuring absolute cross sections, this example shows that in certain cases it may be adapted to provide useful information about total cross section behaviour. With the short wavelength measurements presented in this work, the first indication of above ¹D threshold cross section behaviour was obtained. The ratios presented in Table 7.2 may also be applied to other predictions of the ³P behaviour. Interestingly if the recent data of Genevriez is used for calibration as opposed to Branscomb's data, the ¹D cross section behaviour would follow a similar path to the prediction of Bartschat *et al.*^[156]. This highlights how studies of even simple species, which are often considered already complete, may still provide new and important information.

7.2.3 Molecular oxygen

Molecular oxygen, O₂, is a species that has received a large amount of attention due to its importance in both atmospheric and biological systems. As such, spectroscopic results of the neutral have been well established, however spectroscopic constants of the anion are less well defined. Early estimates of the O₂ electron affinity varied widely, with values as low as 0.15(5) eV^[163] and as high as 1.27(20)^[164] reported as being measured in the literature. In 1972 Celotta *et al.*^[165] investigated this problem using laser photoelectron spectroscopy, and defined a value for the electron affinity of 0.44(8) eV. This measurement was then repeated in 1989 by Travers *et al.*^[9] (EA=0.451(7) eV), in 1995 by Schiedt and Weinkauf (EA=0.450(2) eV)^[166], and in 2003 by Ervin *et al.*^[20] (EA=0.448(6) eV). Each successive measurement recorded higher resolution in the O₂⁻ photoelectron spectrum, with the electron affinity measurements all in exceedingly good agreement. The Ervin study also confirmed that O₂⁻ X² Π_g is the only adiabatically bound anion state, stable with respect to autodetachment, refuting counter claims from electron capture experiments^[167]. However, it should be noted that signatures of the excited anion state O₂⁻ (A² Π_u) have been observed as vibrational resonances in the photoelectron spectrum, close to the dissociation limit^[168].

Photodetachment of O₂⁻ has been previously studied with the HR-PEI spectrometer from this work, with a vibrational dependence of the electron anisotropy found and examined in detail^[65,169]. Khuseynov *et al.*^[170] have also investigated O₂⁻ photodetachment, in their work on anionic clusters. Many new O₂⁻ photoelectron spectra were measured throughout this body of work, with some of the more important results discussed below.

To investigate the vibrational and electronic structure of O₂ (and O₂⁻), ions were produced in a gas discharge of pure O₂ and then photodetached using the third harmonic

of the Nd:YAG laser (35 nm). The photoelectron spectroscopy study of Ervin *et al.*^[20] defined the electron affinity of O₂ as EA = 0.448(6) eV. Hence, at 355 nm the fastest electrons will have kinetic energies of up to 3 eV, requiring a high VMI repeller voltage of V_r = -2800 V to map all of the detached electrons onto the detector. The resulting photoelectron spectrum, including raw VMI inset, is presented in Fig. 7.10.

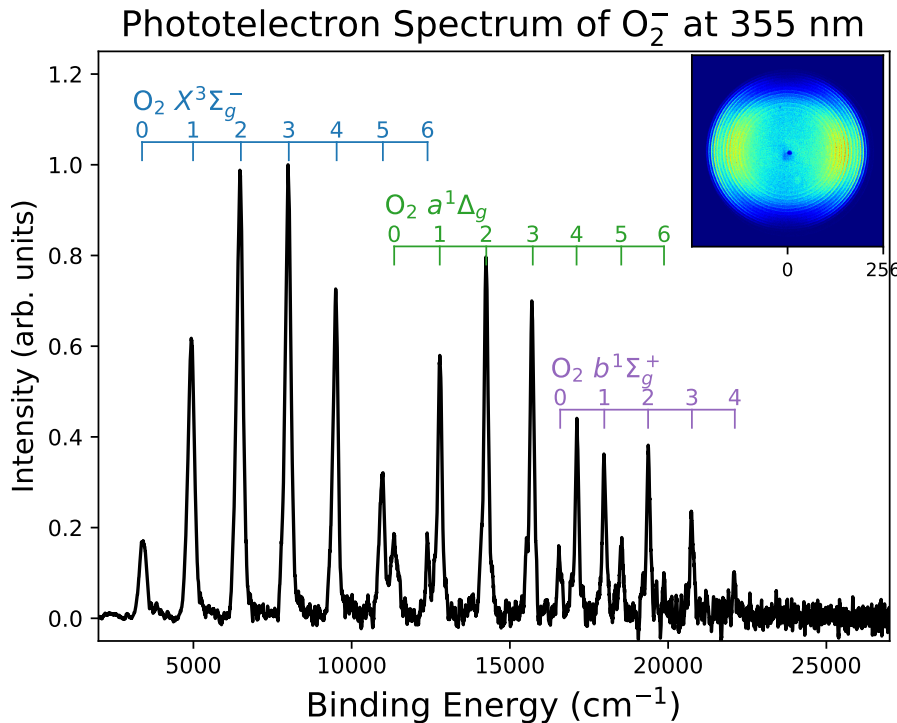
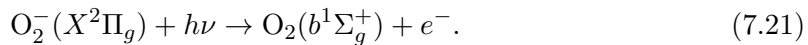
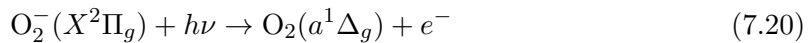
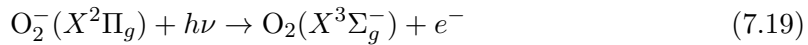


Figure 7.10: Photoelectron spectrum of O₂⁻ at 355 nm. Three vibrational progressions are observed, corresponding to the electronic transitions O₂(X³Σ_g⁻) → O₂⁻(X²Π_g), O₂(a¹Δ_g) → O₂⁻(X²Π_g), and O₂(b¹Σ_g⁺) → O₂⁻(X²Π_g). A raw velocity map image of the detachment is inserted in the top right corner.

The velocity-mapped image in Fig. 7.10 contains 15,847,811 electrons, and displays three electronic transitions,



Each electronic transition also includes a vibrational progression from $v = 0$ in the anion to $v = 0 - 6$ in the neutral. The result is a very busy photoelectron spectrum, with many transitions. However the vibrational constants and electronic term energies of the neutral ³Σ_g⁻, ¹Δ_g, ¹Σ_g⁺ states are already well defined, while the 400 – 800 nm region of the O₂⁻ photoelectron spectrum has previously been well studied by Van Duzor *et al.*^[65]. However if the fine structure of the O₂⁻(X²Π_g) anion could be resolved, then new precise values for the electron affinity and spin orbit splitting constant of the anion may be obtained. To achieve this, long wavelength measurements close to the threshold of O₂(X³Σ_g⁻) → O₂⁻(X²Π_g) detachment are required.

O₂ rotational model

First, a rotational band model may be created so that the true band origin of each transition may be found. A similar model to the one described for NO in section 7.1.2 can be constructed for O₂. O₂(X³Σ_g⁻) → O₂⁻(X²Π_g) photodetachment is an example of a Hunds case (a) to Hunds case (b) transition, due to the strong spin-orbit coupling of the anion ²Π_g state. Again, we may use the formula of Kramers^[143,144] to determine the positions of rotational transition lines, with energy levels in the anion ²Π_g state given by,

$$F_{\Omega} = B \left((J + 1/2)^2 - \Lambda^2 + (1 - \Omega) [(2J + 1)^2 + Y(Y - 4)\Lambda^2]^{1/2} \right), \quad (7.22)$$

where Ω is the axial projection of the total angular momentum, taking values of 1/2 and 3/2 for ²Π, J is the total angular momentum quantum number, Λ is the axial orbital angular momentum (Λ = 1 for O₂⁻) and Y is the ratio of the fine structure and rotational constants Y = A_{SO}/B. Similarly, the energy levels of the neutral ³Σ_g⁻ state are given by,

$$F_1 = BN(N + 1) - \frac{2\lambda(N + 1)}{2N + 3} + \gamma(N + 1) \quad (7.23)$$

$$F_2 = BN(N + 1) \quad (7.24)$$

$$F_3 = BN(N + 1) - \frac{2\lambda N}{2N - 1} - \gamma N, \quad (7.25)$$

where F₁, F₂, and F₃ are the triplet fine structure components, N is the total nuclear (rotational+orbital) angular momentum quantum number, B is the rotational constant, and constants λ = 1.984 and γ = -0.0084 are defined in the literature^[144]. These are the same formula used in the NO rotational model, except instead of a ²Π ← ³Σ⁻ transition we are now looking at a ³Σ_g⁻ ← ²Π_g.

From Eqs. (7.22)–(7.25) the energy positions of all the allowed rotational transitions may be determined. As shown in the NO model, the method of Buckingham *et al.*^[27] may be used to calculate the transition intensities. However, this time the Q-factor for a case (a) to case (b) transition must be used,

$$Q = \sum_{\chi=j_t-1/2}^{j_t+1/2} (2\chi + 1) \begin{pmatrix} j_t & S'' & \chi \\ -\Delta\Lambda & \Sigma'' & \Delta' - \Omega'' \end{pmatrix}^2 \begin{pmatrix} N' & \chi & J'' \\ -\Lambda' & \Lambda' - \Omega'' & \Omega'' \end{pmatrix}^2, \quad (7.26)$$

where *j_t* is the total angular momentum of the initial electron, and Λ and Σ are the axial components of the orbital and spin angular momentum respectively. For the case of O₂, S'' = 1/2, Λ'' = 1, Λ' = 0, ΔΛ = -1, Ω = Λ + Σ, so the Q-factor becomes,

$$Q = \sum_{\chi=j_t-1/2}^{j_t+1/2} (2\chi + 1) \begin{pmatrix} j_t & 1/2 & \chi \\ 1 & \Omega'' - 1 & -\Omega'' \end{pmatrix}^2 \begin{pmatrix} N' & \chi & J'' \\ 0 & -\Omega'' & \Omega'' \end{pmatrix}^2, \quad (7.27)$$

which may be computed for every transition from level J'', Ω'' in the anion to N' in the neutral.

This model was fitted to a 1064 nm photoelectron spectrum of O₂⁻, as shown in Fig. 7.11. A VMI repeller voltage of VR = -1000 V was used, mapping 5,099,640 electrons onto the detector to create the raw image, shown as an inset in the top left of the spectrum. With the higher resolution achieved close to threshold, the doublet fine struc-

ture of the anion is now clearly resolved. By calibrating the spectrum to the well defined vibrational spacings of the neutral molecule ($\omega_e = 1580.19(3) \text{ cm}^{-1}$, $\omega_e x_e = 11.98 \text{ cm}^{-1}$) a precise value for the electron affinity and spin-orbit splitting of the anion could be determined. This established an electron affinity of EA $3586(1) \text{ cm}^{-1}$, in agreement with the previous estimate of Ervin *et al.*^[20] (EA = $3613(48) \text{ cm}^{-1}$). The model measures an effective spin orbit splitting of $A_{\text{effec}} = 164(1) \text{ cm}^{-1}$, corresponding to a spin-orbit coupling of $A_{SO} = 162(1) \text{ cm}^{-1}$, which is also in agreement with the previous measurement of $A_{SO} = 160(4) \text{ cm}^{-1}$ ^[166]. A value for the anion rotational constant of $B'' = 1.08(5) \text{ cm}^{-1}$ is also obtained, smaller than the prediction of $B'' = 1.161(7)$ ^[20].

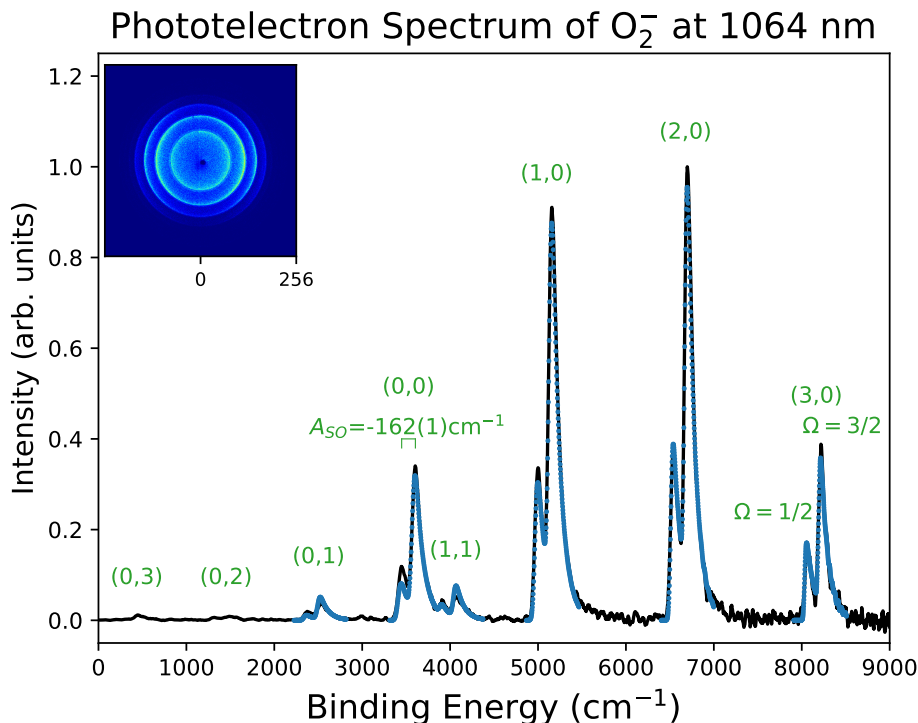


Figure 7.11: Photoelectron spectrum of O_2^- at 1064 nm. A rotational model (··· - see text) is fitted to the data, in order to determine accurate peak positions. The anion doublet fine structure is clearly resolved. The raw velocity-map image is an inset.

7.2.4 Hot band transitions

The photoelectron spectrum in Fig. 7.11 also shows the presence of several hot bands, assigned to transitions from vibrationally excited states in the anion to the ground vibrational state of the neutral. The rotational fit extracted a source temperature of T = 307(4) K, which is hotter than usual for the ANU anion source. This was a result of trialling new modifications to the discharge source, as was discussed in section 3.2. Normally, a hot source is problematic, as it leads to more rovibrational structure that may clutter the spectrum. However it is useful for determining the vibrational energy structure of the anion - something which is typically not as well defined as the neutral structure.

By employing a larger aperture in the pulsed jet discharge source, to reduce the cooling via the adiabatic expansion of the gas into the vacuum, a hot O_2^- photoelectron spectrum is obtained. The spectrum is presented in Fig. 7.12, with several hot band transitions

clearly visible. Fitting the rotational model described above, the positions of the hot band transition origins may be determined. Fitting these positions to the anharmonic oscillator equation,

$$G(v) = \omega_e(v + 1/2) - \omega_{exe}(v + 1/2)^2 \quad (7.28)$$

allows for the vibrational frequency ω_e and anharmonicity constant ω_{exe} for $O_2^- (X^2\Pi_g)$ to be determined. Doing so for the clearly resolved hot bands (0,3), (0,2), (0,1), and (1,1) in Fig. 7.12 produces values $\omega_e = 1111(3) \text{ cm}^{-1}$ and $\omega_{exe} = 11(1) \text{ cm}^{-1}$. These values are in good agreement with the previous measurement of Lineberger *et al.*^[20] of $\omega_e = 1108(20) \text{ cm}^{-1}$ and $\omega_{exe} \sim 9 \text{ cm}^{-1}$.

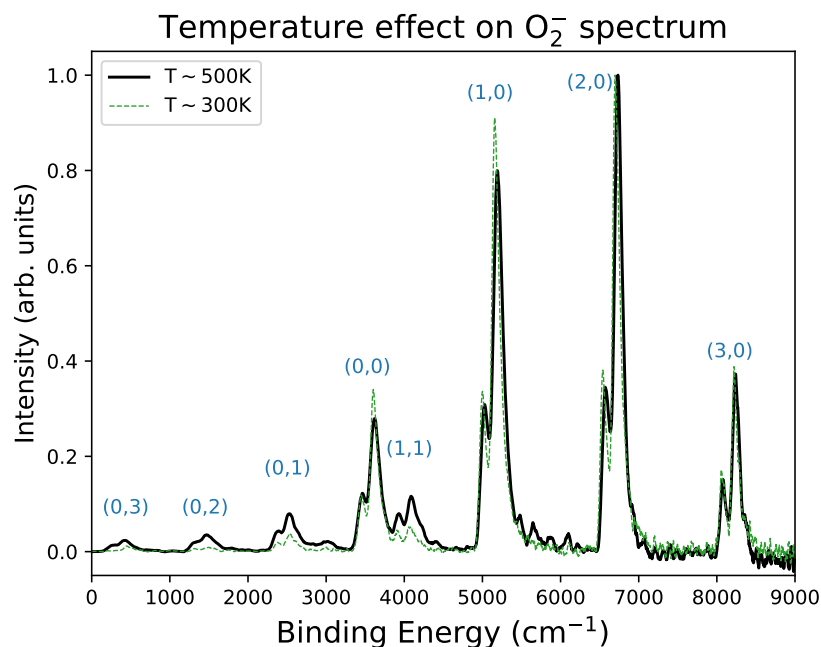


Figure 7.12: Photoelectron spectra of 1064 nm at different source temperatures. In the hot spectrum ($- T \sim 500 \text{ K}$) the hot band transitions are much more prominent than in the cold ($-- T \sim 300 \text{ K}$) measurement.

By studying O_2^- photodetachment close to threshold at 1064 nm, high resolution spectra have been recorded. Fitting a rotational band model to determine accurate band origin positions has allowed for precise values of the anion spectroscopic constants to be determined. These constants, listed in Table 7.3, are generally in good agreement with previous work, but provide more exact values with smaller uncertainties. Improving our knowledge of the spectroscopic and photophysical properties of O_2^- in studies such as this, help provide useful information to atmospheric and biological scientists investigating the many systems involving this molecule.

Table 7.3: Spectroscopic constants of the oxygen anion $O_2^- X^2\Pi_g$, measured using photo-electron spectroscopy. All constants are given in cm^{-1} .

$O_2^- X^2\Pi_g$	HR-PEI	Previous Work
EA	3586(1)	3613(48) ^a
B	1.08(6)	1.161(7) ^a
A_{SO}	-162(1)	-160(4) ^b
ω_e	1111(3)	1108(20) ^a
ω_{ex_e}	11(1)	$\sim 9^a$

^a from photoelectron spectroscopy study of Ervin *et al.*^[20]

^b from photoelectron spectroscopy study of Schiedt *et al.*^[166]

Part III

Vinylidene - A mechanism for isomerisation

Motivation

Part III of this thesis focuses on the vinylidene molecule H₂CC, a small hydrocarbon of great importance in organic chemistry^[171,172], with this section particularly interested in the isomerisation reaction between vinylidene and its linear isomer acetylene HCCH. The mechanism through which the isomerisation proceeds is a prototype of the 1,2-Hydrogen migration, common to the formation and annihilation of many organic radicals^[173]. Furthermore, the story behind the vinylidene molecule is well known in the spectroscopic community, with numerous studies over the past 30 years dedicated to investigating the dynamics and stability of this molecule^[53]. However, despite these efforts, the chemistry and structure of this molecule still remains a mystery.

To finally decipher the behaviour of the vinylidene molecule, a collaboration was initiated as part of an Australian Research Council discovery project. This project aims to measure state of the art vinylidene spectra by combining the results from the high resolution photoelectron imaging spectrometer (HR-PEI) at the ANU with the Neumark group's cryogenic slow electron velocity-map imaging spectrometer (Cryo-SEVI) at UC Berkeley. These results may then be analysed with help from theoretical *ab-initio* methods (University of New Mexico), and insights from the acetylene side of the barrier (MIT). Through the culmination of this multifaceted approach, the dynamics of this benchmark molecule is finally understood.

8.1 The story of vinylidene

Carbenes (R=C:) are a class of chemical compounds that possess a neutral carbon atom with two unshared valence electrons. Due to the reactivity of the electron lone pair, these molecules are highly reactive, and play important roles in many organic reactions^[174]. This often involves an intramolecular 1,2-hydrogen shift, where a migrating hydrogen moves across the double bond towards the lone pair electrons - a mechanism that plays a critical role in more complex organic reactions such as dehydration of alcohols (or hydration of alkenes), and the gas-phase combustion of hydrocarbons^[175,176]. The simplest unsaturated carbene is the vinylidene molecule, making the vinylidene-acetylene isomerisation reaction an ideal prototype for studying this 1,2-H migration^[177].

The study of vinylidene provides a novel example of transition-state spectroscopy. Transitions state theory (TST) states that the dynamics of a reaction are controlled by the formation of reactive intermediates, at the rate determining step. Therefore, studying these intermediate states, and their associated chemistry, is vital to the understanding and possibly controlling of how large multi-step organic reactions proceed. Vinylidene is widely invoked as a reaction intermediate in a host of different chemical processes, making it an attractive target for spectroscopic studies^[178-182]. But, by definition these intermediate species are transient in nature, making them unsuitable for measurement via most common spectroscopic techniques. However, if a transient species possesses a stable parent anion (as is the case for vinylidene), it is possible to use photoelectron spectroscopy of the negative ion to obtain information about the neutral intermediate state.

This makes the vinylidene-acetylene isomerisation an appealing benchmark unimolecular process in chemical physics, and as such, has been the focus of many theoretical studies^[183–189]. However, while the existence of acetylene has been known and studied for well over a century^[177,189], the existence of the vinylidene isomer as a stable bound molecule was much less certain^[172,190]. Numerous attempts failed to isolate the vinylidene molecule^[171], and hence it was long believed to be extremely difficult, if not impossible, to observe vinylidene either chemically or spectroscopically^[172].

The difficulty in observing vinylidene directly, arises from the remarkably low barrier to isomerisation ($\sim 0.1 - 0.2$ eV^[53,191]). Isomerisation reactions of carbenes involving 1,2-hydrogen shifts are known to occur very rapidly^[174], and it has long been established that if vinylidene indeed exists, its lifetime would be very short^[172,178,192]. However, despite these difficulties, the first spectroscopic measurement of isolated vinylidene was achieved in 1983 by the Lineberger group at JILA^[193], by applying photoelectron spectroscopy to the vinylidene anion. This measurement, shown in Fig. 8.1, reveals some of the vibrational structure of the vinylidene isomer, and confirmed the existence of vinylidene as a bound molecule^[190,193]. The deuterated species D₂CC was also measured, and found to show similar spectroscopic features. Importantly this result confirmed that the structure of neutral vinylidene could be accessed via spectroscopy of the negative ion.

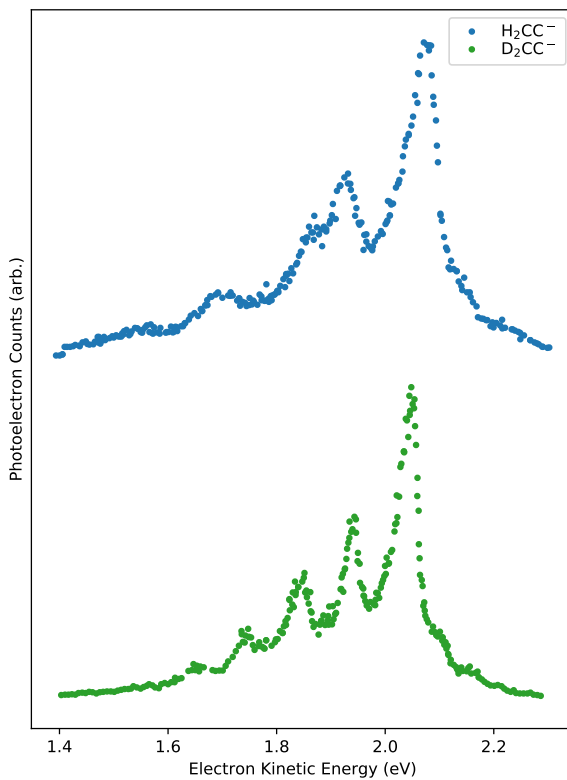
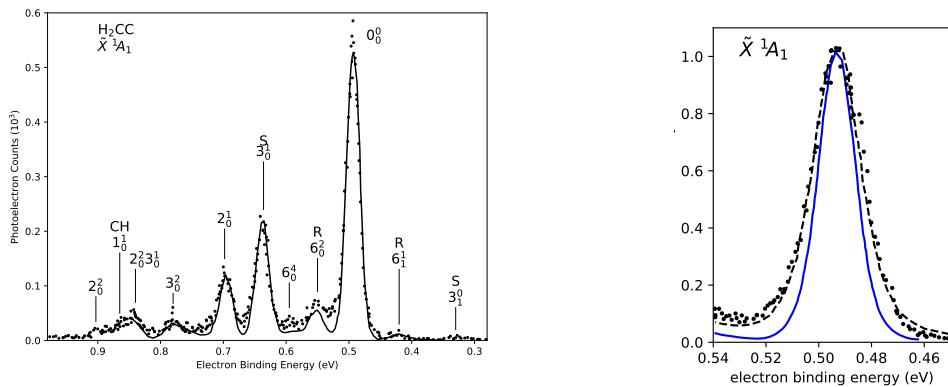


Figure 8.1: The first spectroscopic measurement of the vinylidene molecule, recorded by the Lineberger group in 1983 via photodetachment of the vinylidene anion at 488 nm, reproduced from Ref^[193].

The measurement in Fig. 8.1 finally gave a definitive answer about the existence of vinylidene, however this was really only the start of the vinylidene story, with attention now turned to studying the lifetime and dynamics of this deceptively complex molecule.

8.1.1 The lifetime conundrum

In 1989 a seminal second photoelectron spectrum of the vinylidene ion was published by the Lineberger group, where implementation of a new ion source created a colder, higher density packets of ions, and greatly improved spectral resolution^[11]. The high resolution photoelectron spectrum, presented in Fig. 8.2, is able to resolve more of the vibrational structure of the molecule, with a much lower background. However, the electron kinetic energy resolution remained insufficient to fully resolve the rotational band shape of these vibrational resonances. This result was greeted with much fanfare, as the resolved peak widths provided a prediction for the lifetime of the vinylidene molecule. The experimental peak widths observed in Fig. 8.2 have three key contributions, with broadening due to the unresolved rotational structure, the instrumental resolution, and the lifetime of the state. The lifetime broadening arises from the uncertainty principle, $\Delta E \Delta \tau \geq \hbar/2$, and results in a Lorentzian line shape with width $\Gamma_{1/2} = 1/2\pi\tau$, where τ is the lifetime of the state.



(a) 1989 photoelectron spectrum of the vinylidene molecule, with vibrational structure of the ground $\tilde{X}^1 A_1$ state resolved^[11]

(b) Rotational band contour (—) fitted to experimental data (---). $25 - 120 \text{ cm}^{-1}$ of excess broadening is attributed to lifetime broadening.

Figure 8.2: Improved high resolution photoelectron spectrum of vinylidene at 351.1 nm measured by the Lineberger group in 1989, reproduced from Ref^[11]. Observed peak widths suggest a vinylidene lifetime of $\tau = 0.04 - 0.2 \text{ ps}$.

Rotational contours were constructed to estimate the amount of spectral broadening due to rotational transitions (shown in blue in Fig. 8.2). Convoluting the rotational contour with the known instrument resolution function (Lorentzian broadening with 9meV FWHM) leaves $\Gamma_{1/2} \sim 25 - 120 \text{ cm}^{-1}$ of additional broadening present on top of the rotational/instrument width, with this extra broadening attributed to the short lifetime of the vinylidene isomer. This was supported by comparison between the photoelectron spectra of H₂CC and D₂CC which showed the extra broadening was only present in the H₂CC spectrum (and only in the ground electronic state), suggesting that it must therefore be linked to the isomerisation process. The excess linewidth corresponds to an estimated lifetime of $\tau = 0.04 - 0.2 \text{ ps}$ ^[11]. It was carefully noted by the authors, however that it is possible that all of the observed broadening may be accounted for by the rotational contour plus instrument resolution, due to large uncertainties in the simulations. Despite this careful qualification, subsequent research interpreted all of the observed additional width as definite measured lifetime broadening^[172,175]. As such, vinylidene lifetimes ranging

from a few picoseconds to as short as \sim 100 femtoseconds have been cited as being experimentally measured in the PES spectrum^[55,194,195]. This consensus for a sub-picosecond vinylidene lifetime was generally agreed upon for 9 years, until a subsequent coulomb explosion imaging study appeared to alarmingly contradict this interpretation.

In 1998 the Vager research group at the Weizmann Institute^[196,197] reinvestigated the stability of the vinylidene molecule using a coulomb explosion imaging (CEI) apparatus, which also accessed the transient neutral vinylidene state by exploiting the stable negative ion. Vinylidene anions were produced in a microwave discharge source, mass separated, photodetached, and then accelerated towards a thin strip of gold foil. The subsequent impact strips the remaining electrons from the molecule, with the position and arrival times of the resulting cationic fragments ($2 \times \text{H}^+$ and $2 \times \text{C}^{6+}$) measured on a multi-particle detector^[12]. From the coincidental temporal and spatial information, the geometry of the molecule at the point of contact with the gold foil is calculated.

The CEI experiment provided an extraordinary result - even when photodetachment (forming the transient neutral vinylidene molecule) occurred $3.5 \mu\text{s}$ before the collision, $\sim 50\%$ of the molecules retained the vinylidene geometry at the point of contact^[12]. This surprising observation appeared to contrast with the commonly accepted notion of vinylidene being a short-lived isomer with a sub-picosecond lifetime.

Many future studies have attempted to reconcile the stark discrepancy between these two experimental results, with little success^[53,189,198]. One reason for this is the continued difficulty in observing the vinylidene molecule experimentally^[188], with the stable vinylidene anion hard to produce^[199]. Difficulties also arise from the complexity of the physics involved in the isomerisation. As the barrier to isomerisation lies $\sim 2 \text{ eV}$ above the acetylene minimum, vinylidene is believed to tunnel through a small barrier, into a quasi-continuum of acetylene vibrational states. However, calculations and experimental studies that focused on the acetylene side of the barrier by Field and co-workers suggest that vinylidene may only be able to interact with a select few vibrational door-way states on the acetylene side^[200,201]. Consequently, this process is not a simple textbook tunnelling process, where vinylidene tunnels through a barrier into a continuum of states. Instead, periodic reversible dynamics are expected, with predicted long-lived eigenstates consisting of both vinylidene and acetylene character^[53]. Finding evidence of these long-lived eigenstates holds the key to understanding the dynamics of the isomerisation process, and is the main aim of the work in this section of the thesis. This requires a concerted effort using multiple experimental techniques on both sides of the vinylidene-acetylene barrier, coupled with state of the art full quantum dynamic calculations.

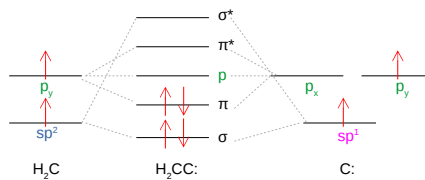
8.2 Introducing vinylidene

To understand the dynamics of the isomerisation, the energetic structure and symmetry constraints of the vinylidene and acetylene molecules must first be determined. From valence shell electron pair repulsion (VSEPR) theory we can predict that vinylidene is planar in geometry, belonging to the C_{2v} point group, whereas acetylene is a linear molecule with an inversion centre, belonging to the $D_{\infty h}$ point group. The orbital structure and relative stability of the vinylidene and acetylene isomers may be predicted by employing hybrid orbital theory. Atomic orbitals are mixed to form new hybrid orbitals based on the geometry of the molecule, to form valence bonds consistent with predictions from VSEPR theory. This provides a simple method to predict the electronic structure of a molecule without the need for high-level quantum chemistry calculations.

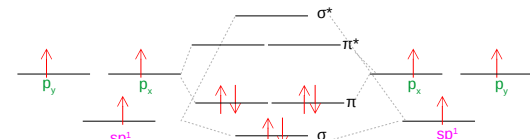
Hybrid orbital diagrams for \tilde{X}^1A_1 vinylidene and $\tilde{X}^1\Sigma_g^+$ acetylene are presented in Fig. 8.3. One carbon in vinylidene has three bonding groups around it, requiring sp^2 hybridisation with s , p_z , and p_x atomic orbitals combined to form $3 \times sp^2$ orbitals. The other carbon only has two bonding groups, requiring sp^1 hybridisation with the s and p_z orbitals combined to form $2 \times sp^1$ orbitals. This results in $3 \times \sigma$ bonds, $1 \times \pi$ bond, and an electron lone pair in the free sp^1 orbital. Both carbons in acetylene have sp^1 hybridisation, resulting in $3 \times \sigma$ bonds and $2 \times \pi$ bonds.



(a) Hybrid-orbitals of ground state \tilde{X}^1A_1 vinylidene. (b) Hybrid-orbitals of ground state $\tilde{X}^1\Sigma_g^+$ acetylene.



(c) Orbital energy diagram for \tilde{X}^1A_1 vinylidene. The additional electron to form the anion is added to a non-bonding p orbital.



(d) Orbital energy diagram for $\tilde{X}^1\Sigma_g^+$ acetylene. The additional electron to form the anion is added to an anti-bonding π^* orbital.

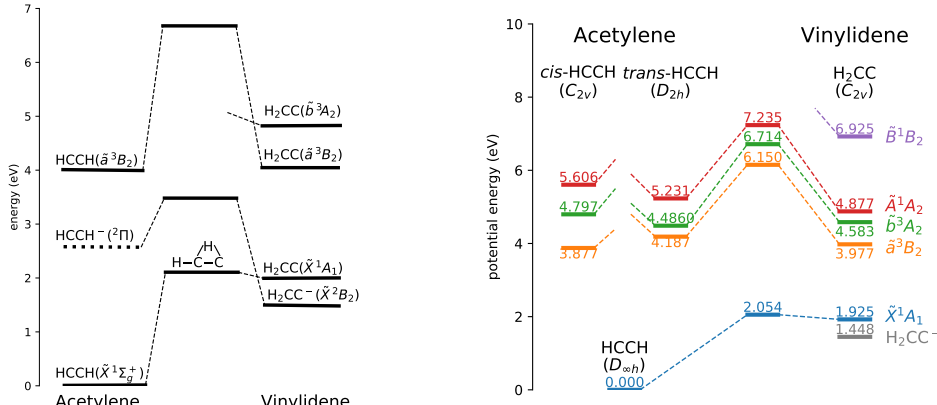
Figure 8.3: Hybrid-orbital description of the vinylidene and acetylene isomers. From the orbital energy diagrams in Fig. 8.3 it can be seen that the outermost electron in H_2CC^- (\tilde{X}^2B_2) is in a non-bonding p orbital, whereas the additional electron in $HCCH^-$ ($\tilde{X}^2\Pi$) is in an anti-bonding π^* orbital.

The orbital make-up of a molecule often provides a helpful description of its bonding structure. From the orbital energy diagrams in Fig. 8.3 it is seen that neutral vinylidene has 4 electrons in bonding orbitals, giving it a bond order of 2, whereas acetylene has 6 bonding electrons giving it a bond order of 3. When an additional electron is added to vinylidene (to form the \tilde{X}^2B_2 anion state), it is added to a non-bonding p orbital, only having a small effect on the bonding and stability of the molecule. However when an electron is added to acetylene (to form the $\tilde{X}^2\Pi$ anion state), it is added to an anti-bonding π^* orbital, substantially reducing the bond order and stability of the molecule.

The addition of an electron into an anti-bonding orbital vs a non-bonding orbital accounts for the switch in stability of the isomers, with the vinylidene anion stable with respect to the acetylene geometry, opposite to the neutral case. This switch is important, as it is the stability of the vinylidene anion that allows measurement of the unstable neutral vinylidene molecule. The lifetime of the vinylidene anion has been measured to be $\tau \approx 110$ s^[199], more than long enough for most spectroscopic techniques.

Quantitative values for the energies of various ground and excited states of vinylidene and acetylene have been determined through a combination of experimental results^[11,191] and *ab-initio* calculations^[198,202], with the potential energy curves of the lower lying states

presented in Fig. 8.4. This shows the \tilde{X}^1A_1 ground state of vinylidene lying ~ 2 eV higher than $\tilde{X}^1\Sigma_g^+$ acetylene, with only a small ~ 0.2 eV barrier to isomerisation. The lowest lying triplet state of vinylidene lies ~ 2 eV above the ground state, with the first excited singlet state ~ 3 eV above.



(a) Energies of vinylidene and acetylene ground and excited states, which have been measured experimentally^[11].

(b) Energies of the excited states of vinylidene and acetylene, calculated using Multi-Reference Configuration Interaction wavefunctions^[191,202].

Figure 8.4: Energies for various ground and excited states of vinylidene and acetylene, determined through a combination of experimental results^[11] and *ab-initio* calculations^[191,202].

8.2.1 Vibrational levels

The vibrational structure of the vinylidene isomer is analysed by employing symmetry considerations combined with *ab-initio* calculations. As discussed in section 2.1.4, the symmetry of the 6 (3N-6) vibrational modes may be determined by using the character table for the correct point group of the target molecule. The C_{2v} character table, including the number of reducible representations for each symmetry element when applied to H_2CC , is presented in Table 8.1.

Table 8.1: Character table of the C_{2v} point group. Γ_{red} for each symmetry element as applied to H_2CC is also included.

C_{2v}	E	$C_2(z)$	$\sigma(xz)$	$\sigma(yz)$	
A_1	1	1	1	1	z
A_2	1	1	-1	-1	R_z
B_1	1	-1	1	-1	x, R_y
B_2	1	-1	-1	1	y, R_x
No. Stationary Atoms	4	2	2	4	
Character Contribution	3	-1	1	1	
Γ_{red}	12	-2	2	4	

Following the same procedure as outlined in section 2.1.4, the number of irreducible

representation may be calculated,

$$\Gamma_{\text{irrep}} = 3A_1 + B_1 + 2B_2$$

Only the three totally symmetric A_1 vibrational modes will be active in the photo-electron spectrum, with the antisymmetric B_1 and $2 \times B_2$ modes forbidden. The vectors depicting these normal modes, along with their corresponding vibrational frequency, may be computed through *ab-initio* methods using quantum chemistry code. Coupled cluster CCSD(T) calculations with a cc-pVTZ basis were computed in this work using NWChem^[94] software, with the resulting normal mode vectors displayed in Fig. 8.5, with the frequencies listed in Table 10.3 at the end of chapter 10.

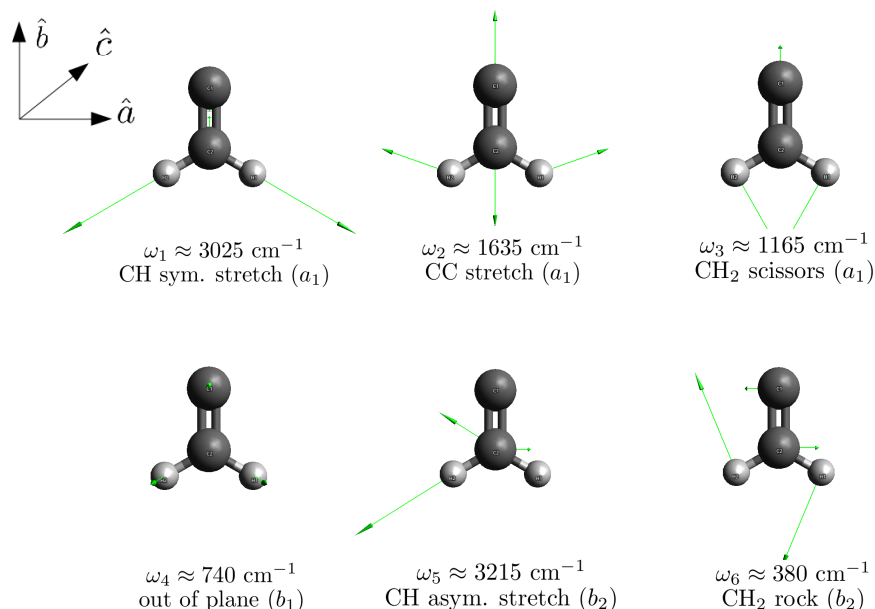


Figure 8.5: Normal mode vectors of the vibrational modes of H_2CC calculated at the CCSD(T) cc-pVTZ level of theory.

Rotational constants of $\text{H}_2\text{CC} \tilde{X}^1A_1$ and $\text{H}_2\text{CC}^- \tilde{X}^2B_2$ were also calculated from the CCSD(T) geometries, as shown in Table 10.3. In both the neutral and anion ground state geometries $A > B \approx C$, so most of the rotational energy is distributed around the principle a axis along the C=C double bond. While vinylidene is strictly an asymmetric top, as $A \gg B \approx C$ it may be treated as a near prolate symmetric top.

Table 10.3 compares these calculated geometric and energetic constants to values from the literature^[11,189,198]. Experimental values, measured in this work (in chapter 10) and in previous experimental studies^[11,193] are also listed here. By determining the rovibrational symmetry structure of vinylidene, a foundation is formed from which we may now delve into the finer complexities of this interesting molecule.

The other side of the barrier: Acetylene

To understand the dynamics of the vinylidene isomer, the acetylene molecule on the other side of the barrier also needs to be investigated. Acetylene is of particular interest to physical chemists as it is a polyatomic molecule small enough for detailed calculations to be computed, while still displaying interesting physics due to the large depth of its potential well. Vibrational eigenfunctions of polyatomics at high, chemically relevant energies, are of significant interest to chemists wanting to understand molecular dynamics at reaction doorways^[203,204]. As such, the energetic structure of acetylene has been the key focus of a large number of experimental and theoretical studies^[39,205]. This chapter discusses the vibrational structure of the acetylene molecule at both low and high energies, giving an introduction to polyad structure and local modes, which will become vital in determining doorway states through which the vinylidene-acetylene isomerisation may proceed.

9.1 An introduction to polyads

The ground $\tilde{X}^1\Sigma_g^+$ state of acetylene is linear, belonging to the $D_{\infty h}$ point group. For the other molecules studied in this thesis, the symmetry of the 6(3N-6) vibrational normal modes are determined by using the correct character table. However, $D_{\infty h}$ is a non Abelian point group, with an infinite number of irreducible representations. Therefore, the symmetry of the vibrational levels is best determined from the observed shape of the normal mode motion. A linear molecule, acetylene will have one less normal mode than the non-linear vinylidene isomer, with the 5 normal mode vectors shown in Fig. 9.1.

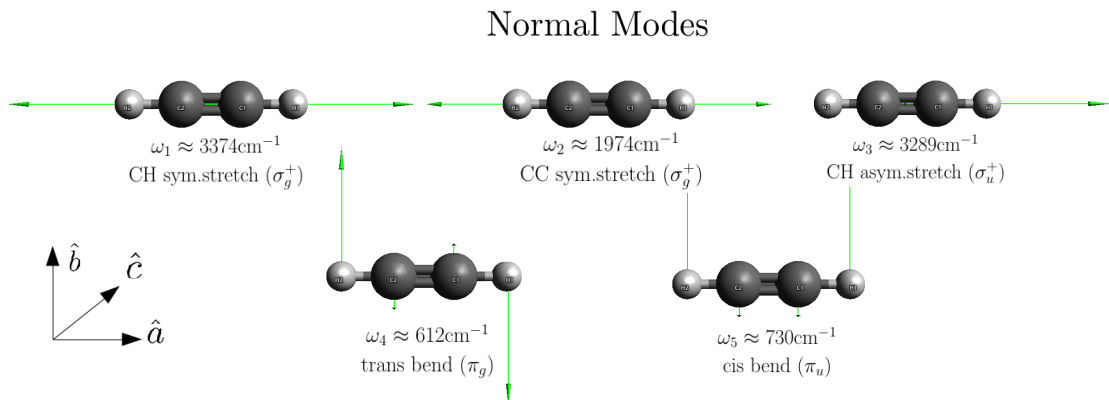


Figure 9.1: Normal mode vectors for $\tilde{X}^1\Sigma_g^+$ HCCH calculated at the CCSD(T) level of theory using NWChem software. Vibrational frequencies are determined from experimental measurements of Field *et al.*^[206]

Fig. 9.1 shows that acetylene has three stretching vibrational modes; two symmetric (σ_g^+), one antisymmetric (σ_u^+), and two bending modes with a trans bend (π_g) and a cis

bend (π_u). Near the bottom of the potential well, the vibrational motion of acetylene may be readily assigned to combinations of these normal vibrational modes. However, at higher energies, the dense quantity of vibrational states can prove problematic, with large quanta of excitation in multiple vibrational modes to deal with. To account for this polyad notation is introduced, where vibrational modes that posses similar behaviour are grouped together in blocks of the effective Hamiltonian.

The polyad quantum numbers in acetylene are defined as,

$$\begin{aligned} N_{\text{res}} &= 5v_1 + 3v_2 + 5v_3 + v_4 + v_5, \\ N_s &= v_1 + v_2 + v_3, \\ \ell &= \ell_4 + \ell_5, \end{aligned}$$

where N_s represents the total quanta of stretching excitation, and ℓ represents the total vibrational angular momentum. N_{res} reflects the approximate ratios among the normal mode frequencies, which represents a restriction that only states with similar zero-order energy may interact^[203]. An important subset of polyads that have been observed experimentally are pure bending polyads, where all of the vibrational excitation is in bending modes with no stretching excitation,

$$\begin{aligned} N_s &= 0 \\ \therefore N_{\text{res}} &= v_4 + v_5 = N_b, \end{aligned}$$

where N_b is the quanta of bending excitation. These polyads have been observed experimentally for $6 \leq N_b \leq 22$, with 31 observed spectral lines in the dispersed fluorescence spectrum of acetylene assigned to pure-bending polyad levels^[207,208].

A pure bending polyad may be uniquely described by the quanta of bending excitation N_b , the vibrational angular momentum ℓ , the parity label g/u and symmetry label +/-, using the notation,

$$[N_b, \ell]^{g+}.$$

Each polyad contains a number of zero-order states, eigenfunctions of the individual system, which may be described by,

$$|v_4^{\ell_4}, v_5^{\ell_5}\rangle^{g+},$$

where v_4 and v_5 are the quanta of excitation in the trans-bend and cis-bend modes depicted in Fig. 9.1.

Low energy example

Near the bottom of the potential well, where there are only a few quanta of excitation (say $N_b \leq 8$), we expect the eigenfunctions to be a mixture of the normal modes in Fig. 9.1. For example, the polyad $[4, 0]^{g+}$ will contain 4 zero-order states,

$$[4, 0]^{g+} : \{|4^0, 0^0\rangle^{g+}, |2^0, 2^0\rangle^{g+}, |2^{+2}, 2^{-2}\rangle^{g+}, |0^0, 4^0\rangle^{g+}\}.$$

In the experimental dispersed fluorescence spectrum of acetylene measured by Field *et al.*^[209] 4 lines were observed around $\sim 2600 \text{ cm}^{-1}$, corresponding to the $N_b = 4$ polyad. The lowest energy eigenstate observed in this region was found to have $\sim 99\% |4^0, 0^0\rangle^{g+}$

character (pure trans-bending state) whereas the highest energy eigenstate has $\sim 99\%$ $|0^0, 4^0\rangle^{g+}$ character (pure cis-bending state).

The two intermediate energy eigenstates were found to be mixtures of the $|2^0, 2^0\rangle^{g+}$ and $|2^{+2}, 2^{-2}\rangle^{g+}$ zero-order states. This mixing occurs due to vibrational ℓ -resonance coupling, which couples states that satisfy $v_4 = v_5$ and $\Delta\ell_4 = -\Delta\ell_5 = 2$. Another common form of mixing occurs for states where $\Delta v_4 = -\Delta v_5 = 2$ via Darling-Dennison coupling^[210,211].

27 other spectral lines of the acetylene dispersed fluorescence spectrum were assigned to pure bending polyads in a similar fashion^[207]. By breaking a large problem into small blocks using polyad notation, complex molecular vibrational spectra may be systematically decoded, which proves to be especially helpful at high excitation energies.

9.2 Local mode large amplitude motion

Typically molecular vibrational motion may be described by a set of normal mode vectors, which may be used to assign observed vibrational transitions in molecular spectra. However, in moving up a potential well to higher excitation energies, successive vibrational levels get closer together due to effect of anharmonicity, creating a dense manifold of states. At high energies, more quanta of excitation allows for more complex combinations of zero-order states to occur. This is further complicated by the presence of various coupling methods, introducing multiple non-diagonal terms to the effective Hamiltonian. Consequently, the molecular motion becomes chaotic, and nearly impossible to assign^[203].

The transition into complex motion occurs about $\sim 8,000 \text{ cm}^{-1}$ above the well minimum. At $10,000 \text{ cm}^{-1}$, corresponding to 14-16 quanta of excitation, attempts to assign the observed motion totally break down, with chaos gradually increasing in prominence^[212]. However, an extraordinary observation was made when continuing to move up the potential well. Above $\sim 11,000 \text{ cm}^{-1}$, the molecular motion again begins to exhibit well defined shapes and nodal coordinates, similar to the low energy regime^[206,213].

This is a surprising result: the addition of vibrational excitation energy seems to transform the molecule motion from a chaotic system to a set of well defined large amplitude motions. Observing well defined behaviour, for states which are described by a complex combination of coupled zero-order states, suggests that the normal mode vectors in Fig. 9.1 no longer provide a good basis for the motion at high energy. Therefore, we need to develop a coordinate transformation, to better describe the large amplitude motion in a more appropriate coordinate set.

High energy example

To explore this high energy large amplitude motion, we will examine the polyad $[22, 0]^{g+}$ representing 22 quanta of bending excitation, corresponding to $\sim 15,000 \text{ cm}^{-1}$ above the well minimum. This pure bending polyad contains 42 zero order states, compared to 4 zero order states for the $[4, 0]^{g+}$ polyad, with much larger off-diagonal coupling elements due to their harmonic oscillator scaling properties^[207]. Furthermore, at high energy the zero-order states do not cluster in the same fashion they did near the bottom of the well; while the pure cis-bending eigenstate $|0^0, 22^0\rangle^{g+}$ remains the highest energy level within the polyad, the pure trans-bending eigenstate $|22^0, 0^0\rangle^{g+}$ is now also near the top of the polyad, not the bottom.

The reason for this is that the trans-bend mode has a positive anharmonicity, opposite in sign to the cis-bend mode. In fact, at high N_b the pure cis-bend and pure trans-bend

eigenstates become near isoenergetic. Consequently, the majority of eigenstates may only be described by a complicated superposition of many normal mode eigenstates, despite the observed simplicity of the motion for a large number of the eigenstates.

Probability densities plotted for the lowest eigenstate in the $[22, 0]^{g+}$ polyad by Field *et al.* in Fig. 9.2 (a), with the distribution centred around the torsional coordinate $\Phi_{45} = 0$, corresponding to in-plane motion, with a nodal line along the $\rho_4 = \rho_5$ normal mode radial coordinates^[203]. This may be interpreted classically as simultaneously exciting both the cis and trans bending motions with equal amplitude, which would result in a local bending motion where only one of the hydrogens executes an in-plane bending motion, while the other hydrogen remains stationary. These local bender states are observed in nearly degenerate g/u pairs, as quantum mechanically the bending motion of the two equivalent hydrogens should be indistinguishable.

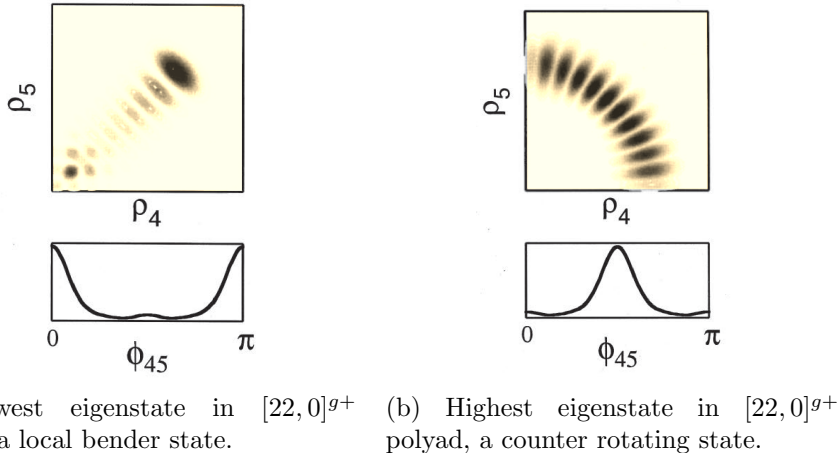


Figure 9.2: Probability densities of the lowest and highest eigenstates in the $[22, 0]^{g+}$ pure bending polyad of acetylene, as calculated by Jacobson *et al.*^[203]

Probability densities were also plotted for the highest energy eigenstate within the polyad in Fig. 9.2 (b), which exhibit a very different behaviour to the local-bender motion observed at the bottom of the polyad. For this eigenstate, the distribution is centred around the torsional coordinate $\Phi_{45} = \pi/2$, with very low density around $\rho_4 = \rho_5 = 0$ suggesting that the molecule never passes through the linear configuration. However, as the nodal line follows $\sqrt{\rho_4^2 + \rho_5^2} = C$ with density at $\rho_4 = 0, \rho_5 \neq 0$ (and $\rho_5 = 0, \rho_4 \neq 0$), the motion does pass through the trans and cis planar geometries. This corresponds to a molecular motion where the two hydrogens are executing an internal rotation, while maintaining a given angle with respect to the CC axis. As total vibrational angular momentum must be conserved the two hydrogens must rotate in the opposite direction, so we can identify this high energy eigenstate as a counter rotating mode. Unlike local bender modes, which appear in g/u pairs, the counter rotating modes are observed in pairs with opposite g/u symmetry and opposite $+/-$ parity. Quantum mechanically this is because the two equivalent hydrogens are rotating in different directions (clockwise/anticlockwise), and therefore have counter-rotating states which should be indistinguishable. The motion of the local bender and counter rotating local modes are depicted in Fig. 9.3.



(a) Local bender mode, with one hydrogen bending in-plane.
(b) Counter rotating mode, with hydrogens rotating in opposite directions.

Figure 9.3: Depictions of the local modes present in highly vibrationally excited acetylene. Despite the high internal energy, molecule motion is well behaved, with well defined nodal coordinates.

9.2.1 Transforming to local-mode coordinates

We have seen from our examination of the $[22,0]^{g+}$ polyad that eigenstates of vibrationally excited acetylene possess well defined shapes and nodal coordinates, despite requiring a complex combination of coupled normal mode states to describe them. Consequently, this suggests that the vibrationally excited eigenstates may be better described in terms of a combination of local modes (local bender + counter rotating) rather than the normal modes used at low energies. Essentially this requires a coordinate transformation from $(\rho_4, \rho_5, \Phi_{45})$, where ρ_4 and ρ_5 are the normal mode radial coordinates in Fig. 9.1, to a new set $(\rho_A, \rho_B, \Phi_{AB})$, where ρ_A and ρ_B are defined as the symmetric and antisymmetric combinations of the trans and cis bend vectors. These new coordinates represent the bending motion of the individual hydrogens, while the torsion angle Φ_{AB} represents the angle between the hydrogens, providing a more natural coordinate system to describe the local modes displayed in Fig. 9.3.

We may apply this coordinate transformation to our zero-order eigenstates, to rewrite them in our new coordinate system as $|v_A^{\ell_A}, v_B^{\ell_B}\rangle_L^{g+}$. By plotting the same eigenstates from Fig. 9.2 of the $[22,0]^{g+}$ polyad in the new coordinate system, the highest and lowest eigenstates may be readily assigned to zero-order states in our local mode basis, as shown in Fig. 9.4. This shows that the local bender modes found near the bottom of the polyad may be readily described in our new local-mode coordinate system by the zero order state $|22^0, 0^0\rangle_L$, while the counter rotating modes near the top of the polyad are described by the state $|11^{+11}, 11^{-11}\rangle_L$. This is a much simpler, and more usable description than the corresponding descriptions in the normal mode basis, which allows for the vibrational levels at high energy in the acetylene spectrum to be more readily assigned. The work of Field and co-workers have now assigned multiple acetylene eigenstates using this local mode basis^[203,206–208].

9.3 At the barrier to isomerisation

Now we may turn our attention back towards the vinylidene-acetylene isomerisation barrier, to try and identify what role this local mode motion may have on our isomerisation problem. First, we need to determine where the transition from normal to local modes occurs. For this, we may use the knowledge that local bender modes are observed in near degenerate $g+/u+$ pairs with counter rotating modes in $g+/u-$ pairs, while normal trans/cis modes will be non-degenerate. Therefore, calculating E_{g+} , E_{u+} and E_{u-} at

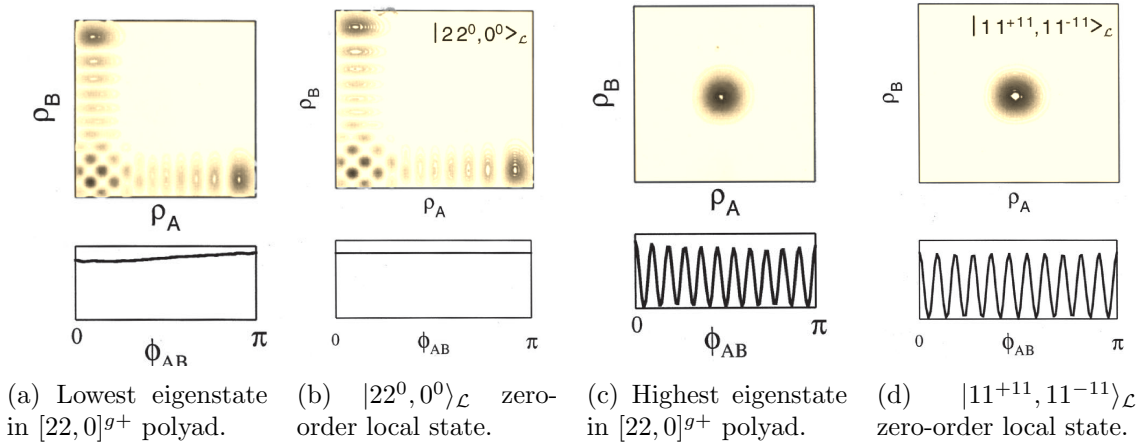


Figure 9.4: Probability densities of the lowest and highest eigenstates in the $[22, 0]^{g+}$ pure bending polyad of acetylene in the new local-mode coordinates, compared to the $|22^0, 0^0\rangle_L$ and $|11^{+11}, 11^{-11}\rangle_L$ zero-order states. In the local-mode coordinates the observed eigenstates may be readily assigned to a simple combination of local-mode zero order states^[203].

various N_b will reveal where the transition to local modes occurs, as shown in Table 9.1.

Table 9.1: Exploring the degeneracy of $g+/u+$ and $g+/u-$ pairs as a function of N_b using energy calculations of Field *et al.*^[203].

N_b	$E_{g+} - E_{u+}$	$E_{g+} - E_{u-}$
10	-10.3	48.1
12	-0.22	25.1
14	-1.7×10^{-4}	5.5
16	4.4×10^{-6}	0.39
18	6.5×10^{-7}	1.5×10^{-2}
20	1.2×10^{-7}	4.1×10^{-4}

From Table 9.1 it can be seen that $g+/u+$ pairs become degenerate at $N_b \sim 12 - 14$, while $g+/u-$ pairs become degenerate at $N_b \sim 16 - 18$. This reveals exactly where the acetylene vibrational levels transform from normal to local mode behaviour. Converting quanta of excitation to energy shows that up to $\sim 8,000 \text{ cm}^{-1}$ acetylene vibrational levels may be described by the normal mode basis, whereas above this level the motion begins to transition into local mode behaviour. Above $\sim 11,000 \text{ cm}^{-1}$ this transition is complete, and acetylene levels may be readily assigned using local mode coordinates. During the transition period ($8,000 - 11,000 \text{ cm}^{-1}$) the motion becomes chaotic, and is an area attracting a lot of research interest as groups try to understand this transition process^[210, 212–214].

The barrier to isomerisation sits $15,000 \text{ cm}^{-1}$ above the well minimum^[53], corresponding to ~ 22 quanta of bending excitation ($N_b \sim 22$). As this is well above the transition from normal to local modes, the vinylidene isomer will interact purely with local modes of acetylene. This is an important factor in explaining the observed lifetime conundrum described in section 8.1.1. From the vector depiction of the local modes in Fig. 9.3 it is clear that the 1-2 hydrogen shift required for acetylene to isomerise with vinylidene will occur through the local-bender modes, not the counter rotating modes. The top of the vinylidene barrier is calculated to coincide with the top of the $[22, 0]^{g+}$ polyad, however

analysis of the $[22,0]^{g+}$ eigenstates showed that the top of the polyad is densely populated by counter rotating modes, with the majority of local-bender modes found near the bottom of the polyad, below the isomerisation barrier. Consequently, despite the presence of a dense manifold of acetylene states at the barrier height, it is predicted that there may only be one or two local bender modes present in the proximity of the vinylidene barrier^[186], as described in Fig 9.5.

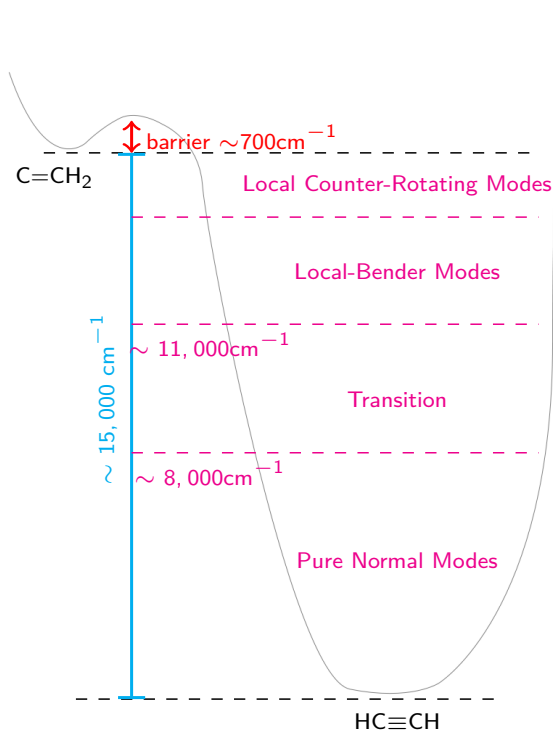


Figure 9.5: Vibrational energy structure of acetylene. Below $8,000 \text{ cm}^{-1}$ normal mode descriptions may be used, however above $11,000 \text{ cm}^{-1}$ eigenstates are best described in local mode coordinates. At the isomerisation barrier the majority of levels will be counter rotating, with only one or two local bender modes present.

The initial picture of vinylidene-acetylene isomerisation that was used to interpret the results of Lineberger^[11] and Vager^[12], was of a vinylidene molecule that tunnelled through a small potential barrier into a dense manifold of acetylene levels, treated as a quasi-continuum. Thereby, the small size of the barrier ($\sim 700 \text{ cm}^{-1}$) suggested the vinylidene isomer would decay irreversibly into linear acetylene, at a possible sub-picosecond rate, seemingly in contradiction to the long-lived vinylidene observed in Coulomb explosion imaging experiments. However, studying the high energy motion of acetylene has revealed that the vibrational modes transition into a local mode regime, where most of the levels near the isomerisation barrier will have counter rotating character. As the isomerisation pathway proceeds along the local bender coordinate, these counter rotating modes are not seen by the vinylidene molecule. Consequently, instead of there being a dense manifold of vibrational states available to vinylidene, only a few local bender levels will be visible for isomerisation. In fact, there are only one or two doorway local-bender states expected to be in proximity of the barrier. This drastically changes the picture from a textbook style bound \leftrightarrow free tunnelling problem, to a more complex bound \leftrightarrow bound problem, setting up the possibility of long-lived eigenstates that are a mix of both vinylidene and local-bender acetylene character. As a result, it is likely that the dynamics will be reversible, periodic

in nature, rather than the irreversible decay that was originally predicted^[53].

This hypothesis would help to explain the lifetime conundrum that arose from the photoelectron and CEI experiments of Lineberger and Vager, as the reversibility of the dynamics would explain the presence of neutral vinylidene 3.5 μs after photodetachment (see section 8.1.1). However, there has been no experimental evidence to date that these long lived vinylidene – acetylene eigenstates exist. The next chapter of this thesis looks at high resolution photoelectron spectra of the vinylidene anion, in an attempt to find evidence that may help prove or disprove this theory.

High resolution photoelectron imaging of vinylidene

Photoelectron spectroscopy of the vinylidene anion appears to be the best approach to search for evidence of the long-lived vinylidene-acetylene eigenstates that were proposed in the preceding chapter. While the resolution of the seminal photoelectron spectrum of Lineberger *et al.*^[11] in Fig. 8.2 was able to resolve much of the vibrational structure, it was insufficient to resolve any information about the isomerisation process. However, high resolution spectra from the HR-PEI spectrometer (described in detail in chapter 3), may help uncover signatures of the isomerisation, including the vinylidene doorway states through which the reaction proceeds.

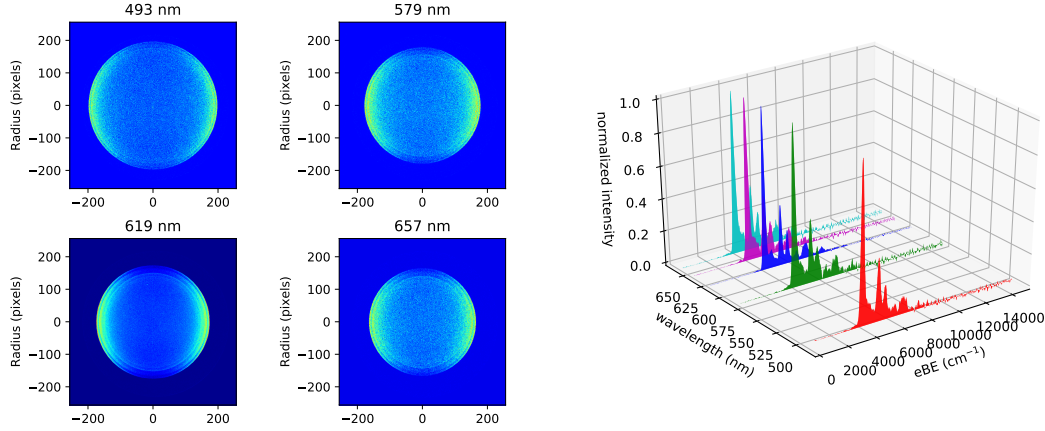
However, for the past 30 years there has not been any progress on the vinylidene problem, with the 1989 measurement by Lineberger still considered state of the art, despite several attempts to remeasure the vinylidene spectrum^[53,189]. One of the major reasons for this is that the vinylidene anion is difficult to produce. Furthermore, the anion source temperature has a large impact on the outcome of a measurement, with rotationally cold vinylidene required (as will be discussed later in this chapter). Various different vinylidene production methods were designed and implemented throughout this work, as described in detail in section 3.2, which lead to the recording of several high resolution photoelectron spectra of the vinylidene anion at a range of detachment wavelengths. These results, including observation of isomerisation signatures, are discussed here.

10.1 Photoelectron spectra of vinylidene

Before any spectra may be measured, an efficient anion production recipe needs to be developed. Multiple different methods were trialled, involving various gas composition mixtures and pressures, as well as variations (electrical and mechanical) to the high voltage discharge source. However, vinylidene ion production turned out to be very limited, with photoelectron counts less than $\sim 1e^-$ per laser shot, immensely limiting the resolution that could be achieved due to signal to noise issues. Eventually, after a full refurbishment of the pulsed jet discharge source, optimal operating conditions were discovered capable of vastly improving the vinylidene ion (and corresponding photoelectron) signal, achieving yields of $\sim 20 e^-/\text{shot}$.

With this improved count rate, a number of spectra were measured at a range of detachment wavelengths from 494 nm up to 657 nm, with a selection of the raw velocity-mapped images presented in Fig. 10.1, along with their corresponding photoelectron spectra. Obtaining the best possible resolution, requires balancing of multiple influences. A well known characteristic of velocity map imaging lenses is that the imaging resolution depends on the kinetic energy of the target particle, with $\Delta E \propto E$, resulting in higher resolution at longer detachment wavelengths. However, the characteristics of the Sunlite Ex Optical Parametric Oscillator (the tuneable photon source) make the laser output power wavelength dependent, with maximum powers typically achieved around 550 nm. Optimal

operating conditions were achieved at a detachment wavelength of 619 nm, where the laser power at the experiment averaged ~ 20 mJ/pulse, producing a high electron count rate. At wavelengths longer than 620 nm, the laser power quickly dropped off, reducing down to ~ 5 mJ/pulse by 640 nm.



(a) Raw velocity-mapped images of H_2CC^- photodetachment at 493, 578, 619, and 657 nm. The best signal to noise ratio is visibly achieved at 619 nm (bottom-left quadrant).

(b) Photoelectron spectra of H_2CC^- photodetachment at a range of wavelengths from 549–657 nm. Best resolution is achieved in the 619 nm measurement.

Figure 10.1: High resolution photoelectron imaging spectra of the vinylidene anion, measured over a range of detachment wavelengths.

The best spectrum from Fig. 10.1 consists of 7,400,649 photoelectrons, detected at an average rate of $21e^-/\text{shot}$, at a detachment wavelength 619 nm. As the photodetachment events observed on the detector are recorded using a sub-pixel centroiding algorithm in real-time, as discussed in chapter 3, the binned file may be read into an image of arbitrary pixel size. Larger image sizes provide more detail (resolution), at the expense of greater statistical uncertainty in individual pixel intensities. Therefore, measurements with larger photoelectron counts may be analysed using a larger image size, producing the best resolution spectra. A 2048×2048 image (cf. 512×512 image size used in Fig. 10.1) of the detachment at 618.950 nm was analysed, producing the photoelectron spectrum shown in Fig. 10.2. This spectrum resolves vibrational structure of the transient vinylidene neutral, and has an appearance similar to Lineberger's measurement (shown in Fig. 8.2), with the observed peaks assigned to the normal modes calculated in Fig. 8.5. Surprisingly, 3 of the observed peaks (6_1^1 , 6_0^2 , 6_0^4) have spacings that correspond to the v_6 rock mode, which is antisymmetric (b_2). Under the harmonic oscillator Frank-Condon approximation, transitions between non-totally symmetric modes involving an even quanta of excitation, ie. $\Delta v_6 = 2$, may be allowed, but are usually very weak. The observation of relatively strong transitions in the v_6 mode in Fig. 10.2 indicates an unusual vibrational potential along the rock mode coordinate. It is predicted that the vinylidene-acetylene isomerisation coordinate should involve the v_6 mode, which may possibly explain the unusually strong antisymmetric v_6 transitions^[53].

Furthermore, the improved resolution of the photoelectron spectrum in Fig. 10.2, reveals that there are more transitions between the origin 0_0^0 and 3_0^1 peaks than just the 6_0^2 and 6_0^4 peaks identified in Fig. 8.2. Specifically, it looks as if there may be transitions 6_0^1 (* in Fig. 10.2) and 6_0^3 . Transitions involving an odd quanta of excitation in a non-

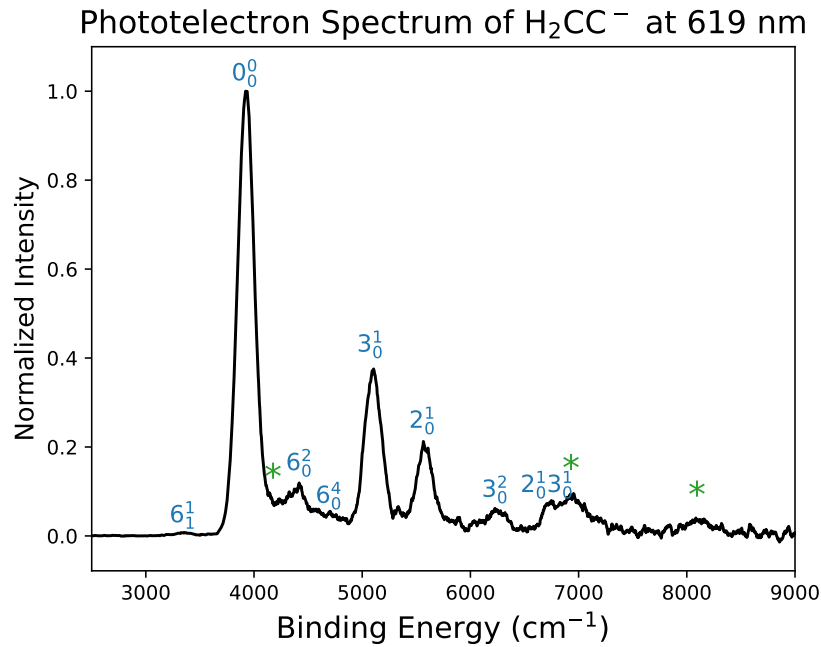


Figure 10.2: Photoelectron spectrum of the vinylidene anion at 619 nm. Observed structure is assigned to the normal modes calculated in Fig. 8.5, however some of the peaks (*) can not be readily assigned to symmetric allowed transitions.

totally symmetric mode, ie. $\Delta v_6 = 1$, are totally forbidden, making their presence in the spectrum surprising. On top of this, there are peaks observed at higher binding energy which also cannot be readily assigned to symmetrically allowed vibrational transitions of the vinylidene molecule. These extra peaks may be tentatively assigned to transitions 5_0^1 and $5_0^1 3_0^1$, however as the v_5 asymmetric stretch mode is also not totally symmetric (b_2), these transitions should also be forbidden in the photoelectron spectrum. The peak at $\sim 7,000 \text{ cm}^{-1}$ could also be assigned to the symmetrically allowed transition 1_0^1 , however as the C–H bond lengths of the anion and neutral differ by less than 0.05 Å, the Franck-Condon intensity of this transition will be extremely small^[198]. It is possible the unexpected structure is linked to the vinylidene-acetylene isomerisation pathway, but it is not yet obvious how those isomerisation signatures are encoded.

10.1.1 Vinylidene photodetachment at 1064 nm

To improve on the resolution of H_2CC^- photodetachment in Fig. 10.2, long wavelength measurements are recorded using the direct output of the Nd:YAG laser fundamental. A high resolution photoelectron image of $\text{H}_2\text{CC}(\tilde{X}^1\text{A}_1) \leftarrow \text{H}_2\text{CC}^-(\tilde{X}^2\text{B}_2)$ photodetachment at 1064 nm is shown in Fig. 10.3, consisting of 10,382,636 electrons from 370,000 laser shots. By moving closer to threshold, a lower repeller voltage of $V_R = -800 \text{ V}$ may be used (cf. $V_R = -2200 \text{ V}$), improving the spatial resolution of electron structure on the detector. The velocity map image shows several clearly defined rings, representing the different vibrational transitions. The outer rings show the characteristic negative anisotropy of detachment from a p orbital, with the photoelectron intensity distributed around the horizontal centre of the image. However, two central rings, corresponding to the forbidden vibrational transitions labelled (*) in the 619 nm PES of Fig. 10.2, are

notably different to the other rings, showing a near perfect isotropic distribution. This is unexpected, given that all of the observed transitions correspond to the same electronic state, involving detachment from the same non-bonding p orbital. This effect is also observed in the H_2CC^- photoelectron spectra measured by Gerardi *et al.*^[215], in a study of Ar-tagged predissociation and vibrationally mediated photodetachment of vinylidene, however the anomalous anisotropy was not commented on by the author.

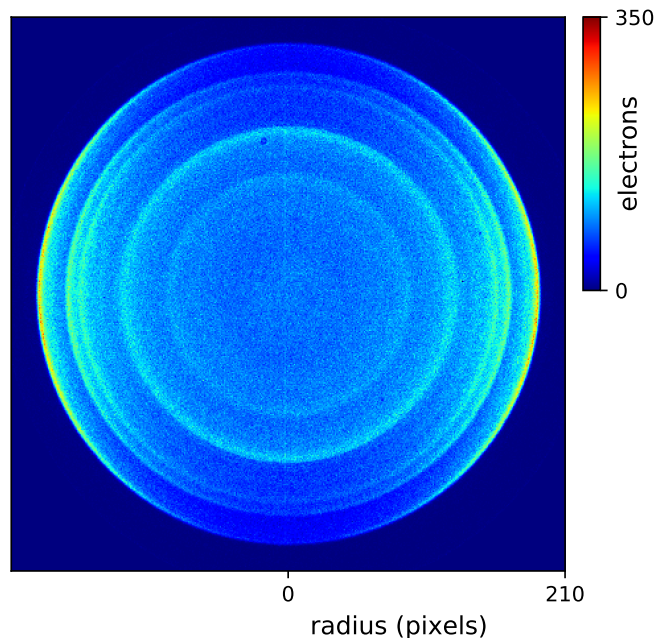


Figure 10.3: Raw velocity-mapped image of $\text{H}_2\text{CC}(\tilde{\chi}^1\text{A}_1) \leftarrow \text{H}_2\text{CC}^-(\tilde{\chi}^2\text{B}_2)$ photodetachment at 1064 nm. The outer rings show the characteristic negative anisotropy of detachment from a p orbital, with the intensity centred at the hemisphere of the image. However the two central rings, corresponding to forbidden vibrational transitions labelled (*) in the 619 nm PES of Fig. 10.2, are clearly distinct to the rest of the image, displaying a more isotropic distribution.

A more quantitative description of this variation may be obtained by plotting the radial distribution of electrons for distinct angular slices, as shown in Fig. 10.4. Each of the angular slices is normalised to the origin peak, with 0 degrees defined as the top of the image, aligned with the laser vertical polarisation, while 90 degrees defines the horizontal. Most of the peaks in the spectrum show a small variation in the relative intensity of each angular slice, which represents moving along the Cooper-Zare curve for detachment from a p orbital. However, the forbidden peaks at 6_0^1 and 5_0^1 show a much larger variation in the angular slices, with the intensity of the $10 - 30^\circ$ slice (pole of the image) many times higher than the $70 - 90^\circ$ slice (hemisphere). This tells us that the β parameters for transitions 6_0^1 and 5_0^1 are significantly more positive than for the origin 0_0^0 transition. This figure is important, as it confirms the positive anisotropy parameter for the 6_0^1 transition, which is often hard to resolve from the dominant origin peak. Consequently, this confirms that the anisotropy jump is a vibrational mode related phenomenon, as opposed to a simple high binding energy effect.

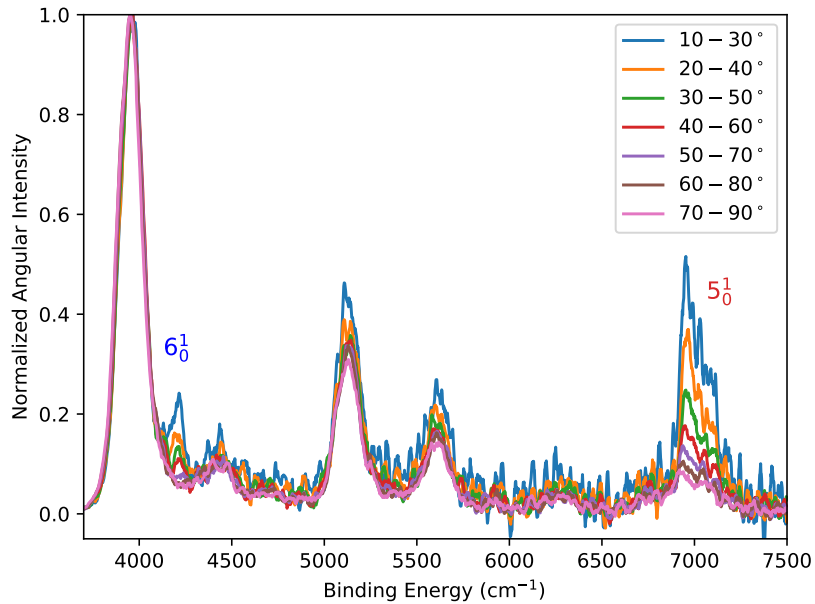


Figure 10.4: Radial distributions of angular slices from the velocity-mapped image (Fig. 10.3) highlight the positive anisotropy of the forbidden modes. Angular slice profiles are normalised to the origin peak, with 0 degrees defined as the top of (a) while 90 degrees represents the horizontal. At the forbidden peaks 6_0^1 and 5_0^1 , the angular slices near the pole of the image (— and —) are dramatically higher than for the rest of the spectrum, illustrating a positive jump in β for these modes.

10.1.2 Rovibrational model of H₂CC

As was shown in the study of NO₂⁻ in chapter 5, we may apply symmetry considerations to model the rotational and vibrational structure of vinylidene. A complete recreation of the experimental photoelectron spectrum may be constructed by combining a rotational band model, to determine the peak contours, with a Franck-Condon analysis of the vibrational transitions.

In the dipole approximation, the intensity of one-electron transitions between two vibrational states is proportional to the square of the electric dipole transition moment,

$$|\langle \Psi'(Q)|\vec{\mu}|\Psi''(Q)\rangle|, \quad (10.1)$$

where Ψ' and Ψ'' are the total wavefunctions of the initial and final state, Q is the nuclear coordinate, and $\vec{\mu}$ is the dipole moment operator. Therefore, the transition intensity will depend on the vibrational wavefunction overlap of the initial and fine state, known as the Franck-Condon factor,

$$|\langle \chi'(Q)|\chi''(Q)\rangle|^2. \quad (10.2)$$

The vibrational motion of a molecule is quantised and constrained along 6(3N-6) normal mode coordinates, with the normal mode vectors of vinylidene depicted in Fig. 8.5. In the harmonic approximation, vibrational wavefunctions are products of one dimensional harmonic oscillators, where each harmonic potential lies along one of these normal mode coordinates Q . By orthogonality conditions of the normal mode vectors, the multidimen-

sional Franck-Condon factors may be expressed as simple products of one dimensional overlaps,

$$\langle \chi'(Q) | \chi''(Q) \rangle = \langle \chi'_1(Q_1) | \chi''_1(Q_1) \rangle \cdot \langle \chi'_2(Q_2) | \chi''_2(Q_2) \rangle \dots \quad (10.3)$$

where Q_n represent the n normal mode coordinates. This reduces a multidimensional problem to a series of simple one dimensional calculations.

Normal mode vectors of the vinylidene neutral and anionic molecules were computed using NWChem software^[94] using the gold-standard CCSD(T) approach. EzSpectrum software^[216] is then able to produce harmonic potentials along the calculated coordinates, allowing for the Franck-Condon factors (Eq. 10.2) to be computed. This provides an estimate for the vibrational transition intensities measured in the experimental photoelectron spectrum, based from purely *ab-initio* methods. The Franck-Condon Factors (FCF) calculated for symmetrically allowed $\text{H}_2\text{CC}(\tilde{X}^1\text{A}_1) \leftarrow \text{H}_2\text{CC}^-(\tilde{X}^2\text{B}_2)$ vibrational transitions are listed in Table 10.1. Note that the Franck-Condon factor for the v_1 CH stretch mode is expected to be very small, as the C–H bond lengths of the anion and neutral differ by less than 0.05 Å^[198].

Table 10.1: Franck-Condon factors calculated using NWChem^[94] and ezSpectrum^[216] software, for the symmetrically allowed $\text{H}_2\text{CC}(\tilde{X}^1\text{A}_1) \leftarrow \text{H}_2\text{CC}^-(\tilde{X}^2\text{B}_2)$ vibrational transitions.

Transition	FCF
0^0	0.56599
6^2	0.14226
6^4	0.04379
3^1	0.32282
2^1	0.19722
3^2	0.11580
$2^1 3^1$	0.11248
1^1	~ 0

Next, rotational band contours need to be determined for convolution with the vibrational transition intensities calculated above. The rotational constants for vinylidene were calculated from the equilibrium geometries, and are presented in Table 10.3. While vinylidene has three distinct rotational constants, technically making it an asymmetric top, as $A \gg B \approx C$ it may be treated as a near prolate symmetric top. Furthermore, like NO_2 , vinylidene has C_{2v} symmetry, which allows for the relevant selection rules to be determined using the same method used in chapter 5.

As was discussed previously, it has been shown that for a planar C_{2v} molecules, such as H_2CC , the symmetry of consecutive rotational levels follows a distinct pattern^[103],

- C_2^a : Lowest energy level (τ_{-J}) = +,
then consecutive levels up are $-,-,+,-,-,\dots$
- C_2^c : Highest energy level (τ_{+J}) = +,
then consecutive levels down are $-,-,+,-,-,\dots$

where + and – refers to the molecule being symmetric or antisymmetric under a 180 degree rotation around the a and c rotational axes. Unlike NO_2 , where the symmetry line was along the intermediate b axis, the symmetry line in H_2CC lies along the primary

rotational axis a . Therefore, the overall symmetry of a rotational level is defined by C_2^a , with the lowest τ_{-J} level symmetric for all J , followed by two asymmetric levels, two symmetric levels, and so on (see Fig. 5.6, looking at label under C_2^a).

When a molecule has two identical nuclei which are symmetric with respect to the symmetry line of the molecule, the statistical weightings of symmetric : antisymmetric rotational levels is determined by the spin of these nuclei. The hydrogens in H₂CC have nuclear spin of 1/2, which corresponds to a 3:1 weighting of antisymmetric:symmetric levels. Furthermore, only transitions that follow the correct selection rules may be observed. For a molecule with a dipole transition moment and C_{2v} symmetry line along the principle a axis, allowed transitions must follow^[102,104]

$$\Delta J = 0, \pm 1,$$

$$++ \leftrightarrow -+ \quad \text{and} \quad + - \leftrightarrow --.$$

Finally, line intensities and positions may be calculated. Applying the near prolate symmetric top approximation, the energy of a rotational level can be defined by two quantum numbers J and K , along with the rotational constants listed in Table 10.3, using the equation

$$E(J,K) = \frac{1}{2}(B+C)J(J+1) + (A - \frac{1}{2}(B+C))K^2. \quad (10.4)$$

The relative intensity of each H₂CC(\tilde{X}^1A_1) \leftarrow H₂CC⁻(\tilde{X}^2B_2) rotational transition is given by,

$$I \propto \langle \psi' | \vec{\mu} | \psi'' \rangle \times \langle \chi'(Q) | \chi''(Q) \rangle \times A_{J,K} \times g_{J,K} \times e^{(-Ehc/kT)}, \quad (10.5)$$

where $\langle \psi' | \vec{\mu} | \psi'' \rangle$ is the electronic dipole moment, $\langle \chi'(Q) | \chi''(Q) \rangle$ is the vibrational Franck-Condon factor (Eq. 10.2), $A_{J,K}$ is the rotational transition moment (see Eq. 5.6), $g_{J,K}$ is the degeneracy of the rotational level, and $e^{(-Ehc/kT)}$ is the Boltzmann factor for the anion. By combining all of the above information, including the rotational selection rules and Franck-Condon factors from Table 10.1, a total recreation fo the vinylidene photo-electron spectrum may be constructed using PGOPHER spectroscopy software^[217]. The resulting rovibrational model is presented in Fig. 10.5, alongside the experimental 1064 nm photoelectron spectrum of H₂CC⁻, constructed from the velocity map image in Fig. 10.3.

As can be seen in Fig. 10.5, the rovibrational model successfully recreates the experimental spectrum. In particular, the calculated Franck-Condon factors (Table 10.1) appear to be in great agreement with the experimentally observed transition intensities. Importantly, as the model only includes symmetrically allowed modes (transition 6_0^2 is included as antisymmetric modes involving an even quanta of vibrations may be allowed, but typically at very small intensities), discrepancies between the measured spectrum and the model highlight the presence of structure that is forbidden. Additional peak intensity is observed in between the origin 0_0^0 and 3_0^1 peaks, that is assigned to the forbidden transitions 6_0^1 and 6_0^3 . Likewise, the additional peaks at $\sim 7,000\text{ cm}^{-1}$ and $\sim 8,000\text{ cm}^{-1}$ are assigned to the forbidden transitions 5_0^1 and $5_0^13_0^1$.

10.2 Anomalous anisotropy parameters

To investigate the origin of the forbidden transitions 6_0^1 , 6_0^3 , 5_0^1 , and $5_0^13_0^1$, and the corresponding anomalous anisotropy observed in the velocity map image in Fig. 10.3, the

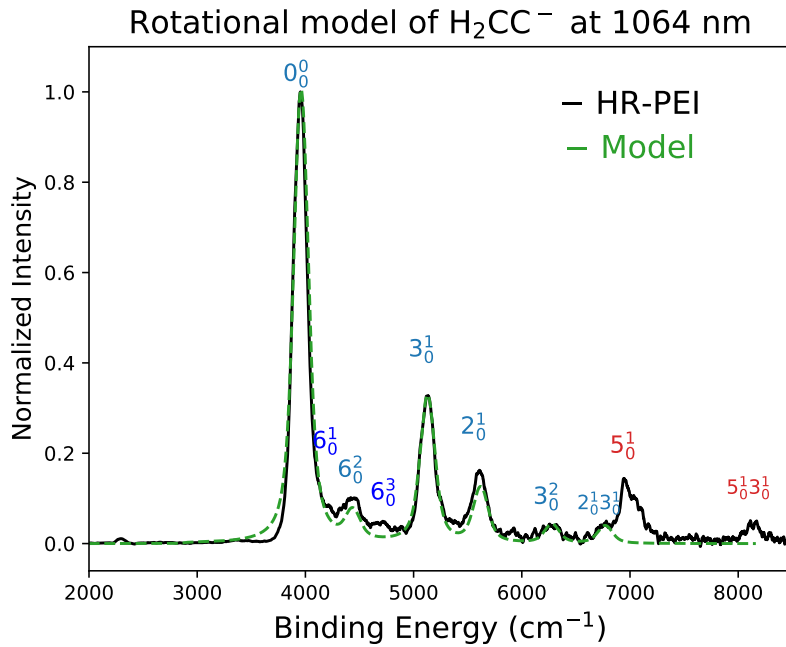


Figure 10.5: Experimental photoelectron spectrum of vinylidene at 1064 nm (—), compared to a full rovibrational model (---) constructed using a combination of NWChem, ezSpectrum, and PGOPHER software (see text for details).

angular distribution of the photoelectrons may be examined. The angular distribution of photoelectrons is typically not isotropic, with the anisotropy of the distribution (quantified by the parameter β), dependent on the character of the parent anion molecular orbital.

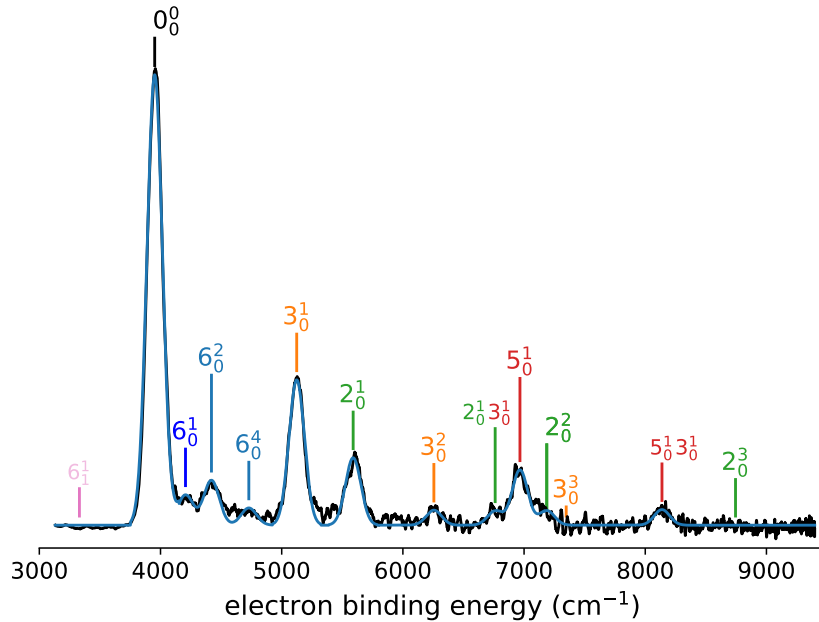
The anisotropy parameter β , defined in Eq. (2.38), may vary from -1 to $+2$, corresponding to an electron distribution centred at the equator or the poles of the velocity-mapped image respectively. As has been shown previously, the kinetic energy dependence of β may be described by the interference of the relevant partial waves. Therefore, measuring the anisotropy curve over a range of energies may provide a fingerprint for the character of the orbital from which the electron was detached.

From the hybrid-orbital diagram of vinylidene in Fig. 8.3, we can see that the outermost electron in \tilde{X}^2B_2 H_2CC^- resides in a non-bonding p orbital. When the electron absorbs a photon and is detached, conservation of angular momentum demands that the outgoing electron must have angular momentum of $\Delta\ell = \pm 1$, corresponding in this case to an s and a d partial wave. Therefore, the energy dependence of the anisotropy parameter will be governed by the Cooper-Zare equation (Eq. 2.37) for $\ell = 1$. Introducing Hanstorp coefficients, this becomes

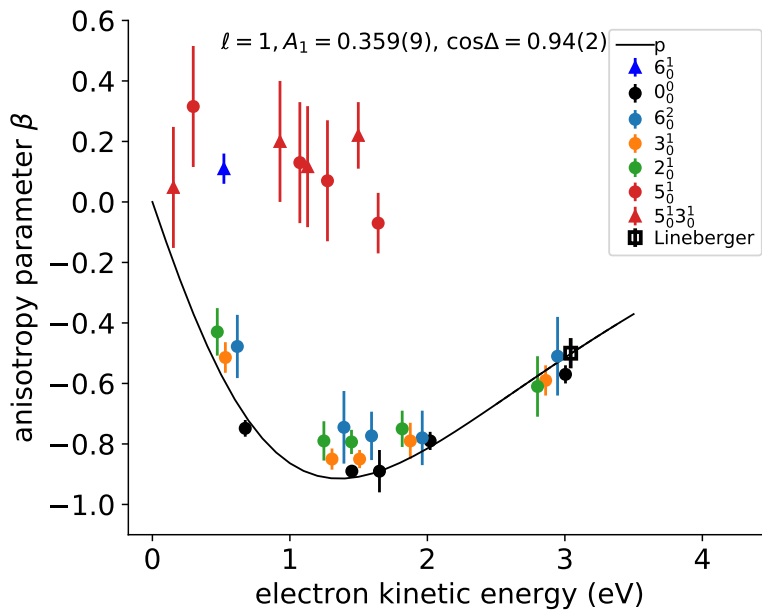
$$\beta_p = \frac{2A_1^2\epsilon^2 - 4A_1\epsilon \cos \Delta\ell_{\pm 1}}{1 + 2A_1^2\epsilon^2}, \quad \text{where } A_1 = \frac{1}{\epsilon^2} \frac{\chi_{1,2}^2}{\chi_{1,0}^2}. \quad (10.6)$$

Eq. (10.6) illustrates explicitly how the anisotropy parameter β will vary with electron kinetic energy. Close to threshold the s partial wave will dominate the detachment, giving $\beta \sim 0$. However as the kinetic energy of the detached electrons increases, the d partial wave begins to have a larger influence, with β eventually heading toward $+1$ for very high energies.

Anisotropy parameters from $\text{H}_2\text{CC}(\tilde{X}\ ^1\text{A}_1) \leftarrow \text{H}_2\text{CC}^-(\tilde{X}\ ^2\text{B}_2)$ photodetachment were measured at a range of wavelengths (355 – 1064 nm), with the results plotted in Fig. 10.6.



(a) High resolution photoelectron spectrum of vinylidene at 1064 nm, from 1 million photoelectrons. Spectrum shows signatures of the forbidden modes 5_0^1 , $5_0^1 3_0^1$ and 6_0^1 .



(b) Anisotropy parameters of vinylidene photodetachment, measured at a range of wavelengths (355 – 1064 nm), with colours corresponding to vibrational transitions in (a). All of the symmetrically allowed modes follow the Cooper-Zare expression for p orbital detachment (Eq. 10.6). However the symmetrically forbidden modes 5_0^1 , $5_0^1 3_0^1$ and 6_0^1 exhibit a very different behaviour, with $\beta \sim 0$.

Figure 10.6: The H_2CC^- photoelectron spectrum (a) with signatures of symmetrically forbidden transitions. These forbidden transitions appear to have an isotropic angular distribution (b), very different to the β parameters measured for the allowed modes.

The corresponding photoelectron spectrum at 1064 nm is given in Fig. 10.6 (a), with assigned vibrational transitions colour coded to match the anisotropy parameters plotted in (b). A Cooper-Zare p model (Eq. 10.6) is fitted to the symmetrically allowed v_2 , and v_3 transitions, giving a Hamstorp coefficient of $A_1 = 0.359(9)$ eV $^{-2}$ and a partial wave phase shift of $\cos \Delta = 0.94(2)$. This provides insight into the structure of the parent non-bonding p orbital.

However, while all of the allowed transitions follow the p -orbital curve, with negative anisotropy parameters ranging from -0.4 to -0.8 , all of the forbidden mode transitions (shown in red and blue in Fig. 10.6) recorded a positive, near isotropic distribution, with β values of 0 to $\sim +0.3$. A small variation in the anisotropy parameter may be observed between different vibrational levels, as was shown by Van Duzor *et al.*^[65] in a high resolution study of O₂, however these variations are typically smaller than ~ 0.1 , making this a negligible effect in most photoelectron experiments.

The angular slice spectra presented in Fig. 10.4 confirm that a positive anisotropy parameter is also observed for the 6_0^1 transition, implying that this jump in β is vibrational mode dependent, and not merely a slow electron or high binding energy effect. Furthermore, this work shows that the anisotropy change is associated exclusively with forbidden vibrational transitions. Therefore, the anisotropy anomaly suggests that potential character mixing between electronic states may be responsible for the appearance of the forbidden transitions. One possibility is the presence of a vibronic coupling mechanism between vinylidene electronic states, as will be explored in more detail in chapter 11.

10.3 Excited states of vinylidene

The large change in the anisotropy of the forbidden transitions suggests that there may be some level of character mixing within the parent molecular orbital. To investigate this possibility, the excited states of neutral vinylidene (see Fig. 8.4) were investigated. To access higher electronic states of the neutral vinylidene molecule, the third harmonic of the direct Nd:YAG output was used as the detachment laser. This provides a high power (~ 40 mJ/pulse), short wavelength (355 nm), photon source for probing high energy H₂CC structure. The resulting photoelectron spectrum is presented in Fig. 10.7.

Recent computational work has confirmed the relative energies of the first few excited states of vinylidene^[191], as shown in the energy diagram inserted in Fig. 10.7. The first 4 excited states have been observed experimentally in photoelectron spectroscopy work of the Neumark group^[191,218], which has been carried out in collaboration with the work presented in this thesis. Consequently, the observed structure in Fig. 10.7 may be assigned to the ground \tilde{X}^1A_1 state as well as the \tilde{a}^3B_2 , \tilde{b}^3A_2 , and \tilde{A}^1A_2 excited states. Interestingly, in the ANU PES an additional peak in Fig. 10.7 (*) was observed at $\sim 24,000$ cm $^{-1}$ (~ 3 eV) which could not be assigned to any of the known excited state structure of vinylidene, and is not present in the previously published work of DeVine *et al.*^[191].

10.3.1 Vinylidene photofragmentation

One possible explanation for the observation of the peak (*) in Fig. 10.7 may be the presence of photofragmentation. With a shorter detachment wavelength of 355 nm, the high photon energy ($h\nu = 3.5$ eV) may open fragmentation channels that were closed in the longer wavelength 1064 nm measurements. During the course of this work, many

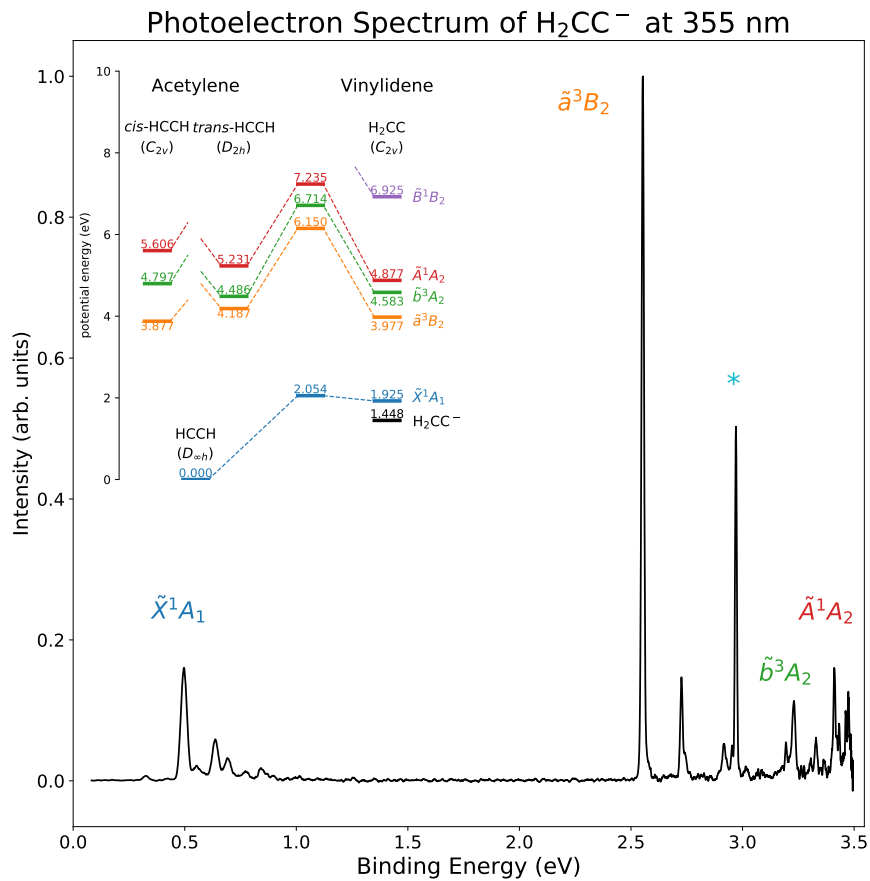
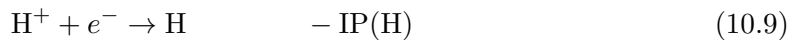
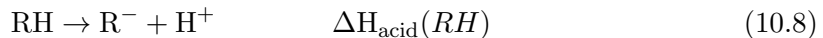


Figure 10.7: Photoelectron spectrum of H_2CC at 355 nm, accessing the ground $\tilde{X}^1\text{A}_1$ state as well as the three lowest lying excited states $\tilde{a}^3\text{B}_2$, $\tilde{b}^3\text{A}_2$, and $\tilde{A}^1\text{A}_2$. An energy level diagram, with positions calculated at the ic-MRCI-F12 level by DeVine *et al.*^[191], is inserted in the top left corner. An additional peak (*) is observed, which is not assigned to an excited state of vinylidene.

molecules similar in nature to H_2CC were also measured, including C_2 and C_2H , as will be discussed in detail in chapter 12.

To assess what channels will be open at $h\nu = 3.5$ eV, dissociation energies may be calculated. First we will look at removing one hydrogen from vinylidene, calculating $D_0(\text{C}_2\text{H}\cdots\text{H})$ of the neutral using a thermodynamic cycle,



Applying this method to neutral vinylidene, taking thermodynamic values from the liter-

ature^[219] gives,

$$\begin{aligned} D_0(C_2H \cdots H) &= EA(C_2H) + \Delta H_{\text{acid}}(C_2H_2) - IP(H) \\ &= 68 + 330 - 313 = 85 \text{ kcal/mol.} \end{aligned} \quad (10.11)$$

Now the bond dissociation energy of the anion may be determined, using heats of formations, and knowing that $\Delta H = \Delta H_f(\text{products}) - \Delta H_f(\text{reactants})$,

$$\Delta H_f(C_2H_2^-) = \Delta H_f(C_2H_2) - EA(C_2H_2) \quad (10.12)$$

$$\Delta H_f(C_2H^-) = \Delta H_f(C_2H) - EA(C_2H). \quad (10.13)$$

The dissociation energy of the anion is thus given by,

$$\begin{aligned} D_0(C_2H \cdots H^-) &= \Delta H_f(C_2H^-) + \Delta H_f(H) - \Delta H_f(C_2H_2^-) \\ &= \Delta H_f(C_2H) - EA(C_2H) + \Delta H_f(H) - [\Delta H_f(C_2H_2) - EA(C_2H_2)] \\ &= D_0(C_2H \cdots H) + EA(C_2H_2) - EA(C_2H). \end{aligned} \quad (10.14)$$

Therefore, substituting in Eq. (10.11) and literature values for the electron affinities^[219] gives a dissociation value of,

$$\begin{aligned} D_0(C_2H \cdots H^-) &= 85 + 11 - 69 = 27 \text{ kcal/mol} \\ &= 1.17 \text{ eV.} \end{aligned} \quad (10.15)$$

This calculation shows that the photofragment channel $H_2CC^- + h\nu \rightarrow HCC^- + H$ will be open at wavelengths shorter than ~ 1067 nm. So photofragmentation actually occurs even in the longer wavelength measurements in Fig. 10.2 and Fig. 10.1, however because of the high EA of C_2H (2.969 eV^[13]) photoelectrons from this channel will only be observed at wavelengths shorter than ~ 417 nm.

It may also be possible for photofragment C_2H^- to also undergo a secondary photofragmentation process to form C_2^- . To check whether this secondary channel will also be open, $D_0(C_2 \cdots H^-)$ may be calculated using a similar method as above. Applying the thermodynamic cycle Eq. (10.10) to C_2H^- gives,

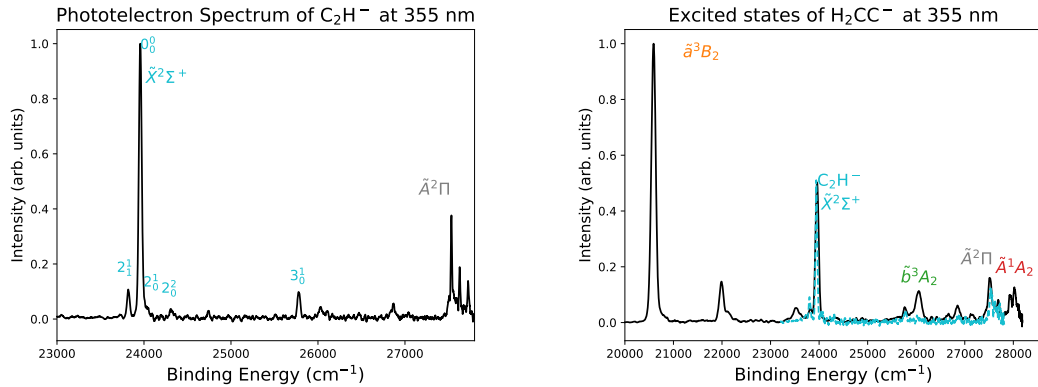
$$\begin{aligned} D_0(C_2 \cdots H) &= EA(C_2) + \Delta H_{\text{acid}}(C_2H) - IP(H) \\ &= 75 + 348 - 313 = 110 \text{ kcal/mol.} \end{aligned} \quad (10.16)$$

Using Eq. (10.14), the corresponding dissociation energy for the anion is,

$$\begin{aligned} D_0(C_2 \cdots H^-) &= D_0(C_2 \cdots H) + EA(C_2H) - EA(C_2) \\ &= 110 + 69 - 75 = 104 \text{ kcal/mol} \\ &= 4.51 \text{ eV.} \end{aligned} \quad (10.17)$$

Hence, the $HCC^- + h\nu \rightarrow C_2^- + H$ photofragment channel is closed at wavelengths longer than ~ 275 nm.

Consequently, we would expect to see evidence of only the C_2H^- photofragment in the 355 nm vinylidene photoelectron spectrum in Fig. 10.7. To confirm whether this is responsible for the unassigned peak (*), a photoelectron spectrum of C_2H^- at 355 nm is presented in Fig. 10.8. In the C_2H^- photoelectron spectrum, two electronic transitions are



(a) Photoelectron spectrum of C_2H^- , measured at 355 nm. Structure is assigned to vibrational transitions of the ground $\tilde{X}^2\Sigma^+$ and first excited $\tilde{A}^2\Pi$ states.

(b) H_2CC^- photoelectron spectrum of excited states, measured at 355 nm, with C_2H^- photoelectron spectrum overlay (—).

Figure 10.8: Photoelectron spectrum of C_2H^- at 355 nm confirms the unassigned peak (*) in Fig. 10.7 is due to the photofragment C_2H^- .

observed, $\text{C}_2\text{H}(\tilde{X}^2\Sigma^+) \leftarrow \text{C}_2\text{H}^- (\tilde{X}^1\Sigma^+) + h\nu$ and $\text{C}_2\text{H}(\tilde{A}^2\Pi) \leftarrow \text{C}_2\text{H}^- (\tilde{X}^1\Sigma^+) + h\nu$. These transitions will be discussed in more detail in chapter 12.

It is clear from Fig. 10.8 that the unassigned peak in Fig. 10.7 is the origin 0_0^0 transition of $\text{C}_2\text{H}(\tilde{X}^2\Sigma^+) \leftarrow \text{C}_2\text{H}^- (\tilde{X}^1\Sigma^+)$ photodetachment. Other vibrational transitions of the C_2H^- photofragment, such as 2_1^1 and 3_0^1 , may also be observed in the vinylidene photoelectron spectrum, including the origin transition of the first excited state $\tilde{A}^2\Pi$.

10.3.2 Excited state analysis

Each of the excited states observed in Fig. 10.7 possess slightly different geometries and normal mode vibrational frequencies. These frequencies may be determined from the experiment by fitting Gaussians to the observed peaks in the 355 nm photoelectron spectrum, with the positions and vibrational frequency shifts of the observed structures listed in Table 10.2. The term energies of each excited electronic state are shown to be in good agreement with the values from Neumark's Cryo-SEVI spectra^[191], while the vibrational frequencies are also in good agreement with *ab-initio* calculations^[198].

The electron angular distribution for each electronic state may also be examined. Transitions to different electronic states often involves detachment from a different molecular orbital of the anion. This is observed in a photoelectron experiment through changes to the anisotropy of the angular distribution, as can be seen in the 355 nm velocity map image in Fig. 10.9. The outermost ring, representing ground state $\text{H}_2\text{CC}(\tilde{X}^1A_1) \leftarrow \text{H}_2\text{CC}^- (\tilde{X}^2B_2)$ detachment, displays a slight negative anisotropy, consistent with the 1064 nm velocity map image of Fig. 10.3. However the next ring, corresponding to $\text{H}_2\text{CC}(\tilde{a}^3B_2) \leftarrow \text{H}_2\text{CC}^- (\tilde{X}^2B_2)$ detachment, shows a strong positive anisotropy, with the electrons distributed around the poles of the image. The H_2CC hybrid orbital diagram in Fig. 8.3 shows that detachment to the ground state involves a non-bonding p orbital, whereas detachment to the first excited triplet state occurs from an sp^1 hybrid orbital. So by examining anisotropy parameters for excited states, different H_2CC^- orbitals may be investigated.

Anisotropy parameters were measured for every electronic and vibrational transition

Table 10.2: Position of peaks in Fig. 10.10 in cm^{-1} , with the frequency shift of vibrational transitions compared to values from Cryo-SEVI^[191] and theory^[198].

Peak	$e\text{BE}$	Shift	Cryo-SEVI ^[191]	Theory ^[198]
$\tilde{a}^3B_2 \leftarrow \tilde{X}^2B_2$				
0_0^0	20,590 (10)		20,602 (12)	
3_0^1	21,989 (12)	1,399 (22)	1,366 (10)	1358
2_0^1	22,106 (40)	1,516 (50)	1,467 (12)	1439
1_0^1	23,534 (15)	2,944 (25)	2,951 (70)	2921
$\tilde{b}^3A_2 \leftarrow \tilde{X}^2B_2$				
0_0^0	26,048 (10)		26,035 (2)	
2_0^1	27,414 (40)	1,366 (50)	1,403 (20)	1425
$\tilde{A}^1A_2 \leftarrow \tilde{X}^2B_2$				
0_0^0	28,024 (10)		28,077 (3)	

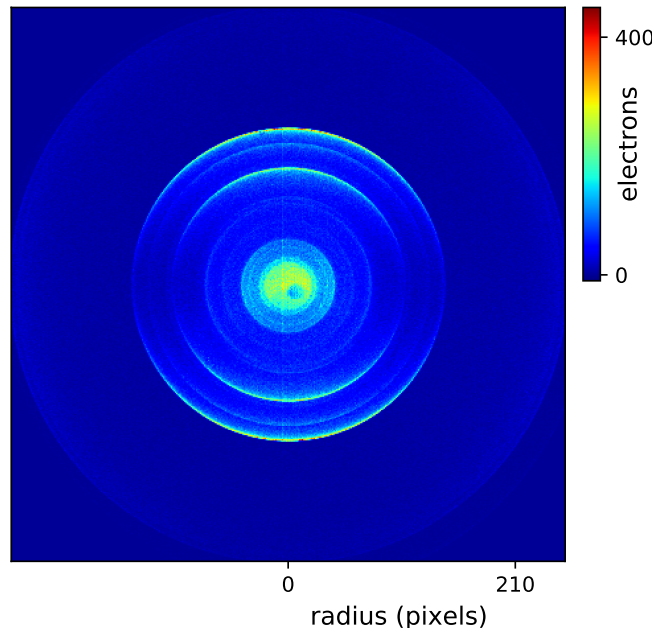
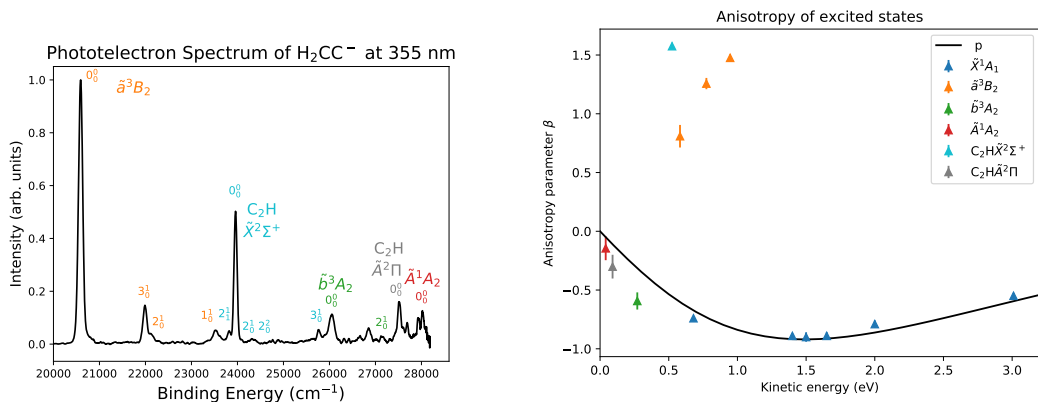


Figure 10.9: Raw velocity-mapped image of vinylidene photodetachment at 355 nm. The image consists of 3,500,000 photoelectrons, with the fastest mapped to the detector edge and the slowest mapped to the centre. The anisotropy variation between different electronic states can be clearly seen, with the excited state $\text{H}_2\text{CC } \tilde{a}^3B_2$ and ground state $\text{C}_2\text{H } \tilde{X}^2\Sigma^+$ showing positive anisotropies, opposite in sign to the other measured transitions.

observed in the 355 nm photoelectron spectrum, with the results presented in Fig. 10.10. A photoelectron spectrum showing all of the assigned transitions is also shown, with each peak colour coded to match the angular distribution figure. All of the vinylidene electronic states measured have negative anisotropy parameters, that follow a similar p orbital Cooper-Zare curve as the ground \tilde{X}^1A_1 state, except for the first excited state \tilde{a}^3B_2 . The other positive anisotropy transition visible in the velocity map image corresponds to the C_2H^- photofragment. Given the positive anisotropy recorded for forbidden transitions in the \tilde{X}^1A_1 ground state at 1064nm, any character mixing in the electronic wavefunction will need to be with an orbital that displays a positive anisotropy. This rules out the



(a) Photoelectron spectrum of H_2CC^- at 355 nm, with all of the observed structure assigned to vibrational transitions of $\text{H}_2\text{CC}^- \leftarrow \text{H}_2\text{CC}$ photodetachment and photofragment $\text{C}_2\text{H} \leftarrow \text{C}_2\text{H}^-$.

(b) Anisotropy parameters for the vinylidene excited states observed in the 355 nm photoelectron spectrum. The Cooper-Zare p curve of the ground H_2CC $\tilde{X}^1\text{A}_1$ state is included.

Figure 10.10: Anisotropy parameters for the excited states observed in the vinylidene photoelectron spectrum (a). The observed β parameters are all different to the values for the ground state, showing that a large change in β is often observed between different electronic states.

possibility of mixing between \tilde{X}^1A_1 and the excited states \tilde{b}^3A_2 and \tilde{A}^1A_2 .

In terms of the anomalous angular distribution observed in the ground state of vinylidene, only the first excited \tilde{a}^3B_2 electronic state exhibits the positive anisotropy required to be considered as a possible cause. However, most vibronic coupling mechanisms do not act between states of different multiplicity. Therefore, any vibronic coupling must occur with a high lying excited state, at least 3 eV higher in energy than the \tilde{X}^1A_1 ground state.

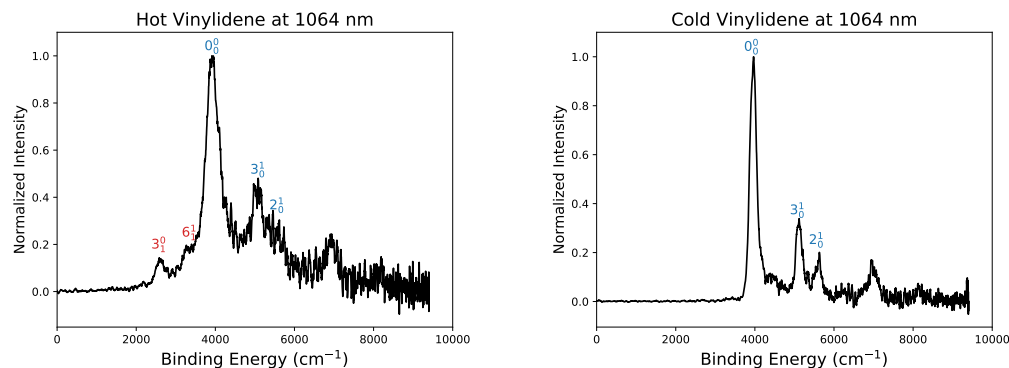
10.3.3 Temperature effects

While experimenting with different ion sources, in order to maximise the vinylidene anion production, a correlation was observed between the measured ion source temperature and the width of the spectral features in the vinylidene spectrum. As was discussed in section 6.1.2, photodetachment measurements of O^- anions may be used to accurately determine the discharge source temperature. By comparing the relative population of the anion fine structure levels, using the ratio of the $^3P_2 \leftarrow ^2P_{3/2}$: $^3P_2 \leftarrow ^2P_{1/2}$ transition intensities, the Boltzmann factor, and corresponding anion temperature, may be extracted. O^- also provides a good measure of the spectrometer resolution, from the FWHM of the fine-structure transitions. Therefore, whenever a vinylidene measurement is recorded, it is typically followed by O^- under identical conditions to help determine the temperature and resolution of the initial spectrum.

However, as O^- has a relatively large EA (1.14611100(7) eV^[123]), this method is only useful for measurements at wavelengths shorter than ~ 900 nm. For longer detachment wavelengths, O_2^- , with an EA = 0.446(1) eV (chapter 7), may be used to characterise the spectrometer performance, in lieu of an O^- spectrum. An indication of the source temperature is given by the presence and intensity of hot bands in the O_2^- photoelectron spectrum, along with the relative intensity of the anion $^2\Pi_g$ fine structure peaks, which

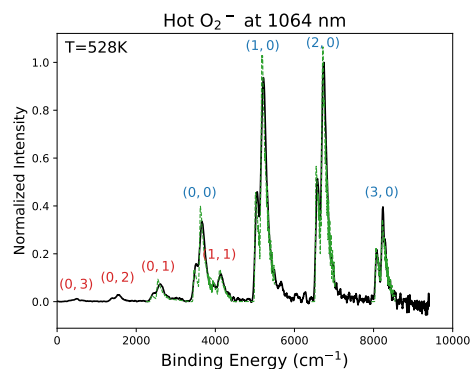
may be resolved in high resolution measurements. By fitting a full rotational band model, as described in section 7.2.3, quantitative values for the source temperature and spectral resolution may also be obtained.

The effect of ion temperature on the vinylidene photoelectron spectrum is shown in the spectra presented in Fig. 10.11. Both of these spectra are of vinylidene photodetachment at 1064 nm, measured on consecutive days, with both images consisting of ~ 1 million electrons. The only change made between the two measurements was in the anion source conditions. The vinylidene in Fig. 10.11 (a) is produced using a mixture of C₂H₄ and O₂ gas in a dual cross jet source, whereas the vinylidene in Fig. 10.11 (b) was produced using pure C₂H₄ in a single jet source (see section 3.2 for more detail on the anion sources). Yet, there is clear change, with the second measurement showing more detailed spectral structures with a much lower background. An increase in temperature of the anion will typically lead to rotational broadening, however this effect is normally relatively small compared to the large change observed in the vinylidene spectrum. The anion temperature in each case is determined from measurements of O₂⁻ recorded under identical conditions in (c) and (d).

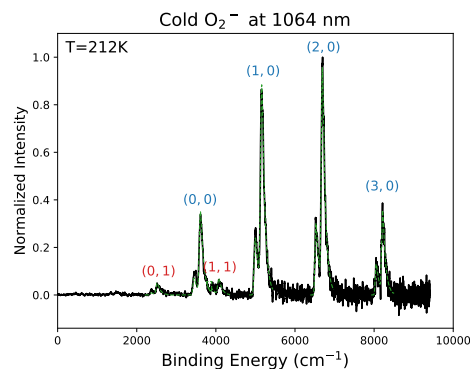


(a) 1 million e^- from photodetachment of H₂CC⁻ at 1064nm. Anions produced in a hot source mixture of C₂H₄/O₂.

(b) 1 million e^- from photodetachment of H₂CC⁻ at 1064nm. Anions produced in a cold source of pure C₂H₄.



(c) O₂⁻ measured at 1064 nm using the hot source of (a). A rotational band model is fitted to the data (—) which determines a temperature of T=528 K.



(d) O₂⁻ measured at 1064 nm using the cold source of (b). A rotational band model is fitted to the data (—) which determines a temperature of T=212 K.

Figure 10.11: Photoelectron spectra of vinylidene, recorded under similar conditions, displaying the effect of anion temperature on the resulting spectrum.

A fitted rotational band model to the O₂⁻ photoelectron spectra produced in both

the crossed jet and single jet sources, confirmed there was a large difference in the anion temperature, with the crossed jet spectrum \sim 300 degrees hotter than the single jet ($T = 528$ K cf 212 K). This correlation between anion temperature and vinylidene resolution was observed for multiple spectra, at different wavelengths and operating conditions. Hence it became apparent that producing cold vinylidene ions was an essential requirement to achieve a less cluttered spectrum. Significantly, it was found that while gas mixtures containing both O_2 and C_2H_4 tended to produce high rates of vinylidene production, ions produced in these conditions were typically rotationally hot (in both the single and dual jet sources), making the mixture unsuitable for achieving low background vinylidene spectra.

To investigate whether the observed temperature broadening is simply due to a larger number of vibrational and rotational transitions, the rotational band model constructed in section 10.1.2 may be used. The model, set to $T = 212$ K and $T = 528$ K is shown along with the hot vinylidene spectrum from above, in Fig. 10.12. This shows that the increase in temperature does cause some rotational broadening of the peak profiles, however this is a small effect compared to the broadening observed in the hot vinylidene spectrum. Interestingly, calculation of the Franck-Condon factors using ezSpectrum software only found a small increase in the intensity of hot-bands, much smaller than the observed intensities of peaks assigned to 6^1_1 and 3^0_1 .

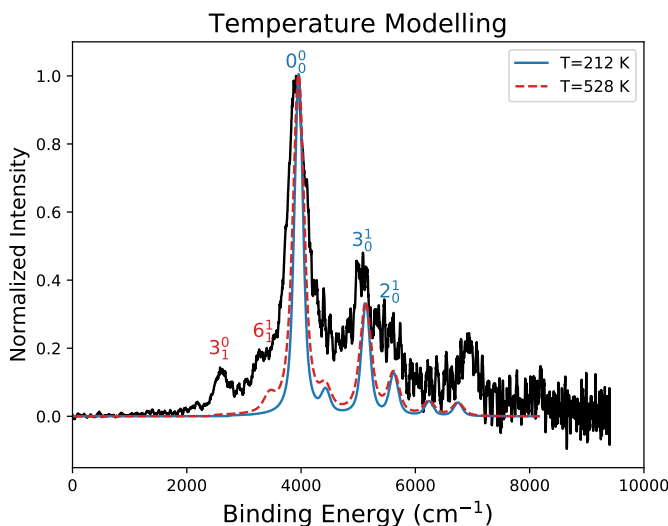


Figure 10.12: Rovibrational model of the vinylidene spectrum at $T = 212$ K and $T = 528$ K. The increase in temperature causes some rotational broadening, with small changes in the vibrational hot band intensities, however this is not enough to explain all of the broadening in the spectrum.

One possible explanation for this temperature dependence comes from considering what happens on the acetylene side of the barrier. As depicted in Fig. 9.5, at the $H_2CC \leftrightarrow HCCH$ isomerisation barrier $\sim 99.5\%$ of the dense manifold of acetylene vibrational levels are expected to be counter rotating modes, with only one or two local-bender modes in close proximity. It is the bound \leftrightarrow bound nature of this tunnelling problem that leads to the existence of long-lived eigenstates, and periodic reversible dynamics. However, if the molecule is rotationally hot, Coriolis and rotational ℓ -resonance mixing may mix a small fraction of local-bender character into all of the nearby acetylene eigenstates. Consequently the full density of acetylene eigenstates will become available to interact

with the vinylidene levels, profoundly changing the nature of the problem, and potentially leading to very short vinylidene lifetimes with wide spectral features^[53].

Previous attempts to measure vinylidene through photolysis of larger compounds, such as vinyl cyanide^[220], vinyl bromide, and vinyl chloride^[221], have all been unsuccessful for similar reasons. Photolysis of a molecule produces fragments in highly rotationally excited states, making them unsuitable for vinylidene detection. However it was believed that photodetachment experiments represented the rotationally cold limit of vinylidene production, where Coriolis mixing would be insignificant^[53]. However present results (Fig. 10.12) suggest that an ion temperature of T~500 K may be hot enough for rotational mixing effects to become significant. This effect can also be observed in Lineberger's earlier work, where an initial low resolution vinylidene measurement^[193] was improved by moving to a much colder source^[11].

Table 10.3: Calculated and measured geometric properties of H₂CC \tilde{X}^1A_1 and H₂CC⁻ \tilde{X}^2B_2 , including rotational and normal mode vibrational constants.

	Molecule Geometry					
	r _{CC} (Å)	r _{CH} (Å)	θ	A (cm ⁻¹)	B (cm ⁻¹)	C (cm ⁻¹)
<u>H₂CC \tilde{X}^1A_1</u>						
CCSD(T) cc-pVTZ ^a	1.327	1.101	119.6	9.24	1.26	1.11
PIP-NN ^b ^[189]	1.300	1.086	120.1			
PES ^d ^[11]	1.299*	1.080*	119.3*			
<u>H₂CC⁻ \tilde{X}^2B_2</u>						
CCSD(T) cc-pVTZ ^a	1.325	1.104	116.7	9.46	1.26	1.11
PIP-NN ^b ^[198]	1.343	1.106	123.5			
PES ^d ^[11]	1.347(7)	1.119(6)	112.0(2)			
Vibrational Frequencies (cm ⁻¹)						
	ω ₁ (a ₁)	ω ₂ (a ₁)	ω ₃ (a ₁)	ω ₄ (b ₁)	ω ₅ (b ₂)	ω ₆ (b ₂)
<u>H₂CC \tilde{X}^1A_1</u>						
CCSD(T) cc-pVTZ ^a	3136	1651	1210	724	3238	355
PIP-NN ^b ^[189]	3121	1682	1221	725	3223	327
HR-PEI ^c	2995.8(8)	1632.3(7)	1174.5(3)		3120.9(9)	292.5(7)
PES ^d ^[11]	3025(30)	1635(10)	1165(10)	835*	3050*	320*
cryo-SEVI ^e		1662(4)	1168(5)		3008(12)	255(50)
<u>H₂CC⁻ \tilde{X}^2B_2</u>						
CCSD(T) cc-pVTZ ^a	2327	1541	1251	892	2489	510
PIP-NN ^b ^[198]	2869	1460	1297	776	2840	875
HR-PEI ^c						
PES ^d ^[11]	2770*	1485(30)	1305(10)	765*	2765*	900*

^a calculations of this work, computed with NWChem software

^b calculations of Guo *et al.* using permutation invariant polynomial-neural network method^[189,198]

^c values from photoelectron spectra taken in this work, presented in chapter 10

^d values from photoelectron spectra of Lineberger *et al.*^[11]

^e values from cryo-SEVI spectrum at UC Berkeley by Neumark *et al.*^[218]

* values of non-active modes estimated from Hartree-Fock calculations^[11]

Isomerisation at a barrier

The HR-PEI study of vinylidene in the previous chapter, discovered that transitions involving totally forbidden anti-symmetric vibrational modes appear to be active in the photoelectron spectrum of the ground state. Furthermore, these forbidden transitions are observed with a corresponding anomalous jump in the anisotropy parameter. As the anisotropy of a photoelectron distribution describes the character of the detachment orbital, large variations in β usually correspond to different electronic states, as was observed in the study of vinylidene excited states at 355 nm.

However, there is still no clear link between the isomerisation process and the observed spectral structure. Furthermore, it is not apparent why these forbidden transitions are active, or where the cause of the anomalous anisotropy arises from. As none of the excited vinylidene electronic states are accessible at 1064 nm, the character mixing responsible for the β variation may arise from coupling between the ground and a high lying excited state. Before spectral signatures of isomerisation can be identified, the cause of these forbidden transitions will need to be determined.

11.1 Vibronic Coupling

Vibronic coupling is a term used to describe interactions between electronic and vibrational motion of a molecule. There are many different mechanisms through which vibronic coupling can occur, relating to a breakdown of the Born-Oppenheimer approximation^[40]. One mechanism of particular interest for this work is Herzberg-Teller coupling, where electronic character from another state may be mixed into an original state through a vibrational promoter.

The Hamiltonian for a molecule may be described by,

$$H(r, Q) = T_e(r) + T_N(Q) + U(r, Q) + V(Q), \quad (11.1)$$

where $T_e(r)$ and $T_N(Q)$ are the kinetic energy operators for the electronic and nuclear motion respectively, $U(r, Q)$ is the Coulombic potential energy and $V(Q)$ the potential of the nuclei. Exact solutions to the Schrödinger equation $[H(r, Q) - E_{jt}]\Psi_{jt}(r, Q) = 0$, can not be solved as the Hamiltonian is non-separable. This is where the Born-Oppenheimer approximation is often invoked, assuming that the motion of the electrons and the nuclei may be treated as separable due to the differing (by a factor of $\sim 10^3$) period of their motion. This allows for the wavefunction of the molecule to be rewritten,

$$\Psi_{jt}^{\text{CA}}(r, Q) = \psi_j^0(r, Q_0)\chi_{jt}^{\text{CA}}(Q), \quad (11.2)$$

where ψ_j^0 is the electronic wavefunction of the j^{th} electronic state at a specified set of fixed nuclear coordinates Q_0 , and $\chi_{jt}(Q)$ is the vibration-rotation wavefunction of the nuclear motion. This is often called the crude adiabatic^[38,39] or static wavefunction^[40], and may be used to describe most chemistry that occurs within the Born-Oppenheimer approximation.

To now include nuclear-electronic interactions, perturbation theory is necessary to account for small nuclear movement away from the Q_0 geometry. Applying the Herzberg-Teller expansion to rewrite $\Psi_{jt}(r, Q)$,

$$\Psi_{jt}(r, Q) = \Psi_{jt}^{\text{CA}}(r, Q) + \sum_{kr \neq jt} \frac{\langle \psi_{jt}^{\text{CA}} | \Delta U | \psi_{kr}^{\text{CA}} \rangle}{E_{jt}^{\text{CA}} - E_{kr}^{\text{CA}}} \psi_{kr}^{\text{CA}}(r, Q), \quad (11.3)$$

substituting Eq. (11.2) in for $\Psi_{jt}^{\text{CA}}(r, Q)$ gives,

$$\Psi_{jt}(r, Q) = \psi_j^0(r, Q_0) \chi_{jt}^{\text{CA}}(Q) + \sum_{k \neq j} \sum_r \frac{\left(\chi_{kr}^{\text{CA}} | \langle \psi_k^0 | \Delta U | \psi_j^0 \rangle | \chi_{jt}^{\text{CA}} \right)}{E_{jt}^{\text{CA}} - E_{kr}^{\text{CA}}} \times \psi_k^0(r, Q_0) \chi_{kr}^{\text{CA}}(Q), \quad (11.4)$$

where the term,

$$\gamma_{kr,jt} = \frac{\left(\chi_{kr}^{\text{CA}} | \langle \psi_k^0 | \Delta U | \psi_j^0 \rangle | \chi_{jt}^{\text{CA}} \right)}{E_{jt}^{\text{CA}} - E_{kr}^{\text{CA}}}, \quad (11.5)$$

is known as the vibronic mixing coefficient.

The term ΔU represents the change in the potential, from moving from the fixed nuclear coordinate Q_0 to the displaced coordinate Q . As we know that the vibrational motion of a molecule is quantised along n normal mode coordinates, we may describe the displacement $Q_0 \rightarrow Q$ by expanding ΔU in a power series about Q_0 along each of these normal mode coordinates,

$$\Delta U = \Delta U(r, Q_0) + \sum_n \left[\frac{\partial U(r, Q)}{\partial Q_n} \right]_0 Q_n + \frac{1}{2} \sum_{n,m} \left[\frac{\partial^2 U(r, Q)}{\partial Q_n \partial Q_m} \right]_0 Q_n Q_m \dots \quad (11.6)$$

Therefore, combining with Eq. (11.5) and neglecting the higher order terms allows us to redefine the mixing coefficient as

$$\gamma_{kr,jt}^n = \frac{\langle \psi_k^0(r, Q_0) | \left[\frac{\partial U}{\partial Q_n} \right]_0 | \psi_j^0(r, Q_0) \rangle \langle \chi_{kt}^{\text{CA}} | Q_n | \chi_{jt}^{\text{CA}} \rangle}{E_{jt}^{\text{CA}} - E_{kr}^{\text{CA}}}. \quad (11.7)$$

Consequently, the molecule wavefunction $\Psi_{jt}(r, Q)$ may now be written as

$$\Psi_{jt}(r, Q) = \psi_j^0(r, Q_0) \chi_{jt}^{\text{CA}}(Q) + \sum_{k \neq j} \sum_r \sum_n \gamma_{kr,jt}^n \psi_k^0(r, Q_0) \chi_{kr}^{\text{CA}}(Q). \quad (11.8)$$

Each summation may be linked to a corresponding energy state, with $\sum_{k \neq j}$ summing over the electronic states, \sum_r summing over vibrational states, and \sum_n summing over the promoter modes.

By applying symmetry considerations we can see that the vibronic mixing coefficient $\gamma_{kr,jt}$ will vanish if it does not abide by the electronic and vibrational selection rules,

$$\Gamma_k \otimes \Gamma_j \not\subseteq \Gamma_{Q_n} \quad \text{or} \quad \Gamma_r \otimes \Gamma_t \not\subseteq \Gamma_{Q_n}.$$

In other words, vibronic coupling will only occur when,

$$\Gamma_{kr} \otimes \Gamma_{jt} \not\subseteq \Gamma_{\text{totally symmetric}} \quad (\text{and } Q_n \text{ is not totally symmetric}).$$

It is also important to take careful note of the subscripts on the electronic and vibrational wavefunctions, as surprisingly, the wavefunctions associated with the vibronic coupling coefficient are different to the Q_0 static wavefunctions. In short hand Eq. (11.8) may be written as,

$$|\Psi_{jt}\rangle = |\psi_j \chi_{jt}\rangle + \gamma_{kr,jt} Q_n |\psi_k \chi_{kr}\rangle. \quad (11.9)$$

This highlights that the vibronic mixing coefficient is linked to the k^{th} electronic state, not the original j^{th} state.

11.1.1 The 1B_2 state of vinylidene

Forbidden transitions that are observed in Fig. 10.6, include the non-totally symmetric v_5 asymmetric stretch and v_6 rock mode, both of which have b_2 symmetry. The ground state of vinylidene is $\tilde{X} {}^1A_1$, and so coupling may only occur to excited states with symmetry,

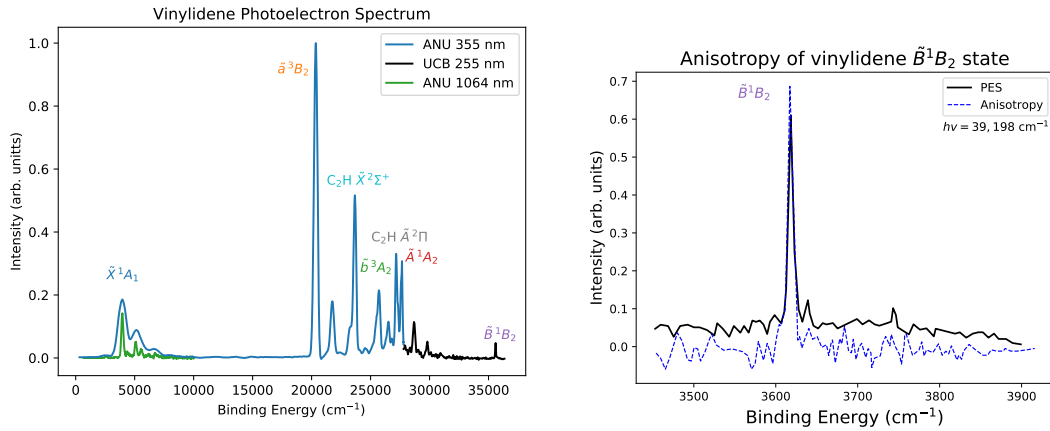
$${}^1A_1 \otimes b_2 = {}^1B_2.$$

However, no excited states with 1B_2 symmetry were measured in the 355 nm photoelectron spectrum in Fig. 10.10 (vibronic coupling can not change the spin of the state, so coupling with $\tilde{X} {}^1A_1$ will only occur with another singlet state). *Ab-initio* calculations of DeVine *et al.*^[191] predict a high lying $\tilde{B} {}^1B_2$ state, 6.925 eV above the acetylene minimum, ie. 5 eV above the $\tilde{X} {}^1A_1$ state. Hence this would require a laser detachment wavelength shorter than ~ 250 nm, to be observed.

At the time, obtaining a wavelength short enough to probe the high lying $\tilde{B} {}^1B_2$ state was not possible with the laser set-up at the ANU, however our collaborators at Berkeley were able to get a measurement of this state by using a 255nm output from their dye Nd:YAG laser. From the resulting photoelectron spectrum, presented in Fig. 11.1, they found that the $\tilde{B} {}^1B_2$ state actually lies ~ 4 eV above the ground state $\tilde{X} {}^1A_1$, less than the predicted 5 eV. However this is still a large energy gap, which will require a very large coupling coefficient if it is to have any significant effect on the ground state chemistry.

A key signature of the forbidden mode transitions in the photoelectron spectrum is the change in sign of the anisotropy parameter, with a small positive β parameter measured for these modes, compared with a large negative β for the allowed transitions. Therefore, there must be a change in the wavefunction character associated with these transitions. Importantly, Eq. 11.9 shows that Herzberg-Teller coupling terms are related to the excited, mixed electronic k^{th} state, rather than the original ground j^{th} state. Consequently, if the vibronically coupled states have different anisotropies, this would explain the jump in β between Franck-Condon allowed and forbidden transitions. This also provides a test for this hypothesis, as if $\text{H}_2\text{CC}(\tilde{B} {}^1B_2) \leftarrow \text{H}_2\text{CC}^-(\tilde{X} {}^1A_1)$ photodetachment displays a positive anisotropy, then it is possible that Herzberg-Teller coupling between $\tilde{X} {}^1A_1$ and $\tilde{B} {}^1B_2$ is responsible for both the appearance of v_5 and v_6 transitions, as well as the discontinuity in β .

From the 255 nm photoelectron spectrum measurement of DeVine *et al.*^[191], the anisotropy of the $\tilde{B} {}^1B_2$ state may be measured by looking at the angular variation in the photoelectron distribution. Neumark's group use a slightly different method to describe the anisotropy, where the plotted anisotropy is multiplied by the intensity of the



(a) Photoelectron spectra of vinylidene, taken at 1064 nm and 355 nm (ANU), and at 255 nm (UC Berkeley^[191]), showing the position of the \tilde{B}^1B_2 state.

(b) Anisotropy measurement of the \tilde{B}^1B_2 excited state of vinylidene, measured by the Neumark group at UC Berkeley^[191].

Figure 11.1: Photoelectron spectrum of the high lying \tilde{B}^1B_2 state of vinylidene, measured at ~ 255 nm by the Neumark group at UC Berkeley, showing a slight positive anisotropy, similar to the forbidden v_5 and v_6 transitions.

spectrum, as in Fig. 11.1. However, dividing the anisotropy (—) by the spectrum intensity (—) will give a β parameter comparable to the ones used in this work. Importantly, Fig. 11.1 shows that \tilde{B}^1B_2 does have a positive anisotropy, similar to the measured v_5 and v_6 modes in Fig. 10.6. Consequently, this would make vibronic coupling between the \tilde{X}^1A_1 and \tilde{B}^1B_2 states, a prime candidate to explain the presence of forbidden modes in the photoelectron spectrum.

11.1.2 Coupling strengths and transition moments

While vibronic coupling between the ground \tilde{X}^1A_1 and excited \tilde{B}^1B_2 states via the promoting modes v_5 and v_6 , may explain the presence, and associated anisotropy jump, of forbidden modes in the 1064 nm vinylidene photoelectron spectrum, the relatively large intensity of these transitions is still surprising, given the large ~ 4 eV energy gap between the coupled states.

The strength of the vibronic coupling constant may be determined from examining the transition dipole moment. From Eq. (11.9), the initial and final state wavefunctions may be described by

$$|\Psi_{\text{anion}}\rangle = |\psi''_m \chi''_{ms}\rangle \quad (11.10)$$

$$|\Psi_{\text{neutral}}\rangle = |\psi'_j \chi'_{jt}\rangle + \gamma_{kr,jt} Q_n |\psi'_k \chi'_{kr}\rangle. \quad (11.11)$$

The transition moment integral along α , where α is one of the principle (a, b, c) axes of the molecule, is then given by^[38]

$$\begin{aligned} \mu_{\alpha}^{a-n} &= \langle \Psi_{\text{anion}} | \vec{\mu}_{\alpha} | \Psi_{\text{neutral}} \rangle \\ &= \langle \psi''_m | \vec{\mu}_{\alpha} | \psi'_j \rangle \langle \chi''_{ms} | \chi'_{jt} \rangle + \gamma_{kr,jt} \langle \psi''_m | \vec{\mu}_{\alpha} | \psi'_k \rangle \langle \chi''_{ms} | Q_n | \chi'_{kr} \rangle \end{aligned} \quad (11.12)$$

If we apply this to vibronic coupling in vinylidene, we see that term $\langle \psi''_m | \vec{\mu}_{\alpha} | \psi'_j \rangle$ represents

the electronic transition moment $\mu_{\alpha:0}^{\tilde{X}-\tilde{X}}$ for the $\text{H}_2\text{CC}(\tilde{X}^1A_1) \leftarrow \text{H}_2\text{CC}^-(\tilde{X}^2B_2)$ transition at the anion geometry. Likewise, the $\langle \psi''_m | \vec{\mu}_\alpha | \psi'_k \rangle$ term represents the electronic transition moment $\mu_{\alpha:0}^{\tilde{B}-\tilde{X}}$ for the $\text{H}_2\text{CC}(\tilde{B}^1B_2) \leftarrow \text{H}_2\text{CC}^-(\tilde{X}^2B_2)$ transition. Hence, we may rewrite the transition moment as,

$$\mu_\alpha^{a-n} = \mu_{\alpha:0}^{\tilde{X}-\tilde{X}''} \langle \chi''_{ms} | \chi'_{jt} \rangle + \gamma_{kr,jt} \mu_{\alpha:0}^{\tilde{B}-\tilde{X}} \langle \chi''_{ms} | Q_n | \chi'_{kr} \rangle. \quad (11.13)$$

Eq. (11.13) describes the transition moment for $\text{H}_2\text{CC}(\tilde{X}^1A_1) \leftarrow \text{H}_2\text{CC}^-(\tilde{X}^2B_2)$ photodetachment as a sum of the standard ground state $\tilde{X} - \tilde{X}$ transition (electronic moment \times Franck-Condon vibrational overlap), plus the vibronic coupling term, which depends on the vibronic coupling constant $\gamma_{kr,jt}$, the electronic moment from the anion to the coupling state $\tilde{B} - \tilde{X}$, and a vibrational overlap involving the promoting mode coordinate Q_n .

However another way to account for the vibronic coupling dependence on the transition moment, would be to expand the general $\tilde{X} - \tilde{X}$ transition dipole function as a Taylor series in Q_n about the anion equilibrium geometry^[222],

$$\mu_\alpha^{a-n} = \mu_{\alpha:0}^{\tilde{X}-\tilde{X}''} \langle \chi''_{ms} | \chi'_{jt} \rangle + \left(\frac{\partial \mu_{\alpha}^{\tilde{X}-\tilde{X}''}}{\partial Q_n} \right)_0 \langle \chi''_{ms} | Q_n | \chi'_{kr} \rangle + \dots \quad (11.14)$$

Comparing Eq. (11.13) and Eq. (11.14) one obtains,

$$\left(\frac{\partial \mu_{\alpha}^{\tilde{X}-\tilde{X}''}}{\partial Q_n} \right)_0 = \gamma_{kr,jt} \mu_{\alpha:0}^{\tilde{B}-\tilde{X}''}. \quad (11.15)$$

From this we can see that the vibronic coupling constant, corresponding to a vibronic interaction between the $\tilde{B} - \tilde{X}$ states, is related to the slope of the $\tilde{X} - \tilde{X}''$ electronic transition moment, along the promoting mode Q_n coordinate. Therefore, in order to evaluate the strength of the vibronic coupling between the \tilde{X}^1A_1 and \tilde{B}^1B_2 states responsible for the presence of forbidden modes v_5 and v_6 in the photoelectron spectrum, one needs to evaluate the slope of $\mu_{\alpha}^{\tilde{X}-\tilde{X}''}$ with respect to Q_n at the equilibrium anion geometry^[223].

Calculating transition dipole moments for photodetachment can be difficult, as standard quantum chemistry programs are unable to calculate transition properties between states with a different number of electrons. Consequently, a manual approach had to be derived. Interestingly, Eq. (11.15) states that the behaviour of the $\tilde{B} - \tilde{X}''$ coupling can be inferred from the $\tilde{X} - \tilde{X}''$ interaction, so only the ground state wavefunctions of the anion and neutral are required. These wavefunctions may be obtained from CCSD(T) calculations using Q-Chem software^[114]. It is useful to note however, that the calculation to determine the ground state wavefunction also calculates and accounts for interactions with excited states, including \tilde{B}^1B_2 , which helps to explain how $\tilde{B} - \tilde{X}''$ coupling can be encoded into the $\tilde{X} - \tilde{X}''$ interaction.

The *ab-initio* output may be decoded using Multiwfn software^[224], which is able to decode *ab-initio* electronic wavefunction files, rewriting them into a XYZ/value mesh grid format. In this format, a python script can be written to read in the neutral and anion ground state wavefunctions in order to calculate $|\langle \Psi_{\text{anion}} | \vec{\mu}_\alpha | \Psi_{\text{neutral}} \rangle|^2$, along each principle axis a, b, c (see Fig.8.5), using numerical integration. $|\langle \Psi | \Psi \rangle|^2$ is also calculated to check that the *ab-initio* wavefunctions are correctly normalized, and that the grid captures the entire extent of the wavefunction.

The above process allows for the transition dipole moment, $\mu_\alpha^{\tilde{X}-\tilde{X}''}$, to be determined

for any given input geometry. Consequently, using the normal mode vectors calculated in Fig. 8.5, $\mu_{\alpha}^{\tilde{X}-\tilde{X}''}$ may be calculated as a function of Q_n along the v_5 and v_6 forbidden mode coordinates, with the result presented in Fig. 11.2.

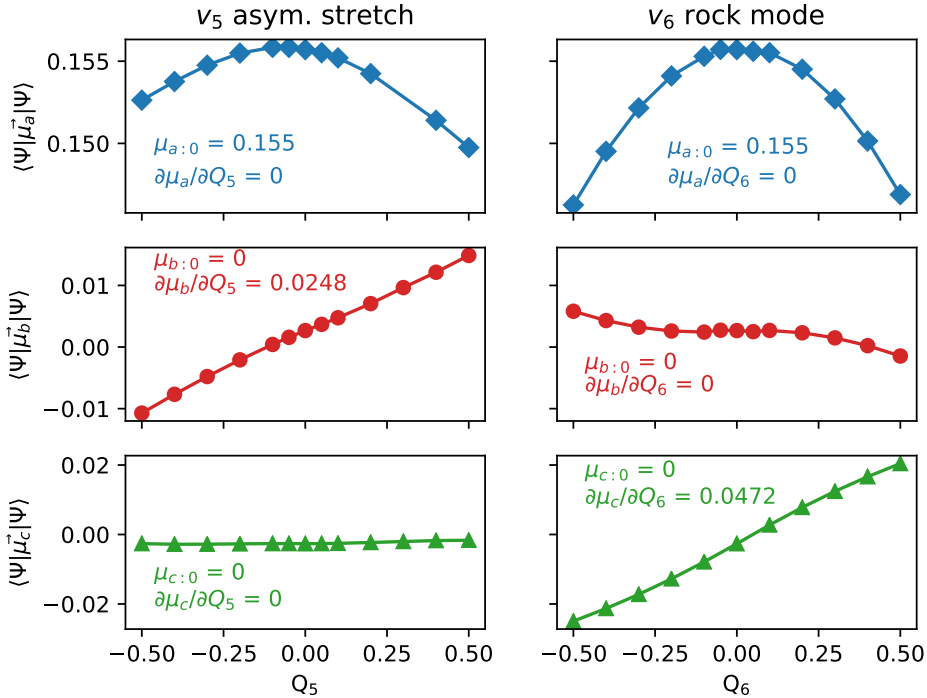


Figure 11.2: Transition dipole moments calculated for the $\tilde{X} - \tilde{X}''$ vinylidene photodetachment transition, along the asymmetric v_5 and v_6 normal mode coordinates. Dipole transition moments along the principle a (◇), b (○), and c (△) axes are shown. The value of $\mu_{\alpha}^{\tilde{X}-\tilde{X}''}$ at $Q_n = 0$ represents the strength of the allowed v_1 , v_2 , v_3 transitions, while the value of the slope $\partial\mu_{\alpha}^{\tilde{X}-\tilde{X}''}/\partial Q_n$ at $Q_n = 0$ represents the strength of the $\tilde{X}^1A_1 - \tilde{B}^1B_2$ vibronic coupling.

Fig. 11.2 shows the transition dipole moments calculated using Q-chem^[95] and Multi-wfn^[224] software, for the $\tilde{X} - \tilde{X}$ vinylidene photodetachment transition, along the asymmetric v_5 and v_6 normal mode coordinates. Dipole moments along each of the principle axes, a (◇), b (○), and c (△), are shown. From Eq. (11.14), we can see that the value of $\mu_{\alpha}^{\tilde{X}-\tilde{X}''}$ and the slope $\partial\mu_{\alpha}^{\tilde{X}-\tilde{X}''}/\partial Q_n$ at the equilibrium geometry $Q_n = 0$ will be important for determining the strength of the allowed and forbidden transitions respectively.

Interestingly, for both v_5 and v_6 $\mu_{b:0} = \mu_{c:0} = 0$, while for v_5 $\left(\frac{\partial\mu_a}{\partial Q_5}\right)_0 = \left(\frac{\partial\mu_c}{\partial Q_5}\right)_0 = 0$ and for v_6 $\left(\frac{\partial\mu_a}{\partial Q_6}\right)_0 = \left(\frac{\partial\mu_b}{\partial Q_6}\right)_0 = 0$. Having a non-zero transition dipole (or dipole gradient) along only one of the principle axes is fairly common, as shown by a study of vibronic coupling of the vinoxy radical^[222]. Consequently, the entire vinylidene photoelectron spectrum, including both allowed and forbidden transitions, may be accounted for by the

non-zero terms,

$$\begin{aligned}\mu_{\alpha}^{a-n} &= \mu_{a:0}^{\tilde{X}-\tilde{X}''} \langle \chi''_{ms} | \chi'_{jt} \rangle + \left(\frac{\partial \mu_b^{\tilde{X}-\tilde{X}''}}{\partial Q_5} \right)_0 \langle \chi''_{ms} | Q_5 | \chi'_{kr} \rangle + \left(\frac{\partial \mu_c^{\tilde{X}-\tilde{X}''}}{\partial Q_6} \right)_0 \langle \chi''_{ms} | Q_6 | \chi'_{lp} \rangle \\ &= 0.155 \langle \chi''_{ms} | \chi'_{jt} \rangle + 0.0248 \langle \chi''_{ms} | Q_5 | \chi'_{kr} \rangle + 0.0472 \langle \chi''_{ms} | Q_6 | \chi'_{lp} \rangle,\end{aligned}\quad (11.16)$$

where the values for the transition moment/gradient are from the calculations in Fig. 11.2. The intensity of any observed transition is given by the square of the transition moment, which is therefore given by,

$$|\mu^{\tilde{X}-\tilde{X}''}|^2 = 24.025 \times 10^{-3} \langle \chi''_{ms} | \chi'_{jt} \rangle^2 + 0.615 \times 10^{-3} \langle \chi''_{ms} | Q_5 | \chi'_{kr} \rangle^2 + 2.228 \times 10^{-3} \langle \chi''_{ms} | Q_6 | \chi'_{lp} \rangle^2 \quad (11.17)$$

In Eq. (11.17) the first term represents transitions to the allowed v_1, v_2, v_3 vibrational levels, while the second and third terms represent transitions that occur due to vibronic coupling between the $\tilde{X}^1A_1 - \tilde{B}^1B_2$ electronic states, through promoting mode v_5 and v_6 respectively. From this we can see that the vibronic coupling constant for mode v_6 is ~ 4 times larger than the coupling constant for v_5 .

11.1.3 Forbidden mode transition intensities

In order to compare transition intensities between the allowed and vibronically coupled forbidden modes, the Franck-Condon and ‘modified Franck-Condon’ factors $|\langle \chi''_{ms} | \chi'_{jt} \rangle|^2$ and $|\langle \chi''_{ms} | Q_n | \chi'_{lp} \rangle|^2$ from Eq. (11.17) need to be calculated.

The Franck-Condon factors for some of the allowed transitions observed in the vinylidene photoelectron spectrum in Fig 10.2, have already been listed in Table 10.1. These were calculated using ezSpectrum software^[216], which calculates vibrational wavefunction overlap integrals $|\langle \chi''_{ms} | \chi'_{jt} \rangle|^2$ using the normal mode vectors from *ab-initio* frequency calculations. However, the modified Franck-Condon factors responsible for the vibronic coupling can not be obtained directly from quantum chemistry software, so will require a more detailed approach.

As has been discussed, the vibrational motion of a molecule is quantized along 3N-6 normal mode coordinates, with vinylidene possessing 3 totally symmetric (a_1) modes and 3 non-symmetric ($b_1, 2 \times b_2$) modes. Near the equilibrium geometry, along each mode coordinate the vibrational wavefunction may be modelled by a one-dimensional harmonic oscillator, with the shape of the potential governed by the normal mode frequency. The Hamiltonian for the system can therefore be described by,

$$\hat{H} = \frac{\hat{p}^2}{2m} + \frac{1}{2}\omega^2 \hat{q}_n^2, \quad (11.18)$$

where \hat{q}_n is the mass weighted normal mode coordinate and ω is the corresponding harmonic frequency (obtained from CCSD(T) Q-Chem^[95] calculations). The solution to the Schrödinger equation for this system is well known, and given by the harmonic wavefunction

$$\psi_k(q_n) = \frac{1}{\sqrt{2^k k!}} \cdot \left(\frac{m\omega}{\pi} \right)^{1/4} \cdot e^{-\frac{\omega q_n^2}{2}} \cdot H_k(\sqrt{\omega}q_n), \quad (11.19)$$

where H_k are the Hermite polynomials, defined as

$$H_k(z) = (-1)^k e^{z^2} \frac{d^k}{dz^k} (e^{-z^2}). \quad (11.20)$$

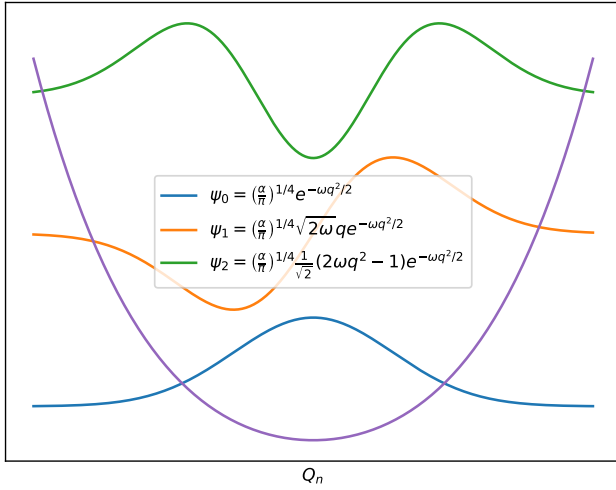


Figure 11.3: First three harmonic oscillator wavefunctions from (Eq. 11.19). The Potential curve was calculated along q_5 using NWChem software.

The lowest three harmonic oscillator wavefunctions ψ_0 , ψ_1 , ψ_2 are calculated and shown in Fig. 11.3. A standard one dimensional Franck-Condon factor calculation then involves the integral,

$$\langle \chi''_l | \chi'_k \rangle = \int \psi'_k(q_n) \psi''_l(\beta q_n + \delta) dq_n \quad (11.21)$$

where β represents the change in harmonic frequency between the two states, $\beta = \left(\frac{\omega''}{\omega'}\right)^{1/2}$, and δ represents the change in equilibrium geometry, $\delta = \Delta Q \sqrt{\omega'}$ ^[225]. Using known properties of Hermite polynomials, Eq. (11.21) may then be numerically integrated.

However we now need to calculate the modified Franck-Condon overlap $\langle \chi''_{ms} | Q_n | \chi'_{lp} \rangle$. If the initial and target electronic state were identical, this integral would be zero, however due to small differences in the states, a non unity value will be obtained. To calculate these integrals we may use the well known recursion relationship for Hermite polynomials^[226] (Eq. 11.20),

$$x H_n(x) = n H_{n-1}(x) + \frac{1}{2} H_{n+1}(x). \quad (11.22)$$

This shows how the product, $x \times H_n(x)$, may be related to the H_{n-1} and H_{n+1} polynomials. Applying this to our harmonic oscillator wavefunction in Eq. (11.19) gives,

$$Q_n | \psi_k \rangle = \alpha^{1/2} \left[\left(\frac{k+1}{2} \right)^{1/2} | \psi_{k+1} \rangle + \left(\frac{k}{2} \right)^{1/2} | \psi_{k-1} \rangle \right]. \quad (11.23)$$

Rewriting $Q_n | \psi_k \rangle$ into the format of Eq. (11.23) is useful, as our modified Franck-Condon factors may then be determined from the sum of two standard vibrational overlaps^[226],

$$\langle \psi''_l | Q_n | \psi'_k \rangle = \alpha^{1/2} \left[\left(\frac{k+1}{2} \right)^{1/2} \langle \psi''_l | \psi'_{k+1} \rangle + \left(\frac{k}{2} \right)^{1/2} \langle \psi''_l | \psi'_{k-1} \rangle \right], \quad (11.24)$$

where α is a normalisation constant (related to $m\omega/\hbar$), $\psi'_k(q_n)$ is the neutral wavefunction

given by Eq. (11.19), and $\psi_l''(\beta q_n + \delta)$ is the anion wavefunction in Eq. (11.21). The standard vibrational overlaps $\langle \psi_l'' | \psi_{k\pm 1}' \rangle$ may then be computed using ezSpectrum software^[216], and the normal mode vectors calculated at the CCSD(T) level by NWChem^[94].

Using the Franck-Condon factors calculated in Table 10.1, the relative intensity of the forbidden vibronically coupled transitions are determined. The totally forbidden odd-quanta transitions $|\langle 0|Q_6|6^1\rangle|^2$, and $|\langle 0|Q_6|6^3\rangle|^2$ have been calculated using Table 10.1 and Eq. (11.24). This finds that the 6^1 transition is predicted to be twice as strong as the 6^3 transition, which agrees with the measured intensities in the photoelectron spectrum in Fig. 10.6. Combination bands involving a mixture of forbidden and allowed transitions, such as 1^16^1 may also be calculated, using the procedure set out by Johnson *et al.*^[226]. However, the key question lies in determining how the intensity of vibronically coupled peaks compare to the allowed transitions. As a multidimensional Franck-Condon factor may be written as a product of N one dimensional overlaps (Eq. 10.3), all but the origin transition along the promoting modes may be factored out, in order to compare the 0_0^0 transition with the pseudo origin of the forbidden modes. Doing so, finds origin overlaps of ~ 0.97 , only slightly reducing the intensities in Eq. 11.17. This corresponds to intensity ratios of $\sim 1 : 3.6 : 40$ for the $v_5 : v_6 : v_{1,2,3}$ transitions respectively. Importantly, this reveals that the vibronically coupled intensities are about 10% of the allowed transitions, which appears to be consistent with the photoelectron spectrum measured in Fig. 10.6. Furthermore, the calculation confirms that, despite a large ~ 4 eV gap between the \tilde{X}^1A_1 and \tilde{B}^1B_2 electronic states, the vibronic coupling constant is sufficiently large for totally forbidden non-symmetric transitions to be observed in the experimental photoelectron spectrum. The peak assigned to the transition 5_0^1 has a larger intensity in the photoelectron spectrum than 6_0^1 , despite having a coupling constant that is $\times 4$ smaller. However this is explained by an additional anharmonic coupling interaction between the modes 5_0^1 and $1_0^16_0^1$, that will be examined in section 11.2.2.

11.2 Acetylene character inside vinylidene eigenstates

The spectral features observed in the photoelectron spectrum of vinylidene may all now be assigned to either allowed (v_1 , v_2 , v_3) or forbidden, vibronically coupled (v_5 , v_6) transitions. Attention can now turn back towards the goal of understanding the H₂CC \leftrightarrow HCCH isomerisation mechanism. While the HR-PEI vinylidene spectra presented in chapter 10 were vital in uncovering the anomalous anisotropy jump which lead to the discovery of vibronic coupling between the \tilde{X}^1A_1 and \tilde{B}^1B_2 states, at the high electron kinetic energies arising from photodetachment at 1064 nm, the resulting peak widths are too broad to directly observe any mixing between vinylidene and acetylene local-bender eigenstates. This is where the cryo-SEVI spectrometer at the University of California in Berkeley is useful. The Neumark research group obtain extremely high resolution (sub meV), over a narrow range of electron kinetic energies, by cooling the anions to ~ 10 K, reducing the spectral congestion, while scanning a tuneable detachment laser very close to threshold^[227]. This collaborative project is a nice demonstration of how together, the HR-PEI and cryo-SEVI techniques are able to provide a more complete picture of the photoelectron spectrum.

11.2.1 Searching for eigenstates with Cryo-SEVI

To search for evidence of acetylene isomerisation, a high resolution composite spectrum of the vinylidene anion was obtained by the Neumark group. The cryo-SEVI spectrometer at Berkeley operates in a similar fashion to the HR-PEI spectrometer at the ANU, with the major differences occurring in the source and laser systems. A more detailed description of the cryo-SEVI set-up may be found elsewhere^[227–229].

Vinylidene ions were produced in a supersonic expansion of C₂H₄ gas mixed with trace amounts of N₂O, through a pulsed filament ioniser. An injection of electrons from the ioniser results in dissociative electron attachment of N₂O to form O⁻. The fragment O⁻ then reacts with C₂H₄ to produce H₂CC⁻ ions^[218]. The ions are then guided through a radio-frequency hexapole ion guide and quadrupole mass filter before being deposited into a rf octopole ion trap. The trap is held at 5 K and filled with a buffer gas mixture of 20% H₂ in He, which undergoes collisions with resulting in thermalisation of the vinylidene anions^[227]. These cold ions are then extracted from the trap, mass filtered, and photodetached.

Slow electron velocity map imaging (SEVI) exploits the VMI characteristic that imaging very slow electrons, close to the detachment threshold, gives the best electron kinetic energy resolution. This requires a tunable laser source, with high stability, narrow bandwidth, and a large tunable region. The spectrometer at Berkeley satisfies these requirements using a home-built IR difference frequency generation (IR-DFG) set-up, similar to one designed by the Lineberger group^[56], which is described in detail elsewhere^[218]. This system is tuned over the mid-IR region (2500–7692 cm⁻¹), with a composite photoelectron spectrum constructed by combining scans close to the threshold of each vibrational transition. The resulting spectrum is presented in Fig. 11.4, shown with a HR-PEI measurement at 1064 nm for reference.

Fig. 11.4 (A) shows the cryo-SEVI spectra of H₂CC⁻ (top) and D₂CC⁻ (bottom) measured by Neumark *et al.*^[218], including an overview scan at 1064 nm (—), together with a high resolution composite spectra which combines measurements at multiple wavelengths close to threshold (—)^[218]. A theoretical simulation by Guo *et al.* using a global acetylene-vinylidene potential energy surface (—)^[198] is also shown. Inserts (B) and (C) show the HR-PEI spectra and anisotropy parameters from H₂CC⁻ photodetachment as discussed in chapter 10, with the peaks re-labelled for reference to the cryo-SEVI spectrum. This shows that peaks labelled B, I, and K are responsible for the anomalous jump in the anisotropy parameter β . As such, (D) focuses on peak I of the H₂CC⁻ spectrum, showing the underlying structure observed for different wavelength traces of the cryo-SEVI spectrum, along with a continuous trace of the anisotropy parameter from the HR-PEI spectra.

The detailed spectrum of peak I shows that there are multiple individual peaks that contribute to the overall peak shape measured by the HR-PEI spectrum. Furthermore, it is seen that the anisotropy parameter varies across the peak, with the structure labelled (a) displaying a significantly lower β parameter than structure (b). This highlights that the anisotropy jumps measured in Fig. 10.6 are state specific. Different cross-section behaviour at threshold is also observed for each of the individual peaks. Interestingly, this found that peak (a) decreases slower than the other peaks as the photon energy is lowered. Both of these observations suggest that there is a variation in the partial wave contribution to photodetachment across this region, indicating that the character of each individual eigenstate is highly variable. This observation has also been noted for peak I

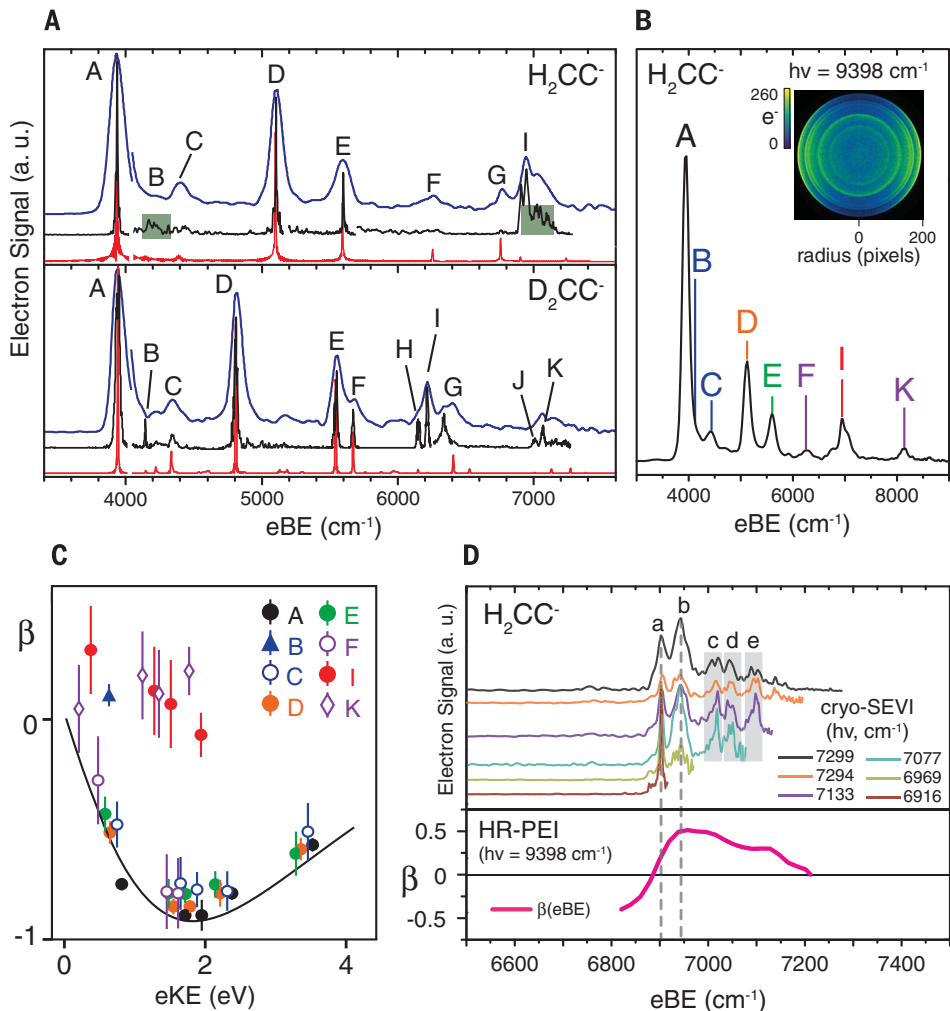


Figure 11.4: Photoelectron spectra of vinylidene. (A) cryo-SEVI spectra of H_2CC^- (top) and D_2CC^- (bottom), including an overview scan at 1064 nm (—), and a higher resolution composite spectra from multiple wavelengths (—) [218]. A theoretical simulation by Guo *et al.* is also shown (—) [198]. (B) HR-PEI spectra of H_2CC^- , with peaks labelled for reference to cryo-SEVI spectrum. (C) Anisotropy parameters from the HR-PEI spectrum, showing an anomalous jump in β for peaks B, I, and K. (D) Peak I of the H_2CC^- photoelectron spectrum, showing the underlying structure observed for different wavelength traces of the cryo-SEVI spectrum. The anisotropy parameter variation from the HR-PEI spectrum across peak I is also included.

in angular slice spectra from the HR-PEI spectrometer, similar to Fig. 10.4.

From the normal mode vectors in Fig. 8.5, peak I appears to be in the region of the forbidden transitions 5_0^1 and $1_0^1 6_0^1$. From the transition dipole moment calculations (Eq. 11.17) it was shown that vibronic coupling between the $\tilde{X}^1\text{A}_1$ and $\tilde{B}^1\text{B}_2$ states was strongest through mode v_6 , with only weak coupling through v_5 . However, full quantum dynamical calculations of the vinylidene wavefunction (see Fig. 11.5) show that the 5_0^1 state mixes with the nearby $1_0^1 6_0^1$ state through an anharmonic interaction, giving peak I a larger than expected intensity. This interaction is enhanced by an energy shift to the $1_0^1 6_0^1$ state due to the intermode anharmonicity between the stretching and rocking modes, which brings the two mixed modes closer together [218].

During these cryo-SEVI measurements, it was noted that at laser detachment energies close to the adiabatic electron affinity of H₂CC, some of the photoelectron structure depended non-trivially on the photon energy, no longer following the standard $eKE = h\nu - eBE$ relationship^[230]. This effect is attributed to autodetachment of vibrationally excited vinylidene anions. First observed in the predissociation spectroscopy measurements of Gerardi *et al.*^[215], who examined Ar-tagged H₂CC⁻ ions, autodetachment can occur when the photon energy $h\nu$ is resonant with a transition in the anion. The anion then undergoes vibrational (rather than electronic) excitation, before detaching an electron. This can result in constant eKE structure, where the electron energy appears indifferent to small changes in photon energy.

11.2.2 Full quantum dynamics and eigenstate decomposition

The lifetime conundrum (section 8.1.1), described two seminal vinylidene experiments with contradictory results. The photoelectron spectrum published by Lineberger *et al.*^[11], observed peak widths that were larger than expected, with the excess width attributed to lifetime broadening, suggesting a vinylidene lifetime of $\tau \sim 0.04\text{--}0.2$ picoseconds. However a subsequent coulomb explosion imaging experiment found neutral vinylidene molecules with lifetimes longer than 3.5 μs , clearly contradicting the previous conclusion^[12].

From the high resolution cryo-SEVI spectrum in Fig. 11.4, linewidths of most of the peaks were measured at $\sim 10\text{ cm}^{-1}$ and $\sim 30\text{ cm}^{-1}$ for H₂CC⁻ and D₂CC⁻ respectively. This suggests the linewidths are primarily due to rotational contours, containing a single eigenstate, with the differing widths of the two isotopes due to the spin statistics of the H and D atoms^[218]. Significantly, the majority of features in the spectrum do not display appreciable broadening with respect to the cryo-SEVI spectra of excited state vinylidene^[191]. This is in contrast to the Lineberger vinylidene spectra, suggesting that the claimed lifetime broadening in the original measurements were in fact due to instrument resolution or a possible temperature effect (see section 10.3.3).

However, there are several regions in the spectrum (B, C, and I) where anomalous broadening does occur. Importantly, this broadening appears to be state specific, unlike the previous estimates. Even at high resolution, features B and C (assigned to transitions 6₀¹ and 6₀²) appear as broad weak features, indicating participation of multiple eigenstates in these anomalous transitions^[218]. To gain insight into how the isomerisation mechanism may be encoded in these eigenstates, full quantum dynamical vinylidene wavefunctions were calculated for the origin 0₀⁰, allowed 6₀², and totally forbidden 5₀¹ modes, along the θ_1 and θ_2 Jacobi coordinates by Guo *et al.*^[218] as part of our ARC collaboration. The resulting wavefunctions are plotted in Fig. 11.5, with the radial coordinate r_0 constrained to the equilibrium value of vinylidene (top) and acetylene (bottom), and the wave functions summed over the remaining coordinates.

In the wavefunctions in Fig. 11.5, the vinylidene geometry is described by Jacobi coordinates $\theta_1 = 120^\circ$ and $\theta_2 = 30^\circ$, while the acetylene geometry is represented by $\theta_1 = \theta_2 = 180^\circ$. The ground state of vinylidene (0₀⁰) shows very little mixing, with most of the intensity localised at the vinylidene minimum ($\theta = 120^\circ, 30^\circ$). However excitation in the rock mode (6₀²) is shown to introduce appreciable acetylene character, with intensity along the angular coordinates heading towards the acetylene geometry ($\theta = 180^\circ$). The large number of nodes along the angular coordinates in the HCCH plot show that this acetylene character features highly excited states in the local-bending coordinate. Similarities between the 6₀² and 5₀¹ wavefunctions arise due to the mixing that occurs

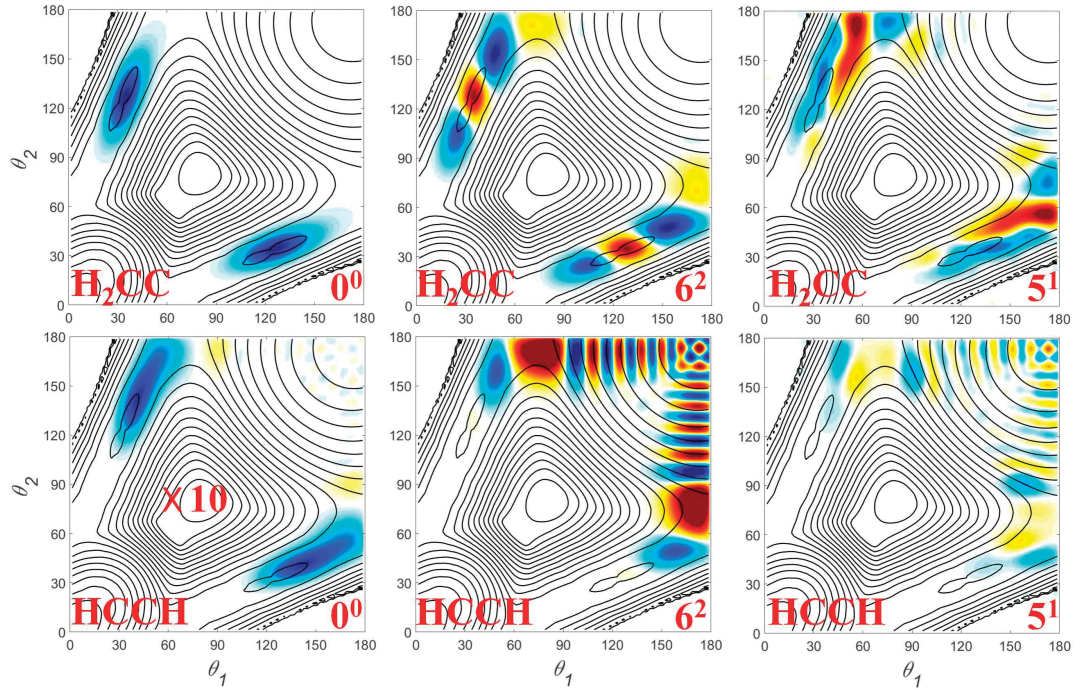


Figure 11.5: Full quantum dynamical wavefunctions of the 0_0^0 , 6_0^2 , and 5_0^1 modes are shown along the θ_1 and θ_2 Jacobi coordinates, as calculated by Guo *et al.*^[218] The radial coordinate r_0 is constrained to the equilibrium value of H₂CC (top) and HCCH (bottom), with the wave functions summed over the remaining coordinates. The vinylidene geometry is described by Jacobi coordinates $\theta_1 = 120^\circ$ and $\theta_2 = 30^\circ$ while the acetylene geometry is represented at $\theta_1 = \theta_2 = 180^\circ$.

between states $1_0^1 6_0^1$ and 5_0^1 through an anharmonic interaction, as discussed earlier. From the wavefunction plot we can see that this mixed $1_0^1 6_0^1 \sim 5_0^1$ state also shows appreciable acetylene character along the local bending coordinate, with similar nodal structure as that seen for the 6_0^2 state. The anharmonic coupling of states $1_0^1 6_0^1$ and 5_0^1 explains the large intensity of peak I in the photoelectron spectrum, despite the small vibronic coupling interaction of the v_5 mode.

This result links the spectroscopic observations (HR-PEI + cryo-SEVI) to the vinylidene–acetylene isomerisation dynamics. From this, we have learnt that the minimum energy isomerisation pathway follows the v_6 rock mode of vinylidene, which ultimately connects with the highly excited local bending states of acetylene. The acetylene contributions to the 6_0^2 and $1_0^1 6_0^1 \sim 5_0^1$ eigenfunctions involve strong admixtures of the local bending states of excited acetylene, states which have been extensively probed spectroscopically through the work of Field and co-workers^[200]. Wavefunctions for the other modes of H₂CC, and D₂CC, do not show any appreciable acetylene character, with much narrower eigenfunctions resulting from suppressed tunnelling^[218].

To understand the isomerisation dynamics involving this 1,2-hydrogen shift mechanism, transitions between vibrational eigenstates with different amplitudes for the vinylidene and acetylene zeroth-order basis states need to be quantum mechanically simulated. The intensity of a transition in the measured photoelectron spectra is primarily determined by,

$$I_n \approx |cn^{(1)}|^2 |\langle \psi_n^{(1)} | \Psi^{(\text{anion})} \rangle|^2, \quad (11.25)$$

where $\Psi^{(\text{anion})}$ is the wavefunction of the vinylidene anion, and $\psi_n^{(1)}$ is the vinylidene character from the mixed neutral wavefunction defined by,

$$\Psi^{(\text{neutral})} \approx c_n^{(1)} \psi_n^{(1)} + c_m^{(2)} \psi_m^{(2)}, \quad (11.26)$$

where $\psi_n^{(1)}$ and $\psi_m^{(2)}$ represent zeroth-order acetylene and vinylidene basis states respectively. The extent of mixing between the states, which encodes the isomerisation, depends on the energy difference between $\psi_n^{(1)}$ and $\psi_m^{(2)}$, as well as the strength of the interaction matrix between them. As mentioned above, the states primarily involved in the mixing are vinylidene rock modes 6_0^n (including anharmonically mixed modes $1_0^1 6_0^1 \sim 5_0^1$), and acetylene local-bender modes, which have a much smaller density of states than the total density of acetylene vibrational levels (see Fig. 9.5). The vinylidene weights $|c_n^{(1)}|^2$ may be approximated from the calculated eigenfunctions (Fig. 11.5), with the results presented in Table 11.1.

Table 11.1: Vinylidene weights (as a %) for the peaks measured in the cryo-SEVI spectrum (Fig. 11.4), along with normal mode assignments. Vinylidene weights are also included for the D₂CC isotopologue.

Peak	Assignment	H ₂ CC%	D ₂ CC%
A	0 ₀ ⁰	100	100
B	6 ₀ ¹	84	100
C	6 ₀ ²	58	98
D	3 ₀ ¹	97	100
E	2 ₀ ¹	97	97
F	3 ₀ ²	96	
G	2 ₀ ¹ 3 ₀ ¹	97	
H	1 ₀ ¹		
I	5 ₀ ¹	82	99
	1 ₀ ¹ 6 ₀ ¹	68	95

From Table 11.1 we can see that appreciable vinylidene–acetylene eigenstate mixing only occurs for H₂CC states involving the rock mode v_6 (including transition 5_0^1 which is anharmonically mixed with doorway state $1_0^1 6_0^1$), with all other H₂CC states possessing predominant vinylidene character. All of the transitions in the isotopologue D₂CC show predominant vinylidene character, with much smaller mixing due to the more confined wave functions. This suggests less barrier tunnelling for D₂CC, which may result in different dynamics compared with H₂CC.

11.3 The unravelling of 1,2-hydrogen shifts

Chapters 8–11 of this thesis have been dedicated to the vinylidene molecule, with the ultimate goal of trying to study the 1,2-hydrogen shift mechanism through which isomerisation with acetylene proceeds. This process is a common occurrence in many important organic reactions, and so by studying the dynamics on an isolated prototypical molecule, such as H₂CC, experimental spectroscopic techniques may be complemented by full quantum mechanical dynamic simulations. By approaching the reaction from multiple angles, it was hoped that a detailed description of this unimolecular reaction may be obtained.

HR-PEI spectra of the vinylidene anion, measured in this work using the ANU pho-

toelectron spectrometer, uncovered the first anomaly in an otherwise innocuous looking spectrum. Transitions involving odd quanta of excitation in vibrational modes $v_5(b_2)$ and $v_6(b_2)$ were observed in the vibrational spectrum, despite the fact that transitions involving non-symmetric modes should be totally forbidden. Furthermore, these transitions seemed to be accompanied by an anomalous jump in the anisotropy parameter β . This surprising variation in the anisotropy suggested that character from multiple electronic states may be involved in the detachment process, which lead to the possibility of vibronic coupling.

While vibronic (Herzberg-Teller) coupling is a possible mechanism to explain the presence of forbidden modes, symmetry dictated that coupling via modes v_5 and v_6 may only occur between states \tilde{X}^1A_1 and \tilde{B}^1B_2 . With the lowest lying \tilde{B}^1B_2 state measured to lie ~ 4 eV above the ground \tilde{X}^1A_1 state, any significant interaction between these two states would be surprising. However through calculation of transition dipole gradients, it was shown that the vibronic coupling strength between these states was large enough to reproduce the measured photoelectron spectrum.

Attention then turned back towards the hunt for acetylene character mixed into the neutral vinylidene states. Cryo-SEVI spectra, measured at UC Berkeley, determined that the previously reported lifetime broadening observed in previous measurements, was not present at high resolution. However, anomalous broadening was observed for a few specific peaks - namely the v_5 and v_6 peaks present due to vibronic coupling. When one of these anomalous peaks was examined in detail, multiple components were found to contribute, with each component displaying distinct threshold and anisotropic behaviour. This indicated that the electronic character of each individual eigenstate was highly variable.

Vinylidene wavefunctions were calculated across 2 dimensional Jacobian coordinate space, for each of the normal mode vibrations. The origin transition 0^0 displayed predominant localisation in the vinylidene equilibrium well, whereas mode 6^2 showed appreciable mixing with acetylene. A large number of nodes were observed along the angular coordinates for 6^2 , indicating that the corresponding acetylene character features highly excited states in the local-bending coordinate. Similarities were also observed between the 6^2 and 5^1 wavefunctions, due to anharmonic mixing between the states 5^1 and 1^16^1 . The ratio of vinylidene–acetylene character was approximated from the calculated eigenfunctions for each measured state of neutral vinylidene. These values, presented in Table 11.1, show that appreciable acetylene character is only found in states involving mode v_6 (or v_5 due to anharmonic coupling).

This combination of spectroscopic and quantum dynamic approaches implies that, in the range of energies probed here, the isomerisation from vinylidene to acetylene is highly state specific, and is promoted exclusively through excitation of the v_6 mode. Significantly, excitation through mode v_6 may occur through one of three different channels, either through a Franck-Condon allowed transition (6_0^2), vibronic coupling to an excited state (6_0^1), or via anharmonic coupling between ground state vibrational levels ($5_0^1 \sim 1_0^16_0^1$). These insights form a quantum mechanical foundation for understanding how the 1,2-hydrogen shift reaction may proceed.

Puzzles of vinylidene relatives

Other small hydrocarbons were also studied during this work, including the dicarbon molecule C₂ and the ethynyl radical C₂H. By investigating molecules similar to vinylidene, further insight into the isomerisation dynamics may be gained. Importantly, this work revealed that vinylidene undergoes photofragmentation at short wavelengths - something not mentioned in previous studies. This chapter examines the dicarbon bonding puzzle, and the interplay of various coupling mechanisms between the electronic states of C₂H.

12.1 Ethynyl and the coupling conundrum

The ethynyl radical (C₂H) is a simple linear triatomic molecule, with a surprisingly complex photoelectron spectrum. Ethynyl has been observed in abundance in interstellar mediums, with high C₂H densities observed in a range of astronomical processes^[231], including in planetary atmospheres^[232], comets^[233], and heavy star formation^[234]. The reactivity of the C≡C triple bond makes ethynyl a highly reactive radical^[231]. It is often involved in high temperature combustion processes^[235], and polycyclic aromatic hydrocarbon production^[236]. As such, it is a molecule of considerable interest to both chemists and astrophysicists^[237].

It is the spectral characteristics of C₂H that have drawn recent interest, due to the interactions between the ground and low lying excited electronic states. Previous spectroscopic^[238,239] and theoretical^[44,45] studies have confirmed that the interplay between vibronic Herzberg-Teller, Jahn-Teller, and Renner-Teller coupling mechanisms, results in a complex vibronic energy structure of the $\tilde{A}^2\Pi$ state. These coupling mechanisms, introduced in section 2.2, provide the key to decoding the spectral observations of this work.

Due to the relatively low C–H bond strength in vinylidene of 1.17 eV (see section 10.3.1) C₂H photofragments were observed in the 355 nm vinylidene spectrum (Fig. 10.7). Photoelectron spectra of C₂H[−] were recorded at the same wavelength, to help decode the spectrum in Fig. 10.7, and assign spectral features to either vinylidene or ethynyl vibrational transitions. Furthermore, as vibronic coupling plays a prominent role in both the vinylidene and ethynyl spectra, studying the photoelectron spectrum of C₂H[−] may provide some useful insight into the mechanisms involved in the vinylidene-acetylene isomerisation.

12.1.1 Vibronic structure of the ethynyl radical

As we have seen with the other molecules studied in this work, symmetry can be a powerful tool in decoding the energetic structure of a molecule. The ground state of the neutral C₂H radical $\tilde{X}^2\Sigma^+$, has a linear equilibrium configuration, and belongs to the point group $C_{\infty v}$. As a linear molecule, ethynyl will have $3N-5 = 4$ normal vibrational modes, 2 totally symmetric (σ) C–C and C–H stretch modes, and 2 degenerate non-totally symmetric (π) CCH out of plane bend modes. Equilibrium geometries are calculated for the anion C₂H[−]($\tilde{X}^1\Sigma^+$) and the neutral C₂H($\tilde{X}^2\Sigma^+$) and C₂H($\tilde{A}^2\Pi$) states at the CCSD(T) level

of theory, followed by harmonic frequency calculations, with the resulting normal mode vectors shown in Fig. 12.1. Geometric and energetic constants are listed in Table 10.3 for comparison to experimental measurements.

Under the Franck-Condon approximation, only transitions involving the v_1 and v_3 totally symmetric modes should be active in the ethynyl photoelectron spectrum, while transitions involving an even quanta of excitation in the non-totally symmetric v_2 mode may be present with a diminished intensity. Transitions involving an odd quanta of excitation in the v_2 CCH bend modes are totally forbidden.

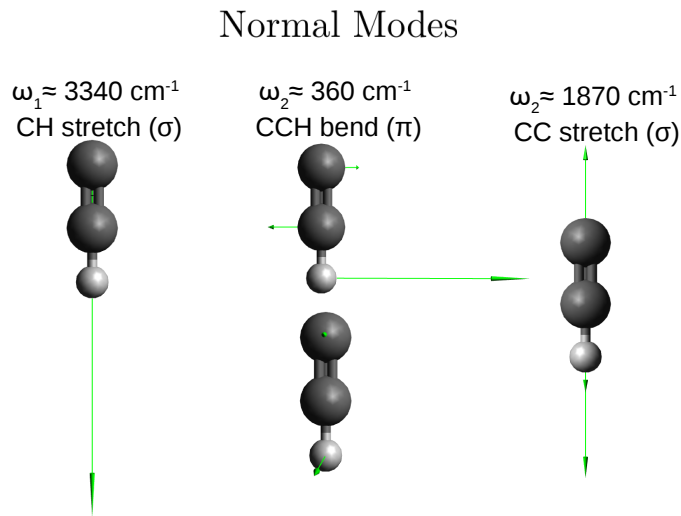


Figure 12.1: Normal mode vectors for the ground $\tilde{X}^2\Sigma^+$ state of C_2H , calculated at the CCSD(T) level of theory using NWChem software^[94].

However, due to interactions of the ground state with the low lying excited $\tilde{A}^2\Pi$ electronic state, significant coupling between the electronic and nuclear motion is present, leading to a break down in the Born-Oppenheimer approximation. As a result, adiabatic corrections are applied, to account for three key coupling mechanisms involved, as shown below.

Herzberg-Teller coupling

From our work on vinylidene (section 11.1), we have seen that the interaction between electronic and vibrational motion of a molecule may lead to Herzberg-Teller coupling, where the electronic character from one state is mixed into an original state through a vibrational promoter. In this case, the full wavefunction of a molecule, including perturbations to account for nuclear-electronic interactions, may be described using the Herzberg-Teller expansion

$$\Psi_{jt}(r, Q) = \psi_j^0(r, Q_0)\chi_{jt}^{\text{CA}}(Q) + \sum_{k \neq j} \sum_r \sum_n \gamma_{kr,jt}^n \psi_k^0(r, Q_0)\chi_{kr}^{\text{CA}}(Q). \quad (12.1)$$

Eq. (12.1) describes the full molecular electronic and nuclear wavefunction, with the first term representing the standard Franck-Condon allowed transitions of the target electronic state ψ_j^0 , whereas the second term accounts for coupling that may occur between the ground and close lying excited states. The vibronic coupling that occurs between electronic

states ψ_j^0 and ψ_k^0 , is facilitated through the promoting vibrational mode χ_{kr} , with the strength of this coupling interaction determined by the vibronic coupling constant $\gamma_{kr,jt}^n$, defined in Eq. (11.7).

By applying the correct product tables for a molecule with $C_{\infty v}$ symmetry, we can see that the forbidden π bending vibrational mode (v_2) may be active in the ethynyl spectrum if there is significant vibronic coupling between the ground $\tilde{X}^2\Sigma^+$ and excited $\tilde{A}^2\Pi$ states as,

$$\Sigma^+ \otimes \pi = \Pi.$$

In other words, the presence of transitions involving odd quanta of bending vibration (v_2) provides direct evidence of Herzberg-Teller coupling between the $\tilde{X}^2\Sigma^+$ and $\tilde{A}^2\Pi$ electronic states.

Renner-Teller coupling

The v_2 bending mode in Fig. 12.1 is degenerate, and has a vibronic quantum number ℓ_i , representing the angular momentum associated with the bending vibration. This may take a value of $\ell_i = v_i, v_i - 2, v_i - 4, \dots, 1$ or 0, where v_i is the quanta of bending excitation. In the Born-Oppenheimer approximation different vibronic energy levels ℓ_i are degenerate, however in cases with strong rovibronic coupling this degeneracy in ℓ_i is lost.

This creates a Renner-Teller pair in the excited state, where the usually degenerate Π surfaces separate to form two non-degenerate electronic states $\Pi^+(2A')$ and $\Pi^-(1A'')$. This involves separating a single potential energy surface (V) into two distinct but connected surfaces (V^+) and (V^-). Due to the strong coupling along the linear axis, between the electronic and vibrational angular momenta of the $2A'$ and $1A''$ components of the $^2\Pi$ state, vibrational levels cannot be assigned explicitly to either of the $\Pi^+(2A')$ or $\Pi^-(1A'')$ electronic states, and instead exist as a combination of both states.

Pseudo Jahn-Teller coupling

Due to the close lying nature of the ground $\tilde{X}^2\Sigma^+$ and excited $\tilde{A}^2\Pi$ electronic states, separated by $\sim 3700 \text{ cm}^{-1}$, a pseudo Jahn-Teller effect is also observed. The Jahn-Teller theorem states that stability and degeneracy are not possible simultaneously unless the molecule is linear^[42], meaning that non-linear molecules with degenerate electronic states will undergo a symmetry breaking distortion in order to remove the degeneracy. However a similar effect has also been observed where coupling exists between a non-degenerate state and a nearby pair of degenerate states, even if a molecule is linear.

In the case of ethynyl this is seen as coupling between the ground $\Sigma^+(1A')$ and excited $\Pi^+(2A')$ states, induced by the bending motion of v_2 . The ground state only couples to one of the Renner-Teller pair $\Pi^+(2A')$, as the other state $\Pi^-(1A'')$ has incorrect symmetry. This results in a very complex vibronic structure for the $\tilde{A}^2\Pi$ electronic state, with contributions from three coupled states $\Sigma^+(1A')$, $\Pi^+(2A')$, and $\Pi^-(1A'')$.

12.1.2 The photoelectron spectrum and coupling calculations

Three previous photoelectron studies of the ethynyl radical have been reported, including an early measurement by Lineberger *et al.*^[13] which observed vibrational transitions involving only the ground state $e^- + \text{C}_2\text{H}(\tilde{X}^2\Sigma^+) \leftarrow \text{C}_2\text{H}^-(\tilde{X}^1\Sigma^+) = h\nu$, followed by two more recent studies by Neumark *et al.*^[14,240] which report on detachment to both the

ground $\tilde{X}^2\Sigma^+$ and excited $\tilde{A}^2\Pi$ electronic levels. The later study presented a composite photoelectron spectrum, constructed by scanning a Nd:YAG pumped dye laser over a range of wavelengths down to ~ 320 nm, using the Berkeley cryo-SEVI spectrometer (described in section 11.2.1)^[14]. From this, the Neumark group determined a \tilde{A} term energy of ~ 3677 cm⁻¹. However it should be noted that the coupling mechanisms described above complicate the assignment of spectral features, with an electronic origin not defined as clearly as it is in usual photoelectron spectra^[241].

These measurements all observed transitions in the ground state spectrum, involving odd quanta of the bending vibration mode v_2 , transitions which should be forbidden within the harmonic oscillator Franck-Condon approximation. This strongly suggests the presence of substantial vibronic Herzberg-Teller coupling between the ground $\tilde{X}^2\Sigma^+$ and excited $\tilde{A}^2\Pi$ states. A similar effect was observed in the photoelectron spectrum of vinylidene (chapter 11), where vibronic coupling between states lead to the observation of forbidden transitions involving the rock mode v_6 . The forbidden ethynyl v_2 transitions also appear to be accompanied with a sign change in the anisotropy parameter, with the allowed v_1 and v_3 transitions noted to exhibit *p*-wave character, opposite to the forbidden v_2 transitions which appeared *s*-like^[14].

Coupling calculations

Due to the combination of the three coupling mechanisms (Herzberg-Teller, Renner-Teller, pseudo Jahn-Teller), the spectral structures of the $\tilde{A}^2\Pi$ state in the spectrum^[14] cannot be simply assigned to normal mode vibrations of the molecule. These interactions spread out the electronic origin of the \tilde{A} state over several vibronic levels, with higher energy spectral structure also expected to be composed of multiple overlapping vibronic transitions. The observed peaks in the spectrum of C₂H⁻ may therefore be assigned to coupled admixtures of vibronic transitions involving the three potential energy surfaces,

$$\Psi_f = \sum_{\xi} \psi_e^{\xi} \sum_k C_{fk}^{\xi} \phi_{fkm}^{\xi}, \quad (12.2)$$

where ψ_e^{ξ} is the diabatic electronic wavefunction, and ϕ_{fkm}^{ξ} is the spin-rovibrational wavefunction. ξ represents the electronic states used in the expansion, and in this case $\xi = \Sigma^+(1A'), \Pi^+(2A'), \Pi^-(1A'')$. A depiction of these three interacting surfaces is given in Fig. 12.2.

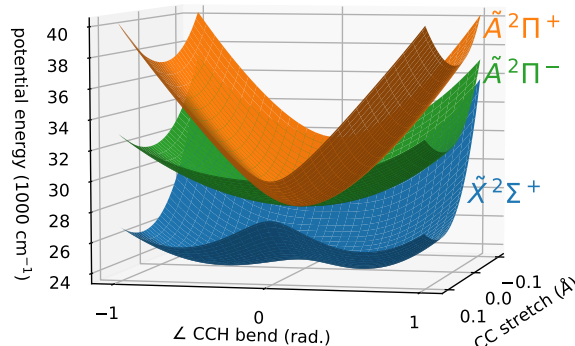


Figure 12.2: Adiabatic potential energy surfaces of $\tilde{X}^2\Sigma^+$, $\tilde{A}^2\Pi^-$, and $\tilde{A}^2\Pi^+$ states, from the coupling calculations of Tarroni and Carter^[241] ($E_{1A'}$, $E_{2A'}$, and $E_{1A''}$ in Eq. 12.3).

In order to calculate the vibronic levels involved in the photodetachment of ethylene, 10 dipole surfaces are required in the XZ plane, $2 \times \Sigma^+$, $2 \times \Pi^+$, $2 \times \Pi^-$ permanent dipole moments and $2 \times (\Sigma^+ \Pi^+)$, $1 \times (\Sigma^+ \Pi^-)$, $1 \times (\Pi^+ \Pi^-)$ transition dipole moments. Tarroni and Carter^[241] have shown that these surfaces may be obtained by calculating diabatic potential energy surfaces for the $\tilde{X}^2\Sigma^+(1A')$ and $\tilde{A}^2\Pi(2A', 1A'')$ states, and applying the variational method of Palmieri *et al.*^[45] to then calculate the spin-rovibronic levels of C₂H. The adiabatic energies from the potential energy surfaces may be transformed by^[241],

$$\begin{pmatrix} V_{\Sigma^+} & V_{12} & 0 \\ V_{21} & V_{\Pi^+} & 0 \\ 0 & 0 & V_{\Pi^-} \end{pmatrix} = \begin{pmatrix} T_{11} & T_{21} & 0 \\ T_{12} & T_{22} & 0 \\ 0 & 0 & 1 \end{pmatrix} \times \begin{pmatrix} E_{1A'} & 0 & 0 \\ 0 & E_{2A'} & 0 \\ 0 & 0 & E_{1A''} \end{pmatrix} \times \begin{pmatrix} T_{11} & T_{21} & 0 \\ T_{12} & T_{22} & 0 \\ 0 & 0 & 1 \end{pmatrix}, \quad (12.3)$$

where $E_{1A'/2A'/1A''}$ are the adiabatic energies for the $\Sigma^+(1A')$, $\Pi^+(2A')$, $\Pi^-(1A'')$ states (Fig. 12.2), and the matrix elements T_{ij} may be obtained from diagonalization. Similarly, the same unity transformation matrix T may be used to diabatize the dipole moments. Once the diabatic energies and 10 non-zero diabatic dipole moments listed above have been determined, the potential energy surfaces may be calculated,

$$V_a(q_1, q_2, q_3) = \sum_{ijk} C_{ijk}^a q_1^i q_2^j q_3^k, \quad (12.4)$$

for $a = \Sigma^+, \Pi^+, \Pi^-$, where q_1, q_2, q_3 are the internal coordinates representing the CC, CH, bond lengths and CCH bond angle respectively^[241]. Following this method, Tarroni and Carter have published a list of ethynyl rovibronic levels up to 10,000 cm⁻¹ above the electronic origin^[44]. Examination of the mixed wavefunctions, allowed for transitions in the infra-red^[242,243] and photoelectron^[14] spectra, to be assigned to various admixed combinations of \tilde{X} and \tilde{A} state vibrational levels^[14].

12.1.3 HR-PEI of C₂H⁻ and C₂D⁻

In order to investigate the vibronic coupling mechanisms present in the ethynyl radical, the photoelectron spectrum of the C₂H⁻ anion was measured at 355 nm, using the ANU's HR-PEI spectrometer. C₂H⁻ ions were produced in a pulsed-jet discharge of pure C₂H₄ gas, under similar conditions to that for the production of C₂⁻ and H₂CC⁻ ions. Due to the large C₂H electron affinity of 2.969 eV^[13], photodetachment at 355 nm occurs close to threshold, yielding slow electrons, allowing for a low repeller voltage (-600 V) on the VMI lens. The resulting photoelectron spectrum, containing 4,017,819 electrons and shown together with the source velocity-map image, is presented in Fig. 12.3.

Below an electron binding energy of $\sim 27,000$ cm⁻¹, transitions may be assigned to the normal mode vectors of $\tilde{X}^2\Sigma^+$. Importantly, transitions involving 1 and 3 quanta of excitation in mode v_2 are observed, confirming the presence of vibronic Herzberg-Teller coupling. Above 27,000 cm⁻¹, peaks are labelled G-L to be consistent with the labelling of the cryo-SEVI spectrum of Ref^[14].

A rotational band model (— — —) for the origin transitions is constructed using NWChem^[94] and PGOPHER^[217] software. Using the rotational constants from the *ab-initio* calculations, and applying the correct symmetry considerations through PGOPHER, the observed rotational band shape in the experimental photoelectron spectrum is modelled. A list of important geometric and spectroscopic constants are given at the end of this chapter in Table 12.4, including values from the *ab-initio* calculations and

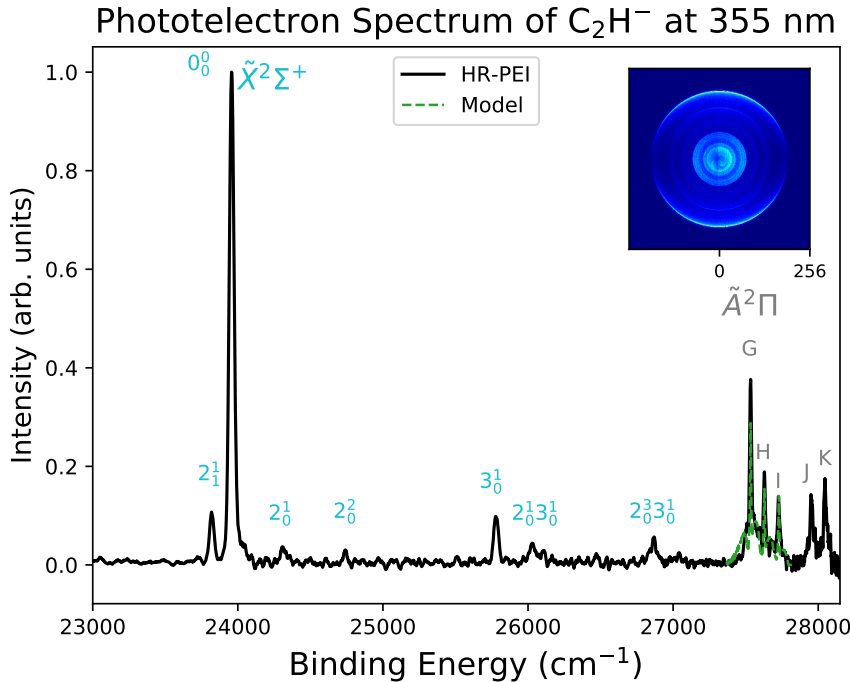


Figure 12.3: Photoelectron spectrum of C_2H^- measured at 355 nm, showing detachment to the ground $\tilde{X}^2\Sigma^+$ and first excited $\tilde{A}^2\Pi$ electronic states. Vibrational transitions in the ground state are assigned to the normal mode vectors in Fig. 12.1, whereas the vibronic transitions of the excited state are labelled alphabetically due to coupling complications in this region. A rotational band model of the origin transitions is included (— — —), along with a raw velocity-mapped image of the detachment as an insert in the top right corner.

the photoelectron spectra of this work, alongside previous theoretical^[244] and experimental^[13,237,238,242,243,245,246] results.

Assigning vibronic levels

Using the calculations of Tarroni and Carter^[241], the observed spectral structure of the $\tilde{A}^2\Pi$ state in the photoelectron spectrum in Fig. 12.3 may be assigned. The large number of vibronic levels present, combined with the often small energy spacings, means that assigning spectral features to the calculated levels is not always straightforward. However symmetry considerations could be used to help narrow down the list of probable assignments, with many of the neutral states exhibiting mixed character.

The electronic origin $\tilde{X}^1\Sigma^+(0,0,0)$ of the anion has Σ^+ symmetry and zero total vibrational angular momentum ℓ (Eq. 2.53). Therefore, only transitions to neutral levels with Σ^+ or Π vibronic symmetry and an even quanta of ℓ will be allowed. The molecular orbital diagram of $\text{C}_2\text{H}^-(\tilde{X}^1\Sigma^+)$ (Fig. 12.4) shows that transitions to the neutral $\tilde{X}^2\Sigma^+$ ground state involve detachment from a σ orbital, whereas transitions to the first excited state $\tilde{A}^2\Pi$ involve a π orbital. Hence, anisotropy measurements may help determine the dominant character of a vibrational transition, with transitions corresponding to the ground state expected to display p -wave character, whereas close to threshold excited state transitions should follow s -wave behaviour.

In the cryo-SEVI experiment, Zhou *et al.*^[14] noted that the magnitude of the spin-orbit

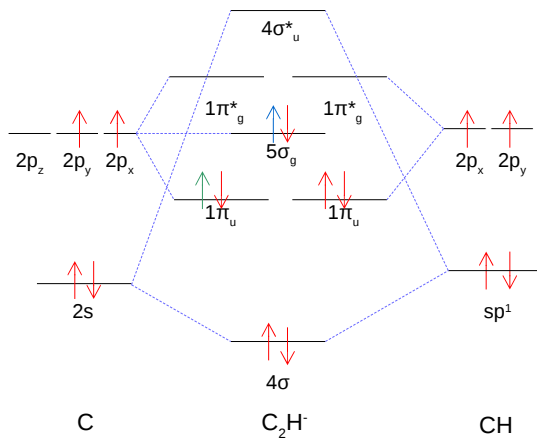


Figure 12.4: Schematic molecular orbital diagram of C_2H^- , showing the bonding structure between the sp^1 bonded CH and the pure C. \uparrow and \downarrow show the electrons that are detached to form the $\tilde{X}^2\Sigma^+$ and $\tilde{A}^2\Pi$ states of the neutral respectively.

splitting of the vibronic levels may also be used as an indicator to estimate the amount of Σ^+ and Π character in the peaks (G–k) in Fig. 12.3, as calculations predict a spin orbit splitting of $\sim 25 \text{ cm}^{-1}$ for the $^2\Pi$ state^[237], as opposed to the small coupling of the Σ^+ state. However, infra-red measurements find spin-orbit splittings for the peaks labelled (G–K) vary from $2.2 - 7.2 \text{ cm}^{-1}$ ^[246], suggesting that these levels contain a mixture of both Σ^+ and Π character, with the magnitude of the splitting separation providing a direct indicator of the percentage of Σ^+ and Π character present.

The assignment of the experimental peaks (G–K), using the energy of vibronic levels of correct symmetry (Σ^+ , Π) calculated by Tarroni and Carter^[241], are given in Table 12.1. As was noted by Zhou *et al.*^[14], the photoelectron intensities correlate with the magnitude of the spin-orbit splitting. This suggests that the measured intensities in the spectrum provide an indication of the extent of \tilde{A} state mixing - likely a result of the good Franck-Condon overlap between the ground anion $\tilde{X}(0, 0, 0)$ and excited neutral $\tilde{A}(0, 0, 0)^1$ origin vibrational levels.

Table 12.1: Assignment of peaks in the C_2H^- photoelectron spectrum around the \tilde{A} origin^[14]. Binding energies and spin-orbit splittings are given in cm^{-1} and intensities in arbitrary units, normalised to the $\tilde{X}^2\Sigma^+(0, 0, 0) \leftarrow \tilde{X}^1\Sigma^+(0, 0, 0)$ origin.

Peak	Assignment	eBE ^b	Intensity ^b	A_{SO}^a	β^b
G	$\tilde{X}(0, 1^1, 2), \tilde{X}(1, 1^1, 0), \tilde{A}(0, 0, 0)^1$	27,535	0.37	-7.22	-0.31(3)
H	$\tilde{X}(1, 1^1, 0), \tilde{X}(0, 1^1, 2), \tilde{A}(0, 0, 0)^1$	27,629	0.19	-5.41	-0.27(5)
I	$\tilde{X}(0, 5^1, 1), \tilde{A}(0, 0, 0)^1$	27,726	0.14	-2.51	-0.23(5)
J	$\tilde{X}(0, 9^1, 0), \tilde{X}(0, 5^1, 1), \tilde{A}(0, 0, 0)^1$	27,951	0.14	-2.22	-0.20(4)
K	$\tilde{X}(0, 9^1, 0), \tilde{A}(0, 0, 0)^1$	28,048	0.17	-3.28	-0.22(4)

^a from infra-red measurements^[247]

^b this work

Table 12.1 shows the correlation between the measured peak intensities and the reported spin-orbit splittings. There is no single $\tilde{A}(0, 0, 0)^1$ electronic origin band, with the transition spread over several mixed vibronic levels, spaced by $\sim 95 \text{ cm}^{-1}$. Interestingly, all of the transitions have similar anisotropy parameters, despite the different percentage

of Σ^+ and Π character estimated for each level by the varying spin-orbit splittings.

Deuterium substitution

A photoelectron spectrum of deuterated ethynyl has been measured at 355 nm, with C_2D^- ions produced in a discharge of pure C_2D_4 gas under similar conditions to those of the C_2H^- measurements. The resulting spectrum, from 4,413,994 electrons, is presented in Fig. 12.5. The C_2H^- photoelectron spectrum is also included for comparison (—). This shows that deuterium substitution has little effect on the ground \tilde{X} state spectrum, however a large change is observed in the region of the \tilde{A} state. At first glance, peaks a – d appear to belong to the \tilde{A} state as the intensity of the transitions looks to rule out pure highly vibrationally excited levels of the ground state. However, assigning the origin $\tilde{A}(0,0,0)^1$ then poses a challenge, as the largest intensity (peak d) occurs at a higher binding energy than peaks a – c. Carter^[44] and Neumark^[14] approached this problem by using the correlation between spin-orbit coupling and \tilde{A} state character observed in the C_2H^- spectrum. Infra-red measurements found that peak d has the largest spin-orbit coupling of -11.17 cm^{-1} , and so it was assumed the largest amount of \tilde{A} character. Due to the large difference in intensity and spin-orbit splitting of peak d Carter and Neumark assigned this to the origin of the $\tilde{A}(0,0,0)^1$ state, while the other peaks a – c were assigned to pure \tilde{X} states, as shown in Table 12.2. However, due to the non-zero spin-

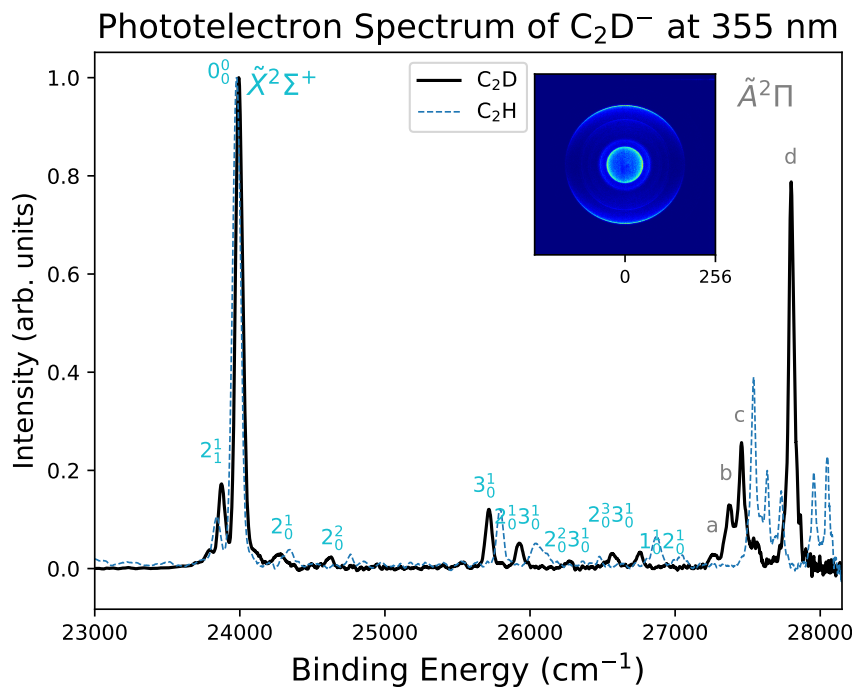


Figure 12.5: Photoelectron spectrum of C_2D^- at 355 nm, showing detachment to the ground $\tilde{X}^2\Sigma^+$ and first excited $\tilde{A}^2\Pi$ electronic states. Transitions near the \tilde{A} state are labelled alphabetically. The C_2H^- PES is included (—) for comparison.

orbit splittings of peaks b and c , along with their corresponding relatively large intensities, this assignment is only an approximation, as these vibronic transitions must possess some \tilde{A} state character. Likewise, the spin-orbit splitting of peak d is still much smaller than the predicted 25 cm^{-1} , suggesting that peak d is also an admixture of \tilde{X} and \tilde{A} states.

Again we see that the anisotropy parameters for peaks a-d all follow a similar anisotropy behaviour. The small variation in β measurements is likely because of the differing electron energies, rather than the character of transitions.

Table 12.2: Assignment of peaks in the C_2D^- photoelectron spectrum around the \tilde{A} origin^[14]. Binding energies and spin-orbit splittings are given in cm^{-1} and intensities in arbitrary units, normalised to the $\tilde{X}^2\Sigma^+(0,0,0) \leftarrow \tilde{X}^1\Sigma^+(0,0,0)$ origin.

Peak	Assignment	eBE ^b	Intensity ^b	A_{SO}^a	β^b
a	$\tilde{X}(0, 5^1, 1)$	27,268	0.02	-	-0.39(5)
b	$\tilde{X}(1, 3^1, 0)$	27,359	0.12	-2.25	-0.37(1)
c	$\tilde{X}(0, 1^1, 2)$	27,444	0.25	-6.36	-0.31(2)
d	$\tilde{A}(0, 0, 0)^1$	27,792	0.71	-11.17	-0.19(3)

^a from infra-red measurements^[247]

^b this work

The large difference in the spectra in Figs. 12.3 and 12.5 around the \tilde{A} origin at $\sim 25,000\text{ cm}^{-1}$ is a remarkable result, as this shows that adding a neutron to the hydrogen has a large effect on the coupling mechanism. However the reason for this effect is not yet understood, as shown by the difficulty that exists in trying to assign the deuterated spectral features.

A 266 nm photoelectron spectrum

To get a better understanding of the $\tilde{A}^2\Pi$ state structure, a shorter wavelength measurement further from photodetachment threshold, is required. For this, the fourth harmonic of the Nd:YAG may be used, however at 266 nm the high photon energy introduces a new set of problems. At 266 nm, the photon energy 4.66 eV is higher than the work function of most metals, and will produce stray electrons from collisions with any metal surfaces. High electron kinetic energies also lower the imaging resolution of the VMI lens. Despite these challenges, careful shaping of the laser beam allowed a 266 nm measurement of C_2H^- photodetachment to be recorded. The resulting spectrum, consisting of 5,003,222 electrons, is shown in Fig. 12.6. The 266 nm spectrum displays similar intensities for transitions around the \tilde{X} ground state, however a difference in the relative intensity between peaks G and K of the \tilde{A} excited state is observed. In the 355 nm spectrum, the intensity of peak G is $\sim 2\times$ peak K, mainly due to the effect of the Wigner law close to threshold, with the 266 nm spectrum showing a much smaller difference. Additional spectral structure of the $\tilde{A}^2\Pi$ state is also observed, with peaks labelled M-S for consistency with the cryo-SEVI spectrum^[14]. These transitions have much lower intensity, suggesting that all of the \tilde{A} origin character is accounted for in peaks G-K.

The velocity map image, inset in Fig. 12.6, possesses a diffuse disk of electrons around the centre of the image. This represents the introduction of background electrons from stray photons hitting metal surfaces. As all of the electrons from anion photodetachment (represented by sharp rings) have kinetic energies significantly higher than the background electrons, a clean spectrum may still be obtained. This is supported by a control measurement of the background noise to help with the image analysis.

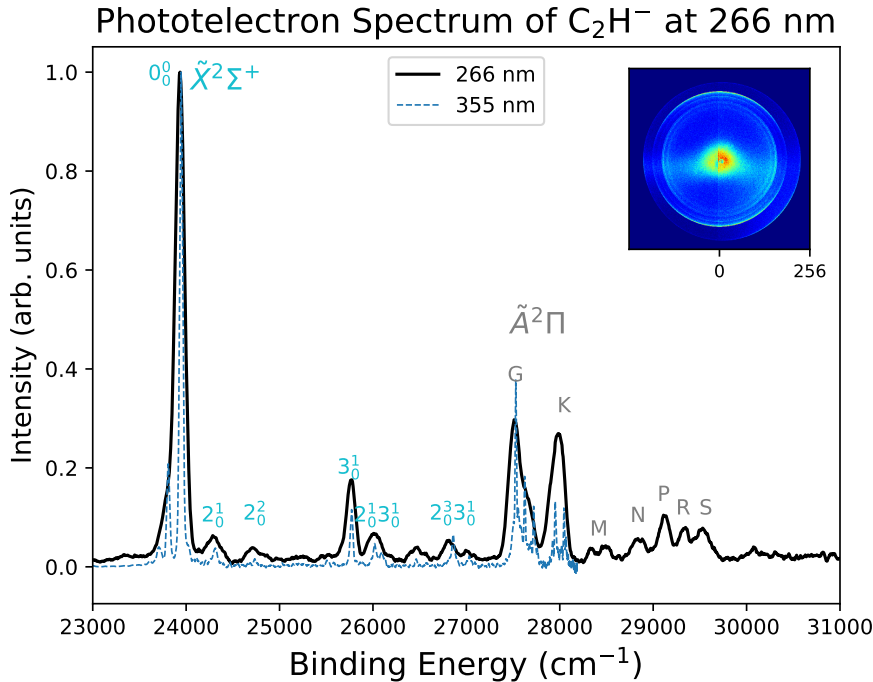


Figure 12.6: 266 nm photoelectron spectrum of C_2H^- . $\tilde{A}^2\Pi$ peaks are labelled alphabetically for consistency with the cryo-SEVI spectrum, with the 355 nm spectrum also shown (—) for comparison. The velocity map image (inset) shows a dramatic change in the anisotropy for the inner rings. The intensity near the image centre is from slow scattered electrons due to the short wavelength.

12.1.4 Questions from the anisotropy

The molecular orbital diagram of C_2H^- in Fig. 12.4 shows that C_2H ($\tilde{X}^2\Sigma^+$) $\leftarrow \text{C}_2\text{H}^-$ ($\tilde{X}^1\Sigma^+$) photodetachment involves ejecting an electron from an s-like $5\sigma_g$ orbital, whereas C_2H ($\tilde{A}^2\Pi$) $\leftarrow \text{C}_2\text{H}^-$ ($\tilde{X}^1\Sigma^+$) detachment occurs from a p-like $1\pi_u$ orbital. The corresponding kinetic energy dependence of the anisotropy parameters in each case may be described using the mixed sp model of Sanov^[34],

$$\beta(\epsilon)_{sp} = \frac{2Z\epsilon + 2A\epsilon^2 - 4\epsilon \cos \Delta_{\ell\pm 1}}{\frac{1}{A} + 2A\epsilon^2 + Z\epsilon} \quad (12.5)$$

where,

$$Z = \frac{1-f}{f} \frac{8}{3} \quad \text{and} \quad |\psi\rangle = \sqrt{1-f}|s\rangle + \sqrt{f}|p\rangle \quad (12.6)$$

and A is the Hanstorp coefficient, $\Delta_{\ell\pm 1}$ the difference in the phase shifts of the partial waves ($\delta_{\ell+1} - \delta_{\ell-1}$), and f is the percentage of p character of the orbital^[248]. Vibrational transitions that belong purely to the $\tilde{X}^2\Sigma^+$ state should follow a curve with $f \sim 0$ whereas $\tilde{A}^2\Pi$ transitions will follow $f \sim 1$. Vibrational levels that are an admixed combination of \tilde{X} and \tilde{A} levels may then be expected to lie somewhere in-between these two curves, allowing for the level of \tilde{X} and \tilde{A} character to be determined.

Anisotropy parameter measurements for transitions in the 355 nm photoelectron spectra of C_2H^- and C_2D^- are shown in Fig. 12.7, alongside the experimental spectra for reference. In the region below 27,000 cm^{-1} , the symmetric transitions all display positive

anisotropies, following the sp curve with $f = 0.1$ (—). Conversely, the totally forbidden modes (odd quanta of v_2) display negative anisotropies, instead following the excited state $f = 0.1$ sp curve (—). This is an indication of vibronic Herzberg-Teller coupling, where forbidden modes display the character of the excited coupled electronic state, as was seen in the study of vinylidene (chapter 11). Transitions in C_2H and C_2D both appear to follow the same anisotropy curves, suggesting that deuteration has little effect on the angular distributions.

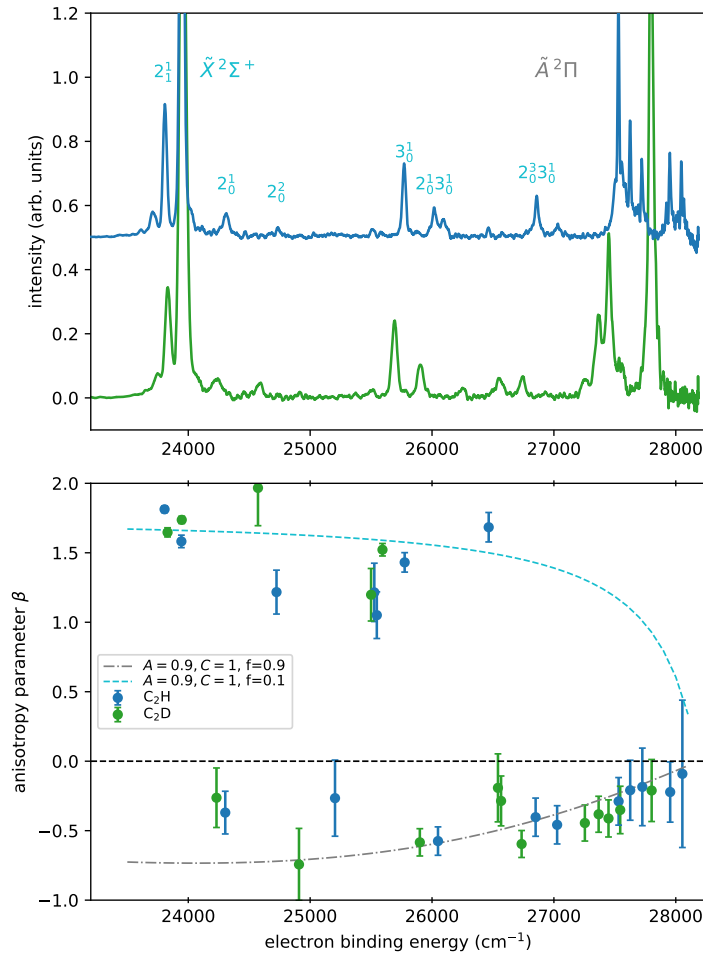


Figure 12.7: Anisotropy parameters for C_2H^- and C_2D^- photodetachment at 355 nm. The photoelectron spectra are included for reference. Transitions to the ground $\tilde{X}^2\Sigma^+$ state follow $f = 0.1$ sp curve (—) while transitions to the excited state $\tilde{A}^2\Pi$ follow $f = 0.9$ (—).

Above 27,000 cm^{-1} , all of the observed transitions show a negative anisotropy, following an $f = 0.9$ sp curve. This would be expected if the transitions in this region were to pure $\tilde{A}^2\Pi$ levels, however the calculations and assignments in section 12.1.3 suggested that these peaks represented an admixture of both \tilde{A} and \tilde{X} state vibrations. Critically, the peaks labelled B and C in the deuterated spectrum in Fig. 12.5 have been assigned to pure ground state vibrational levels $\tilde{X}(1,3^1,0)$ and $\tilde{X}(0,1^1,2)$, however these transitions display a negative anisotropy, consistent with an \tilde{A} state level.

To check that the recorded anisotropy parameters were not influenced by being close to detachment threshold, values were also calculated from the 266 nm C_2H^- spectrum,

and plotted alongside the 355 nm data and the previous 266 nm measurement of Taylor *et al.*^[240], as presented in Fig. 12.8. This shows a similar trend, with the data points between $8,000 - 11,000 \text{ cm}^{-1}$ (representing transitions around the excited $\tilde{A}^2\Pi$ state origin) all following a $f \sim 1$ anisotropy curve, despite the prediction that some of these transitions involve vibrational levels possessing significant \tilde{X} state character.

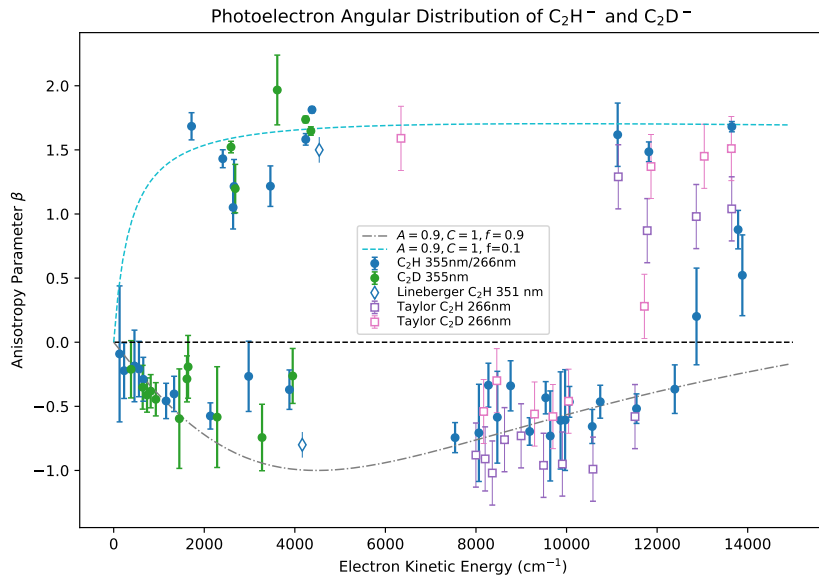
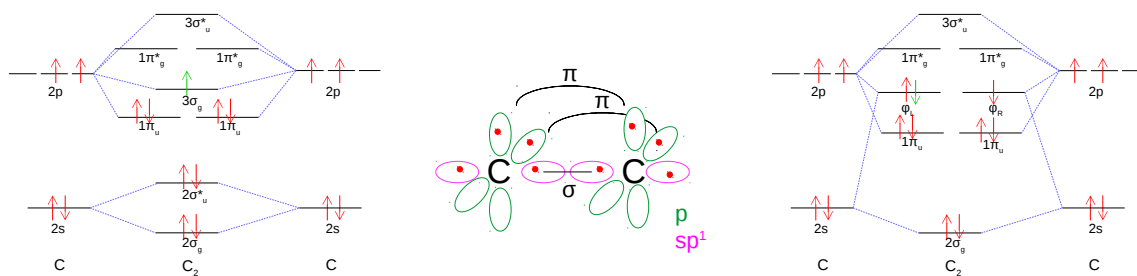


Figure 12.8: Photoelectron angular distribution of C_2H^- and C_2D^- at 355 nm and 266 nm. Previous measurements from Taylor^[240] and Lineberger^[13] are also included.

This suggests that the coupling mechanism responsible for the spectral structure near the \tilde{A} origin may have little effect on the photoelectron angular distribution, as opposed to Herzberg-Teller coupling which plays a dominant role. While the anisotropy of forbidden v_2 transitions is entirely driven by the vibronically coupled state, anisotropies in the \tilde{A} state region show no sign of the pseudo Jahn-Teller ($\Sigma^+ - \Pi^+$) and Renner-Teller ($\Pi^- - \Pi^+$) coupling between the surfaces. This also questions the assignment of peaks B and C in the C_2D^- spectrum, with the anisotropy parameters showing that these levels must possess at least some $\tilde{A}^2\Pi$ character, with the origin of the \tilde{A} level spread over multiple nearby spectral features as it was in the C_2H^- spectrum. The large change in the photoelectron spectrum of C_2H^- and C_2D^- around $27,000 - 28,000 \text{ cm}^{-1}$ suggested that the addition of a neutron to the hydrogen has a large effect on the Renner-Teller and pseudo Jahn-Teller coupling mechanisms. Therefore, the fact that no change was observed in the angular distributions of these two species further suggests that these couplings are not seen by the anisotropy, and thus behave differently to the Herzberg-Teller mechanism.

12.2 Dicarbon and the bonding puzzle

At first glance dicarbon, C_2 , would appear to be a very simple homonuclear diatomic molecule. However, the bonding structure of C_2 has long been a topic of debate, more recently driven by advances in computational methods, with various studies suggesting the carbon-carbon bond may have a bond order of 2, 3, or even 4, with the latter from



(a) Molecular orbital diagram for C_2 , predicting a double bond between the C atoms consisting of 2 π bonds, without an accompanying σ bond. The additional electron for the anion C_2^- is shown in green.

(b) Hybrid-orbital picture of C_2 , involving sp^1 hybridization on the carbon atoms. This approach suggests a triple bonded carbon, with one σ and 2 π bonds.

(c) Orbital diagram for C_2 from a valence-bond viewpoint. Due to the quasi-degenerate nature of orbitals $2\sigma_u$, $3\sigma_g$ and $1\pi_u$, the $2\sigma_u^*$ and $3\sigma_g$ orbitals mix to form sp^1 like hybrid orbitals on each of the carbons. VB theory suggests a fourth bond involving the interaction between the outward pointing φ orbitals.

Figure 12.9: Orbital descriptions of C_2 using different approaches, highlighting the uncertain bond nature of dicarbon, with a double, triple, or quadruple bond structure possible.

ab-initio studies^[16]. Standard qualitative theories predict different values for the dicarbon bond order^[249,250]. From a simple Lewis electron pair repulsion description, the 8 valence electrons in C_2 are predicted to form a quadruple bond. However this bonding assignment seems unlikely, with stable quadruple bonds typically only found between transition metal elements with partially full d -orbitals^[251]. Conversely, a hybrid-orbital (HO) style approach predicts a σ bond and 2 π -bonds between the p -orbitals on the carbons, suggesting that C_2 must be a triple bonded structure (see Fig. 12.9b). However, if molecular-orbital (MO) theory is used, a ground state valence electron configuration for C_2 of $\text{KK}(\sigma_{2s})^2(\sigma_{2s}^*)^2(\pi_{2p})^4$ is predicted, yielding a bond order of 2, and an unusual case of a double π bond with no accompanying σ bond (see Fig. 12.9a). Therefore, reasonable qualitative arguments may be made to predict a bond order of 2, 3, or 4.

With new computational capabilities, more recent theoretical studies suggest that the C–C bond may be best described by a triple or even quadruple bond^[252]. From generalised valence bond theory, the ground state of C_2 is believed to possess a triple bond, consisting of a σ bond and two π bond contributions^[253–255]. However, debate surrounding the nature of C_2 bonding gained momentum when a high level full configuration interaction calculation, combined with valence bond theory (see Fig. 12.9c), suggested the presence of a C_2 quadruple bond, with bonding contributions from a σ bond, $2\times\pi$ bonds, and an interaction between the outward pointing sp^1 hybrid orbitals^[16]. The strength of this inverted bond between the sp^1 orbitals has been calculated at various levels of theory to sit about ~ 12 – 20 kcal/mol^[16,252,256,257]. This description has been supported by subsequent quantum chemistry calculations, also suggesting a bond order above 3, arising from an increase in the electron shielding calculated for C_2 , relative to C_2H_2 ^[258]. However, not all recent studies are in agreement, with some research preferring the notion of a double^[259], triple^[250] or quasi double-triple^[260] bond, while other studies note that the theoretical approaches that have been used are not definitive enough to clearly state whether or not C_2 possesses a quadruple bond^[261–263].

Despite advances in spectroscopic techniques, experimental studies have not been able to confirm any of the suggested bonding structures, with the majority of the debate driven by the results of *ab-initio* calculations^[249]. Due to the highly reactive nature of C₂, most experimental studies have relied on flame emission^[15,264–266] or plasma discharge^[267,268] spectroscopy^[249]. These studies support a bond order between 2 and 3, with a measured C–C bond length of 124.24pm, longer than a typical alkyne triple bond, but shorter than a typical alkene double bond^[15]. Likewise, a measured C–C bond dissociation energy of 602 kJ/mol, as well as a calculated bond resting force of 12 N^[261], also lie between the double and triple bond limits^[269].

However since the dicarbon anion C₂[−] is stable, photoelectron spectroscopy may also be used to probe the unstable C₂ neutral molecule^[13,270,271]. In the case of dicarbon, photoelectron spectroscopy also has the advantage of producing molecules that are vibrationally and rotationally cold, with a typical source temperatures of ∼ 200 K. This produces spectra which are less cluttered by the high rovibrational excitations that are present in flame emission experiments.

The first dicarbon photoelectron experiment was measured by Lineberger *et al.*^[13], in which C₂[−] anions were produced in a O[−]/HCCH afterglow ion source. This ion source produced hotter anions, with multiple hot bands present in the published spectrum. Nevertheless, these earlier results demonstrated one of the most striking observations of the C₂ spectrum: at 355 nm two electronic transitions are observed, but only one vibrational (origin) transition. This contrasts the usual expectation of electronic spacings being three orders of magnitude larger than the typical vibrational spacing - a key assumption of the Born-Oppenheimer approximation. This phenomenon arises from the unusually high vibrational frequency ($\omega_e \approx 1855 \text{ cm}^{-1}$ ^[252]) due to the strong C-C bond, combined with the large number of low lying electronic states from the quasi-degeneracy of the 2σ_u, 3σ_g and 1π_u orbitals.

In the photoelectron paper the C=C bond was stated to be a double bond, on the basis of molecular orbital theory (Fig. 12.9a)^[13]. However, this assignment was made before high level multiconfigurational calculations were available, postulating the possibility of a dicarbon quadruple bond. A later study in 2003 investigated photoelectron imaging of excited states of C₂ and C₂[−] at 264 nm, in coincidence with a 541 nm femtosecond pump laser, to investigate the time-resolved dynamics of the upper states^[271]. However this study did not examine the ambiguity in the dicarbon bonding structure. Consequently, this work revisits the photoelectron spectrum of C₂[−], using the high resolution photoelectron imaging (HR-PEI) spectrometer at the ANU. By examining the electron angular distribution the orbital structure of C₂ may be investigated, in an attempt to try and solve this enigmatic bonding puzzle.

12.2.1 Theoretical discrepancies

While the double-bonded structure described by the molecular orbital diagram in Fig. 12.9a may be considered the standard picture of C₂ bonding from most experimental studies^[13], there has been a lot of discussion from a theoretical viewpoint suggesting that a triple or quadruple bond may provide a more accurate picture of the molecule structure^[252]. These complications arise from the quasi-degeneracy of the 2σ_u, 3σ_g and 1π_u orbitals (responsible for many low-lying excited states of C₂). A lot of this uncertainty is encoded in the nature of the 2σ_u^{*} orbital, which is predicted to be a very weak anti-bonding orbital, with a low occupation number when treated in multiconfigurational space^[16,272].

To account for this, hybridization of the $2\sigma_u^*/3\sigma_g$ states has been proposed, to form sp^1 like orbitals from hybrid orbital theory^[252]. This hybridization produces the quadruple bonded configuration, with bonds formed in the $2\sigma_g$ and $2 \times 1\pi_u$ orbitals, and a fourth bond involving an interaction between the electrons in the sp^1 hybrid orbitals on each carbon (see Fig. 12.9c).

In order to visualize the differences between these possible bonding pictures, *ab-initio* calculations were computed in this work using NWChem^[94] and Q-Chem^[95] software. Most standard methods for approximately solving the Schrödinger equation for molecules are based on Hartree-Fock (or self consistent field) theory, utilising a mean-field approximation. However for molecules with quasi-degenerate or low lying excited states, a multiconfigurational (MCSCF) approach may be required. This approach accounts for states which are a linear combination of different, quasi-degenerate, configurations, allowing for non-integer orbital occupation numbers.

The molecular orbitals for C_2 , using both a SCF/cc-pVTZ and CASSCF/cc-pVTZ methods, were calculated with the results displayed in Fig. 12.10. The key difference between the two approaches is the ordering of the $2\sigma_u^*$ orbital, with the multiconfigurational calculation increasing the orbital energy due to possible mixing between the $2\sigma_u^*/3\sigma_g$ orbitals. This mixing is further encoded in the occupation numbers, with a substantial (~ 0.4) occupation found in the $3\sigma_g$ orbital. As the dominant weight in this mixed orbital lies with the anti-bonding $2\sigma_u^*$, these occupation numbers suggest a bond order of three, consistent with a pure hybrid orbital theory argument^[253]. However if this $2\sigma_u^*/3\sigma_g$ mixing is allowed to occur before the calculation, using hybrid orbitals $\varphi_L = 2\sigma_u + 3\sigma_g$ and $\varphi_R = 2\sigma_u - 3\sigma_g$, the predominant configuration is for each orbital to be singly occupied, with one electron on each of the carbons^[252]. This is consistent with the valence bond picture (Fig. 12.9c), used to suggest a dicarbon quadruple bond, whereas the SCF results are consistent with the double bonded MO picture (Fig. 12.9a). This highlights how reasonable arguments may be made for either bond description.

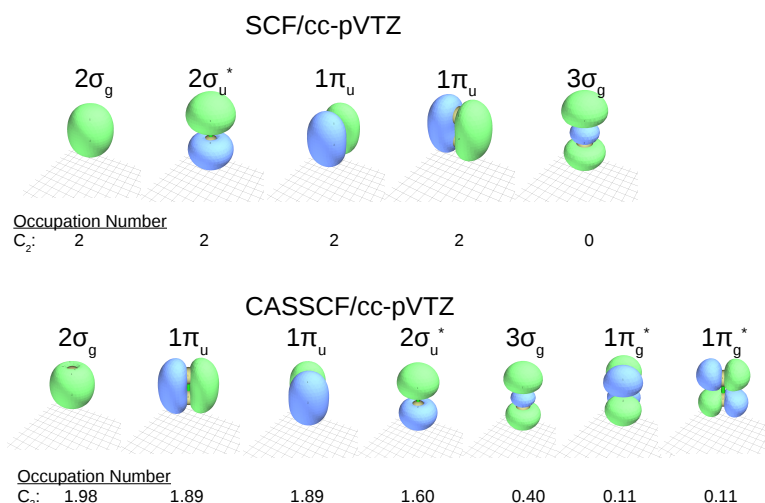


Figure 12.10: Valence molecular orbitals of C_2 (and C_2^-) calculated using NWChem software^[94] for a self consistent field (SCF) and a multiconfigurational complete active space (CASSCF) approach. Orbital occupation numbers are given, with the SCF calculation recreating the molecular orbital diagram in Fig. 12.9a, while the CASSCF orbitals better agree with the VB orbital diagram (Fig. 12.9c).

12.2.2 Problem solving with photoelectron spectroscopy

To try and resolve the uncertainty regarding the bonding nature of dicarbon, photoelectron spectra of C_2^- were measured using the HR-PEI spectrometer. Dicarbon anions are produced in a single pulsed-jet discharge source of pure ethylene, with the subsequent ions mass separated by time-of-flight. Ions are then photodetached at 355 nm using the third harmonic of a Nd:YAG laser, with the electrons mapped onto a detector using velocity map imaging. A photoelectron spectrum, corresponding to 414,511 electrons, is presented in Fig. 12.12. The velocity-mapped image in Fig. 12.11 contains two rings, that correspond to the $\text{C}_2 X^1\Sigma_g^+ \leftarrow \text{C}_2^- X^2\Sigma_g^+$ and $\text{C}_2 a^3\Pi_u \leftarrow \text{C}_2^- X^2\Sigma_g^+$ electronic transitions. However, due to the unusually large bond frequency of $\omega_e \approx 1855 \text{ cm}^{-1}$ ^[252], only the origin vibrational transitions appear to be observed. By modelling the rotational contour of the recorded peaks, precise values for the spectroscopic constants, including the C_2 electron affinity, may be determined as discussed below.

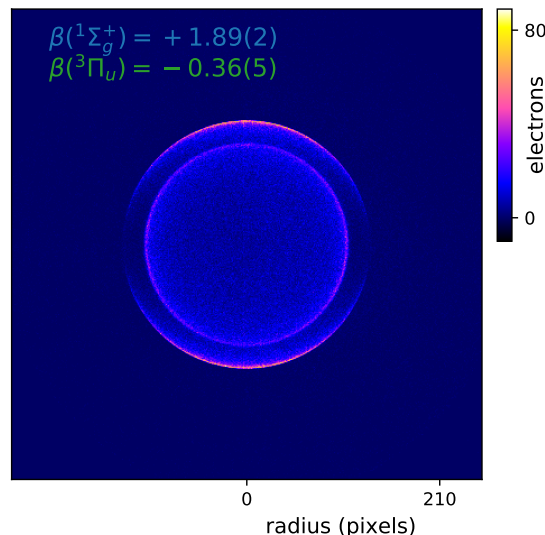


Figure 12.11: Velocity map image of C_2^- at 355 nm containing 414,511 photoelectrons, with the laser polarisation aligned along the vertical axis. Two rings are observed, with the ground ${}^1\Sigma_g^+$ state on the outside, and the first excited $a^3\Pi_u$ state inside. The two rings display opposite anisotropies, with the ${}^1\Sigma_g^+$ electrons preferentially distributed at the poles of the image, and the $a^3\Pi_u$ electrons focused around the centre.

Dicarbon rotational model

Rotational band models for the $\text{C}_2(X^1\Sigma_g^+) \leftarrow \text{C}_2^-(X^2\Sigma_g^+)$ and $\text{C}_2(a^3\Pi_u) \leftarrow \text{C}_2^-(X^2\Sigma_g^+)$ electronic transitions were constructed using similar methods to those in sections 2.1.5 and 5.2. First, the angular momentum coupling scheme involved in each electronic state must be determined. The anion ${}^2\Sigma_g^+$ and ground neutral ${}^1\Sigma_g^+$ states belong to Hund's case (b), where there is small/no spin-orbit coupling. The position of the rotational lines

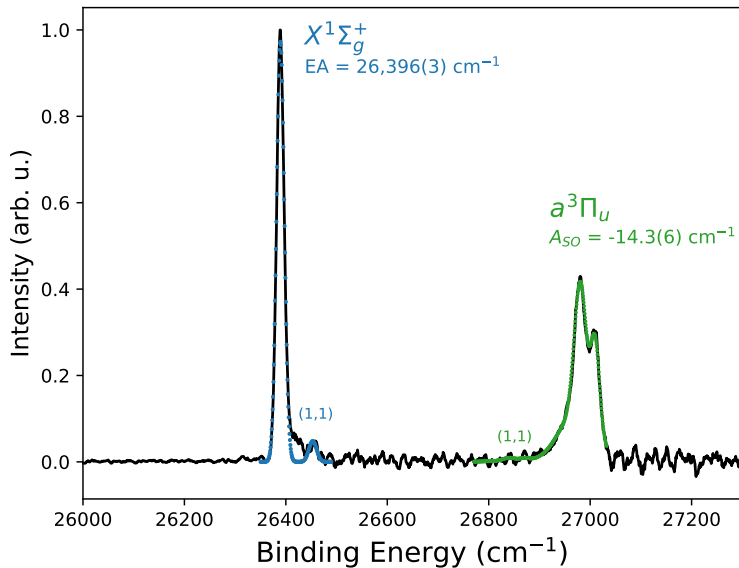


Figure 12.12: Photoelectron spectrum of C_2^- at 355 nm, showing two electronic transitions $\text{C}_2(X^1\Sigma_g^+) + e^- \leftarrow \text{C}_2^-(X^2\Sigma_g^+) + h\nu$ and $\text{C}_2(a^3\Pi_u) + e^- \leftarrow \text{C}_2^-(X^2\Sigma_g^+) + h\nu$, separated by 612 cm^{-1} , with only the origin vibrational transitions present due to the large $\omega_e \approx 1855 \text{ cm}^{-1}$. The splitting on the $a^3\Pi_u$ state is a result of the triplet fine structure splitting combined with the rotational band shape. A rotational model constructed with PGOPHER is also included (\cdots), highlighting the presence of a hot band (1,1).

of the anion ${}^2\Sigma_g^+$ state can then be given by the formula of Mulliken^[273],

$$F_1 = BN(N + 1) + \frac{1}{2}\gamma N \quad (12.7)$$

$$F_2 = BN(N + 1) - \frac{1}{2}\gamma N, \quad (12.8)$$

where F_1 and F_2 are the doublet fine structure components, B is the rotational constant, N is the total nuclear (rotational+vibrational) angular momentum quantum number, and γ is the splitting constant ($= 0.001274 \text{ cm}^{-1}$ ^[104]). For the neutral ground state, where there is no spin-orbit splitting, the levels are simply given by,

$$F = BN(N + 1). \quad (12.9)$$

However the excited ${}^3\Pi_u$ state of the neutral belongs to Hund's case (a) as it experiences strong spin-orbit (LS) coupling. For triplet Π states, Budó^[144,274] has shown that the rotational levels are given by,

$$F_1 = B \left[J(J + 1) - \sqrt{Z_1} - 2Z_2 \right] \quad (12.10)$$

$$F_2 = B \left[J(J + 1) + 4Z_2 \right] \quad (12.11)$$

$$F_3 = B \left[J(J + 1) + \sqrt{Z_1} - 2Z_2 \right] \quad (12.12)$$

$$(12.13)$$

with the values Z_1 and Z_2 are defined as,

$$Z_1 = Y(Y - 4) + \frac{4}{3} + 4J(J+1) \quad (12.14)$$

$$Z_2 = \frac{1}{3Z_1} \left[Y(Y - 1) - \frac{4}{9} - 2J(J + 1) \right] \quad (12.15)$$

where B is the rotational constant of the molecule, Y is the ratio of the spin-orbit and rotational constants $Y = A_{SO}/B$, and J is the total angular momentum quantum number.

Next, selection rules need to be applied to determine the allowed transitions. For electronic states with $\Lambda = 0$ (ie. Σ) the molecule may be treated as a rigid rotor with $\Delta J = \pm 1$, whereas states with $\Lambda \neq 0$ (ie. Π) may be treated as a symmetric top with $\Delta J = 0, \pm 1$. For all cases, in the dipole approximation only transitions from symmetric to antisymmetric, or antisymmetric to symmetric are allowed,

$$+ \rightarrow - \quad \text{and} \quad - \rightarrow +$$

Furthermore, for homonuclear diatomics (such as C_2) the symmetry of subsequent rotational levels alternate. For electronic states which are symmetric under inversion (ie. Σ_g^+) even J levels are symmetric (+) while odd J levels are antisymmetric (-). Finally, as C^{12} has a net nuclear spin of zero ($I = 0$), only the symmetric transitions are allowed^[144].

Lastly, the intensity of each transition may be calculated. As C_2 is a diatomic molecule, the method of Buckingham *et al.* may be used, which employs Wigner 3-j symbols to calculate the angular momentum couplings involved in the transitions.^[27] For the ground state $C_2(X^1\Sigma_g^+) \leftarrow C_2^-(X^2\Sigma_g^+)$ photodetachment, the Q-factor for a case (b) to case (b) transition may be used,

$$Q = (2N' + 1) \begin{pmatrix} N' & j_t & N'' \\ -\Lambda' & \Delta\Lambda & \Lambda'' \end{pmatrix}^2 \quad (12.16)$$

where j_t is a variable ranging from $|\lambda - 1|$ to λ , and Λ is the axial component of the orbital angular momentum. For the case of ground state C_2 , $\Lambda' = \Lambda'' = \Delta\Lambda = 0$, so the Q-factor becomes,

$$Q = (2N' + 1) \begin{pmatrix} N' & j_t & N'' \\ 0 & 0 & 0 \end{pmatrix}^2 \quad (12.17)$$

which may be computed for every transition from level N'' in the anion to N' in the neutral.

Similarly, the rotational transition intensities involved in the excited state $C_2(a^3\Pi_u) \leftarrow C_2^-(X^2\Sigma_g^+)$ photodetachment may be calculated using the Q-factor for a case (b) to case (a) transition,

$$Q = \frac{2J' + 1}{2S' + 1} \sum_{\chi=j_t-1/2}^{j_t+1/2} (2\chi + 1) \begin{pmatrix} j_t & S' & \chi \\ \Delta\Lambda & \Sigma' & \Lambda'' - \Omega' \end{pmatrix}^2 \begin{pmatrix} J' & \chi & N'' \\ -\Omega' & \Omega' - \Lambda'' & \Lambda'' \end{pmatrix}^2 \quad (12.18)$$

where S' is the spin of the neutral, Σ' is the axial component of the spin, and Ω' is the combined LS momentum. For C_2 , $S' = 1$, $\Lambda' = 1$, $\Lambda'' = 0$, $\Delta\Lambda = 1$, and $\Omega' = \Lambda' + \Sigma'$, so

the Q-factor becomes,

$$Q = \frac{2J' + 1}{2S' + 1} \sum_{\chi=j_t-1/2}^{j_t+1/2} (2\chi + 1) \begin{pmatrix} j_t & 1 & \chi \\ 1 & \Omega' - 1 & -\Omega' \end{pmatrix}^2 \begin{pmatrix} J' & \chi & N'' \\ -\Omega' & \Omega' & 0 \end{pmatrix}^2 \quad (12.19)$$

which may be computed for every transition from level N'' in the anion to $J'\Omega'$ in the neutral.

From the above equations, a rotational band model may be constructed and fitted to the experimental photoelectron spectrum (Fig. 12.12). The rotational contour highlights additional structure to the right (high binding energy) side of the origin $C_2(X^1\Sigma_g^+) \leftarrow C_2^-(X^2\Sigma_g^+)$ transition. This is likely a signature of the (1,1) hot band, expected to sit ~ 73 cm $^{-1}$ above the (0,0) origin. An anion source temperature of $T = 197(2)$ K is extracted from the model, while the energy resolution for each peak $\Gamma_{X^1\Sigma} = 17(1)$ cm $^{-1}$ and $\Gamma_{a^3\Pi} = 19(1)$ cm $^{-1}$ is also reasonable for the ANU spectrometer at electron kinetic energies of $E \sim 0.5$ eV.

The rotational band model provides an accurate position for the band origin, allowing for precise determination of spectroscopic constants, which are presented in Table 12.4. The spectrum may be calibrated using the term energy ($T_e = 718.318(1)$ cm $^{-1}$) of the excited $a^3\Pi_u$ state, which is already well defined from neutral microwave spectroscopy studies^[275]. As the term energy is defined as the energy from the bottom of the $X^1\Sigma$ potential well to the bottom of the $a^3\Pi$ well, the expected energy spacing between the $X^1\Sigma$ and $a^3\Pi$ transitions in the photoelectron spectrum is given by,

$$\begin{aligned} \Delta E &= T_e + {}^3\Pi_{ZPE} - {}^1\Sigma_{ZPE} \\ &= 612.1 \text{ cm}^{-1} \end{aligned}$$

where ZPE refers to the zero potential energy.

From this calibration of the high resolution spectrum presented here, a precise value for the electron affinity of $EA = 3.2727(4)$ eV is determined, which is in good agreement with the previously accepted value of Lineberger *et al.* of $EA = 3.269(6)$ eV^[13]. A precise value for the anion rotational constant of $B = 1.746(1)$ is also extracted.

Table 12.3: Spectroscopic constants (cm $^{-1}$) of C_2 and C_2^- , extracted from the HR-PEI spectrum of this work (Fig. 12.12), compared to previous measurements.

		HR-PEI	Previous Work
C_2^-	$X^2\Sigma_g^+$	B	1.746(1)
C_2	$X^1\Sigma_g^+$	EA	26,396(3)
		B	1.820(1)
C_2	$a^3\Pi_u$	T_e	718(1)
		A_{SO}	-14.3(6)
		B	1.635(4)
			718.318(1) ^d
			-15.272(3) ^d
			1.6324(6) ^d

^a from infrared study of Rehfuss *et al.*^[276]

^b from photoelectron spectroscopy of Lineberger *et al.*^[13]

^c from infrared study of Davis *et al.*^[277]

^d from flame emission spectroscopy of Amiot *et al.*^[275]

Answer in the anisotropy

A qualitative description of the anisotropy parameter may be determined by visual inspection of the velocity map image in Fig. 12.11. Noticeably, the two electronic transitions have opposite anisotropies, with the $X^1\Sigma_g^+$ electrons preferentially distributed at the poles of the image signalling a strong positive anisotropy, whereas the $a^3\Pi_u$ electrons appear to have a slight negative anisotropy, with the distribution skewed towards the horizontal.

Quantitative values are obtained by fitting Eq. (2.26) to radially integrated transition intensities, as a function of angle. Applying this to the velocity mapped image in Fig. 12.11 gives anisotropy parameters $\beta(X^1\Sigma_g^+) = +1.89(2)$, and $\beta(a^3\Pi_u) = -0.36(5)$.

The measured anisotropy parameters may be linked directly to the interference of detachment partial waves by the well known Cooper-Zare anisotropy formula, applicable for a central potential

$$\beta_\ell = \frac{\ell(\ell-1)\chi_{\ell,\ell-1}^2 + (\ell+1)(\ell+2)\chi_{\ell,\ell+1}^2 - 6\ell(\ell+1)\chi_{\ell,\ell+1}\chi_{\ell,\ell-1}\cos\Delta_{\ell\pm 1}}{(2\ell+1)[\ell\chi_{\ell,\ell-1}^2 + (\ell+1)\chi_{\ell,\ell+1}^2]}, \quad (12.20)$$

where $\chi_{\ell,\ell\pm 1}$ is the radial transition dipole matrix element for the $\ell \pm 1$ partial wave emitted from the initial atomic orbital ℓ , and $\Delta_{\ell\pm 1}$ is the difference in the corresponding phase shifts^[29]. Qualitatively, Eq. (12.20) describes the variation of the anisotropy of an electron distribution with kinetic energy, for detachment from an orbital with angular momentum ℓ . Therefore a measurement of the anisotropy of C_2^- detachment, gives the character of the relevant molecular orbitals.

For an s orbital, with $\ell = 0$, Eq. (12.20) becomes,

$$\beta_s = \frac{2\chi_{0,1}^2}{\chi_{1,0}^2} = 2. \quad (12.21)$$

A strong positive anisotropy close to +2, such as $\beta(X^1\Sigma_g^+) = +1.89(2)$, is indicative of s orbital character. Conversely, for a p orbital with $\ell = 1$, Eq. (12.20) becomes,

$$\beta_p = \frac{2A^2\epsilon^2 - 4A\epsilon\cos\Delta_{\ell\pm 1}}{1 + 2A^2\epsilon^2}, \quad \text{where } A\epsilon = \frac{\chi_{1,2}^2}{\chi_{1,0}^2} \quad (12.22)$$

Eq. (12.22) shows that as $\epsilon \rightarrow 0$, $\beta \rightarrow 0$. A negative β parameter close to threshold, such as $\beta(a^3\Pi_u) = -0.36(5)$, is typical of detachment from a p -like orbital, as seen in similar diatomic molecules BN^- ^[278] and NO^- ^[108,279] where an electron is detached from a π orbital.

Assuming that the relevant molecular orbitals in C_2^- may be accurately described by a mixture of s and p character, photodetachment will be governed by the modified Cooper-Zare equation^[56,280],

$$\beta_{sp} = \frac{2Z\epsilon + 2A\epsilon^2 - 4\epsilon\cos(\delta_2 - \delta_0)}{\frac{1}{A} + 2A\epsilon^2 + Z\epsilon}, \quad (12.23)$$

where

$$Z = \frac{1-f}{f} \frac{B}{A} \quad \text{and} \quad |\psi_{\text{HOMO}}\rangle = \sqrt{1-f}|s\rangle + \sqrt{f}|p\rangle \quad (12.24)$$

Parameters A and B from Eq (12.24) represent the scaling of the different radial dipole integrals, with the ratio $B/A=8/3$ for $2s/2p$ mixing, while $\cos(\delta_2 - \delta_0)$, the phase shift

between the outgoing waves, is ≈ 1 ^[280]. This leaves the parameter f , associated with the fractional percentage of s and p character ($f=0$ for pure s , $f=1$ for pure p), and the Hanstorp coefficient A in Eq. 12.23, as the only fitting parameters.

The anisotropy measurements of C_2^- photodetachment at 355 nm to the ground and first excited neutral states are plotted in Fig. 12.13. In a study of excited-state C_2^- photoelectron imaging, Bragg *et al.*^[271] measured anisotropy parameters for detachment at 264 nm which are also included. By fitting the anisotropy measurements from both wavelengths to the sp character model (Eq. 12.23) values for the Hanstorp coefficients A and fractional character percentage f may be determined. This fitting process gave a value of $A = 0.4 \text{ eV}^{-1}$ for $X^1\Sigma_g^+ \leftarrow X^2\Sigma_g^+$ detachment, and a value of $A = 0.7 \text{ eV}^{-1}$ for the excited $a^3\Pi_u \leftarrow X^2\Sigma_g^+$ transition.

The effect of varying the orbital character f on the anisotropy curve may then be examined. Anisotropy curves are plotted as a function of electron kinetic energy in Fig. 12.13 for a variety of values of f , representing different sp orbital character percentages. This graph highlights a general rule of sp mixing, with a higher percentage of s character associated with a β close to +2, while orbitals with more p character produce β parameters close to -1. This suggests that the transition $C_2 X^1\Sigma_g^+ + e^- \leftarrow C_2^- X^2\Sigma_g^+ + h\nu$ involves the ejection of an electron from a predominantly s -like orbital, whereas the excited state $a^3\Pi_u \leftarrow X^2\Sigma_g^+$ transition involves an electron ejected from a p -like orbital. Quantitative values for the amount of s and p orbital character may be determined using the Hanstorp coefficients from above, with detachment to the neutral ground state involving an orbital with at least 90% s character, whereas the excited state transition involves an orbital with ~5% s character.

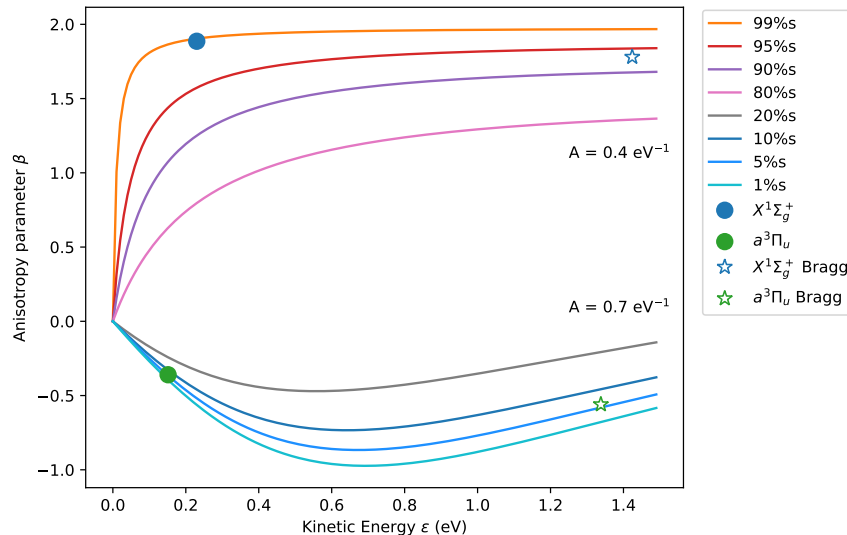


Figure 12.13: Anisotropy parameters for C_2^- photodetachment at 355 nm (this work) and at 264 nm (Neumark^[271]). Detachment to the ground $X^1\Sigma_g^+$ state has a Hanstorp coefficient of $A = 0.4 \text{ eV}^{-1}$ with an orbital character of $f > 90\%$ s , whereas detachment to the excited $a^3\Pi_u$ state has a Hanstorp coefficient of $A = 0.7 \text{ eV}^{-1}$ and an orbital character of $f = 5\%$ s .

Each of the bonding schemes, double, triple, and quadruple, may be compared with

the above limits to deduce which one best aligns with the orbital information gained from the experimental measurements. The double bonded structure suggested by the molecular orbital diagram in Fig. 12.9a, predicts the $\text{C}_2\text{X}^1\Sigma_g^+ + e^- \leftarrow \text{C}_2^-\text{X}^2\Sigma_g^+ + h\nu$ transition involves detaching an electron out of the $3\sigma_g$ bonding orbital. Conversely, the transition to form the lowest triplet state ($a^3\Pi_u$) would involve detachment from the $1\pi_u$ bonding orbital. As the $3\sigma_g$ orbital possesses predominant *s*-character, and the $1\pi_u$ orbital possesses significant *p*-character (Fig. 12.10), this orbital scheme is consistent with the angular distributions measured in Fig. 12.11, satisfying the orbital character requirements of at least 90% *s* and 95% *p* for the singlet and triplet transitions respectively.

The triple bonded structure, predicted by hybrid orbital theory (Fig. 12.9b), suggests C_2 possesses a σ bond, 2 π bonds, and singly occupied sp^1 orbitals on each of the carbons. However as the sp^1 hybrid orbitals will have close to 50% *s* and 50% *p* character, they are not suitable for either the singlet or triplet detachment. Multiconfigurational CASSCF calculations have also been used to predict a C_2 bond order of 3, with a calculated electron configuration of $\text{KK}(2\sigma_g)^2(1\pi_u)^2(1\pi_u)^2(2\sigma_u^*)^{1.6}(3\sigma_g)^{0.4}$ (Fig. 12.10). Detachment to the $\text{X}^1\Sigma_g^+$ ground state would most likely occur out of what is primarily a $3\sigma_g$ orbital, however as this is mixed with both the $2\sigma_u^*$ and higher lying $1\pi_g^*$ orbitals, achieving an *s* character purity of over 90% would seem unlikely. Furthermore, the triplet transition may involve detachment from what is primarily a $2\sigma_u^*$ orbital which, especially when orbital mixing with $3\sigma_g$ is accounted for, is unlikely to satisfy the 95% *p* character requirement.

Likewise, the suggestion of a quadruple bond faces a similar problem. In this scenario it is suggested there is a σ and 2 π bonds, as before, as well as a weak bond-like interaction between the singly occupied sp^1 hybrid orbitals on the carbons. However even if the HOMO/LUMO orbitals are not pure 50:50 sp^1 orbitals, it is very unlikely that they would represent over 90% *s* purity, as is required for the $\text{C}_2(\text{X}^1\Sigma_g^+) + e^- \leftarrow \text{C}_2^-(\text{X}^2\Sigma_g^+) + h\nu$ transition.

Therefore, the experimental anisotropy measurements of C_2^- recorded in this work, indicate that an electron configuration for the $\text{C}_2^-(\text{X}^2\Sigma_g^+)$ anion of $\text{KK}(2\sigma_g)^2(2\sigma_u^*)^2(1\pi_u)^2(1\pi_u)^2(3\sigma_g)^1$ is most likely. This would appear to best support the notion of a $\text{C}=\text{C}$ double bonded structure, with the unusual property of having 2π bonds without an accompanying σ bond. This would also appear to be in agreement with the other experimental observations that have been made, namely the measured C-C bond length of 1.243 Å^[15], which lies between the standard length of a double and triple bond. As has been suggested previously, the fact that this is slightly shorter than a typical hydrocarbon $\text{C}=\text{C}$ double bond may be due to the unique nature of having 2π bonds as opposed to the standard $\sigma+\pi$ bond configuration^[252,281]. The experimental measurement presented here indicates that a double bonded dicarbon molecule appears the most likely equilibrium structure, despite what some calculations and theoretical approaches have suggested recently.

Table 12.4: Geometric and spectroscopic constants of the anion $\text{C}_2\text{H}^- (\tilde{X}^1\Sigma^+)$ and the neutral $\text{C}_2\text{H} (\tilde{X}^2\Sigma^+)$ and $\text{C}_2\text{H} (\tilde{A}^2\Pi)$ states. Values from both experimental and *ab-initio* studies are included.

	r_{CC} (Å)	r_{CH} (Å)	B_e (cm $^{-1}$)	A_{SO} (cm $^{-1}$)	ω_1 (cm $^{-1}$)	ω_2 (cm $^{-1}$)	ω_3 (cm $^{-1}$)
$\text{C}_2\text{H}^- \tilde{X}^1\Sigma^+$							
CCSD(T) ^a	1.266	1.086	1.3513	0	3343	556	1868
QFF ^b	1.252	1.058	1.387	0	3387	541	1884
HR-PEI ^c			1.34(2)			518(5)	
PES ^d			1.3889354(1)	0		505(20)	1800(20)
$\text{C}_2\text{H} \tilde{X}^2\Sigma^+$							
CGSD(T) ^a	1.294	1.075	1.3039	0	3455	360	1788
QFF ^b	1.219	1.043	1.4581	0	3451	413	2029
HR-PEI ^c			1.46(1)		3490(30)	367(4)	1839(4)
Infra-red ^e			1.4568256(2)		3398.853(1)	371.6034(3)	1840.5711(4)
$\text{C}_2\text{H} \tilde{A}^2\Pi$							
EOM-CCSD(T) ^a	1.270	1.075	1.3439		3424	470	1714
QFF ^b	1.273	1.071	1.3448		3091	593	1867
HR-PEI ^c			1.39(2)				
Matrix ^f			-8.423(3)	3021	542	1852	
Infra-red ^g	1.289	1.060	1.40529(1)	-7.219(2)			

^a Calculations of this work, computed with NWChem software^[94]

^b Quartic force field *ab-initio* calculations by Morgan *et al.*^[244]

^c Values from the experimental C_2H^- high resolution photoelectron imaging spectra, presented in this work.

^d Photoelectron spectrum of C_2H^- measured by Lineberger *et al.*^[13]

^e Experimental values from infra-red experiments by Killan *et al.*^[242] and Kanamori *et al.*^[243,245]

^f Values from solid neon matrix experiments of Forney *et al.*^[238]

^g Experimental values from infra-red study of the excited state by Sharp-Williams *et al.*^[246] and Yan *et al.*^[237]

Concluding Remarks

The research of this thesis has employed high resolution photoelectron imaging, combined with theoretical and *ab-initio* approaches, to study various isomerization puzzles. Anion photoelectron spectroscopy obtains information about both the parent negative ion and the neutral molecule, including transient species, not accessible by standard spectroscopic techniques. This has allowed species with very fast isomerization dynamics, such as vinylidene, to be investigated in detail. Other molecules with high chemical reactivity, such as C₂ and NOO, also benefit from the stability of a parent negative anion, which is used to provide spectroscopic information. In this thesis, HR-PEI state of the art resolution, with full angular information, presents new detail on spectroscopic signatures that characterise the dynamics of isomerisation, and transient species, while also providing precise determination of various spectroscopic constants.

In a benchmark study of NO₂⁻ photodetachment, the missing peroxy isomer NOO has been observed for the first time and characterised spectroscopically. Previous photodetachment cross section experiments have hinted that another isomer of nitrogen dioxide may exist, however studies before this work had failed to find any further evidence. High kinetic energy electrons were observed in a near threshold photodetachment experiment of NO₂⁻ at 519 nm, that can not be associated with the C_{2v} isomer of NO₂. Spectral analysis confirmed that this high energy structure is from the C_s peroxy isomer NOO. The similarity of the NOO⁻ photoelectron spectrum to that from NO⁻, including the small electron affinity (335 cm⁻¹) and negative anisotropy, suggests that the molecule may behave more like NO than its C_{2v} isomer ONO. This isomer is also likely to be much more reactive than the common isomer ONO due to its weak, long O–O bond. Previous work has predicted that the existence of NOO may have large implications in atmospheric science, particularly in relation to the formation of NO in the Earth's ionosphere^[4]. Similar reactions have also been observed for HOON, where photolysis of the weak O–O peroxy bond is involved in many radical reactions^[122]. These works, suggest that any presence of peroxy NOO is likely to play a significant role in the chemistry of planetary atmospheric NO₂.

A second section of this work tackles the long-standing problem of the vinylidene – acetylene isomerisation. The 1,2-hydrogen migration is a common mechanism in more complex organic reactions, making this an attractive area of research as a prototypical study. However, the dynamics of the vinylidene isomer are still poorly understood, in part due to conflicting experimental results. Photoelectron spectra of the vinylidene anion reveal the presence of forbidden non-totally symmetric vibrational modes, that are associated with a discrete jump in the anisotropy parameter. This is interpreted as a consequence of Herzberg-Teller coupling between the ground \tilde{X}^1A_1 and a high lying (~ 4 eV) \tilde{B}^1B_2 excited state. This vibronic coupling proved to be vital to the isomerization mechanism, with vinylidene-acetylene pathways found through allowed 6², Herzberg-Teller 6¹, and an-harmonically coupled 5¹ \sim 1¹6¹ transitions. Spectral signatures possessing an admixture of both vinylidene and highly excited acetylene local-bender character were discovered, providing a map of the doorway vibrational states through which the isomerization proceeds.

Similar coupling phenomena are also seen in a study of the ethynyl radical C_2H^- . Forbidden non-totally symmetric vibrational modes are observed in the photoelectron spectrum, with an associated sign change in the anisotropy parameter. This is due to Herzberg-Teller coupling between the ground $\tilde{X}^2\Sigma^+$ and excited $\tilde{A}^2\Pi$ electronic states. However, the spectrum is further complicated by additional coupling mechanisms, with Renner-Teller coupling causing the Π surface to split into non-degenerate Π^+ and Π^- states, accompanied by a pseudo Jahn-Teller effect between the Σ^+ and Π^+ surfaces. The calculations of Tarroni and Carter^[241] assign the observed spectral features in both C_2H^- and C_2D^- , however discrepancies between the assignments and the measured anisotropy parameters suggest that this picture is not yet complete.

Another long-standing problem, regarding the bond nature of dicarbon, has also been investigated. Qualitative arguments may be made to support either a double, triple, or quadruple bonding scheme, with recent *ab-initio* studies suggesting that a quadruple bond may be most likely. Anisotropy measurements of C_2^- photodetachment reveal important information about the molecule orbital structure, with detachment to the ground state involving an orbital with at least 90% *s*-character, and detachment to the excited state involving an orbital with $\sim 5\%$ *p*-character. This is only consistent with the molecular orbital view of the bonding, supporting a dicarbon bond order of 2.

High resolution studies of NO_2^- , NO^- , O_2^- , and O^- demonstrate the versatility of the HR-PEI spectrometer, with photoelectron spectra resolving electronic, vibrational, spin-orbit, and in the case of NO_2^- , rotational structure. Together with information from the photoelectron angular distributions, along with *ab-initio* calculations, and spectral modelling, this provides a more complete picture of both the detachment process, and the structure of the neutral and anionic molecules. Near threshold anisotropy measurements have highlighted the importance a small amount of *p* orbital character can have on the photodetachment dynamics, with the corresponding *s* partial wave shown to dominate the anisotropy at very low electron kinetic energies. Studies of NO_2^- and NO^- both observed this effect, even though the *p* orbital character accounted for less than 2% of the detachment orbital.

Future Directions

This study has focussed on isomerisation systems where one of the isomers is much less stable, a reactive species that sits at higher energy, in a shallow potential well. Consequently, these isomers have many interactions, with vibronic couplings found to have signatures in the photoelectron kinetic energy and angular distributions. Better understanding of excited state vibronic structure, from short wavelength HR-PEI and cryo-SEVI measurements, combined with studies of similar molecules, has helped to decompose the observed spectral structure. This research combines cutting edge photoelectron spectroscopy with rovibrational modelling and high-level *ab-initio* calculations, to produce a more complete picture of the isomerisation dynamics, providing insights that help solve complex problems. With several problems successfully examined, this approach provides a template for future studies.

Other carbene isomer systems would also be an interesting area to examine, providing a window for 1,2-hydrogen migration in more complex molecules. Examples of similar isomerisation systems, such as methyl-acetylene and allene, keto-enol, and tropolone, would all be interesting systems to study. More detailed, short wavelength HR-PEI measurements of H_2CC^- , accessing the excited $\tilde{B}^1\text{B}_2$ state may also provide further information

on how Herzberg-Teller coupling between two states is encoded in the anisotropy of a photoelectron distribution. In particular, comparing the value of β for the excited \tilde{B}^1B_2 state to those of the forbidden v_5 and v_6 transitions, to see whether the coupled vibrations lie between the ground and excited state values, or if they exhibit the pure character of the excited coupled state. This may provide some insight to the ethynyl coupling conundrum, where states of supposed mixed $\tilde{X}^1\Sigma_g^+$ and $\tilde{A}^3\Pi_u$ character all exhibit the same excited state anisotropy behaviour.

Modifications to the HR-PEI spectrometer is also an interesting area to examine. The source end of the spectrometer operates at 30 Hz, with the imaging section at 10 Hz (only every third ion packet is photodetached), it is possible to reconfigure the spectrometer so that absolute photodetachment cross sections may be measured. Switching the MCP at 30 Hz to detect the ion signal when the laser is off, and the electrons when the laser is on, would allow for the ion density to be recorded simultaneously in real time during a photoelectron spectroscopy experiment. Monitoring variations in the laser power at the output window of the spectrometer, combined with the ion density and electron count rate measurements would then allow for absolute cross sections to be measured.

Development of an electron ionisation (EI) source may help increase the production of negative ions, allowing for more exotic ions to be investigated. A dual cage EI source, based on the work of Amirav *et al.*[²⁸²] has been proposed as a suitable option for implementation in the HR-PEI spectrometer. Improved anion production will enhance the photoelectron signal, to provide better photoelectron spectra and angular distributions. This may also allow for individual quadrant analysis of the velocity map images, which involves less image distortion, providing higher energy resolution, but requires a larger photoelectron signal.

Ultimately, this thesis has shown how intriguing molecular puzzles may be solved by carefully decoding spectral signatures. By tackling a problem from various different approaches, both experimental and theoretical, a more complete description of a molecule and its dynamics may be obtained, allowing for various interesting questions to be answered. As high resolution photoelectron imaging collects both angular and energetic information over a wide detection range, it has proven to be an excellent technique with which to investigate negative ions, neutral molecules, and the nature of isomerization.

Bibliography

- [1] H. Eyring, “The activated complex in chemical reactions,” *The Journal of Chemical Physics*, vol. 3, pp. 107–115, 1935.
- [2] M. G. Evans and M. Polanyi, “Some applications of the transition state method to the calculation of reaction velocities, especially in solution,” *Transactions of the Faraday Society*, vol. 31, pp. 875–894, 1935.
- [3] D. M. Neumark, “Transition state spectroscopy,” *Science*, vol. 272, pp. 1446–1447, 1996.
- [4] M. A. A. Clyne and B. A. Thrush, “Kinetics of the reactions of active nitrogen with oxygen and with nitric oxide,” *Proceedings of the Royal Society of London A*, vol. 261, pp. 259–273, 1961.
- [5] E. Herbst, T. A. Patterson, and W. C. Lineberger, “Laser photodetachment of NO_2^- ,” *The Journal of Chemical Physics*, vol. 61, pp. 1300–1304, 1974.
- [6] J. H. Richardson, L. Stephenson, and J. I. Brauman, “Photodetachment of NO_2 : experimental evidence for a new isomer,” *Chemical Physics Letters*, vol. 25, pp. 318 – 320, 1974.
- [7] D. Dunkin, F. Fehsenfeld, and E. Ferguson, “Thermal energy rate constants for the reactions $\text{NO}_2^- + \text{Cl}_2 \rightarrow \text{Cl}_2^- + \text{NO}_2$, $\text{Cl}_2^- + \text{NO}_2 \rightarrow \text{Cl}^- + \text{NO}_2\text{Cl}$, $\text{SH}^- + \text{NO}_2 \rightarrow \text{NO}_2^- + \text{SH}$, $\text{SH}^- + \text{Cl}_2 \rightarrow \text{Cl}_2^- + \text{SH}$, and $\text{S}^- + \text{NO}_2 \rightarrow \text{NO}_2^- + \text{S}$,” *Chemical Physics Letters*, vol. 15, pp. 257 – 259, 1972.
- [8] E. R. Grumbling, K. Pichugin, L. Velarde, and A. Sanov, “Further evidence for resonant photoelectron-solvent scattering in nitrous oxide cluster anions,” *The Journal of Physical Chemistry A*, vol. 114, pp. 1367–1373, 2010.
- [9] M. J. Travers, D. C. Cowles, and G. B. Ellison, “Reinvestigation of the electron-affinities of O_2^- and NO ,” *Chemical Physics Letters*, vol. 164, 1989.
- [10] C. Blondel, W. Chaibi, C. Delsart, C. Drag, F. Goldfarb, and S. Kröer, “The electron affinities of O, Si, and S revisited with the photodetachment microscope,” *The European Physics Journal D*, vol. 33, pp. 335–342, 2005.
- [11] K. M. Ervin, J. Ho, and W. C. Lineberger, “A study of the singlet and triplet states of vinylidene by photoelectron spectroscopy of $\text{H}_2\text{C}=\text{C}^-$, $\text{D}_2\text{C}=\text{C}^-$, and $\text{HDC}=\text{C}^-$. vinylideneacetylene isomerization,” *The Journal of Chemical Physics*, vol. 91, pp. 5974–5992, 1989.
- [12] J. Levin, H. Feldman, A. Baer, D. Ben-Hamu, O. Heber, D. Zajfman, and Z. Vager, “Study of unimolecular reactions by coulomb explosion imaging: The nondecaying vinylidene,” *Physical Review Letters*, vol. 81, pp. 3347–3350, 1998.

- [13] K. M. Ervin and W. C. Lineberger, “Photoelectron spectra of dicarbon(1-) and ethynyl(1-),” *The Journal of Physical Chemistry*, vol. 95, pp. 1167–1177, 1991.
- [14] J. Zhou, E. Garand, and D. M. Neumark, “Vibronic structure in C₂H and C₂D from anion slow electron velocity-map imaging spectroscopy,” *The Journal of Chemical Physics*, vol. 127, p. 114313, 2007.
- [15] L. Brewer, W. T. Hicks, and O. H. Krikorian, “Heat of sublimation and dissociation energy of gaseous C₂,” *The Journal of Chemical Physics*, vol. 36, pp. 182–188, 1962.
- [16] S. Shaik, D. Danovich, W. Wu, P. Su, H. Rzepa, and P. Hiberty, “Quadruple bonding in C₂ and analogous eight-valence electron species,” *Nature Chemistry*, vol. 4, pp. 195–200, 2012.
- [17] B. Brehm, M. A. Gusinow, and J. L. Hall, “Electron affinity of helium via laser photodetachment of its negative ion,” *Physical Review Letters*, vol. 19, pp. 737–741, 1967.
- [18] W. C. Lineberger, “Once upon anion: A tale of photodetachment,” *Annual Review of Physical Chemistry*, vol. 64, pp. 21–36, 2013.
- [19] L. A. Posey, M. J. Deluca, and M. A. Johnson, “Demonstration of a pulsed photo-electron spectrometer on mass-selected negative ions: O⁻, O₂⁻, and O₄⁻,” *Chemical Physics Letters*, vol. 131, pp. 170 – 174, 1986.
- [20] K. M. Ervin, I. Anusiewicz, P. Skurski, J. Simons, and W. C. Lineberger, “The only stable state of O₂⁻ is the X 2Π_g ground state and it (still!) has an adiabatic electron detachment energy of 0.45 ev,” *The Journal of Physical Chemistry A*, vol. 107, pp. 8521–8529, 2003.
- [21] J. C. Rienstra-Kiracofe, G. S. Tschumper, H. F. Schaefer, S. Nandi, and G. B. Ellison, “Atomic and molecular electron affinities: photoelectron experiments and theoretical computations,” *Chemical Reviews*, vol. 102, pp. 231–282, 2002.
- [22] D. W. Chandler and P. L. Houston, “Twodimensional imaging of state-selected photodissociation products detected by multiphoton ionization,” *The Journal of Chemical Physics*, vol. 87, pp. 1445–1447, 1987.
- [23] A. Eppink and D. H. Parker, “Velocity map imaging of ions and electrons using electrostatic lenses: Application in photoelectron and photofragment ion imaging of molecular oxygen,” *Review of Scientific Instruments*, vol. 68, pp. 3477–3484, 1997.
- [24] S. J. Cavanagh, S. T. Gibson, M. N. Gale, C. J. Dedman, E. H. Roberts, and B. R. Lewis, “High resolution velocity-map imaging photoelectron spectroscopy of the O⁻ fine-structure transitions,” *Physical Review A*, vol. 76, p. 052708, 2007.
- [25] M. L. Weichman and D. M. Neumark, “Slow photoelectron velocity-map imaging of cryogenically cooled anions,” *Annual Review of Physical Chemistry*, vol. 69, pp. 101–124, 2018.
- [26] G. Herzberg, *Electronic spectra and electronic structure of polyatomic molecules*, vol. II. Van Nostrand Reinhold Company, 1966.

- [27] A. D. Buckingham, B. J. Orr, and J. M. Sigel, “A discussion on photoelectron spectroscopy - Angular distributions and intensity in molecular photoelectron spectroscopy I. General theory for diatomic molecules,” *Philosophical Transactions of the Royal Society of London A: Mathematical, Physical and Engineering Sciences*, vol. 268, pp. 147–157, 1970.
- [28] S. Thorin, *Design and construction of a velocity map imaging spectrometer*. Lund Reports on Atomic Physics, 2004.
- [29] J. Cooper and R. N. Zare, “Angular distribution of photoelectrons,” *The Journal of Chemical Physics*, vol. 48, pp. 942–943, 1968.
- [30] E. P. Wigner, “On the behavior of cross sections near thresholds,” *Physical Review*, vol. 73, pp. 1002–1009, 1948.
- [31] D. Hanstorp, C. Bengtsson, and D. J. Larson, “Angular distributions in photodetachment from O⁻,” *Physical Review A*, vol. 40, pp. 670–675, 1989.
- [32] W. Lineberger, H. Hotop, and T.A.Patterson, *Photodetachment threshold processes*. New York: Plenum Press, 1976.
- [33] K. J. Reed, A. H. Zimmerman, H. C. Andersen, and J. I. Brauman, “Cross sections for photodetachment of electrons from negative ions near threshold,” *The Journal of Chemical Physics*, vol. 64, pp. 1368–1375, 1976.
- [34] A. Sanov, “Laboratory-frame photoelectron angular distributions in anion photodetachment: Insight into electronic structure and intermolecular interactions,” *Annual Review of Physical Chemistry*, vol. 65, pp. 341–363, 2014.
- [35] C. M. Oana and A. I. Krylov, “Dyson orbitals for ionization from the ground and electronically excited states within equation-of-motion coupled-cluster formalism: Theory, implementation, and examples,” *The Journal of Chemical Physics*, vol. 127, p. 234106, 2007.
- [36] E. Surber, R. Mabbs, and A. Sanov, “Probing the electronic structure of small molecular anions by photoelectron imaging,” *The Journal of Physical Chemistry A*, vol. 107, pp. 8215–8224, 2003.
- [37] L. Velarde, T. Habteyes, E. R. Grumblig, K. Pichugin, and A. Sanov, “Solvent resonance effect on the anisotropy of NO⁻(N₂O)_n cluster anion photodetachment,” *The Journal of Chemical Physics*, vol. 127, p. 084302, 2007.
- [38] R. W. Field, *Small-Molecule Spectroscopy and Dynamics*. Massachusetts Institute of Technology: MIT OpenCourseWare, 2008.
- [39] R. W. Field, *Spectra and Dynamics of Small Molecules*. Springer International Publishing, 2015.
- [40] T. Azumi and K. Matsuzaki, “What does the term vibronic coupling mean?,” *Photochemistry and Photobiology*, vol. 25, pp. 315–326, 1977.
- [41] J. Nishida, S. Shigeto, S. Yabumoto, and H. o Hamaguchi, “Anharmonic coupling of the CH-stretch and CH-bend vibrations of chloroform as studied by near-infrared electroabsorption spectroscopy,” *The Journal of Chemical Physics*, vol. 137, p. 234501, 2012.

- [42] H. A. Jahn and E. Teller, “Stability of polyatomic molecules in degenerate electronic states - I Orbital degeneracy,” *Proceedings of the Royal Society of London A: Mathematical, Physical and Engineering Sciences*, vol. 161, pp. 220–235, 1937.
- [43] I. B. Bersuker, “Pseudo–Jahn Teller effect: A two-state paradigm in formation, deformation, and transformation of molecular systems and solids,” *Chemical Reviews*, vol. 113, pp. 1351–1390, 2013.
- [44] R. Tarroni and S. Carter, “Theoretical calculation of absorption intensities of C₂H and C₂D,” *Molecular Physics*, vol. 102, pp. 2167–2179, 2004.
- [45] S. Carter, N. C. Handy, C. Puzzarini, R. Tarroni, and P. Palmieri, “A variational method for the calculation of spin-rovibronic energy levels of triatomic molecules with three interacting electronic states,” *Molecular Physics*, vol. 98, pp. 1697–1712, 2000.
- [46] E. H. Roberts, *PhD thesis: High resolution photoelectron spectroscopy of the oxygen anion*. Atomic and molecular physics laboratories, Australian National University, 2008.
- [47] R. A. Smith, T. Ditmire, and J. W. G. Tisch, “Characterization of a cryogenically cooled high-pressure gas jet for laser/cluster interaction experiments,” *Review of Scientific Instruments*, vol. 69, pp. 3798–3804, 1998.
- [48] D. L. Osborn, D. J. Leahy, D. R. Cyr, and D. M. Neumark, “Photodissociation spectroscopy and dynamics of the N₂O₂⁻ anion,” *The Journal of Chemical Physics*, vol. 104, pp. 5026–5039, 1996.
- [49] R. E. Smalley, D. H. Levy, and L. Wharton, “The fluorescence excitation spectrum of the HeI₂ van der Waals complex,” *The Journal of Chemical Physics*, vol. 64, pp. 3266–3276, 1976.
- [50] D. R. Miller, *Free Jet Sources*. Oxford University Press, first edition ed., 1988.
- [51] J. H. Moore, C. C. Davis, and M. A. Coplan, *Building scientific apparatus. A practical guide to design and construction*. Perseus Books, third edition ed., 2003.
- [52] M. J. Wilhelm, M. Nikow, L. Letendre, and H.-L. Dai, “Photodissociation of vinyl cyanide at 193 nm: Nascent product distributions of the molecular elimination channels,” *The Journal of Chemical Physics*, vol. 130, p. 044307, 2009.
- [53] K. Prozument, R. G. Shaver, M. A. Ciuba, J. S. Muenter, G. B. Park, J. F. Stanton, H. Guo, B. M. Wong, D. S. Perry, and R. W. Field, “A new approach toward transition state spectroscopy,” *Faraday Discussions*, vol. 163, pp. 33–57, 2013.
- [54] W. Lindinger, D. L. Albritton, F. C. Fehsenfeld, and E. E. Ferguson, “Reactions of O⁻ with N₂, N₂O, SO₂, NH₃, CH₄, and C₂H₄ and C₂H₂⁻ with O₂ from 300K to relative kinetic energies of 2 eV,” *The Journal of Chemical Physics*, vol. 63, pp. 3238–3242, 1975.
- [55] Y. Guo and J. J. Grabowski, “Gas phase ion chemistry of the vinylidene radical anion and the acidity of the vinyl radical,” *International Journal of Mass Spectrometry and Ion Processes*, vol. 97, pp. 253 – 264, 1990.

- [56] A. M. Oliveira, Y.-J. Lu, J. H. Lehman, P. B. Changala, J. H. Baraban, J. F. Stanton, and W. C. Lineberger, “Photoelectron spectroscopy of the methide anion: Electron affinities of CH_3 and CD_3 and Inversion Splittings of CH_3^- and CD_3^- ,” *Journal of the American Chemical Society*, vol. 137, pp. 12939–12945, 2015.
- [57] K. A. Cowen and J. V. Coe, “A new and simple time of flight mass filter for cw ion sources,” *Review of Scientific Instruments*, vol. 61, pp. 2601–2604, 1990.
- [58] C. J. Dedman, E. H. Roberts, S. T. Gibson, and B. R. Lewis, “Fast 1 kv metal-oxide-semiconductor field-effect transistor switch,” *Review of Scientific Instruments*, vol. 72, pp. 3718–3720, 2001.
- [59] C. J. Dedman, E. H. Roberts, S. T. Gibson, and B. R. Lewis, “An ion gating, bunching, and potential re-referencing unit,” *Review of Scientific Instruments*, vol. 72, pp. 2915–2922, 2001.
- [60] D. W. O. Heddle, “An afocal electrostatic lens,” *Journal of Physics E: Scientific Instruments*, vol. 4, p. 981, 1971.
- [61] *PowerliteTM Precision II Scientific Laser System*. Continuum Lasers, 2002.
- [62] B. Whitaker, *Imaging in Molecular Dynamics*. Cambridge University Press, 2003.
- [63] E. W. Hansen and P.-L. Law, “Recursive methods for computing the abel transform and its inverse,” *Journal of the Optical Society of America A*, vol. 2, pp. 510–520, 1985.
- [64] D. D. Hickstein, R. Yurchak, D. Das, C.-Y. Shih, and S. T. Gibson, “PyAbel (v0.7): A python package for abel transforms.” <https://github.com/PyAbel/PyAbel>, 2016.
- [65] M. Van Duzor, F. Mbaiwa, J. Wei, T. Singh, R. Mabbs, A. Sanov, S. J. Cavanagh, S. T. Gibson, B. R. Lewis, and J. R. Gascooke, “Vibronic coupling in the superoxide anion: The vibrational dependence of the photoelectron angular distribution,” *The Journal of Chemical Physics*, vol. 133, 2010.
- [66] J. Gascooke, *Energy transfer in polyatomic-rare gas collisions, and van der Waals molecule dissociation*. PhD thesis, Flinders University, SA, 2000.
- [67] J. R. Gascooke, S. T. Gibson, and W. D. Lawrance, “A circularisation method to repair deformations and determine the centre of velocity map images,” *The Journal of Chemical Physics*, vol. 147, p. 013924, 2017.
- [68] O. Scharf and M. R. Godefroid, “On the fine structure photodetachment intensities using the irreducible tensorial expression of second quantization operators,” *arXiv.org[physics.atom-ph]*, vol. 1, pp. 1–18, 2008.
- [69] H. Zacharias, M. Geilhaupt, K. Meier, and K. H. Welge, “Laser photofragment spectroscopy of the NO_2 dissociation at 337 nm. a nonstatistical decay process,” *The Journal of Chemical Physics*, vol. 74, pp. 218–225, 1981.
- [70] A. Faustini, R. Rapp, and F. Forastiere, “Nitrogen dioxide and mortality: review and meta-analysis of long-term studies,” *European Respiratory Journal*, 2014.

- [71] H. Walton, D. Dajnak, S. Beevers, M. Williams, P. Watkiss, and A. Hunt., “Understanding the health impacts of air pollution in London,” 2015.
- [72] S. Safieddine, C. Clerbaux, M. George, J. Hadji-Lazaro, D. Hurtmans, P.-F. Coheur, C. Wespes, D. Loyola, P. Valks, and N. Hao, “Tropospheric ozone and nitrogen dioxide measurements in urban and rural regions as seen by IASI and GOME-2,” *Journal of Geophysical Research: Atmospheres*, vol. 118, pp. 10,555–10,566, 2013.
- [73] P. J. Crutzen, “The role of NO and NO₂ in the chemistry of the troposphere and stratosphere,” *Annual Review of Earth and Planetary Sciences*, vol. 7, pp. 443–472, 1979.
- [74] M. Z. Jacobson, *Air Pollution and Global Warming: History, Science, and Solutions*. Cambridge University Press, 2 ed., 2012.
- [75] M. Bell, A. McDermott, S. Zeger, J. Samet, and F. Dominici, “Ozone and short-term mortality in 95 US urban communities, 1987-2000,” *The Journal of the American Medical Association*, vol. 292, pp. 2372–2378, 2004.
- [76] I. Wilkinson, I. A. Garcia, B. J. Whitaker, J.-B. Hamard, and V. Blanchet, “The photodissociation of NO₂ by visible and ultraviolet light,” *Physical Chemistry Chemical Physics*, vol. 12, pp. 15766–15779, 2010.
- [77] I. Wilkinson and B. J. Whitaker, “Some remarks on the photodynamics of NO₂,” *Annual Reports on the Progress of Chemistry Section C*, vol. 106, pp. 274–304, 2010.
- [78] S. J. Matthews, S. Willitsch, and T. P. Softley, “Fully state-selected VMI study of the near-threshold photodissociation of NO₂: variation of the angular anisotropy parameter,” *Physical Chemistry Chemical Physics*, vol. 9, pp. 5656–5663, 2007.
- [79] F. J. Lovas, “Microwave spectral tables II. Triatomic molecules,” *Journal of Physical Chemical Reference Data*, vol. 7, pp. 1445–1750, 1978.
- [80] A. Vredenborg, W. G. Roeterdink, and M. H. M. Janssen, “Femtosecond time-resolved photoelectron-photoion coincidence imaging of multiphoton multichannel photodynamics in NO₂,” *The Journal of Chemical Physics*, vol. 128, p. 204311, 2008.
- [81] A. T. J. B. Eppink, B. J. Whitaker, E. Gloaguen, B. Soep, A. M. Coroiu, and D. H. Parker, “Dissociative multiphoton ionization of NO₂ studied by time-resolved imaging,” *The Journal of Chemical Physics*, vol. 121, pp. 7776–7783, 2004.
- [82] G. P. Bryant, Y. Jiang, M. Martin, and E. R. Grant, “Rovibrational structure of no+2 and statetostate dynamics in the highresolution threshold photoionization of NO₂,” *The Journal of Chemical Physics*, vol. 101, pp. 7199–7210, 1994.
- [83] I. Wilkinson and B. J. Whitaker, “Photodissociation of NO₂ in the (2)²B₂ state: A slice imaging study and reinterpretation of previous results,” *The Journal of Chemical Physics*, vol. 129, pp. –, 2008.
- [84] P. Warneck, “Photodetachment of NO₂⁻,” *Chemical Physics Letters*, vol. 3, pp. 532–533, AUG 1969.

- [85] B. A. Huber, P. C. Cosby, J. T. Moseley, and J. R. Peterson, “Photodetachment of excited NO_2^- ,” *Bulletin of the American Physical Society*, vol. 22, p. 191, 1977.
- [86] S. B. Woo, E. M. Helmy, P. H. Mauk, and A. P. Paszek, “Wide-range absolute photodetachment photodetachment spectrum of NO_2 ,” *Physical Review A*, vol. 24, pp. 1380–1390, 1981.
- [87] W. B. Clodius, R. M. Stehman, and S. B. Woo, “Zero-core contribution calculation of a polyatomic photodetachment cross section: NO_2^- ,” *Physical Review A*, vol. 28, pp. 760–765, 1983.
- [88] K. M. Ervin, J. Ho, and W. C. Lineberger, “Ultraviolet photoelectron-spectrum of NO_2^- ,” *The Journal of Physical Chemistry*, vol. 92, pp. 5405–5412, 1988.
- [89] A. Weaver, R. B. Metz, S. E. Bradforth, and D. M. Neumark, “Observation of the $\tilde{A}(^2B_2)$ and $\tilde{C}(^2A_2)$ states of NO_2 by negative ion photoelectron spectroscopy of NO_2^- ,” *The Journal of Chemical Physics*, vol. 90, pp. 2070–2071, 1989.
- [90] C. Meredith, R. D. Davy, G. E. Quelch, and H. F. Schaefer, “Peroxy and cyclic isomers of NO_2 and NO_2^- ,” *The Journal of Chemical Physics*, vol. 94, pp. 1317–1326, 1991.
- [91] S. P. Walch, “A new potential energy surface for $\text{N}+\text{O}_2$: Is there an NOO minimum?,” *The Journal of Chemical Physics*, vol. 102, pp. 4189–4192, 1995.
- [92] J. Liang, K. Pei, and H. Li, “The geometry of the NO_2^- anion: *ab initio* calculations and Franck Condon analysis,” *Chemical Physics Letters*, vol. 388, pp. 212 – 217, 2004.
- [93] S. Mukherjee, B. Mukherjee, S. Sardar, and S. Adhikari, “Ab initio constructed diabatic surfaces of NO_2 and the photodetachment spectra of its anion,” *The Journal of Chemical Physics*, vol. 143, 2015.
- [94] M. Valiev, E. Bylaska, N. Govind, K. Kowalski, T. Straatsma, H. V. Dam, D. Wang, J. Nieplocha, E. Apra, T. Windus, and W. de Jong, “Nwchem: A comprehensive and scalable open-source solution for large scale molecular simulations,” *Computer Physics Communications*, vol. 181, pp. 1477 – 1489, 2010.
- [95] Y. Shao, Z. Gan, E. Epifanovsky, A. T. Gilbert, J. M. Herbert, A. I. Krylov, P. M. Gill, and M. Head-Gordon, “Advances in molecular quantum chemistry contained in the q-chem 4 program package,” *Molecular Physics*, vol. 113, pp. 184–215, 2015.
- [96] A. Kubas, D. Berger, H. Oberhofer, D. Maganas, K. Reuter, and F. Neese, “Surface adsorption energetics studied with gold standard wave-function-based ab initio methods: Small-molecule binding to $\text{TiO}_2(110)$,” *The Journal of Physical Chemistry Letters*, vol. 7, pp. 4207–4212, 2016.
- [97] K. Wong, Y. Xu, and D. M. York, “Ab initio path integral calculations of kinetic and equilibrium isotope effects on basecatalyzed RNA transphosphorylation models,” *Journal of Computational Chemistry*, vol. 35, pp. 1302–1316, 2014.
- [98] S. M. Bailey, C. A. Barth, and S. C. Solomon, “A model of nitric oxide in the lower thermosphere,” *Journal of Geophysical Research*, vol. 107, pp. 22–1–12, 2002.

- [99] H. F. Schaefer, C. F. Bender, and J. H. Richardson, “A peroxy isomer of nitrogen dioxide,” *The Journal of Physical Chemistry*, vol. 80, pp. 2035–2037, 1976.
- [100] M. Braunstein and J. W. Duff, “Theoretical study of the $\text{N}({}^2D) + \text{O}_2(X{}^3\Sigma_g^-) \rightarrow \text{O} + \text{NO}$ reaction,” *The Journal of Chemical Physics*, vol. 113, pp. 7406–7413, 2000.
- [101] P. C. Engelking, “Approximate rotational band shifts,” *The Journal of Physical Chemistry*, vol. 90, pp. 4544–4545, 1986.
- [102] G. Herzberg, *Molecular Spectra and Molecular Structure*, vol. II. Van Nostrand Reinhold Company, 1945.
- [103] D. M. Dennison, “The infrared spectra of polyatomic molecules part I,” *Review of Modern Physics*, vol. 3, pp. 280–345, 1931.
- [104] G. Herzberg and K. Huber, *Molecular spectra and molecular structure*, vol. IV. Van Nostrand Reinhold Company, 1979.
- [105] R. Signorell and F. Merkt, “General symmetry selection rules for the photoionization of polyatomic molecules,” *Molecular Physics*, vol. 92, pp. 793–804, 1997.
- [106] G. W. King, R. M. Hainer, and P. C. Cross, “The asymmetric rotor I. Calculation and symmetry classification of energy levels,” *The Journal of Chemical Physics*, vol. 11, pp. 27–42, 1943.
- [107] B. A. Laws, S. J. Cavanagh, B. R. Lewis, and S. T. Gibson, “Fine structure in the NO^- photoelectron spectrum,” *The Journal of Physical Chemistry*, 2018. (In Preparation).
- [108] D. Khuseynov, C. C. Blackstone, L. M. Culberson, and A. Sanov, “Photoelectron angular distributions for states of any mixed character: An experiment-friendly model for atomic, molecular, and cluster anions,” *The Journal of Chemical Physics*, vol. 141, p. 124312, 2014.
- [109] J. Sichel, “Angular distribution and intensity in molecular photoelectron spectroscopy,” *Molecular Physics*, vol. 18, pp. 95–100, 1970.
- [110] C. M. Oana and A. I. Krylov, “Cross sections and photoelectron angular distributions in photodetachment from negative ions using equation-of-motion coupled-cluster dyson orbitals,” *The Journal of Chemical Physics*, vol. 131, p. 124114, 2009.
- [111] R. M. Stehman and S. B. Woo, “Zero-core-contribution calculation of photodetachment cross sections of O_2^- and S_2^- ,” *Physical Review A*, vol. 23, pp. 2866–2876, 1981.
- [112] B. M. Gimarc, *Molecular Structure and Bonding*. Academic, New York, 1979.
- [113] C. M. Oana and A. I. Krylov, “Dyson orbitals for ionization from the ground and electronically excited states within equation-of-motion coupled-cluster formalism: Theory, implementation, and examples,” *The Journal of Chemical Physics*, vol. 127, p. 234106, 2007.

- [114] Y. Shao, Z. Gan, E. Epifanovsky, A. T. Gilbert, M. Wormit, J. Kussmann, A. W. Lange, A. Behn, J. Deng, X. Feng, D. Ghosh, M. Goldey, P. R. Horn, L. D. Jacobson, I. Kaliman, R. Z. Khalilullin, T. Ku, A. Landau, J. Liu, E. I. Proynov, Y. M. Rhee, R. M. Richard, M. A. Rohrdanz, R. P. Steele, E. J. Sundstrom, H. L. W. III, P. M. Zimmerman, D. Zuev, B. Albrecht, E. Alguire, B. Austin, G. J. O. Beran, Y. A. Bernard, E. Berquist, K. Brandhorst, K. B. Bravaya, S. T. Brown, D. Casanova, C.-M. Chang, Y. Chen, S. H. Chien, K. D. Closser, D. L. Crittenden, M. Diedenhofen, R. A. D. Jr., H. Do, A. D. Dutoi, R. G. Edgar, S. Fatehi, L. Fusti-Molnar, A. Ghysels, A. Golubeva-Zadorozhnaya, J. Gomes, M. W. Hanson-Heine, P. H. Harbach, A. W. Hauser, E. G. Hohenstein, Z. C. Holden, T.-C. Jagau, H. Ji, B. Kaduk, K. Khistyayev, J. Kim, J. Kim, R. A. King, P. Klunzinger, D. Kosenkov, T. Kowalczyk, C. M. Krauter, K. U. Lao, A. D. Laurent, K. V. Lawler, S. V. Levchenko, C. Y. Lin, F. Liu, E. Livshits, R. C. Lochan, A. Luenser, P. Manohar, S. F. Manzer, S.-P. Mao, N. Mardirossian, A. V. Marenich, S. A. Maurer, N. J. Mayhall, E. Neuscamman, C. M. Oana, R. Olivares-Amaya, D. P. O'Neill, J. A. Parkhill, T. M. Perrine, R. Peverati, A. Prociuk, D. R. Rehn, E. Rosta, N. J. Russ, S. M. Sharada, S. Sharma, D. W. Small, A. Sodt, T. Stein, D. Stck, Y.-C. Su, A. J. Thom, T. Tsuchimochi, V. Vanovschi, L. Vogt, O. Vydrov, T. Wang, M. A. Watson, J. Wenzel, A. White, C. F. Williams, J. Yang, S. Yeganeh, S. R. Yost, Z.-Q. You, I. Y. Zhang, X. Zhang, Y. Zhao, B. R. Brooks, G. K. Chan, D. M. Chipman, C. J. Cramer, W. A. G. III, M. S. Gordon, W. J. Hehre, A. Klamt, H. F. S. III, M. W. Schmidt, C. D. Sherrill, D. G. Truhlar, A. Warshel, X. Xu, A. Aspuru-Guzik, R. Baer, A. T. Bell, N. A. Besley, J.-D. Chai, A. Dreuw, B. D. Dunietz, T. R. Furlani, S. R. Gwaltney, C.-P. Hsu, Y. Jung, J. Kong, D. S. Lambrecht, W. Liang, C. Ochsenfeld, V. A. Rassolov, L. V. Slipchenko, J. E. Subotnik, T. V. Voorhis, J. M. Herbert, A. I. Krylov, P. M. Gill, and M. Head-Gordon, “Advances in molecular quantum chemistry contained in the Q-Chem 4 program package,” *Molecular Physics*, vol. 113, pp. 184–215, 2015.
- [115] S. Gozem, A. O. Gunina, T. Ichino, D. L. Osborn, J. F. Stanton, and A. I. Krylov, “Photoelectron wave function in photoionization: Plane wave or coulomb wave?,” *The Journal of Physical Chemistry Letters*, vol. 6, pp. 4532–4540, 2015.
- [116] M. W. Chase, C. A. Downey, D. J. Frurip, R. A. McDonald, and A. N. Syverud, “JANAF thermochemical tables (third edition),” *The Journal of Physical Chemistry Reference Data*, vol. 14, pp. 1–1856, 1985.
- [117] S. J. Cavanagh, S. T. Gibson, and B. R. Lewis, “Photodetachment of O⁻ from threshold to 1.2 eV electron kinetic energy using velocity-map imaging,” *Journal of Physics: Conference Series*, vol. 212, p. 012034, 2010.
- [118] R. Schinke, S. Grebenschchikov, and H. Zhu, “The photodissociation of NO₂ in the second absorption band: Ab initio and quantum dynamics calculations,” *Chemical Physics*, vol. 346, pp. 99 – 114, 2008.
- [119] S. D. Dalosto, J. M. Vanderkooi, and K. A. Sharp, “Vibrational Stark Effects on Carbonyl, Nitrile, and Nitrosyl Compounds Including Heme Ligands, CO, CN, and NO, Studied with Density Functional Theory,” *The Journal of Physical Chemistry B*, vol. 108, pp. 6450–6457, 2004.
- [120] C. Amiot, “The infrared emission spectrum of NO: Analysis of the $\Delta v = 3$ sequence up to $v = 22$,” *Journal of Molecular Spectroscopy*, vol. 94, pp. 150–172, 1982.

- [121] L. Dinu and W. J. van der Zande, “Photodestruction of NO_2^- using time resolved multicoincidence detection photofragment spectroscopy,” *Chemical Physics*, vol. 300, pp. 133–141, 2004.
- [122] K. N. Crabtree, M. R. Talipov, O. Martinez, G. D. O’Connor, S. L. Khursan, and M. C. McCarthy, “Detection and structure of HOON: microwave spectroscopy reveals an O–O bond exceeding 1.9 Å,” *Science*, vol. 342, pp. 1354–1357, 2013.
- [123] C. Blondel, “Recent experimental achievements with negative ions,” *Physica Scripta*, vol. 1995, p. 31, 1995.
- [124] C. Han and M. A. Johnson, “Nascent vibrational distribution of the O_2^- product ion in the photodissociation of $(\text{O}_2)_n^-$, $n = 2 - 4$,” *Chemical Physics Letters*, vol. 189, pp. 460 – 466, 1992.
- [125] P. Hlavenka, R. Otto, S. Trippel, J. Mikosch, M. Weidemller, and R. Wester, “Absolute photodetachment cross section measurements of the O^- and OH^- anion,” *The Journal of Chemical Physics*, vol. 130, p. 061105, 2009.
- [126] K. Pichugin, E. Grumblig, L. Velarde, and A. Sanov, “Solvation-induced cluster anion core switching from $\text{nno}_2(\text{n}_2\text{o})\text{n}_1$ to $\text{o}(\text{n}_2\text{o})\text{n}$,” *The Journal of Chemical Physics*, vol. 129, p. 044311, 2008.
- [127] B. Ramachandran, N. Balakrishnan, and A. Dalgarno, “Vibrationalrotational distributions of NO formed from $\text{N}+\text{O}_2$ reactive collisions,” *Chemical Physics Letters*, vol. 332, pp. 562 – 568, 2000.
- [128] I. Miquel, J. Hernando, R. Sayós, and M. González, “Influence of collision energy on the $\text{N}(^2D) + \text{O}_2 \rightarrow \text{O}(^3P) + \text{NO}$ reaction dynamics: A quasiclassical trajectory study involving four potential energy surfaces,” *The Journal of Chemical Physics*, vol. 119, pp. 10040–10047, 2003.
- [129] R. A. Sultanov and N. Balakrishnan, “Quantum mechanical investigations of the $\text{N}(^4S) + \text{O}_2(X^3\Sigma_g) \rightarrow \text{NO}(X^2\Pi) + \text{O}(^3P)$ reaction,” *The Journal of Chemical Physics*, vol. 124, 2006.
- [130] P. Swaminathan, D. Strobel, L. Acton, and L. Paxton, “Model update for mesospheric/thermospheric nitric oxide,” *Physics and Chemistry of the Earth, Part C, Solar, Terrestrial and Planetary Science*, vol. 26, pp. 533 – 537, 2001.
- [131] D. R. Smith and M. Ahmadjian, “Observation of nitric oxide rovibrational band head emissions in the quiescent airglow during the cirris1a space shuttle experiment,” *Geophysical Research Letters*, vol. 20, pp. 2679–2682, 1993.
- [132] N. Balakrishnan, V. Kharachenko, and A. Daldarno, “Energetic N(4S) atoms and their role in no formation in the terrestrial atmosphere,” *EOS, Transactions of the American Geophysical Union*, vol. 79, p. 45, 1998.
- [133] P. K. Swaminathan, D. F. Strobel, D. G. Kupperman, C. K. Kumar, L. Acton, R. DeMajistre, J. Yee, L. Paxton, D. E. Anderson, D. J. Strickland, and J. W. Duff, “Nitric oxide abundance in the mesosphere/lower thermosphere region: Roles of solar soft x rays, suprothermal N(4S) atoms, and vertical transport,” *Journal of Geophysical Research: Space Physics*, vol. 103, pp. 11579–11594, 1998.

- [134] M. W. Siegel, R. J. Celotta, J. L. Hall, J. Levine, and R. A. Bennett, "Molecular photodetachment spectrometry. i. the electron affinity of nitric oxide and the molecular constants of NO^- ," *Physical Review A*, vol. 6, pp. 607–631, 1972.
- [135] J. V. Coe, J. T. Snodgrass, C. B. Freidhoff, K. M. McHugh, and K. H. Bowen, "Photoelectron spectroscopy of the negative cluster ions $\text{NO}^-(\text{N}_2\text{O})_{n=1,2}$," *The Journal of Chemical Physics*, vol. 87, pp. 4302–4309, 1987.
- [136] L. A. Posey and M. A. Johnson, "Pulsed photoelectron spectroscopy of negative cluster ions: Isolation of three distinguishable forms of N_2O_2^- ," *The Journal of Chemical Physics*, vol. 88, pp. 5383–5395, 1988.
- [137] J. H. Hendricks, H. L. de Clercq, C. B. Freidhoff, S. T. Arnold, J. G. Eaton, C. Fancher, S. A. Lyapustina, J. T. Snodgrass, and K. H. Bowen, "Anion solvation at the microscopic level: Photoelectron spectroscopy of the solvated anion clusters, $\text{NO}^-(\text{Y})_n$, where $\text{Y}=\text{Ar}, \text{Kr}, \text{Xe}, \text{N}_2\text{O}, \text{H}_2\text{S}, \text{NH}_3, \text{H}_2\text{O}$, and $\text{C}_2\text{H}_4(\text{OH})_2$," *The Journal of Chemical Physics*, vol. 116, pp. 7926–7938, 2002.
- [138] B. Poad, C. J. Johnson, and R. E. Continetti, "Photoelectron-photofragment coincidence studies of $\text{NO}-\text{X}$ clusters ($\text{X} = \text{H}_2\text{O}, \text{CD}_4$)," *Faraday Discussions*, vol. 150, pp. 481–492, 2011.
- [139] M. McCarthy, J. W. Allington, and K. Griffith, "An accurate ab initio calculation of the electron affinity of NO," *Chemical Physics Letters*, vol. 289, pp. 156 – 159, 1998.
- [140] M. Jelisavcic, R. Panajotovic, and S. J. Buckman, "Absolute collision cross sections for low energy electron scattering from NO: The role of resonances in elastic scattering and vibrational excitation," *Physical Review Letters*, vol. 90, p. 203201, 2003.
- [141] M. M. Maricq, N. A. Tanguay, J. C. O'Brien, S. M. Rodday, and E. Rinden, "Vibrational autodetachment of no," *The Journal of Chemical Physics*, vol. 90, pp. 3136–3144, 1989.
- [142] D. J. Nesbitt and M. S. Child, "RotationalRKR inversion of intermolecular stretching potentials: Extension to linear hydrogen bonded complexes," *The Journal of Chemical Physics*, vol. 98, pp. 478–486, 1993.
- [143] H. A. Kramers, "Zur struktur der multiplett-s-zustände in zweiatomigen molekülen. i," *Zeitschrift für Physik*, vol. 53, pp. 422–428, 1929.
- [144] G. Herzberg, *Molecular Spectra and Molecular Structure - Spectra of Diatomic Molecules*, vol. I. Van Nostrand Reinhold Company, 1950.
- [145] P. F. Bernath, *Spectra of Atoms and Molecules*. Oxford University Press, 2016.
- [146] J. Johns, J. Reid, and D. Lepard, "The vibration-rotation fundamental of NO," *Journal of Molecular Spectroscopy*, vol. 65, pp. 155 – 162, 1977.
- [147] R. Engleman and P. Rouse, "The and bands of nitric oxide observed during the flash photolysis of nitrosyl chloride," *Journal of Molecular Spectroscopy*, vol. 37, pp. 240 – 251, 1971.

- [148] D. T. Vier and J. E. Mayer, “A direct experimental determination of the electron affinity of oxygen,” *The Journal of Chemical Physics*, vol. 12, pp. 28–34, 1944.
- [149] D. M. Neumark, K. R. Lykke, T. Andersen, and W. C. Lineberger, “Laser photodetachment measurement of the electron affinity of atomic oxygen,” *Physical Review A*, vol. 32, pp. 1890–1892, 1985.
- [150] C. Blondel, C. Delsart, C. Valli, S. Yiou, M. R. Godefroid, and S. Van Eck, “Electron affinities of ^{16}O , ^{17}O , ^{18}O , the fine structure of $^{16}\text{O}^-$, and the hyperfine structure of $^{17}\text{O}^-$,” *Physical Review A*, vol. 64, p. 052504, 2001.
- [151] J. L. Hall and M. W. Siegel, “Angular dependence of the laser photodetachment of the negative ions of carbon, oxygen, and hydrogen,” *The Journal of Chemical Physics*, vol. 48, pp. 943–945, 1968.
- [152] F. Breyer, P. Frey, and H. Hotop, “High resolution photoelectron spectrometry of negative ions: Fine-structure transitions in O^- and S^- photodetachment,” *Zeitschrift für Physik A Atoms and Nuclei*, vol. 286, pp. 133–138, 1978.
- [153] C. Domesle, B. Jordon-Thaden, L. Lammich, M. Förstel, U. Hergenhahn, A. Wolf, and H. B. Pedersen, “Photoelectron spectroscopy of O^- at 266 nm: Ratio of ground- and excited-state atomic oxygen production and channel-resolved photoelectron anisotropy parameters,” *Physical Review A*, vol. 82, p. 033402, 2010.
- [154] S. J. Cavanagh, S. T. Gibson, and B. R. Lewis, “Approaching the O^- photodetachment threshold with velocity-map imaging,” *Journal of Physics: Conference Series*, vol. 194, p. 022026, 2009.
- [155] L. M. Branscomb, S. J. Smith, and G. Tisone, “Oxygen metastable atom production through photodetachment,” *The Journal of Chemical Physics*, vol. 43, pp. 2906–2907, 1965.
- [156] O. Zatsarinny and K. Bartschat, “Low-energy photodetachment of O^- ,” *Physical Review A*, vol. 73, p. 022714, 2006.
- [157] L. C. Lee and G. P. Smith, “Photodissociation and photodetachment of molecular negative ions. VI. Ions in $\text{O}_2/\text{CH}_4/\text{H}_2\text{O}$ mixtures from 3500 to 8600 Å,” *The Journal of Chemical Physics*, vol. 70, pp. 1727–1735, 1979.
- [158] M. Génévrier, X. Urbain, A. Dochain, A. Cyr, K. M. Dunseath, and M. Terao-Dunseath, “One- and two-photon detachment of O^- ,” *Physical Review A*, vol. 94, p. 023407, 2016.
- [159] K. A. Berrington, W. B. Eissner, and P. H. Norrington, “Rmatrx1: Belfast atomic r-matrix codes,” *Computer Physics Communications*, vol. 92, pp. 290 – 420, 1995.
- [160] W. Jian-Hua, Y. Jian-Min, and V. K. Lan, “Near threshold photodetachment cross section of negative atomic oxygen ions,” *Chinese Physics*, vol. 12, p. 1390, 2003.
- [161] R. M. Stehman and S. B. Woo, “Zero-core-contribution model and its application to photodetachment of atomic negative ions,” *Physical Review A*, vol. 20, pp. 281–290, 1979.

- [162] W. B. Clodius, R. M. Stehman, and S. B. Woo, “Extended zero-core-contribution model applied to multichannel photodetachment,” *Physical Review A*, vol. 27, pp. 333–344, 1983.
- [163] D. S. Burch, S. J. Smith, and L. M. Branscomb, “Photodetachment of O₂⁻,” *Physical Reviews*, vol. 112, pp. 171–175, 1958.
- [164] T. L. Bailey and P. Mahadevan, “Electron transfer and detachment in collisions of lowenergy negative ions with O₂,” *The Journal of Chemical Physics*, vol. 52, pp. 179–190, 1970.
- [165] R. J. Celotta, R. A. Bennett, J. L. Hall, M. W. Siegel, and J. Levine, “Molecular photodetachment spectrometry. ii. the electron affinity of O₂ and the structure of O₂⁻,” *Physical Review A*, vol. 6, pp. 631–642, 1972.
- [166] J. Schiedt and R. Weinkauf, “Spin-orbit coupling in the O₂⁻ anion,” *Zeitschrift fur Naturforschung*, vol. 50, pp. 1041 – 1044, 1995.
- [167] E. S. Chen and E. C. M. Chen, “Semiempirical characterization of homonuclear diatomic ions: 6. Group VI and VII anions,” *The Journal of Physical Chemistry A*, vol. 107, pp. 169–177, 2003.
- [168] C. G. Bailey, D. J. Lavrich, D. Serxner, and M. A. Johnson, “Autodetachment from vibrational levels of the O₂⁻ A²Π_u resonance across its dissociation limit by photoexcitation from O₂⁻ X²Π_g,” *The Journal of Chemical Physics*, vol. 105, pp. 1807–1814, 1996.
- [169] R. Mabbs, F. Mbaiwa, J. Wei, M. Van Duzor, S. T. Gibson, S. J. Cavanagh, and B. R. Lewis, “Observation of vibration-dependent electron anisotropy in O₂⁻ photodetachment,” *Physical Review A*, vol. 82, p. 011401, 2010.
- [170] D. Khuseynov, D. J. Goebbert, and A. Sanov, “Oxygen cluster anions revisited: Solvent-mediated dissociation of the core O₄⁻ anion,” *The Journal of Chemical Physics*, vol. 136, p. 094312, 2012.
- [171] R. Schork and H. Kppel, “Unexpected stability of vinylidene from 5D ab initio quantum-dynamical calculations,” *Chemical Physics Letters*, vol. 326, pp. 277 – 282, 2000.
- [172] M. M. Gallo, T. P. Hamilton, and H. F. Schaefer, “Vinylidene: the final chapter?,” *Journal of the American Chemical Society*, vol. 112, pp. 8714–8719, 1990.
- [173] Y. Ren, B. Li, and W. Bian, “Full-dimensional quantum dynamics study of vinylidene-acetylene isomerization: a scheme using the normal mode hamiltonian,” *Physical Chemistry Chemical Physics*, vol. 13, pp. 2052–2061, 2011.
- [174] J. D. Evanseck and K. N. Houk, “Theoretical predictions of activation energies for 1,2-hydrogen shifts in singlet carbenes,” *The Journal of Physical Chemistry*, vol. 94, pp. 5518–5523, 1990.
- [175] R. L. Hayes, E. Fattal, N. Govind, and E. A. Carter, “Long live vinylidene! a new view of the H₂CC:→ HC≡CH rearrangement from ab initio molecular dynamics,” *Journal of the American Chemical Society*, vol. 123, pp. 641–657, 2001.

- [176] H. F. Schaefer, "The 1,2 hydrogen shift: a common vehicle for the disappearance of evanescent molecular species," *Accounts of Chemical Research*, vol. 12, pp. 288–296, 1979.
- [177] J. F. Stanton and J. Gauss, "Vibrational structure in the vinylidene anion photo-electron spectrum: Closing the gap between theory and experiment," *The Journal of Chemical Physics*, vol. 110, pp. 6079–6080, 1999.
- [178] P. S. Skell, J. E. Villaume, and F. A. Fagone, "Formation of vinylidene intermediates in the reaction of diatomic carbon with propylene," *Journal of the American Chemical Society*, vol. 94, pp. 7866–7867, 1972.
- [179] G. Hatzikos and R. Masel, "Structure sensitivity of ethylene adsorption on pt(100): Evidence for vinylidene formation on (11) pt(100)," *Surface Science*, vol. 185, pp. 479 – 494, 1987.
- [180] M. M. Hills, J. E. Parmeter, and W. H. Weinberg, "Chemisorption and reaction of ethylene on chemically modified ruthenium(001) surfaces," *Journal of the American Chemical Society*, vol. 109, pp. 4224–4232, 1987.
- [181] M. Ahmed, D. S. Peterka, and A. G. Suits, "The photodissociation of the vinyl radical (C_2H_3) at 243 nm studied by velocity map imaging," *The Journal of Chemical Physics*, vol. 110, pp. 4248–4253, 1999.
- [182] J. Bevington, J. Jemmett, and P. Onyon, "Polymerization of methyl - cyanoacrylateii," *European Polymer Journal*, vol. 12, pp. 255 – 257, 1976.
- [183] R. P. Duran, V. T. Amorebieta, and A. J. Colussi, "Pyrolysis of acetylene: a thermal source of vinylidene," *Journal of the American Chemical Society*, vol. 109, pp. 3154–3155, 1987.
- [184] R. Schork and H. Köppel, "Ab initio quantum dynamical study of the vinylidene-acetylene isomerization," *Theoretical Chemistry Accounts*, vol. 100, pp. 204–211, 1998.
- [185] R. Schork and H. Kppel, "Barrier recrossing in the vinylideneacetylene isomerization reaction: A five-dimensional ab initio quantum dynamical investigation," *The Journal of Chemical Physics*, vol. 115, pp. 7907–7923, 2001.
- [186] S. Zou, J. M. Bowman, and A. Brown, "Full-dimensionality quantum calculations of acetylenevinylidene isomerization," *The Journal of Chemical Physics*, vol. 118, pp. 10012–10023, 2003.
- [187] S. Joseph and A. J. C. Varandas, "Accurate MRCI and CC study of the most relevant stationary points and other topographical attributes for the ground-state $c2h2$ potential energy surface," *The Journal of Physical Chemistry A*, vol. 114, pp. 13277–13287, 2010.
- [188] H. Lee, J. H. Baraban, R. W. Field, and J. F. Stanton, "High-accuracy estimates for the vinylidene-acetylene isomerization energy and the ground state rotational constants of :cch2," *The Journal of Physical Chemistry A*, vol. 117, pp. 11679–11683, 2013.

- [189] H. Han, A. Li, and H. Guo, “Toward spectroscopically accurate global ab initio potential energy surface for the acetylene-vinylidene isomerization,” *The Journal of Chemical Physics*, vol. 141, p. 244312, 2014.
- [190] G. A. Petersson, T. G. Tensfeldt, and J. A. Montgomery, “Vinylidene and the hammond postulate,” *Journal of the American Chemical Society*, vol. 114, pp. 6133–6138, 1992.
- [191] J. A. DeVine, M. L. Weichman, X. Zhou, J. Ma, B. Jiang, H. Guo, and D. M. Neumark, “Non-adiabatic effects on excited states of vinylidene observed with slow photoelectron velocity-map imaging,” *Journal of the American Chemical Society*, vol. 138, pp. 16417–16425, 2016.
- [192] P. S. Skell and J. H. Plonka, “Chemistry of the singlet and triplet C₂ molecules. mechanism of acetylene formation from reaction with acetone and acetaldehyde,” *Journal of the American Chemical Society*, vol. 92, pp. 5620–5624, 1970.
- [193] S. M. Burnett, A. E. Stevens, C. Feigerle, and W. Lineberger, “Observation of X¹A₁ vinylidene by photoelectron spectroscopy of the C₂H₂⁻ ion,” *Chemical Physics Letters*, vol. 100, pp. 124 – 128, 1983.
- [194] T. C. Germann and W. H. Miller, “Quantum mechanical calculation of resonance tunneling in acetylene isomerization via the vinylidene intermediate,” *The Journal of Chemical Physics*, vol. 109, pp. 94–101, 1998.
- [195] N. yuan Chang, M. yi Shen, and C. hui Yu, “Extended ab initio studies of the vinylideneacetylene rearrangement,” *The Journal of Chemical Physics*, vol. 106, pp. 3237–3242, 1997.
- [196] D. Kella, M. Algranati, H. Feldman, O. Heber, H. Kovner, E. Malkin, E. Miklazky, R. Naaman, D. Zaifman, J. Zaifman, and Z. Vager, “A system for Coulomb explosion imaging of small molecules at the Weizmann Institute,” *Nuclear Instruments and Methods in Physics Research Section A: Accelerators, Spectrometers, Detectors and Associated Equipment*, vol. 329, pp. 440 – 452, 1993.
- [197] O. Heber, D. Kella, D. Zaifman, H. Feldman, D. Majer, Z. Vager, and R. Naaman, “Carbon cluster imaging at the weizmann institute coulomb explosion system,” *Nuclear Instruments and Methods in Physics Research Section B: Beam Interactions with Materials and Atoms*, vol. 79, pp. 227 – 230, 1993.
- [198] L. Guo, H. Han, J. Ma, and H. Guo, “Quantum dynamics of vinylidene photodetachment on an accurate global acetylene-vinylidene potential energy surface,” *The Journal of Physical Chemistry A*, vol. 119, pp. 8488–8496, 2015.
- [199] M. J. Jensen, U. V. Pedersen, and L. H. Andersen, “Stability of the ground state vinylidene anion H₂CC⁻,” *Physical Review Letters*, vol. 84, pp. 1128–1131, 2000.
- [200] M. P. Jacobson and R. W. Field, “Acetylene at the threshold of isomerization,” *The Journal of Physical Chemistry A*, vol. 104, pp. 3073–3086, 2000.
- [201] J. H. Baraban, P. B. Changala, G. C. Mellau, J. F. Stanton, A. J. Merer, and R. W. Field, “Spectroscopic characterization of isomerization transition states,” *Science*, vol. 350, pp. 1338–1342, 2015.

- [202] S. Boy-Pronne, D. Gauyacq, and J. Livin, “Theoretical description of electronically excited vinylidene up to 10 ev: First high level ab initio study of singlet valence and rydberg states,” *The Journal of Chemical Physics*, vol. 141, p. 174317, 2014.
- [203] M. P. Jacobson, R. J. Silbey, and R. W. Field, “Local mode behavior in the acetylene bending system,” *The Journal of Chemical Physics*, vol. 110, pp. 845–859, 1999.
- [204] B. M. Wong, A. H. Steeves, and R. W. Field, “Electronic signatures of large amplitude motions: dipole moments of vibrationally excited local-bend and local-stretch states of S0 acetylene,” *The Journal of Physical Chemistry B*, vol. 110, pp. 18912–18920, 2006.
- [205] B. J. Orr, “Spectroscopy and energetics of the acetylene molecule: dynamical complexity alongside structural simplicity,” *International Reviews in Physical Chemistry*, vol. 25, pp. 655–718, 2006.
- [206] G. B. Park, A. H. Steeves, J. H. Baraban, and R. W. Field, “Simplified cartesian basis model for intrapolyad emission intensities in the bent-to-linear electronic transition of acetylene,” *The Journal of Physical Chemistry A*, vol. 119, pp. 857–865, 2015.
- [207] M. P. Jacobson, J. P. O'Brien, R. J. Silbey, and R. W. Field, “Pure bending dynamics in the acetylene $X^1\Sigma_g^+$ state up to 15000 cm1 of internal energy,” *The Journal of Chemical Physics*, vol. 109, pp. 121–133, 1998.
- [208] M. P. Jacobson, C. Jung, H. S. Taylor, and R. W. Field, “State-by-state assignment of the bending spectrum of acetylene at 15000 cm1: A case study of quantum-classical correspondence,” *The Journal of Chemical Physics*, vol. 111, pp. 600–618, 1999.
- [209] S. Solina, J. P. O'Brie, R. W. Field, and W. F. Polik, “Dispersed fluorescence spectrum of acetylene from the A^1A_u origin: recognition of polyads and test of multiresonant effective hamiltonian model for the X state,” *The Journal of Physical Chemistry*, vol. 100, pp. 7797–7809, 1996.
- [210] D. S. Perry, J. Martens, B. Amyay, and M. Herman, “Hierarchies of intramolecular vibrationrotation dynamical processes in acetylene up to 13,000cm1,” *Molecular Physics*, vol. 110, pp. 2687–2705, 2012.
- [211] D. B. Moss, Z. Duan, M. P. Jacobson, J. P. O'Brien, and R. W. Field, “Observation of coriolis coupling between $v_2 + ^4v_4$ and 7v_4 in Acetylene $X^1\Sigma_g^+$ by stimulated emission pumping spectroscopy,” *Journal of Molecular Spectroscopy*, vol. 199, pp. 265 – 274, 2000.
- [212] C. Jung, H. S. Taylor, and M. P. Jacobson, “The acetylene bending spectrum at 10000 cm-1: quantum assignments in the midst of classical chaos,” *The Journal of Physical Chemistry A*, vol. 105, pp. 681–693, 2001.
- [213] V. Tyng and M. E. Kellman, “Critical points bifurcation analysis of high- bending dynamics in acetylene,” *The Journal of Chemical Physics*, vol. 131, p. 244111, 2009.
- [214] V. Tyng and M. E. Kellman, “Bending dynamics of acetylene: new modes born in bifurcations of normal modes,” *The Journal of Physical Chemistry B*, vol. 110, pp. 18859–18871, 2006.

- [215] H. K. Gerardi, K. J. Breen, T. L. Guasco, G. H. Weddle, G. H. Gardenier, J. E. Laaser, and M. A. Johnson, "Survey of Ar-tagged predissociation and vibrationally mediated photodetachment spectroscopies of the vinylidene anion, C₂H₂⁻," *The Journal of Physical Chemistry A*, vol. 114, pp. 1592–1601, 2010.
- [216] E. Hossain, S. M. Deng, S. Gozem, A. I. Krylov, X.-B. Wang, and P. G. Wentholt, "Photoelectron spectroscopy study of quinonimides," *Journal of the American Chemical Society*, vol. 139, pp. 11138–11148, 2017.
- [217] C. M. Western, "Pgopher: A program for simulating rotational, vibrational and electronic spectra," *Journal of Quantitative Spectroscopy and Radiative Transfer*, vol. 186, pp. 221 – 242, 2017. Satellite Remote Sensing and Spectroscopy: Joint ACE-Odin Meeting, October 2015.
- [218] J. A. DeVine, M. L. Weichman, B. Laws, J. Chang, M. C. Babin, G. Balerdi, C. Xie, C. L. Malbon, W. C. Lineberger, D. R. Yarkony, R. W. Field, S. T. Gibson, J. Ma, H. Guo, and D. M. Neumark, "Encoding of vinylidene isomerization in its anion photoelectron spectrum," *Science*, vol. 358, pp. 336–339, 2017.
- [219] K. M. Ervin, S. Gronert, S. E. Barlow, M. K. Gilles, A. G. Harrison, V. M. Bierbaum, C. H. DePuy, W. C. Lineberger, and G. B. Ellison, "Bond strengths of ethylene and acetylene," *Journal of the American Chemical Society*, vol. 112, pp. 5750–5759, 1990.
- [220] D. A. Blank, A. G. Suits, Y. T. Lee, S. W. North, and G. E. Hall, "Photodissociation of acrylonitrile at 193 nm: A photofragment translational spectroscopy study using synchrotron radiation for product photoionization," *The Journal of Chemical Physics*, vol. 108, pp. 5784–5794, 1998.
- [221] Y. Huang, Y. Yang, G. He, S. Hashimoto, and R. J. Gordon, "State resolved translational energy distributions of Cl and HCl in the ultraviolet photodissociation of chloroethylenes," *The Journal of Chemical Physics*, vol. 103, pp. 5476–5487, 1995.
- [222] P. S. Thomas, R. Chhantyal-Pun, N. D. Kline, and T. A. Miller, "The A-X absorption of vinoxy radical revisited: Normal and herzbergteller bands observed via cavity ringdown spectroscopy," *The Journal of Chemical Physics*, vol. 132, p. 114302, 2010.
- [223] R. Berger, C. Fischer, and M. Klessinger, "Calculation of the vibronic fine structure in electronic spectra at higher temperatures. 1. benzene and pyrazine," *The Journal of Physical Chemistry A*, vol. 102, pp. 7157–7167, 1998.
- [224] T. Lu and F. Chen, "Multiwfn: A multifunctional wavefunction analyzer," *Journal of Computational Chemistry*, vol. 33, pp. 580–592, 2012.
- [225] E. Hutchisson, "Band spectra intensities for symmetrical diatomic molecules," *Physical Review*, vol. 36, pp. 410–420, 1930.
- [226] P. M. Johnson, H. Xu, and T. J. Sears, "The calculation of vibrational intensities in forbidden electronic transitions," *The Journal of Chemical Physics*, vol. 125, p. 164330, 2006.
- [227] C. Hock, J. B. Kim, M. L. Weichman, T. I. Yacovitch, and D. M. Neumark, "Slow photoelectron velocity-map imaging spectroscopy of cold negative ions," *The Journal of Chemical Physics*, vol. 137, p. 244201, 2012.

- [228] A. Osterwalder, M. J. Nee, J. Zhou, and D. M. Neumark, “High resolution photodetachment spectroscopy of negative ions via slow photoelectron imaging,” *The Journal of Chemical Physics*, vol. 121, pp. 6317–6322, 2004.
- [229] D. M. Neumark, “Slow electron velocity-map imaging of negative ions: Applications to spectroscopy and dynamics,” *The Journal of Physical Chemistry A*, vol. 112, pp. 13287–13301, 2008.
- [230] J. A. DeVine, M. L. Weichman, C. Xie, M. C. Babin, M. A. Johnson, J. Ma, H. Guo, and D. M. Neumark, “Autodetachment from vibrationally excited vinylidene anions,” *The Journal of Physical Chemistry Letters*, vol. 9, pp. 1058–1063, 2018.
- [231] B. Gans, G. A. Garcia, F. Holzmeier, J. Krger, A. Rder, A. Lopes, C. Fittschen, J.-C. Loison, and C. Alcaraz, “Communication: On the first ionization threshold of the C₂H radical,” *The Journal of Chemical Physics*, vol. 146, p. 011101, 2017.
- [232] M. Dobrijevic, J. Loison, K. Hickson, and G. Gronoff, “1D-coupled photochemical model of neutrals, cations and anions in the atmosphere of Titan,” *Icarus*, vol. 268, pp. 313 – 339, 2016.
- [233] W. M. Jackson, V. Blunt, H. Lin, M. Green, G. Olivera, W. H. Fink, Y. Bao, R. S. Urdahl, F. Mohammad, and M. Zahedi, “Non-adiabatic interactions in excited C₂H molecules and their relationship to C₂ formation in comets,” *Astrophysics and Space Science*, vol. 236, pp. 29–47, 1996.
- [234] H. Beuther, D. Semenov, T. Henning, and H. Linz, “Ethynyl (C₂H) in massive star formation: Tracing the initial conditions?,” *The Astrophysical Journal Letters*, vol. 675, p. L33, 2008.
- [235] M. Frenklach, D. W. Clary, W. C. Gardiner, and S. E. Stein, “Detailed kinetic modeling of soot formation in shock-tube pyrolysis of acetylene,” *Symposium (International) on Combustion*, vol. 20, pp. 887 – 901, 1985. Twentieth Symposium (International) on Combustion.
- [236] M. Frenklach and E. D. Feigelson, “Formation of polycyclic aromatic hydrocarbons in circumstellar envelopes,” *The Astrophysics Journal*, vol. 341, pp. 372–384, 1989.
- [237] W. Yan, C. Dane, D. Zeitz, J. L. Hall, and R. Curl, “Color center laser spectroscopy of C₂H and C₂D,” *Journal of Molecular Spectroscopy*, vol. 123, pp. 486 – 495, 1987.
- [238] D. Forney, M. Jacox, and W. Thompson, “The infrared and near-infrared spectra of HCC and DCC trapped in solid neon,” *Journal of Molecular Spectroscopy*, vol. 170, pp. 178 – 214, 1995.
- [239] A. Fahr, “Ultraviolet absorption spectrum and cross-sections of ethynyl (C₂H) radicals,” *Journal of Molecular Spectroscopy*, vol. 217, pp. 249 – 254, 2003.
- [240] T. R. Taylor, C. Xu, and D. M. Neumark, “Photoelectron spectra of the C_{2n}H⁻ (n=14) and C_{2n}D⁻ (n=13) anions,” *The Journal of Chemical Physics*, vol. 108, pp. 10018–10026, 1998.
- [241] R. Tarroni and S. Carter, “Theoretical calculation of vibronic levels of C₂H and C₂D to 10000cm⁻¹,” *The Journal of Chemical Physics*, vol. 119, pp. 12878–12889, 2003.

- [242] T. C. Killian, C. A. Gottlieb, and P. Thaddeus, “Rotational spectra of vibrationally excited CCH and CCD,” *The Journal of Chemical Physics*, vol. 127, p. 114320, 2007.
- [243] H. Kanamori and E. Hirota, “Vibronic bands of the CCH radical observed by infrared diode laser kinetic spectroscopy,” *The Journal of Chemical Physics*, vol. 89, pp. 3962–3969, 1988.
- [244] W. J. Morgan and R. C. Fortenberry, “Theoretical rovibronic treatment of the $X^2\Sigma^+$ and $A^2\Pi$ States of C_2H and the $X^1\Sigma^+$ State of C_2H^- from quartic force fields,” *The Journal of Physical Chemistry A*, vol. 119, pp. 7013–7025, 2015.
- [245] H. Kanamori, K. Seki, and E. Hirota, “Infrared diode laser kinetic spectroscopy of the cch radical 3 band,” *The Journal of Chemical Physics*, vol. 87, pp. 73–76, 1987.
- [246] E. N. Sharp-Williams, M. A. Roberts, and D. J. Nesbitt, “Dark state vibronic coupling in the $A(^2\Pi)$ - $X(^2\Sigma^+)$ band of ethynyl radical via high resolution infrared absorption spectroscopy,” *Physical Chemistry Chemical Physics*, vol. 13, pp. 17474–17483, 2011.
- [247] W. Chiang and Y. Hsu, “Laser spectroscopy of CCH in the 36600–39700 cm¹ region,” *The Journal of Chemical Physics*, vol. 111, pp. 1454–1461, 1999.
- [248] E. R. Grumbling and A. Sanov, “Photoelectron angular distributions in negative-ion photodetachment from mixed sp states,” *The Journal of Chemical Physics*, vol. 135, p. 164302, 2011.
- [249] R. M. Macrae, “Puzzles in bonding and spectroscopy: the case of dicarbon,” *Science Progress*, vol. 99, pp. 1–58, 2016.
- [250] S. Oliveira and N. Chaer, “Is there a quadruple bond in $C_2?$,” *Journal of Chemical Theory and Computation*, vol. 12, pp. 2234–2241, 2016.
- [251] U. Radius and F. Breher, “To boldly pass the metalmetal quadruple bond,” *Angewandte Chemie International Edition*, vol. 45, pp. 3006–3010, 2006.
- [252] R. Zhong, M. Zhang, H. Xu, and Z. Su, “Latent harmony in dicarbon between VB and MO theories through orthogonal hybridization of $3\sigma_g$ and $2\sigma_u$,” *Chemical Science*, vol. 7, pp. 1028–1032, 2016.
- [253] D. R. Huntley, G. Markopoulos, P. M. Donovan, L. Scott, and R. Hoffmann, “Squeezing C-C bonds,” *Angewandte Chemie (International ed. in English)*, vol. 44, pp. 7549–53, 2005.
- [254] C. J. Wu and E. A. Carter, “Ab initio thermochemistry for unsaturated C_2 hydrocarbons,” *The Journal of Physical Chemistry*, vol. 95, pp. 8352–8363, 1991.
- [255] P. J. Hay, W. J. Hunt, and W. A. Goddard, “Generalized valence bond description of simple alkanes, ethylene, and acetylene,” *Journal of the American Chemical Society*, vol. 94, pp. 8293–8301, 1972.
- [256] S. Shaik, D. Danovich, B. Braida, and P. C. Hiberty, “A Response to a Comment by G. Frenking and M. Hermann on: The Quadruple Bonding in C_2 Reproduces the Properties of the Molecule,” *Chemistry A European Journal*, vol. 22, pp. 18977–18980, 2016.

- [257] S. Shaik, D. Danovich, B. Braida, and P. C. Hiberty, “The quadruple bonding in C_2 reproduces the properties of the molecule,” *Chemistry: A European Journal*, vol. 22, pp. 4116–4128, 2016.
- [258] P. B. Karadakov and J. Kirsopp, “Magnetic shielding studies of C_2 and C_2H_2 support higher than triple bond multiplicity in C_2 ,” *Chemistry: A European Journal*, vol. 23, pp. 12949–12954, 2017.
- [259] K. P. Kepp, “Trends in Strong Chemical Bonding in C_2 , CN , CN^- , CO , N_2 , NO , NO^+ , and O_2 ,” *The Journal of Physical Chemistry A*, vol. 121, pp. 9092–9098, 2017.
- [260] W. Zou and D. Cremer, “ C_2 in a box: Determining its intrinsic bond strength for the $X^1\Sigma_g^+$ ground state,” *Chemistry: A European Journal*, vol. 22, pp. 4087–4099, 2016.
- [261] J. Grunenberg, “Quantum chemistry: Quadruply bonded carbon,” *Nature Chemistry*, vol. 4, pp. 154–155, 2012.
- [262] G. Frenking and M. Hermann, “Comment on the quadruple bonding in C_2 reproduces the properties of the molecule,” *Chemistry: A European Journal*, vol. 22, pp. 18975–18976, 2016.
- [263] D. L. Cooper, F. E. Penotti, and R. Ponec, “Why is the bond multiplicity in C_2 so elusive?,” *Computational and Theoretical Chemistry*, vol. 1053, pp. 189 – 194, 2015. Special Issue: Understanding structure and reactivity from topology and beyond.
- [264] G. M. Lloyd and P. Ewart, “High resolution spectroscopy and spectral simulation of C_2 using degenerate four-wave mixing,” *The Journal of Chemical Physics*, vol. 110, pp. 385–392, 1999.
- [265] C. F. Kaminski, I. G. Hughes, and P. Ewart, “Degenerate four-wave mixing spectroscopy and spectral simulation of C_2 in an atmospheric pressure oxy-acetylene flame,” *The Journal of Chemical Physics*, vol. 106, pp. 5324–5332, 1997.
- [266] M. Douay, R. Nietmann, and P. Bernath, “New observations of the $A^1\Pi_u - X^1\Sigma_g^+$ transition (phillips system) of C_2 ,” *Journal of Molecular Spectroscopy*, vol. 131, pp. 250 – 260, 1988.
- [267] M. Martin, “ C_2 spectroscopy and kinetics,” *Journal of Photochemistry and Photobiology A: Chemistry*, vol. 66, pp. 263 – 289, 1992.
- [268] M. Chan, S. Yeung, N. Wang, and C. Cheung, “Laser absorption spectroscopy of the $d^3\Pi_g \leftarrow c^3\Sigma_u^+$ transition of C_2 ,” *The Journal of Physical Chemistry A*, vol. 117, pp. 9578–9583, 2013.
- [269] M. Szwarc, “The determination of bond dissociation energies by pyrolytic methods.,” *Chemical Reviews*, vol. 47, pp. 75–173, 1950.
- [270] D. W. Arnold, S. E. Bradforth, T. N. Kitsopoulos, and D. M. Neumark, “Vibrationally resolved spectra of C_2-C_1 by anion photoelectron spectroscopy,” *The Journal of Chemical Physics*, vol. 95, pp. 8753–8764, 1991.

-
- [271] A. E. Bragg, R. Wester, A. V. Davis, A. Kammrath, and D. M. Neumark, “Excited-state detachment dynamics and rotational coherences of C_2^- via time-resolved photoelectron imaging,” *Chemical Physics Letters*, vol. 376, pp. 767 – 775, 2003.
 - [272] S. Shaik, H. S. Rzepa, and R. Hoffmann, “One molecule, two atoms, three views, four bonds?,” *Angewandte Chemie International Edition*, vol. 52, pp. 3020–3033, 2013.
 - [273] R. S. Mulliken, “The Interpretation of Band Spectra. Parts I, IIa, IIb,” *Review of Modern Physics*, vol. 2, pp. 60–115, 1930.
 - [274] A. Budó, “Die Rotationskonstanten B, D und Y der 3Π-Terme von TiO, C2, CO, PH, A1H, NH,” *Zeitschrift für Physik*, vol. 98, pp. 437–444, 1936.
 - [275] C. Amiot, J. Chauville, and J.-P. Maillard, “New analysis of the C_2 ballik-ramsay system from flame emission spectra,” *Journal of Molecular Spectroscopy*, vol. 75, pp. 19 – 40, 1979.
 - [276] B. D. Rehfuss, D. Liu, B. M. Dinelli, M. Jagod, W. C. Ho, M. W. Crofton, and T. Oka, “Infrared spectroscopy of carboions. IV. The $A^2\Pi_u - X^2\Sigma_g^+$ electronic transition of C_2^- ,” *The Journal of Chemical Physics*, vol. 89, pp. 129–137, 1988.
 - [277] S. P. Davis, M. C. Abrams, J. G. Phillips, and M. L. P. Rao, “Infrared bands of the C_2 phillips system,” *Journal of the Optical Society of America B*, vol. 5, pp. 2280–2285, 1988.
 - [278] K. R. Asmis, T. R. Taylor, and D. M. Neumark, “Anion photoelectron spectroscopy of bn,” *Chemical Physics Letters*, vol. 295, pp. 75 – 81, 1998.
 - [279] B. A. Laws, S. J. Cavanagh, B. R. Lewis, and S. T. Gibson, “NOO Peroxy Isomer Exposed with Velocity-Map Imaging,” *The Journal of Physical Chemistry Letters*, vol. 8, pp. 4397–4401, 2017.
 - [280] A. Sanov, E. R. Grumbling, D. J. Goebbert, and L. M. Culberson, “Photodetachment anisotropy for mixed s-p states: 8/3 and other fractions,” *The Journal of Chemical Physics*, vol. 138, p. 054311, 2013.
 - [281] J. M. Galbraith, E. Blank, S. Shaik, and P. C. Hiberty, “Π Bonding in Second and Third Row Molecules: Testing the Strength of Linus’s Blanket,” *Chemistry: A European Journal*, vol. 6, pp. 2425–2434, 2000.
 - [282] A. Amirav, A. Fialkov, and A. Gordin, “Improved electron ionization ion source for the detection of supersonic molecular beams,” *Review of Scientific Instruments*, vol. 73, pp. 2872–2876, 2002.